



Characterization of banded iron formations associated with gold mineralization: primary geochemical signatures and exploration implications

Blandine Gourcerol

► To cite this version:

Blandine Gourcerol. Characterization of banded iron formations associated with gold mineralization: primary geochemical signatures and exploration implications. Sciences of the Universe [physics]. Laurentian University, 2016. English. NNT: . tel-02569454

HAL Id: tel-02569454

<https://brgm.hal.science/tel-02569454>

Submitted on 11 May 2020

HAL is a multi-disciplinary open access archive for the deposit and dissemination of scientific research documents, whether they are published or not. The documents may come from teaching and research institutions in France or abroad, or from public or private research centers.

L'archive ouverte pluridisciplinaire **HAL**, est destinée au dépôt et à la diffusion de documents scientifiques de niveau recherche, publiés ou non, émanant des établissements d'enseignement et de recherche français ou étrangers, des laboratoires publics ou privés.

CHARACTERIZATION OF BANDED IRON FORMATIONS ASSOCIATED WITH GOLD
MINERALIZATION: PRIMARY GEOCHEMICAL SIGNATURES AND EXPLORATION
IMPLICATIONS

by

Blandine Gourcerol

A thesis submitted in partial fulfillment of the
requirements for the degree of
Doctor of Philosophy (PhD) in Mineral Deposits and Precambrian Geology

The Faculty of Graduate Studies
Laurentian University Sudbury,
Ontario, Canada

© Blandine Gourcerol, 2016

THESIS DEFENCE COMMITTEE/COMITÉ DE SOUTENANCE DE THÈSE

Laurentian University/Université Laurentienne
Faculty of Graduate Studies/Faculté des études supérieures

Title of Thesis
Titre de la thèse

CHARACTERIZATION OF BANDED IRON FORMATIONS ASSOCIATED
WITH GOLD MINERALIZATION: PRIMARY GEOCHEMICAL SIGNATURES
AND EXPLORATION IMPLICATIONS

Name of Candidate
Nom du candidat

Gourcerol, Blandine

Degree
Diplôme

Doctor of Philosophy

Department/Program
Département/Programme

Mineral Deposits and Precambrian Geology

Date of Defence

Date de la soutenance April 15, 2016

APPROVED/APPROUVÉ

Thesis Examiners/Examineurs de thèse:

Dr. Phil Thurston
(Supervisor/Directeur(trice) de thèse)

Dr. Daniel Kontak
(Co-supervisor/Co-directeur(trice) de thèse)

Dr. Steve Piercey
(Committee member/Membre du comité)

Dr. Chris McFarlane
(External Examiner/Examineur externe)

Dr. Pedro Jugo
(Internal Examiner/Examineur interne)

Approved for the Faculty of Graduate Studies
Approuvé pour la Faculté des études supérieures
Dr. David Lesbarrères
Monsieur David Lesbarrères
Dean, Faculty of Graduate Studies
Doyen, Faculté des études supérieures

ACCESSIBILITY CLAUSE AND PERMISSION TO USE

I, **Blandine Gourcerol**, hereby grant to Laurentian University and/or its agents the non-exclusive license to archive and make accessible my thesis, dissertation, or project report in whole or in part in all forms of media, now or for the duration of my copyright ownership. I retain all other ownership rights to the copyright of the thesis, dissertation or project report. I also reserve the right to use in future works (such as articles or books) all or part of this thesis, dissertation, or project report. I further agree that permission for copying of this thesis in any manner, in whole or in part, for scholarly purposes may be granted by the professor or professors who supervised my thesis work or, in their absence, by the Head of the Department in which my thesis work was done. It is understood that any copying or publication or use of this thesis or parts thereof for financial gain shall not be allowed without my written permission. It is also understood that this copy is being made available in this form by the authority of the copyright owner solely for the purpose of private study and research and may not be copied or reproduced except as permitted by the copyright laws without written authority from the copyright owner.

To the Algoma-type BIFs wherever they are,

without them this would not be possible

Abstract

Algoma-type banded iron formations (BIFs), which represent chemical sedimentary rocks characterized by alternating layers of iron-rich minerals and chert intercalated with Eoarchean to late Paleoproterozoic volcano-sedimentary sequences, act as a favorable host rock for orogenic gold mineralization within several Archean cratons (i.e., Pilbara, Kaapvaal, Superior, Slave and Churchill). Besides this economic aspect, these Fe-rich sequences have long been appreciated as an important contributor to furthering our understanding of the geochemical evolution of the Earth. However, these deposits are in general tectonically deformed, metamorphosed and dismembered, thus making reconstruction of their depositional setting and overall geologic setting difficult.

Based on four Canadian BIF-hosted gold deposits (the Meadowbank, Meliadine, Musselwhite and Beardmore-Geraldton deposits), this thesis aims to establish the depositional setting of the Algoma-type BIF using the abundance of REE+Y of chert material used as proxy of the primary signature, as well as assess gold enrichment processes based on textures and trace element zoning of variable sulfides (i.e., pyrite, arsenopyrite and pyrrhotite) and finally study if there is a particular geochemical type of Algoma-type BIF associated with gold mineralization.

Laser ablation-inductively coupled plasma-mass spectrometric (LA-ICP-MS) analyses performed on chert material suggest that BIFs from the four deposits show common depositional settings illustrated by deposition in semi-closed to closed basin under variable influence of high-temperature ($>250^{\circ}\text{C}$) hydrothermal fluids input and detrital contamination. Moreover, evidence of late diagenetic processes involving O isotopic exchange between chert precursor (i.e., opaline material) and seawater originated fluid have been documented. According to their primary

signature, it appears that barren versus mineralized BIFs do not show any geochemical divergence suggesting that the depositional setting may influence the epigenetic gold mineralization. Based on quantitative element distribution maps combined with line traverse and spot analyses by LA-ICP-MS on sulfides, a common gold mineralizing event characterized by intense stratabound sulfide-replacement of Fe-rich material was reported in three studied deposits exhibiting a Au-As-Se-Te-Ag element association. This result suggests that metamorphic/hydrothermal orogenic processes driven by devolatilization of a common weakly to unmetamorphosed source rock have led to generation of gold-bearing fluid which channelled into Algoma-type BIF via major crustal faults and/or shear zones within low tensile strength rocks.

Keywords

Banded iron formation, Precambrian, Algoma, geochemistry, gold, chert, deposition, seawater, hydrothermal footprint

Co-Authorship Statement

This thesis manuscript is the result of several collaborative projects in which co-authors provided supervision, scientific guidance, discussion and sample analysis and are therefore listed as co-authors in chapters 2 to 4.

As first authors of these chapters, I gathered field data, collected samples from the four deposits (i.e., Meadowbank, Musselwhite, Meliadine and Beardmore Geraldton), made petrographic analyses, prepared samples for geochemical analyses (e.g., LA ICP-MS, isotopic analysis), and developed the primary geochemical, isotopic and sulfide geochemical mapping interpretations by writing the first version of these chapters, and finally communicated with the journal editors from the submission through to the acceptance of the manuscript by the refereed scientific journal.

Dr. Olivier Côté-Mantha and John Biczok, respectively from Agnico Eagle Mines Ltd. and Goldcorp Canada Ltd., contributed by discussing the geological context of Meadowbank, Meliadine and Musselwhite, and reviewed the geological setting sections in chapters 2 and 3. Dr. Joseph A. Petrus from the Geochemical Fingerprinting Laboratory at Laurentian University in Sudbury contributed to the analytical method in chapter 4. Finally, Dr. Phillips C. Thurston and Dr. Daniel J. Kontak provided scientific guidance and extensive feedback on the hypotheses, interpretations and writing style for chapters 2 to chapters 4.

Acknowledgments

I would like to, firstly, acknowledge Dr. Phillips C. Thurston and Dr. Daniel J. Kontak for their outstanding support, guidance, confidence and patience over the four years of the project and their contributions in this final manuscript. It was a real pleasure to work with both of them from whom I have learned a lot and could not have imagined having better supervisors and mentors for this PhD study.

Besides my supervisors, I would like to thank Dr. H.L. Gibson, Dr. S.J. Piercey, Dr. Pedro Jugo and Dr. Chris McFarlane from my thesis committee for their insightful comments but also for the difficult questions which incited me to widen my research from various perspectives.

By virtue of their outstanding contributions and patience in the writing process of this manuscript, I would like to acknowledge also Dr. O. Côté-Mantha, J. Biczok and Dr. J.A. Petrus. In addition, a thank you to R. Sharp from the University of Manitoba, for his capable assistance during the oxygen isotope data acquisition and processing.

Input and continued support from the Geological Survey of Canada by Drs. B. Dubé, S. Castonguay, P. Mercier-Langevin, S. Pehrsson and C. Lawley was essential in completing this project and my sincere acknowledgement goes to the staff from Agnico Eagle Mines Ltd. and Goldcorp Ltd. and more particularly the Meadowbank and Meliadine regional exploration crews with whom I worked the three first summers of my PhD thesis and with whom, I hope to stay in touch in the future.

More personally, this thesis would not have been possible without the help and support I received from my Sudburian friends including Remy, Edda, Roxane, Tom, Fred, Hanna, Steve. Among them I would like to thank more particularly Heather and Laura for all the time spent together and all their support.

Je voudrais maintenant remercier énormément ma famille et plus particulièrement mes parents, mes sœurs ainsi que mes grands-parents sans lesquels je n'aurais jamais trouvé la motivation et la force de commencer (et de finir) ce doctorat. Vous êtes et serez toujours une grande source d'inspiration !

A mes amis, Emmanuelle et Nicolas, pour leur amitié tellement importante à mes yeux et leur soutien dans les beaux comme les mauvais jours m'évitant à de nombreuses reprises de faire une *Maleckite*.

Enfin, je remercie mon mari Eric Fournier pour son attention, son soutien, sa patience et son amour sans faille tout au long de cette aventure. *A nous !*

A Norah !

Table of Contents

Thesis Defence Committee.....	ii
Abstract	iv
Co-Authorship Statement	vi
Acknowledgments.....	vii
Table of Contents.....	ix
List of Tables	xvii
List of Appendices	xxiv
Chapter 1: Introduction to the Thesis.....	1
1.1 Statement of the problem	1
1.2 Background and critical review of literature.....	3
1.2.1 Geochemistry applied to BIF.....	3
1.2.2 Sulfide composition.....	5
1.3 Structure of the thesis.....	6
1.4 References	10
Chapter 2: Interpretations and implications of LA ICP-MS analysis of chert for the origin of geochemical signatures in banded iron formations (BIFs) from the Meadowbank gold deposit, Western Churchill Province, Nunavut	17
2.1 Abstract	17
2.2 Introduction	18

2.3 Geological setting	20
2.3.1 Mineralization	23
2.4 Analytical methods and data treatment	24
2.5 REE+Y systematics in BIF	26
2.6 Results	30
2.7 Summary and Discussion	34
2.7.1 Geochemical signatures for the BIFs at Meadowbank	34
2.7.2 Implications for the nature of gold mineralization in BIF at Meadowbank	37
2.7.3 Implications of the results for BIFs	38
2.8 Acknowledgements	39
2.9 Figures and captions	40
2.10 Tables and captions	53
2.11 References	2
Chapter 3: Depositional setting of Algoma-type BIF	11
3.1 Abstract	11
3.2 Introduction	12
3.3 Geological setting of the selected BIFs	14
3.3.1 The Meadowbank gold deposit	14
3.3.2 The Meliadine gold district	15
3.3.3 The Musselwhite gold deposit	15

3.3.4 The Beardmore-Geraldton gold district.....	16
3.4 Analytical Methods and data treatment	17
3.4.1 Scanning electron microscopy and <i>in-situ</i> LA-ICP-MS analysis	18
3.4.2 Oxygen isotopes	20
3.5 Background	22
3.5.1 Rare earth element and yttrium systematics	22
3.5.2 Oxygen isotopes	23
3.6 Results.....	24
3.6.1 Rare earth and yttrium systematics characteristics	24
3.6.2 Oxygen isotopes	30
3.7 Discussion	30
3.7.1 Rare earth element and yttrium systematics	30
3.7.2 Assessing the influence of high-temperature hydrothermal fluids	32
3.7.3 Sources and influence of detrital contamination.....	35
3.7.4 Mechanical versus biological processes controlling chert precipitation	40
3.7.5 Influence of post-depositional events on primary isotopic and trace element signature of the chert	46
3.8 Conclusions	49
3.9 Acknowledgements.....	51
3.10 Figures and captions	53

3.11 Tables and captions.....	8
3.12 References	8
Chapter 4: Gold and trace element distribution in sulfides from mineralized Algoma-type BIFs; Implications for nature of mineralizing fluids, metal sources and deposit models	
4.1 Abstract	23
4.2 Introduction	24
4.3 Geological setting of the selected BIFs	26
4.3.1 The Meadowbank deposit.....	26
4.3.2 The Meliadine gold district.....	29
4.3.3 The Musselwhite deposit	31
4.4 Analytical methods and data treatment.....	34
4.4.1 LA-ICP-MS sulfide trace element chemistry	34
4.4.2 Electron Backscattered Diffraction analysis	35
4.5 Results and interpretation.....	36
4.5.1 The Meadowbank deposit.....	36
4.5.2 The Meliadine gold district.....	41
4.5.3 The Musselwhite deposit	45
4.6 Discussion	48
4.6.1 LA-ICP-MS method: implications for identifying gold events and their chemical signature	48

4.6.2 Comparison of elemental association and implications for source reservoirs of gold mineralizing events	50
4.6.3 Influence of the stratigraphy	53
4.6.4 Influence of late deformation and metamorphism on gold mineralization	54
4.6.5 Source of Au	55
4.7 Conclusions	57
4.8 Acknowledgments	58
4.9 Figure captions	59
4.10 References	97
Chapter 5: Conclusions	112
5.1 Unreturned question and suggestion for future work	114
5.2 References	115
Appendix A: The geochemistry of chert from the Banded Iron Formation-type Musselwhite and Meadowbank gold deposits: Distinguishing primary and mineralization-related signatures of chert.....	117
A.1 Abstract	117
A.2 Résumé	118
A.3 Introduction	119
A.4 Geological Setting.....	120
A.4.1 The Superior Province	120

A.4.2 The Churchill Province.....	124
A.5 Analytical methods and data treatment	126
A.6 Review of REE+Y systematics in BIF.....	128
A.7 Results	130
A.7.1 Musselwhite	130
A.7.2 Meadowbank.....	134
A.8 Summary and Discussion	135
A.8.1 Implications for the depositional processes of BIFs.....	136
A.8.2 Implications for the gold mineralization.....	137
A.9 Acknowledgements.....	137
A.10 Figures and Captions.....	138
A.11 Table and captions	146
A.12 References	147
Appendix B: Do magnetite layers in Algoma-type BIF preserve their primary geochemical signature: A case study of samples from three Archean BIF-hosted gold deposits?.....	156
B.1 Abstract	156
B.2 Introduction.....	157
B.3 Geological setting of the selected BIFs.....	160
B.3.1 The Meadowbank gold deposit	160
B.3.2 The Meliadine gold district	160

B.3.3 The Musselwhite gold deposit.....	161
B.4 Sample description, analytical methods and data treatment.....	161
B.5 REE+Y Systematics	165
B.6 Additional major and trace element data.....	166
B.7 Discussion.....	167
B.7.1 Assessing the primary geochemical signature for magnetite layers.....	168
B.7.2 Assessing and comparing the primary geochemical signatures between chert and magnetite layers	169
B.7.3 Assessment of discriminant diagrams for magnetite layers.....	171
B.8 Conclusions	172
B.9 Acknowledgements	173
B.10 Figures and captions.....	174
B.11 Tables and captions	184
B.12 References.....	187
Appendix C: Chemical concordance of iron oxide and chert layers in Archean Algoma-type BIF: implications for Earth ocean chemistry.....	197
C.1 Abstract	197
C.2 Introduction.....	198
C.3 Materials and methods	199
C.4 Results	200

C.4.1 REE+Y systematics	200
C.4.2 Oxygen isotopes	201
C.5 Discussion.....	201
C.5.1 REE+Y systematics	201
C.6 Oxygen isotopes.....	202
C.6.1 Comparison and implications of the $\delta^{18}\text{O}$ and trace element data for chert	204
C.7 Conclusions	205
C.8 Acknowledgments.....	205
C.9 Figures and captions.....	207
C.10 References.....	211

List of Tables

Table 2.1: Deformation events in the Meadowbank area.....	53
Table 2.2: Metamorphic events in the Meadowbank area.....	54
Table 2.3: Abundances of elements and REE+Y for samples from Central BIF.....	1
Table 2.4: Abundances of elements and REE+Y for samples from the East BIF.....	1
Table 2.5: Abundances of elements and REE+Y for samples from the West IF.....	2
Table 2.6: Abundances of elements and REE+Y for samples from the Far West and Grizzly.....	3
Table 2.7: Estimated LOD values for the analyzed elements.....	1
Table 3.1: Abundances of elements and REE+Y for samples from Pump	9
Table 3.2: Abundances of elements and REE+Y for samples from F-Zone.....	10
Table 3.3: Abundances of elements and REE+Y for samples from Discovery	1
Table 3.4: Abundances of elements and REE+Y for samples from the 4B and 4E facies	1
Table 3.5: Abundances of elements and REE+Y for selected samples from the 4EA and 4F facies	2
Table 3.6: Abundances of elements and REE+Y for samples from the a-type facies	3
Table 3.7: Abundances of elements and REE+Y for samples from the b-type facies.....	4
Table 3.8: Abundances of elements and REE+Y for samples from the b-type facies.....	5
Table 3.9: Oxygen isotope compositions of microquartz	6
Table 3.10: Abundances of elements and REE+Y for KMG samples.....	7
Table A.1: Abundances of elements and REE+Y for samples from the 4F facies.....	146
Table B.1: Abundances of elements and REE+Y for magnetite samples from Meadowbank....	184
Table B.2: Abundances of elements and REE+Y for magnetite samples from Meliadine.....	185
Table B.3: Abundances of elements and REE+Y for magnetite samples from Musselwhite.....	186

List of Figures

Figure 2.1: Simplified regional geological map of the Rae and Hearne Domains	40
Figure 2.2: Geological map of the Meadowbank deposit area	41
Figure 2.3: Photographs of drill core (5 cm in length) and corresponding scanned polished-thin sections	43
Figure 2.4: Back-scattered electron image from the SEM for different samples from the Meadowbank BIFs	45
Figure 2.5: Shale (MUQ)-normalized REE+Y patterns illustrating the chemical signatures of the modern ambient seawater and hydrothermal vent fluid	46
Figure 2.6: Shale (MUQ) - normalized REE+Y patterns of chert sample (black circle) from Thurston et al. (2011), affected by variable concentration of residual contamination	47
Figure 2.7: Shale (MUQ) - normalized REE+Y patterns for chert samples	48
Figure 2.8: Geochemical data for chert samples from the West BIF.....	49
Figure 2.9: Geochemical data for chert samples from the Central BIF	51
Figure 2.10: Geochemical data for chert samples from the East BIF.....	52
Figure 3.1: Field and laboratory photographs of BIF	53
Figure 3.2: MUQ - normalized REE+Y patterns for BIF-hosted cherts from samples in different parts of the Meadowbank area	54
Figure 3.3: MUQ - normalized REE+Y patterns for BIF-hosted cherts from samples in different parts of the Meliadine gold district	55
Figure 3.4: MUQ - normalized REE+Y patterns for BIF-hosted chert from samples in different parts of the Musselwhite area	56
Figure 3.5: MUQ - normalized REE+Y patterns for BIF-hosted chert from samples in different	

parts of the Beardmore-Geraldton gold district	57
Figure 3.6: Variation in the $\delta^{18}\text{O}$ values versus analysis number for chert samples	58
Figure 3.7: Back-scattered electron image from the SEM for different BIF-hosted chert samples from the Meadowbank and Musselwhite	60
Figure 3.8: Binary plots of elemental ratio data (Eu/Sm and Sm/Yb) for chert samples	61
Figure 3.9: Trace element plots (La-Th-Sc and Cr/V and Y/Ni) used to constrain the provenance of detrital contamination	1
Figure 3.10: Binary plots of Y/Ho versus and $(\text{Pr}/\text{Sm})_{\text{MUQ}}$ for chert samples	1
Figure 3.11: Model of Algoma-type BIF deposition on Archean seafloor	3
Figure 3.12: Redox path for precipitation of Fe-oxyhydroxide by mixing of acidic to neutral seawater and alkaline hydrothermal fluids	4
Figure 3.13: Binary plots of Y/Y* and La/La* that illustrate the effect of Fe-oxyhydroxide precipitation	5
Figure 3.14: Plot of MUQ - normalized REE+Y patterns for experimentally produced Fe-oxyhydroxide	6
Figure 3.15: Diagram summarizing the variation of calculated values of $\delta^{18}\text{O}_{\text{chert}}$	7
Figure 4.1: Localization of the three deposits investigated in this study.	59
Figure 4.2: .Paragenetic chart for sulfides minerals and magnetite from BIFs in the Meadowbank deposit.	60
Figure 4.3: Reflected light photomicrographs of sulfide minerals from the Meadowbank deposit.	62
Figure 4.4: Paragenetic chart for sulfides minerals and magnetite from BIFs in the Meliadine gold district.	63

Figure 4.5: Reflected light photomicrographs of sulfide minerals from the Meliadine gold district.....	65
Figure 4.6: Paragenetic chart for sulfides minerals and magnetite from BIFs in the Musselwhite deposit.	66
Figure 4.7: Reflected light photomicrographs of sulfide minerals from the Musselwhite deposit.	67
Figure 4.8: LA ICP-MS maps showing the distribution of selected trace elements in pyrites from sample AMB-126223	68
Figure 4.9: Binary plot of Ag versus Ni (ppm) for selected pyrites from four different sediment-hosted gold deposits	69
Figure 4.10: Selected binary element plots (in ppm) illustrating the distribution of trace elements amongst variable pyrite events for sample AMB-126223.....	71
Figure 4.11: Summary of results for a LA ICP-MS traverse of a metamorphic pyrrhotite grain for sample AMB 126231	72
Figure 4.12: LA ICP-MS maps showing the distribution of selected trace elements in pyrites from sample AMB-126231.....	74
Figure 4.13: Selected element binary plots (in ppm) illustrating the distribution of trace elements amongst variable pyrite events for sample AMB-126231.....	76
Figure 4.14: LA ICP-MS maps showing the distribution of selected trace elements in pyrite from sample AMB-126228	77
Figure 4.15: Selected binary element plots (in ppm) illustrating the distribution of trace elements amongst variable pyrite events for sample AMB-126228.....	79
Figure 4.16: Binary element plot (in ppm) of Ag versus Pb using a compilation of individual	

time-slices of data from the pyrite trace element maps of samples AMB-126223 and AMB-126231	80
Figure 4.17: LA ICP-MS trace element profiles for a traverse done on an arsenopyrite grain in sample MEL-004	81
Figure 4.18: LA ICP-MS trace element profiles for a traverse done on an arsenopyrite grain in sample MEL-018	82
Figure 4.19: LA ICP-MS trace element profiles for a second traverse done on an arsenopyrite grain in sample MEL-018.....	83
Figure 4.20: LA ICP-MS trace element profiles for a traverse done on an arsenopyrite grain in sample MEL-018	84
Figure 4.21: Selected binary plots (in ppm) illustrating distribution of Au and Te content in various element associations from the compilation of traverses analyses done on arsenopyrite grains from the Meliadine gold deposit.....	86
Figure 4.22: LA ICP-MS trace element profiles for a traverse done on a pyrrhotite grain in sample E599654.....	88
Figure 4.23: LA ICP-MS trace element profiles for a traverse done on a pyrrhotite grain in sample E599658.....	90
Figure 4.24: Binary plot (in ppm) of Cu+Ag+Te+Se, representing Au element association in the pyrrhotite core, versus Pb+Bi, which represents Au element association in the pyrrhotite fractures	91
Figure 4.25: LA ICP-MS trace element profiles for a traverse done on a pyrite grain in sample E599658.....	93
Figure 4.26: Selected binary plots (in ppm) showing the distribution of Au and Te for pyrite data	

for sample E599658 from the Musselwhite deposit.....	94
Figure 4.27: Binary element plots (in ppm) of Ag versus Ni for py1 and py2 from the Musselwhite deposit along with the fields for different pyrites, as defined by Large et al. (2009).	95
Figure 4.28: Abundance of selected major and trace elements for py1 and py2 from the Musselwhite deposit.....	96
Figure A.1: Geological map of the Musselwhite area.....	138
Figure A.2: Plots of geochemical data for chert samples from the 4B unit	139
Figure A.3: Geochemical data for chert samples from the 4EA unit.....	140
Figure A.4: Geochemical data for chert samples from the 4E unit	141
Figure A.5: Geochemical data for chert samples from the 4F unit.....	142
Figure A.6: Plot of Th/U versus $(Ce/Ce^*)_{MUQ}$	143
Figure A.7: A plot of elemental ratio data (Eu/Sm and Sm/Yb)	144
Figure A.8: Influence of variable detrital contamination on chert samples	145
Figure B.1: Photographs at different scales that illustrate the nature of the BIFs in the field, their microscopic features and traces of the laser ablation traverses.	174
Figure B.2: Images showing typical Fe-oxide layers sampled for this study:.....	176
Figure B.3: Shale (MUQ) - normalized REE patterns for magnetite.....	177
Figure B.4: Spider-type plots summarize the abundances of major and trace-elements for magnetite	179
Figure B.5: Multi-element extended spider diagrams.....	180
Figure B.6: Shale (MUQ) - normalized REE distribution patterns for metalliferous sediments	181
Figure B.7: Binary plots of elemental ratio data (Eu/Sm and Sm/Yb) for magnetite samples and	

corresponding chert samples	182
Figure B.8: Genetic classification diagrams for magnetite from a variety of ore deposit settings	183
Figure C.1: Photographs taken at different scales that illustrate the nature of the layered chert and magnetite material in the BIFs from the Meliadine area that were used in this study.....	207
Figure C.2: Shale (MUQ) - normalized rare earth element (REE) patterns.....	208
Figure C.3: A histogram plot summarizing the $\delta^{18}\text{O}$ values for three chert samples from Meliadine	209
Figure C.4: Diagram summarizing the variation of calculated values of $\delta^{18}\text{O}_{\text{chert}}$	210

List of Appendices

Appendix A: The geochemistry of chert from the Banded Iron Formation-type Musselwhite and Meadowbank gold deposits: Distinguishing primary and mineralization-related signatures of chert.....	117
Appendix B: Do magnetite layers in Algoma-type BIF preserve their primary geochemical signature: A case study of samples from three Archean BIF-hosted gold deposits?.....	156
Appendix C: Chemical concordance of iron oxide and chert layers in Archean Algoma-type BIF: implications for Earth ocean chemistry.....	197

Chapter 1: Introduction to the Thesis

1.1 Statement of the problem

Gold mineralization in Archean greenstone belts represents an economically important commodity reflecting 13% of the world's gold resource (e.g., Pilbara, Kaapvaal, Zimbabwe, Superior, Slave and Churchill; Phillips et al., 1984; Goldfarb et al., 2001; Bleeker, 2006; Dubé and Gosselin, 2007; Biczok et al., 2012). Among the many types of gold deposits, the Algoma-type BIF illustrates a prime exploration target. In these deposits, gold is associated with simple- to complex networks of laminated quartz-carbonate fault-fill veins hosted within sulfidized parts of the BIF within regionally deformed, metamorphosed and dismembered BIF facies (i.e., oxide-, silicate- or carbonate-facies) of these terranes (e.g., the Homestake, Lupin, Morro Velho, Musselwhite deposits).

Algoma-type BIFs, which have long been appreciated as an important contributor to furthering our understanding of the geochemical evolution of the Earth (e.g., atmosphere and hydrosphere) consist of thinly bedded, chemical sedimentary rocks comprising alternating layers of iron-rich minerals and chert (Gross, 1980) typically intercalated with Eoarchean to late Paleoproterozoic volcano-sedimentary sequences within Archean greenstone belts (Goodwin, 1973; Bekker et al., 2010). The iron-bearing minerals are considered to have originally precipitated as iron oxyhydroxides, such as ferrihydrite, that were transformed during diagenesis to hematite, magnetite and siderite depending in part on the microbial biomass concentration (Posth et al., 2013). Where metamorphosed, the Fe-rich component may include more complex mineral assemblages that comprise a variety of silicate phases (e.g., amphibole, garnet). The

origin of the interbedded chert is controversial, but the consensus is that it may originate either as a seawater precipitate (Bolhar et al., 2005; Thurston et al., 2012), or as a hydrothermal precipitate (Allwood et al., 2010; Thurston et al., 2012) or due to replacement (Hanor and Duchac, 1990). A less common view suggests dissociation of iron silicates into iron oxides and colloidal silica (Lascelles, 2007). Only a few studies explain the alternation of iron-rich and chert bands either by the influence of biological processes and/or temperature variations (e.g., Posth et al., 2013) or by variations of the hydrothermal input (i.e., jasper under weak hydrothermal conditions and siderite under more intense hydrothermal conditions; Van Kranendonk et al., 2003).

Timing (syngenetic versus epigenetic) and the origin of gold within BIF-hosted gold deposits have long been subject of research and genetic debates over the last few decades. In the 1970s, some authors suggested a syngenetic origin characterized by sedimentary exhalative processes in which gold is concentrated in arsenian pyrite introduced into BIFs by hydrothermal fluids during chemical sedimentation or early diagenesis (e.g., Fripp et al., 1976). However, an epigenetic model is supported by the presence of replacement features (e.g., sulfide facies) and the discordant nature of vein systems typically observed in BIF-hosted gold deposits. Lately, the consensus favours an epigenetic (i.e., orogenic) model for gold mineralization related to metamorphic-hydrothermal processes in which BIF represents an efficient chemical trap by virtue of its high iron content for metal- and H₂S-rich fluids focused into favorable structural traps (e.g., fold hinges, shear zones; e.g., Phillips et al., 1984; Phillips and Powell, 2010; Poulsen et al., 2000). However, the source of the gold remains debatable (e.g., mafic volcanic versus sedimentary rocks versus a mantle; Phillips and Powell, 2010; Large et al., 2011; Frimmel and Hennigh, 2015).

In the context outline above, this thesis originated through the Targeted Geoscience Initiative-4 (TGI-4) program of the Geological Survey of Canada (Lode Gold project) and a NSERC Collaborative Research and Development project with funding from Agnico-Eagle Mines Ltd and Goldcorp Inc., was designed to address the fundamental issue of whether there is a particular geochemical type of BIF, that has a greater potential to host gold mineralization. If the latter, then this would be a very opportunistic exploration tool. In detail, this thesis aims to: (1) identify where feasible the primary geochemical signature of BIF and define its depositional setting; (2) based on the latter, assess if one geochemical type of BIF is associated preferentially with Au mineralization; and finally (3) provide insights into understanding of the gold mineralizing processes and its possible identify elemental associations indicative of source reservoirs.

In order to address the above questions, four world-class Canadian gold deposits were studied: (1) the ~4 Moz Au Meadowbank deposit, hosted by the 2.71 Ga Woodburn Lake greenstone belt; (2) the ≥ 2.8 Moz Au Meliadine district, hosted by the 2.6 Ga Rankin Inlet greenstone belt; (3) the ~6 Moz Au Musselwhite deposit, hosted by the 2.9-3 Ga North Caribou greenstone belt; and (4) the ~4 Moz Au Beardmore-Geraldton district, hosted by the 2.7 Ga eponymous greenstone belt (e.g., Dubé et al., 2015).

1.2 Background and critical review of literature

1.2.1 Geochemistry applied to BIF

Geochemical indicators, such as the REE+Y signature, when applied to carefully selected chert bands from Algoma-type BIF (i.e. representing the component least affected by diagenesis and metamorphism; Krapez et al., 2003), provide information that permits one to constrain the

origin of the BIF (e.g. Barrett et al., 1988; Bolhar et al., 2005; Thurston et al., 2012). The abundance of REE+Y are controlled by three possible processes, namely precipitation from open marine seawater (e.g. Bau and Dulski, 1996), precipitation from hydrothermal fluids (e.g. Allwood et al., 2010; Danielson et al., 1992), or replacement processes (e.g. Hanor and Duchac, 1990). All of these aforementioned processes can be further influenced by input of terrigenous material (Alexander et al., 2008) and oceanographic processes, such as precipitation of phosphates (e.g., Pufahl and Hiatt, 2012).

The treatment of chemical data for BIF departs from that of most other rock types (e.g., chondritic plots or mantle normalized spidergrams) and, instead, it is customary to normalize samples to shale specifically with the Mud from Queensland (MUQ) standard (Kamber et al., 2005; Lawrence and Kamber, 2006) now widely referenced in order to decrease the influence of terrigenous input. The MUQ represents a bimodal felsic and mafic volcanic provenance similar to the provenance of detritus in an Archaean granite greenstone belt (Kamber et al., 2005; Lawrence and Kamber, 2006). Yttrium is included with the rare earth element owing to its similar chemistry due to a valence of 3+, though it is not a lanthanide, therefore it is inserted into the conventional rare earth diagram between Dy and Ho.

Due to the anoxic character of Archean seawater, the shale normalized REE and Y patterns for Archean seawater are very similar to modern seawater except the lack of a negative Ce anomaly (Planavsky et al., 2010). Therefore, an Archean seawater pattern normalized to MUQ is characterized by: (1) depletion in LREE relative to middle and heavy REE; (2) a strongly superchondritic Y/Ho ratio due to superchondritic Y content; (3) positive La and Gd anomalies; and (4) a variable, but well developed positive Eu anomaly (Kamber et al., 2004)

Positive La, Y and Gd anomalies indicate precipitation from seawater under anoxic conditions (absence of a negative Ce anomaly) in oceans, whereas the presence of a positive Eu anomaly reflects the influence of high temperature ($> 250^{\circ}\text{C}$) hydrothermal fluids (Kamber et al., 2004).

Previous research at Laurentian University directed by Thurston and Kamber (Baldwin, 2009; Baldwin et al., 2011; Thurston et al., 2012) has geochemically characterized the BIF chert in the Abitibi Greenstone Belt where BIF represents a cap on each mafic-felsic cycle, especially in the ca. 2730 Ma Deloro Assemblage. This work focused on REE+Y and other trace elements and confirmed the previous REE+Y systematics. The present study is thus a continuation of this work and will be the first examination of Algoma-type BIF associated with gold mineralization and the first to relate chert chemistry to proximity to mineralization. Frei et al. (2008) have shown that Au-mineralized BIF at the Homestake mine exhibits LREE enrichment and subdued Eu anomalies, hence indicating of an external source for the sulfides. This study did not consider the development of a footprint of hydrothermal alteration at a broader scale, nor did the study attempt to develop a vectoring tool.

A study of the geochemical characteristics of Algoma-type-BIF may yet define a vectoring tool to proceed from barren or unaltered BIF to altered- and gold mineralized zones, thereby establishing the pre-mineralization composition of BIF to allow a better characterization and understanding of the mineralizing processes and geochemical footprint of any hydrothermal system.

1.2.2 Sulfide composition

In recent years with the advent of LA ICP-MS mapping capability, Large et al. (2007, 2009,

2011) suggested that gold in some sediment-hosted gold deposits (e.g., black shale unit from the Sukhoi Log deposit; turbiditic sandstone facies from the Bendigo deposit) likely originated within the crystal structure of syn-sedimentary to early-diagenetic fine-grained and/or framboidal arsenian pyrite along with a specific suite of trace elements (As, Ni, Pb, Zn, Mo, Te, V, Se). Due to subsequent burial, deformation and metamorphism (i.e., greenschist facies), in addition to granite intrusion, gold and other metals are released from the pyrite lattice (which may be converted into coarse-grained metamorphic pyrrhotite) and/or host rock via structural channels into favorable structural sites by a metal-rich hydrothermal fluid (Large et al., 2011, Bull et al., 2015), which precipitates gold along with various other sulfides such as coarse-grained arsenopyrite, a common mineral phase in sediment-hosted gold systems (e.g., Wagner et al., 2007; Cook et al., 2013). In this context, an important question is whether gold in the BIF-hosted gold deposits originates from the same or similar source rock (i.e., black shale) and may represent a similar process in terms of gold enrichment and deposit formation (e.g., Steadman et al., 2014; Gao et al., 2015).

1.3 Structure of the thesis

This thesis is written in a non-traditional format and is divided into 4 chapters, in which chapters 2 to 4 represent manuscripts for publication in the highest caliber, international, peer-reviewed scientific journals. It is noted that it is inevitable that these chapters may overlap in their introduction due to their preparation as individual papers, and the necessity to introduce the areas and materials in all cases. In addition, there is also reference made to the previous chapters in some instances due to their sequential publication.

The first chapter introduces the research problem and thesis objectives in addition to a brief

review of the critical literature relevant to the project. Moreover, it introduces the thesis and summarizes the following chapters.

Chapter 2, entitled “Interpretations and implications of LA ICP-MS analysis of chert for the origin of geochemical signatures in banded iron formations (BIFs) from the Meadowbank gold deposit, Western Churchill Province, Nunavut” has been published by *Chemical Geology* (2015, *Chemical Geology*, v. 410, p. 89-107) and was written by B. Gourcerol, P.C. Thurston, D.J. Kontak and O. Côté-Mantha. This chapter represents the first step of the project and gives an overview of the methodology applied to all the studied deposits in order to address how chert lithogeochemistry can be used to better understand the nature and origin of Algoma-type BIF-hosted gold deposits. In detail, this chapter examines similarities and/or differences between mineralized and apparently non-mineralized BIFs based on their geochemical signature and petrographic study in order to establish if there is a geochemical signature for the types of BIF that contain gold mineralization and whether a hydrothermal footprint for the mineralization can be detected. It is noted that this chapter is largely based on Gourcerol, B., Thurston, P.C., Kontak, D.J., and Côté-Mantha, O. 2014. Interpretations and implications of preliminary LA ICP-MS analysis of chert for the origin of geochemical signatures in banded iron formations (BIFs) from the Meadowbank gold deposit, Western Churchill Province, Nunavut: Geological Survey of Canada, Current research 2014-1, 26 p. doi:10.4095/293129.

Chapter 3, entitled “Depositional setting of Algoma-type banded iron formation” written by B. Gourcerol, P.C. Thurston, D.J. Kontak, O. Côté-Mantha, and J. Biczok was submitted to *Precambrian Research* and was accepted with revisions required. The revised manuscript has since been returned to the journal as of January 2016. In this chapter, the authors attempt to validate the restricted-basin model as a depositional setting for the Algoma-type BIFs by using

the geochemical signature of the chert bands as a proxy for the primary signature of ocean water chemistry and hydrothermal vent fluids. In addition, the cherts were analyzed *in-situ* using secondary ion mass spectrometry (SIMS) to determine their $\delta^{18}\text{O}$ signature in order to assess post deposition exchange of the chert with later fluids (e.g., diagenetic, metamorphic). An indirect intent of this study was also to establish whether chert beds in these settings retain a geochemical signature that may relate to a subsequent gold mineralizing event. In detail, these hypotheses were tested by: (1) defining the role of chemical reservoirs (i.e., seawater, hydrothermal fluids, and terrestrial detritus) in chert deposition; and (2) using redox-sensitive Ce behavior to assess the oxygenation state of the water column during chert precipitation. It is noted that minor parts of this chapter were published in Gourcerol, B., Thurston, P.C., Kontak, D.J., Côté-Mantha, O., and Biczok, J. 2015. Depositional Setting of Algoma-type Banded Iron Formation from the Meadowbank, Meliadine and Musselwhite gold deposits: *In: Targeted Geoscience Initiative 4: Lode Gold Project Synthesis*, (Eds.) B. Dubé and P. Mercier-Langevin; Geological Survey of Canada, Open File 7852, p. 55-68. doi:10.13140/RG.2.1.1333.2645

Chapter 4, entitled “Gold and trace element distribution in sulfides from mineralized Algoma-type BIFs; Implications for nature of mineralizing fluids, metal sources and deposit models”, was written by B. Gourcerol, D.J. Kontak, P.C. Thurston and J.A. Petrus is formatted to be submitted to *Economic Geology*. This chapter examines the textures and trace element contents and internal zoning of variable sulfides such as pyrite, pyrrhotite and arsenopyrite to evaluate the potential source of metals within three Canadian BIF-hosted gold deposits: (1) the ~4 Moz Au Meadowbank deposit; (2) the ≥ 2.8 Moz Au Meliadine district; and (3) the ~6 Moz Au Musselwhite deposit. These deposits are hosted by Algoma-type BIFs and occur in metamorphosed and moderately to strongly deformed greenstone belts and are considered

orogenic gold deposits. In detail, this study investigates: (1) the distribution of gold and various trace elements in the sulfide lattice in order to identify similarities and differences in the timing and elemental associations of gold mineralization from the three deposits; and (2) compare these features to other orogenic deposits, such as clastic sediment-hosted gold deposits to investigate a potential source of gold.

Finally, chapter 5 concludes this thesis manuscript.

Appendix A comprises a GSC Current Research report written by B. Gourcerol, P.C., Thurston, D.J., Kontak, O., Côté-Mantha, and J., Biczok in 2015 entitled “The geochemistry of chert from the Banded Iron Formation-type Musselwhite and Meadowbank gold deposits: Distinguishing primary and mineralization-related signatures of chert” (Current Research 2015-1, 24 p. doi: 10.4095/295531). This report was not part of any of the previously described chapters and presents the results of *in-situ* laser ablation inductively coupled mass spectrometric (LA-ICP-MS) analysis of chert from the Musselwhite and Meadowbank BIF-hosted lode-gold deposits.

Appendix B comprises a manuscript submitted to *Canadian Mineralogist* entitled “Do magnetite layers in Algoma-type BIF preserve their primary geochemical signal: A case study of samples from three Archean BIF-hosted gold deposits?” written by B. Gourcerol, D.J. Kontak, P.C. Thurston and Q. Duparc. The main objective of this study was to assess the potential of using the REE + Y systematics of magnetite bands to identify their primary geochemical signature, as we have done for the associated cherts in order to constrain the genesis of BIF units. As of December 2015, the revised paper had been returned to the journal and is in press.

Lastly, Appendix C entitled “Chemical concordance of chert and iron-oxide layers in Archean Algoma-type BIF: implications for Earth ocean chemistry” and written by B. Gourcerol, D.J., Kontak and P.C., Thurston (2015), has been submitted to *Geology*. The main objective of this study was to explore the influence of post-depositional processes on the primary signal of chert and iron-oxide layers from several BIF horizons, within the Meliadine gold district (Churchill province, Canada). This study combined three sets of data on the same BIF samples: (1) REE+Y studies on the chert layers to determine the genesis of the cherts; (2) REE+Y study of the magnetite layers to establish whether diagenetic changes affect their systematics; and (3) an oxygen isotope study to establish the diagenetic history on the chert bands and possible influence of later hydrothermal fluids. The study provides the first integration of these data sets to document chemical concordance in the chert and magnetite layers, which validates the earlier results of this thesis, and to show that despite the modification of the oxygen isotopic composition of the chert the primary geochemical signature has remained intact.

1.4 References

- Alexander, B.W., Bau, M., Andersson, P. and Dulski, P., 2008. Continentally-derived solutes in shallow Archean sea water; rare earth element and Nd isotope evidence in iron formation from the 2.9 Ga Pongola Supergroup, South Africa; *Geochimica et Cosmochimica Acta*, v. 72, p. 378-394.
- Allwood, A.C., Kamber, B.S., Walter, M.R., Burch, I.W. and Kanik, I., 2010. Trace element record depositional history of an Early Archean stromatolitic carbonate platform; *Chemical Geology*, v. 270, p. 148-163.
- Barrett, T.J., Fralick, P.W. and Jarvis, I., 1988. Rare-earth-element geochemistry of some

Archean iron formations north of Lake Superior, Ontario: Canadian Journal of Earth Sciences, v. 25, p. 570–580.

Baldwin, G.J., 2009. The sedimentology and geochemistry of banded iron formations of the Deloro Assemblage, Bartlett Dome area, Abitibi greenstone belt, Ontario, Canada: implications for BIF deposition and greenstone belt formation; Unpublished Master's Thesis, Laurentian University, 116 p.

Baldwin, G.J., Thurston, P.C. and Kamber, B.S., 2011. High-precision rare earth element, nickel, and chromium chemistry of chert micro bands pre-screened with in-situ analysis; Chemical Geology, v. 285, p.133-143.

Bau, M. and Dulski, P., 1996. Distribution of Y and rare-earth elements in the Penge and Kuruman Iron Formations, Transvaal Supergroup, South Africa; Precambrian Research, v. 79, p. 37-55.

Bekker, A., Slack, J.F., Planavsky, N., Krapez, B., Hofmann, A., Konhauser, K.O. and Rouxel, J., 2010. Iron formation: the sedimentary product of a complex interplay among mantle, tectonic, oceanic and biospheric processes; Economic Geology, v. 105, p. 467-508.

Biczok, J., Hollings, P., Klipfel, P., Heaman, L., Maas, R., Hamilton, M., Kamo, S. and Friedman, R., 2012. Geochronology of the North Caribou greenstone belt, Superior Province Canada: Implications for tectonic history and gold mineralization at the Musselwhite mine; Precambrian Research, v. 192-195, p. 209-230.

Bleeker, W., 2006. The Slave Craton: Geological and Metallogenic Evolution. In Goodfellow, W.D. (Ed.), Mineral Resources of Canada: A Synthesis of Major Deposit-types, District

Metallogeny, the Evolution of Geological Provinces, and Exploration Methods", Geological Survey of Canada.

Bolhar, R., Van Kranendonk, M.J. and Kamber, B.S., 2005. A trace element study of siderite-jasper banded iron formation in the 3.45 Ga Warrawoona Group, Pilbara craton-Formation from hydrothermal fluids and shallow seawater; *Precambrian Research*, v. 137, p. 93-114.

Cook, N.J., Ciobanu, C.L., Meria, D., Silcock, D. and Wade, B., 2013. Arsenopyrite-Pyrite Association in an Orogenic Gold Ore: Tracing Mineralization History from Textures and Trace Elements; *Economic Geology*, v. 108, p. 1273-1283.

Danielson, A., Moeller, P. and Dulski, P., 1992. The europium anomalies in banded iron formations and the thermal history of the oceanic crust; *Chemical Geology*, v. 97, p. 89-100.

Dubé, B., Mercier-Langevin, P., Castonguay, S., McNicoll, V.J., Bleeker, W., Lawley, C.J.M., De Souza, S., Jackson, S.E., Dupuis, C., Gao, J.-F., Bécu, V., Pilote, P., Goutier, J., Beakhouse, G.P., Yergeau, D., Oswald, W., Janvier, V., Fontaine, A., Pelletier, M., Beauchamp, A.-M., Katz, L.R., Kontak, D.J., Tóth, Z., Lafrance, B., Gourcerol, B., Thurston, P.C., Creaser, R.A., Enkin, R.J., El Goumi, N., Grunsky, E.C., Schneider, D.A., Kelly, C.J. and Lauzière, K., 2015. Precambrian lode gold deposits - a summary of TGI-4 contributions to the understanding of lode gold deposits, with an emphasis on implications for exploration: *In: Targeted Geoscience Initiative 4: Contributions to the Understanding of Precambrian Lode Gold Deposits and Implications for Exploration*, (Eds.) B. Dubé and P. Mercier-Langevin; Geological Survey of Canada, Open File 7852, p. 1–24.

Dubé, B. and Gosselin, P., 2007, Greenstone-hosted quart-carbonate vein deposits; *Geological*

Association of Canada, Mineral Deposits Division, Special Publication 5, p. 49–73.

Frei, R., Dahl, P.S., Duke, E.F., Hansen, T.R., Frandsson, M.M. and Jensen, L.A., 2008. Trace element and isotopic characterization of Neoarchean and Paleoproterozoic iron formations in the Black Hills (South Dakota USA): assessment of chemical change during 2.9-1.9 Ga deposition bracketing the 2.4-2.2 Ga first rise of atmospheric oxygen; *Precambrian Geology*, v. 162, p. 441-474.

Frimmel, H.E. and Hennigh, Q., 2015. First whiffs of atmospheric oxygen triggered onset of crustal gold cycle; *Miner Deposita*, v. 50, p. 5-23.

Fripp, R.E.P., 1976. Stratabound gold deposits in Archean banded iron formation, Rhodesia; *Economic Geology*, v. 71, p. 58-75.

Goldfarb, R.J., Baker, T., Dubé, B., Groves, D.I., Hart, C.J.R. and Gosselin, P., 2005.

Distribution, character and genesis of gold deposits in metamorphic terranes. In: *Economic Geology 100th Anniversary Volume*, J.W. Hedenquist, J.F.H. Thompson, R.J. Goldfarb, and J.P. Richards (eds.), p. 407-450. Goldfarb, R.J., Groves, D.I. and Gardoll, S. 2001, Orogenic gold and geologic time: A global synthesis: *Ore Geology Reviews*, v. 18, p. 1–75.

Gao, J.-F., Jackson, S.E., Dubé, B., Kontak, D.J. and De Souza, S., 2015. Genesis of the Canadian Malartic, Côté Gold, and Musselwhite gold deposits: Insights from LA-ICP-MS element mapping of pyrite; *In: Targeted Geoscience Initiative 4: Contributions to the understanding of Precambrian Lode Gold Deposits and Implications for Exploration*, (ed.) B. Dubé and P. Mercier-Langevin; Geological Survey of Canada, Open File 7852, p. 157-175.

Goodwin, A.M., 1973. Archean iron-formations and tectonic basins of the Canadian Shield;

- Economic Geology, v. 68, p. 915-933.
- Gross, G.A., 1980. A classification of iron-formations based on depositional environments; Canadian Mineralogist, v. 100, p. 1511-1527.
- Hanor, J.S. and Duchac, K.C., 1990. Isovolumetric silicification of early Archean komatiites; geochemical mass balances and constraints on origin; Journal of Geology, v. 98, p. 863-877.
- Kamber, B.S., Greig, A. and Collerson, K.D., 2005. A new estimate for the composition of weathered young upper continental crust from alluvial sediments, Queensland, Australia; Geochimica et Cosmochimica Acta, v. 69, p. 1041-1058.
- Krapez, B., Barley, M.E. and Pickard, A.L., 2003. Hydrothermal and resedimented origins of the precursor sediments to banded iron formation: sedimentological evidence from the Early Palaeoproterozoic Brockman Supersequence of Western Australia; Sedimentology, v. 50, p. 979-1011.
- Large, R.R., Bull, S.W. and Maslennikov, V.V., 2011. A Carbonaceous Sedimentary Source-Rock Model for Carlin- Type and Orogenic Gold Deposits; Economic Geology, v. 106, p. 331-358.
- Large, R.R., Danyushevsky, L., Hollit, C., Maslennikov, V., Meffre, S., Gilbert, S., Bull, S., Scott, R., Emsbo, P., Thomas, H., Singh, B. and Foster, J., 2009. Gold and Trace Element Zonation in Pyrite Using a Laser Imaging Technique: Implications for the Timing of Gold in Orogenic and Carlin-Style Sediment-Hosted Deposits; Economic Geology, v. 104, p. 635-668.

- Large, R.R., Maslennikov, V.V., Robert, F., Danyushevsky, L.V. and Chang, Z., 2007. Multistage sedimentary and metamorphic origin of pyrite and gold in the Giant Sukhoi Log Deposit, Lena Gold Province, Russia; *Economic Geology*, v. 102, p. 1233-1267.
- Lascelles, D.F., 2007. Black smokers and density currents; an uniformitarian model for the genesis of banded iron formations; *Ore Geology Reviews*, v. 32, p. 381-411.
- Lawrence, M. G. and Kamber, B. S., 2006. The behavior of the rare earth elements during estuarine mixing- revisited; *Marine Chemistry*, v. 100, p. 147-161.
- Phillips, G.N. and Powell, R., 2010. Formation of gold deposits: a metamorphic devolatilization model; *Journal of metamorphic geology*, v. 28, p. 689-718.
- Phillips, G.N., Groves, D.N. and Martyn, J.E., 1984. An epigenetic origin for Archean banded iron formation-hosted gold deposits; *Economic Geology*, v. 79, p. 162-171.
- Poulsen K.H., Robert, F. and Dubé, B., 2000. Geological classification of Canadian gold deposits; *Geological Survey of Canada, Bulletin 540*, 106 p.
- Pufahl, P.K. and Hiatt, E.E., 2012. Oxygenation of the Earth's atmosphere-ocean system: A review of physical and chemical sedimentologic sequence; *Marine and Petroleum Geology*, v. 32, p. 1-20.
- Planavsky, N., Bekker, A., Rouxel, O.J., Kamber, B.S., Hofmann, A.W., Knudsen, A. and Lyons, T.W., 2010. Rare Earth Element and yttrium compositions of Archean and Paleoproterozoic Fe formations revisited: New perspectives on the significance and mechanisms of deposition; *Geochimica et Cosmochimica Acta*, v. 74, p. 6387-6405.

- Posth, N.R., Kohler, I., Swanner, E.D., Schroder, C., Wellmann, E., Binder, B., Konhauser, K.O., Neumann, U., Berthold, C., Nowak, M. and Kappler, A., 2013. Simulating Precambrian banded iron formation diagenesis; *Chemical Geology*, v. 362, p. 66-73.
- Steadman, J.A., Large, R.R., Davidson, G.J., Bull, S.W., Thompson, J., Ireland, T. R. and Holden P., 2014. Paragenesis and composition of ore minerals in the Randalls BIF-hosted gold deposits, Yilgarn Craton, Western Australia: Implications for the timing of deposit formation and constraints on gold sources; *Precambrian Research*, v. 243, p. 110-132.
- Thurston, P.C., Kamber, B.S. and Whitehouse, M., 2012. Archean cherts in banded iron formation: Insight into Neoproterozoic ocean chemistry and depositional processes; *Precambrian Research*, v. 214-215, p. 227-257.
- Van Kranendonk, M. J., Webb, G.E. and Kamber, B.S., 2003. Geological and trace element evidence for a marine sedimentary environment of deposition and biogenicity of 3.45 Ga stromatolitic carbonates in the Pilbara Craton, and support for a reducing Archean ocean; *Geobiology*, v. 1, p. 91-108.
- Wagner, T., Klemm, R., Wenzel, T. and Mattson B., 2007. Gold upgrading in metamorphosed massive sulfide ore deposits: direct evidence from laser-ablation-inductively coupled plasma-mass spectrometry analysis of invisible gold; *Geology*, v. 35, n. 9, p. 775-778.

Chapter 2: Interpretations and implications of LA ICP-MS analysis of chert for the origin of geochemical signatures in banded iron formations (BIFs) from the Meadowbank gold deposit, Western Churchill Province, Nunavut

2.1 Abstract

Among the many types of mineral deposits within Archean cratons, gold mineralization is an important economic commodity with over 20 000 metric tons of gold produced from greenstone belts in 2001. Of the Archean-early Paleoproterozoic gold deposits, several different types of mineralization are known, which includes the important Algoma-type Banded Iron Formation (BIF) where gold is locally associated with sulfide-facies zones within regionally extensive oxide-facies. It is commonly accepted that the shale-normalized chemical signature of REE+Y of chert bands in Algoma-type BIFs may reflect one of three processes, each of which may be relevant to the nature and origin of the gold mineralization: (1) direct seawater precipitation, (2) involvement of and contribution from hydrothermal fluids, and (3) replacement of precursor volcanic units due to silicification. An essential question in regards to the mineralization is, therefore, whether the gold mineralizing fluids have a preference for one geochemical type of iron formation versus another. In order to assess the relevance of these competing models, we report herein the results of a LA ICP-MS study of chert samples within different Algoma-type BIFs from the Meadowbank deposit (24.5 Mt proven/probable ore reserves grading 2.8 g/t, 2011) hosted in the Neoarchean Woodburn Lake Group of the Rae Domain of the western Churchill Province, Canada. This study used 39 carefully selected and characterized (i.e., petrography and SEM-EDS imaging) chert samples from the main deposit, the Central BIF, and four additional BIFs, the Far West, West, East and Grizzly zones, with data collected using line traverses along

the chert bands. The geochemical data indicate that an ambient seawater signature (i.e., enrichment in HREE relative to LREE associated with positive La and Y anomalies) dominates the samples with a lesser hydrothermal component (characterized by a positive Eu anomaly) and the influence of detrital contamination can also be detected. These initial results indicate that the methodology and protocol employed provides a reliable means to assess and interpret the chemical signature of BIFs hosting gold mineralization. In the present case, the results for the Meadowbank deposit suggest that chert from mineralized BIF units do not record a typical chemical signature that may be used as a vector for potential gold mineralization.

2.2 Introduction

Algoma-type BIFs are thinly bedded chemical sedimentary rocks comprising alternating layers of iron-rich minerals and chert (James, 1954), which are stratigraphically associated with submarine, volcanic rocks in Eoarchean to Paleoproterozoic greenstone belts (Goodwin, 1973; Bekker et al., 2010). Studies of gold deposits associated with Algoma-type BIF in Archean cratons have shown that gold is associated with localized sulfide-facies zones within regionally extensive oxide-facies units (e.g., Kaapvaal, Zimbabwe, Superior, Slave and Churchill; Phillips et al., 1984; Bleeker, 2006; Biczok et al., 2012). The depositional and geodynamic settings of these deposits are contentious due to post depositional overprinting and the absence of modern analogues. The iron-bearing minerals in iron formations precipitated from basin waters and hydrothermal fluids; they include siderite or/and iron oxyhydroxides that were transformed by diagenesis and metamorphism to hematite, magnetite, iron silicates and sulfides. The origin of chert is controversial, but the consensus is that it, like the iron-bearing minerals, originated as either a seawater (e.g., Bolhar et al., 2005; Thurston et al., 2012) or hydrothermal (e.g., Allwood et al., 2010; Thurston et al., 2012) precipitate or by replacement of a precursor volcanic unit due

to silicification (e.g., Hanor and Duchac, 1990).

In regard to the origin of Algoma-type BIF-hosted gold deposits, an important question is whether the gold mineralizing fluids have a preference for one geochemical type of iron formation versus another? Lode-gold and BIF-hosted gold deposits are both widely conceded to be epigenetic (Goldfarb et al., 2001, 2005), thus, at a regional scale, the geochemical signature of BIFs, using chert chemistry as a proxy for this, may perhaps provide a vector towards zones with an enhanced potential to host gold mineralization. Therefore, a study of the geochemical characteristics of Algoma-type BIF, both barren and those associated with gold mineralization, may prove useful in addressing important issues regarding these deposits by: (1) providing insight into which, if any, type of iron formation is a preferred host for gold mineralization by first identifying and then using the pre-mineralization chemical signal; (2) provide insights into understanding of the mineralizing processes; (3) possibly providing a geochemical footprint of the mineralized system; and (4) if the aforementioned latter exists then providing a vectoring tool from least or unaltered to altered-mineralized zones.

This article presents the results of *in-situ* laser ablation inductively coupled plasma mass spectrometry (LA ICP-MS) study of chert from several BIF zones (i.e., Far West, West IF, Central BIF, East BIF and Grizzly) within the Meadowbank gold deposit in the western Churchill Province of northern Canada (Fig. 2.1). The greenstone belt is characterized by a bimodal volcanism with minor metasedimentary rocks (e.g., Armitage et al., 1996; Pehrsson et al., 2000, 2004; Sherlock et al., 2001a, b, 2004; Hrabí et al., 2003). Since its original discovery, several regional mapping programs (Henderson and Henderson, 1994; Zaleski et al., 1997a, b; Zaleski et al., 1999a, b; Sherlock et al., 2001a, b) and deposit scale studies (Armitage et al., 1996; Pehrsson et al., 2000, 2004; Sherlock et al., 2001a, b, 2004; Hrabí et al., 2003) have been

conducted, which, provide the geological background for this study. In addition, this project forms part of a more comprehensive study of the geology, chert geochemistry, and hydrothermal footprint of the Meadowbank deposit as part of the Geological Survey of Canada's Targeted Geoscience Initiative (TGI-4) Lode-Gold Project (Castonguay et al., 2012). The results of the study presented here represent the first in a series of sub-projects on the geochemistry of BIFs to address how lithogeochemistry of chert may be used to better understand the nature and origin of this gold deposit type. Moreover, the study seeks to identify similarities and/or differences between mineralized (i.e. Central BIF, and Grizzly) and apparently non-mineralized BIFs (i.e. Far West and West IF) based on their geochemical signatures.

2.3 Geological setting

Located in the Rae Domain of the Churchill Province, the Meadowbank deposit is hosted by the ca. 2.7 Ga bimodal Woodburn Lake greenstone belt (Ashton, 1985; Roddick et al., 1992; Aspler and Chiarenzelli, 1996a) consisting of tholeiitic and komatiitic metavolcanic rocks with minor calc-alkaline felsic tuffs and flows overlain by a >2.62 Ga package of iron-formation, quartzite and quartzo-feldspathic metasedimentary rocks (Armitage et al., 1996; Sherlock et al., 2001a, b, 2004; Hrabi et al., 2003; Pehrsson et al., 2004). All these units are intruded by Archean to Paleoproterozoic mafic and felsic plutonic rocks.

The aforementioned rocks were deformed at least by four regional-scale Neoproterozoic to Paleoproterozoic deformation events (Table 2.1; e.g., Henderson et al., 1991; Ashton, 1985), two of which had a significant effect on the geometry of the mineralized bodies in the Third Portage area (Ashton, 1985; Sherlock et al., 2004). The regional metamorphic grade ranges, going from the north- to south, from middle- greenschist to amphibolite facies (Table 2.2; Pehrsson et al.,

2004).

Numerous units of Algoma-type BIF (0.2 to 10 m thick) occur in the area, which include the Far West IF, West IF, Central BIF, East BIF, and Grizzly IF; all of these are generally interlayered with volcanic rocks and locally with a quartzite unit (Sherlock et al., 2001a, b; 2004; Fig. 2.2). Representative core samples and their matching polished thin sections are shown in Fig. 2.3.

The BIFs are oxide-facies units consisting of laminated magnetite and chert layers (0.2 to 5 cm) associated with minor silicate bands which reflect variations of the metamorphic grade: (1) grunerite/biotite in the north; (2) cummingtonite/biotite in the middle; and (3) garnet/biotite in the south (Fig. 2.2; Table 2.2). Minor chlorite, muscovite, sericite, ankerite, siderite, stilpnomelane, and apatite are interlayered with the chert and magnetite bands (Fig. 2.3; Armitage et al., 1996; Hrabí et al., 2003; Sherlock et al., 2004). Discontinuous chlorite-rich bands, 1 to 5 cm thick, locally interlayered with BIF may represent clastic sediments or a transition between chemical and clastic sediments (Armitage et al., 1996; Agnico-Eagle Mines Ltd, 2008), whereas stilpnomelane may reflect the influence of volcanic detritus (Klein, 2005).

The Far West BIF is surrounded by intermediate volcanic rocks, locally quartzite and ultramafic rocks. The chert bands are commonly deformed and folded, may show very diffuse contacts with the magnetite bands, and are now composed of recrystallized subhedral quartz with minor apatite and late-stage sericite (Fig. 2.3A, B); pyrite is the dominant sulfide species associated with the chert bands. The Far West BIF is barren except for a 3.6 m interval which averages 2.81 g/t Au; the gold in this interval is associated with isolated late-stage pyrite (Agnico-Eagle pers. comm. 2012).

The West BIF is surrounded by intermediate volcanic rocks and locally by quartzite and ultramafic rocks; it is composed of pyrrhotite-rich cherty bands (2-10 modal %). Metamorphic grade ranges from upper greenschist to amphibolite and is characterized by a grunerite, hornblende, and stilpnomelane-bearing assemblage. Despite the presence of sulfides, the West IF has not returned significant gold assays (Armitage et al., 1996; Agnico-Eagle pers. comm. 2012). The chert bands are deformed and composed of recrystallized, subhedral quartz grains that are mostly overprinted by later, foliated grunerite-cummingtonite grains, calcite and local hematite (Fig. 2.3C, D).

The Central BIF is host to the main deposit and is composed of four principal mineralized bodies: North Portage Zone, Third Portage Zone, Bay Zone and Goose Island Zone (Fig. 2.2). Generally, the BIFs are associated with intermediate and ultramafic volcanic rocks and are composed of laminated magnetite and chert layers intercalated with variable silicate facies assemblages which vary in their mineralogy depending on the metamorphism (Fig. 2.2, Table 2.2; Armitage et al., 1996). Chert bands are deformed and composed of recrystallized, subhedral quartz grains associated with late hornblende, grunerite-cummingtonite and euhedral magnetite (Fig. 2.3E, F). The mineralized zones consist of pyrrhotite, pyrite, and sparse chalcopyrite and arsenopyrite, and are mainly located at the contacts of the magnetite/chert layers. Pyrite also occurs within vugs in quartz veins and at the margins of quartz veins where it typically replaces pyrrhotite and magnetite (Armitage et al., 1996; Castonguay et al., 2012).

In the mine vicinity, the non-mineralized East BIF is typically surrounded by intermediate volcanic rocks with local ultramafic rocks. This BIF is at middle greenschist facies and is characterized by well-banded magnetite-chert iron formation. The chert bands are deformed with the host rock and composed of recrystallized, subhedral quartz grains associated with late

hornblende, grunerite-cummingtonite, calcite, some euhedral magnetite grains and locally rare hematite (Fig. 2.3G, H).

The Grizzly BIF zone is dominated by intermediate volcanic rocks with local ultramafic rocks. This iron formation displays alteration characterized by quartz flooding. This alteration, which hosts visible gold, is characterized by the presence of ankerite, sericite, and cummingtonite. The chert bands are brecciated and altered by intense silicification, with diffuse ankerite, weak but pervasive chlorite, and moderate hematite; grunerite-cummingtonite grains are also present along the contact with magnetite bands (Fig. 2.3I, J). The Grizzly zone occurs near massive textured Paleoproterozoic granite which cuts the sedimentary package, a feature which is discussed later in the context of an unusual chemical signature for the analyzed chert band from this locality.

2.3.1 Mineralization

The characteristics of the gold mineralization have been documented within the Meadowbank area through government mapping and deposit-scale studies (Roddick et al., 1992; Armitage et al., 1996; Davis and Zaleski, 1998; Kerswill et al., 1998, 2000; Kerswill, 2000; Pehrsson et al., 2000; Sherlock et al., 2001a, b; Pehrsson et al., 2004). These studies, coupled with exploration activities, have delineated four principal mineralized zones (Fig. 2.2) where only three are in the production stage (i.e., The North Portage Zone, the Third Portage Zone and the Bay Zone).

The ore bodies in the Central BIF consist of several sub-parallel bands of auriferous iron formation. Sherlock et al. (2001a, b) suggested that the ore bodies are mostly developed at the contact between an ultramafic body and the volcano-sedimentary package. According to

Armitage et al., (1996) and Sherlock et al., (2001a, b), epigenetic gold mineralization is closely associated with D1-D2 deformation and originated from the circulation of fluids enriched in Mg, K, Ca, S, As, Cu and Au.

The Third Portage Zone and the Bay Zone which contain the majority of the ore reserve (10.59 Mt proven/probable grading 2.98 g/t gold in 2011; Agnico Eagle Mines Ltd, 2012), have an assemblage of fine-grained cummingtonite, minor fine-to medium-grained chlorite and biotite which represents upper-greenschist facies metamorphism. According to Armitage et al. (1996), the cummingtonite grew in the same manner as grunerite did this being at mid-greenschist facies (i.e. at the interface between magnetite and chert bands). Similar mineralogy is present in the north (i.e. pyrrhotite-pyrite-chalcopyrite-arsenopyrite), but the pyrrhotite is more abundant here as massive- to disseminated grains and as pervasive replacement of magnetite. Chalcopyrite and arsenopyrite occur as inclusions in pyrrhotite.

At the northern end of the Central BIF, in the North Portage Zone, additional mineralization occurs and is manifested by disseminated pyrrhotite, pyrite, chalcopyrite and arsenopyrite with the pyrrhotite forming fine-grained clusters and discontinuous, layer-parallel veinlets in grunerite-bearing magnetite-rich bands of BIF (Armitage et al., 1996). Pyrite replaces pyrrhotite and magnetite and chalcopyrite/arsenopyrite are present in the form of inclusions in pyrrhotite.

2.4 Analytical methods and data treatment

Thirty nine samples of BIF from drill core and outcrop in the Far West, West IF, Central BIF, East BIF and Grizzly areas (Fig. 2.2) were collected for petrographic study with an emphasis on the chert or chert-carbonate phases of each sample. An effort was made to avoid BIF with chert bands of <0.05 centimeters thickness, as the analysis of bands of this thickness

presents challenges. In addition, chert bands were analyzed in preference to Fe-rich bands to minimize the effects of diagenetic alteration. Thin sections from these samples were examined in detail, using both transmitted and reflected light microscopy followed by SEM-EDS imaging and analysis (Fig. 2.4).

Trace-elements and REE concentrations were obtained on 100 μm thick polished sections. Based on previous petrographic work, areas for analysis were selected to minimize the presence of phases other than microcrystalline quartz after chert, including alteration, and mineral inclusions. Exploratory *in-situ* analyses were made using a Resonetics Resolution M-50 laser ablation instrument coupled to a Thermo X-Series II quadrupole ICP-MS at the Geochemical Fingerprinting Laboratory of Laurentian University, in Sudbury, Ontario, using the protocol of Kamber and Webb (2007). As chert bands show very low concentrations of REE, spot analyses may be below the limit of detection for many elements, therefore line traverses using both 140 and 190 μm beam diameters with a repetition rate of 10 Hz and an energy density of 7 J/cm^2 , were used to obtain data above the detection limit (Fig. 2.4A, B, C). However, the line traverse method increases the influence of any detrital contaminants either as inclusions or minerals disseminated along the traverse line within the chert bands. Therefore, the Queensland alluvial shale composite (MUQ) was used to normalize the REE+Y values to decrease the influence of terrigenous input. The MUQ represents a bimodal felsic and mafic volcanic provenance (Kamber et al., 2005), which is similar to the expected average terrigenous input from bimodal greenstone belt volcanism into the Archean ocean (e.g., Bolhar et al., 2005; Thurston et al., 2012). Concentrations of elements were determined using off-line calculations, following the protocol of Longerich et al. (1996) using the NIST 612 glass standard as a primary reference material and SiO_2 as an internal standard.

The elemental concentrations reported herein represent, therefore, the integrated signal over the length of the analytical traverses. The elements analyzed included the 14 REEs (^{139}La , ^{140}Ce , ^{141}Pr , ^{146}Nd , ^{147}Sm , ^{153}Eu , ^{157}Gd , ^{159}Tb , ^{163}Dy , ^{165}Ho , ^{166}Er , ^{169}Tm , ^{172}Yb and ^{175}Lu), in addition to ^7Li , ^9Be , ^{29}Si , ^{45}Sc , ^{47}Ti , ^{51}V , ^{52}Cr , ^{55}Mn , ^{56}Fe , ^{59}Co , ^{60}Ni , ^{65}Cu , ^{66}Zn , ^{69}Ga , ^{75}As , ^{85}Rb , ^{88}Sr , ^{89}Y , ^{90}Zr , ^{93}Nb , ^{95}Mo , ^{107}Ag , ^{111}Cd , ^{115}In , ^{118}Sn , ^{121}Sb , ^{133}Cs , ^{137}Ba , ^{178}Hf , ^{181}Ta , ^{182}W , ^{197}Au , ^{205}Tl , ^{208}Pb , ^{232}Th and ^{238}U (Tables 2.3, 2.4, 2.5 and 2.6). The detection limits for the analyzed elements vary based on factors such as the volume of inclusions within chert. The detection limits were calculated using the relationship described in Longerich et al. (1996) and range from 0.001 to 0.002 ppm for the REE and Y (Table 2.7).

Furthermore, where discussed below, La, Gd, Eu and Ce anomalies are calculated following the procedure of Lawrence and Kamber (2005) using extrapolated Pr and Nd values in calculating the La anomaly and similar procedures for Eu, Gd and Ce.

2.5 REE+Y systematics in BIF

The presence and abundance of REE+Y in chert bands may represent a primary signature, which can be influenced by one or more processes: (1) precipitation from marine seawater in temporarily isolated or well-connected basins (e.g., Bau and Dulski, 1996); (2) precipitation from vent-sourced hydrothermal fluids (e.g., Danielson et al., 1992; Allwood et al., 2010); and (3) silicification of precursor volcanic units (e.g., Hanor and Duchac, 1990; Lowe, 1999). Chert geochemistry is also strongly dependent on the extent of contamination by terrigenous detritus (e.g., Alexander et al., 2008), volcanic ash (e.g., Klein, 2005) and oceanographic processes (e.g., phosphate circulation and precipitation).

Several studies have shown that the REE+Y systematics of Archean seawater are analogous

to the modern ocean (Fig. 2.5; e.g., Bau and Dulski, 1996; Thurston et al., 2012) which shows:

- a. Depletion in light rare-earth elements (LREE) relative to heavy rare-earth elements (HREE);
- b. A strongly super-chondritic Y/Ho ratio (i.e., >27), which produces a positive Y anomaly that is often between 40-90;
- c. A positive La anomaly (La/La^* between 1.15 and 1.3);
- d. Positive Gd anomaly (Gd/Gd^* between 1.3 and 1.5);
- e. A well-developed, negative Ce anomaly resulting from the oxidation of Ce^{+3} to Ce^{+4} in the water column.

Therefore, the shale-normalized (i.e., MUQ) REE+Y pattern for Archean cherts influenced by volcanism and especially by high-temperature ($>250^\circ\text{C}$) hydrothermal fluids (Fig. 2.5; Bau and Dulski, 1996; Kamber et al., 2004) will be characterized by a seawater signature with an associated high-temperature hydrothermal fluid signature:

- a. A depletion in light rare earth elements (LREE) relative to heavy rare earth elements (HREE);
- b. Super-chondritic Y/Ho ratio (i.e., >27), yielding a positive $\text{Y}/\text{Y}^*_{\text{MUQ}}$ anomaly, commonly between 40-90;
- c. A slightly positive La anomaly ($\text{La}/\text{La}^*_{\text{MUQ}}$ between 1.15 and 1.3);
- d. Variable but well-developed positive Eu anomaly.

Due to the anoxic character of Archean seawater, the shale normalized REE+Y patterns for Archean seawater are very similar to modern seawater except that Ce shows a negative anomaly (Planavsky et al., 2010).

Hydrothermal precipitates are characterized by a lack of LREE depletion, absence of both La and Gd anomalies, and a variably developed positive Eu anomaly (e.g., Allwood et al., 2010).

It is noticed that Gd anomalies reported in previous articles on REE+Y data from BIF precipitated in Archean seawater (e.g., Bolhar et al., 2005; Thurston et al., 2012) were small to nonexistent and is therefore not referred again in this article. Any Gd anomaly present is considered due to a combination of a small positive Gd anomaly associated with seawater (Bau and Dulski 1996) and slightly-negative Gd anomaly associated with hydrothermal vent fluid (e.g., Allwood et al., 2010). Therefore, as Archean seawater was influenced by hydrothermal vent fluids, the Gd anomalies show a non-depletion and non-enrichment suggesting precipitation under influence of seawater and hydrothermal input.

On the other hand, the chert bands may have been derived from hydrothermal circulation and silica replacement of volcanic and sedimentary rocks, as proposed by Hanor and Duchac (1990), which involved the silicification of various rocks in the Barberton greenstone belt. In this study, evidence for a replacement process in chert bands is evidenced from petrographic studies of the rocks and geochemically by elemental enrichment that is diagnostic of the precursor rock type. Thus, cherts produced by silicification of the different protoliths provided the following geochemistry: (1) silicified komatiites and basalts are enriched in Cr and Ni; and (2) silicified dacite to rhyolite are enriched in Ba, Zr, Sr, and Rb (Lowe, 1999). Neither textural nor geochemical evidence of such silicification processes relevant to chert formation were observed

in this study.

Some chemical heterogeneities in chert may be due to inclusions or presence of disseminated grains, including single mineral phases, such as phosphates, garnets, clay minerals, and/or resistant minerals (e.g., zircon, xenotime, garnet etc.), which reflect either detrital contamination or a late metamorphic event (Fig. 2.4D, E, F). Although sample selection was based on careful petrographic study of the samples in order to avoid such heterogeneities in the chert, the beam diameter was large relative to the size of chert micro-banding and thus, some inclusions may affect the REE+Y concentrations (i.e., normalized patterns) depending on their modal abundances. In order to assess such influence, in Figure 2.6 is illustrated the effect of selected accessory minerals (i.e., Apatite (Fig. 2.6A), xenotime (Fig. 2.6B), zircon (Fig. 2.6C) and garnets (Fig. 2.6D)) on a typical LA-ICP-MS chert band analysis (Thurstun et al., 2012). As the latter figure shows, small quantities of these minerals in the chert bands may affect, in some cases dominate, the REE chemistry and therefore interpretation of the bulk cherts (e.g., 0.3% apatite, 0.003% xenotime, 0.3% of zircon and 0.05% garnets). Therefore, the REE+Y geochemistry also represents an important tool in identifying and assessing the role of potential contamination of low abundance accessory minerals. If such contaminants are recognized through these above enumerated screening processes, then the REE+Y data can be used to constrain the genesis of BIF cherts and assess such contamination. Elements such as Sr, Ga, Sc, Zr and Th, and REE ratios, such as Nd/Yb_{MUQ} (i.e., $Nd/Yb_{MUQ} \approx 1$) and Y/Ho (i.e., chondritic (i.e., 24-27) values), are excellent monitors of detrital contamination (i.e., detrital or volcanic input).

Metamorphism and ore-forming processes (i.e., epigenetic fluids) may remobilize the REE+Y and consequently alter the primary signature of chert bands. Therefore, the REE+Y

signature of seawater and hydrothermal vent fluids will not be detected in MUQ-normalized profiles, as this paper addresses, thus a careful selection of samples was done prior to analytical studies.

2.6 Results

The REE+Y data from the sampled iron formations were normalized to MUQ and, despite some minor exceptions, the REE+Y normalized data (Tables 2.3, 2.4, 2.5 and 2.6; Fig. 2.7), show relatively uniform patterns. The dataset includes a moderate enrichment in the HREE relative to both the LREE and middle REE ($\text{Nd/Yb}_{\text{MUQ}} = 0.05\text{-}0.6$), positive La, Y and Eu anomalies related to the non-depletion of Gd, and super-chondritic to chondritic Y/Ho ratios ($\text{La/La}^*_{\text{MUQ}} = 0.8\text{-}4.6$; $\text{Y/Y}^*_{\text{MUQ}} = 0.8\text{-}1.9$; $\text{Eu/Eu}^*_{\text{MUQ}} = 1.2\text{-}5.1$; $\text{Gd/Gd}^*_{\text{MUQ}} = 0.9\text{-}1.3$; $\text{Y/Ho} = 24\text{-}53$).

Considering the chert data from each of the BIFs individually, some differences are apparent and these are discussed below. Most of samples from Far West (Fig.2.7A), which represents a barren BIF, are not discussed further here due to their very low levels of REEs and, consequently, the very erratic REE_{MUQ} normalized patterns which resulted. This fact suggests that Far West material was chemically reworked after deposition which depleted the REE+Y contents of the chert samples.

The West BIF (Figs. 2.7B, 2.8) data have relatively flat REE+Y patterns compared to the other BIFs and the data can be subdivided into two distinct groupings:

- a. Samples AMB-126233, AMB-126234, AMB-126235, AMB-128328 and AMB-128329 are enriched in the HREE relative to both the MREE and the LREE ($\text{Nd/Yb}_{\text{MUQ}} = 0.04\text{-}0.5$), have positive La, Y and Eu anomalies, non-depletion of Gd, and super-chondritic

Y/Ho ratios ($\text{La/La}^*_{\text{MUQ}} = 1.5\text{-}2.6$, $\text{Y/Y}^*_{\text{MUQ}} = 1.1\text{-}1.6$, $\text{Eu/Eu}^*_{\text{MUQ}} = 1.7\text{-}3.5$, $\text{Gd/Gd}^*_{\text{MUQ}} = 0.9\text{-}1.2$; $\text{Y/Ho} = 32\text{-}46$; Fig. 2.8A);

- b. Samples AMB-128330, AMB-128331 and AMB-128332 show relatively flat patterns (i.e., unfractionated) to weak enrichment in HREE relative to MREE and LREE ($\text{Nd/Yb}_{\text{MUQ}} = 0.5\text{-}2$), weak positive La and Eu anomalies ($\text{La/La}^*_{\text{MUQ}} = 1.3\text{-}1.9$, $\text{Eu/Eu}^*_{\text{MUQ}} = 1.2\text{-}1.3$) along with an absence of both Gd and Y anomalies ($\text{Gd/Gd}^*_{\text{MUQ}} = 0.9\text{-}1.1$, $\text{Y/Y}^*_{\text{MUQ}} = 0.9\text{-}1.1$) and chondritic to super-chondritic Y/Ho ratios ($\text{Y/Ho} = 26\text{-}31$; Fig. 2.8B).

The second group of samples can be explained by detrital contamination and/or the presence of some disseminated subhedral phosphate grains (i.e., fluorapatite), which are observed in the chert bands (Fig. 2.8B), as illustrated by Y/Ho and $\text{Nd/Yb}_{\text{MUQ}}$ values. The presence of detrital contamination is generally reflected by a relationship between $(\text{Pr/Sm})_{\text{MUQ}}$ and Th and Ga, as the latter substitutes for Al and may be enriched in clay minerals of continental provenance (Bolhar et al., 2005). The source and origin of phosphate contamination has, however, yet to be established. In general, phosphate contamination in BIF is not significant (e.g., Thurston et al., 2012; Bau and Alexander 2009).

Generally, samples of Archean shale and volcanic tuff do not display significant positive Eu anomalies, as illustrated by the West IF data. Meanwhile, fluorapatite grains are present in each BIF, thus the shape of the REE plots could suggest a detrital origin, hence representing a component of detrital contamination. Theoretically, because of its presence in each of the BIFs in the area, fluorapatite contamination should affect each BIF sample to some degree, thereby producing a slightly concave downward REE+Y patterns associated with a negative Eu anomaly

(Fig. 2.8B; after Sano et al., 2002).

Based on $\text{Pr}/\text{Sm}_{\text{MUQ}}$ ratios, the Ga, Th and Sr content and a REE+Y pattern similar to apatite (except for a negative Eu anomaly), the data suggest samples AMB-128330, AMB-128331 and AMB-128332 may be influenced by some phosphate contamination (Fig. 2.8C, D, E; after Sano et al., 2002). This pattern suggests an association of these elements with terrigenous input (i.e., due to high concentration of Ga and Th) that consists of phosphate and aluminum with, in addition, a hydrothermal input indicated by the positive Eu anomaly. In the traverse-based sampling method used, the laser could, therefore, have encountered phosphates in these three samples.

The Central BIF (Figs. 2.7C, 2.9) data show relatively constant REE+Y patterns with enrichment in the HREE relative to the MREE ($\text{Nd}/\text{Yb}_{\text{MUQ}} = 0.1\text{-}0.3$), positive La, Y and Eu anomalies, a lack of a Gd anomalies, and mainly super-chondritic Y/Ho ratios ($\text{La}/\text{La}^*_{\text{MUQ}} = 0.8\text{-}4.6$, $\text{Y}/\text{Y}^*_{\text{MUQ}} = 0.8\text{-}1.9$ and $\text{Eu}/\text{Eu}^*_{\text{MUQ}} = 1.5\text{-}3.5$, $\text{Gd}/\text{Gd}^*_{\text{MUQ}} = 0.9\text{-}1.2$, $\text{Y}/\text{Ho} = 24\text{-}53$); these geochemical indices are consistent with contributions from ambient seawater and hydrothermal vent fluids (Fig. 2.9A, B). The lone exception to this explanation is sample AMB-126232 which shows an enrichment in the LREE relative to HREE ($\text{Nd}/\text{Yb}_{\text{MUQ}} = 7$; Fig. 2.9C) and a positive Eu anomaly ($\text{Eu}/\text{Eu}^*_{\text{MUQ}} = 3.2$). Interestingly, the pattern for this latter sample is similar to that for a garnet-quartz alteration envelope in the giant Broken Hill Zn-Pb deposit (Spry et al., 2007), which is shown in Fig. 2.9C for reference. Sample AMB-126232 also shows a strong correlation between $(\text{Eu}/\text{Eu}^*)_{\text{MUQ}}$ (i.e., proxy of calcium) and $(\text{Pr}/\text{Sm})_{\text{MUQ}}$ (Fig. 2.9F), which suggests the influence of garnet on the pattern. This artifact of the pattern could be explained by the presence of a thin layer of garnet adjacent (i.e., 3 mm) to the traverse which may have influenced the chert chemistry (Fig. 2.4B). It is also noted that samples AMB-126223 and AMB-126231 (Fig. 2.9B)

show enrichment in both Ga and Th relative to $(\text{Pr}/\text{Sm})_{\text{MUQ}}$, which suggest some detrital contamination (Fig. 2.9D, E).

The data for the East BIF (Figs. 2.7D, 2.10) show very consistent shale-normalized patterns with enrichment in the HREE relative to MREE ($\text{Nd}/\text{Yb}_{\text{MUQ}} = 0.1\text{-}0.4$) and associated positive La, Y and Eu anomalies, non-depletion of Gd and chondritic to super-chondritic Y/Ho ratios ($\text{La}/\text{La}^*_{\text{MUQ}} = 1\text{-}1.7$, $\text{Y}/\text{Y}^*_{\text{MUQ}} = 0.9\text{-}1.4$ and $\text{Eu}/\text{Eu}^*_{\text{MUQ}} = 2.1\text{-}5.1$, $\text{Gd}/\text{Gd}^*_{\text{MUQ}} = 0.9\text{-}1.1$, $\text{Y}/\text{Ho} = 25\text{-}41$), which suggests the influence of both ambient seawater and, especially, a hydrothermal fluid (Fig. 2.10A). Examination of the data in more detail reveal, however, that samples AMB-126241, AMB-126243 and AMB-126246 have relatively flatter patterns (Fig. 2.10B) which are similar to apatite (after Sano et al., 2002), but which lack a negative Eu anomaly. The contents of Ga, Th, Sr relative to $(\text{Pr}/\text{Sm})_{\text{MUQ}}$ (Fig. 2.10C, D, E) illustrate a correlation between these elements and, in addition, we note that these three patterns also have smaller Eu anomalies. The patterns for these samples could, therefore, be explained by some terrigenous input, similar to the West IF, with the laser traverse analysis potentially having been influenced by some fluorapatite. There are only two samples from the Grizzly BIF for which data have been generated and the two patterns are similar. The patterns show that HREE are strongly enriched relative to both the MREE and LREE ($\text{Nd}/\text{Yb}_{\text{MUQ}} = 0.07\text{-}0.1$, there are positive La, Y and Eu anomalies, a lack of depletion of Gd, and super-chondritic Y/Ho ratios ($\text{La}/\text{La}^*_{\text{MUQ}} = 1.6$, $\text{Y}/\text{Y}^*_{\text{MUQ}} = 1.1\text{-}1.3$, $\text{Eu}/\text{Eu}^*_{\text{MUQ}} = 2.3\text{-}3.5$, $\text{Gd}/\text{Gd}^*_{\text{MUQ}} = 1\text{-}1.1$, $\text{Y}/\text{Ho} = 35$; Fig. 2.7E). Although there is an overall difference in the relative fractionation of these patterns compared to the other chert data (Fig. 7), the general enrichment of the HREEs and the positive La and Y anomalies are consistent with a seawater influence, whereas the strong positive Eu anomalies suggest a hydrothermal input.

2.7 Summary and Discussion

The Meadowbank gold deposit consists of several Algoma-type BIFs which differ in their petrography, geochemistry and gold endowment. The trace-element geochemical signatures for several BIFs in this gold deposit area have been determined in order to constrain the origin of the units in terms of the processes inferred to be relevant to their formation, as well as assess the effect of such geochemical characteristics on the auriferous content of these BIFs and consequent implications for BIF-hosted gold deposits in general. The results of this study also have implications for assessing the origin of chert in the broader context of its environment.

2.7.1 Geochemical signatures for the BIFs at Meadowbank

The Far West BIF is unmineralized except for one area where an interval running 2.8 g/t Au over 3.6 meters was encountered (Agnico-Eagle Mines Ltd, 2012). Most of the chert data from this BIF were not plotted due to their low concentrations of REEs and, consequently (Fig. 2.7A), very erratic REE patterns. As noted already, the low REE contents for these samples is anomalous compared to all the other chert material analyzed in this study (Fig. 2.7) and may reflect subsequent modification (i.e., REE mobility) of the chert post-dating its formation, but at present no further speculation is possible. As for the two unusual shale-normalized patterns recorded for these three chert samples shown in Fig. 2.7A, which contrast with the patterns for most of the other data, we can only speculate that they may also be attributed to modification post their formation.

The West BIF is barren except for a few weakly anomalous gold values (Agnico-Eagle Mines Ltd, 2012) which were not selected in this study. The geochemical data for these samples show very consistent REE patterns (Fig. 2.7B) which are attributed to the influence of ambient

seawater with some hydrothermal input. Some chert bands, however, record the influence of detrital contamination, as represented by the levels of Th and Sr (i.e., proxies for phosphates).

The Central BIF is the most mineralized BIF in the Meadowbank area with 24.5 Mt of proven/probable ore reserves grading 2.8 g/t (2011 data; Agnico-Eagle pers. comm. 2012). The geochemistry for this BIF (Fig. 2.7C) shows the combined influence of both ambient seawater and hydrothermal input with some chert bands reflecting some crustal influence, as indicated by the elevated Ga (i.e., proxy of aluminum) and Th. With regards to the hydrothermal input, the extent of the positive Eu anomaly, used as a proxy for such influence, is among the highest for all of the chert samples analyzed in this study. We cannot at this time, however, rule out the possibility that this increased Eu anomaly relates to the influence of the hydrothermal fluid related to the gold mineralization and further work is required to address this point, such as comparing its ^{18}O value to those cherts lacking such Eu anomalies.

The East BIF, which is mostly barren except for an isolated intersection of 3.23 g/t Au over 2.7 meters (Agnico-Eagle Mines Ltd, 2012), is located to the east of the richly mineralized Central BIF. The chert data from this BIF show very similar REE patterns to the West IF and reflect the influence of both ambient seawater and hydrothermal fluids (Fig. 2.7D), in addition to some detrital contamination, as indicated from the contents of Ga (i.e., proxy of aluminum), Th and Sr (i.e., proxy for phosphates). As with the Central BIF samples, the extent of the positive Eu anomalies are the highest of all the samples analyzed and again indicate significant contribution of a hydrothermal vent fluid.

Located at the extreme east of the property, the Grizzly BIF shows both homogeneous, but very weak gold mineralization, as reflected by one intersection that averages 0.20 g/t over 49

meters, and also some richer intersections in the lower-grade zones (e.g., 0.96 g/t over 24 meters including 7.44 g/t over 2.6 meters; Agnico-Eagle pers. comm. 2012). This BIF shows very distinctive REE patterns compared to the other chert data (Fig. 2.7E) with significant HREE enrichment relative to LREE and a strong positive Eu anomaly. As noted already, the general pattern observed suggests an ambient seawater signature that is, however, also mixed with high-temperature hydrothermal fluid, as indicated by the Eu anomaly. The nature of the pronounced depletion in LREE relative to HREE, can be explain by presence of carbonates (i.e., ankerite) in the chert bands which is uncommon to the region and may be related to a later cross-cutting granitic body dated at ca. 2.61 ± 0.04 Ga localized close to sampling area (i.e., <500 meters). The history of this BIF is different from the other auriferous and barren BIFs in the region and that it may have been influenced by its proximity to the noted younger granitic intrusion.

Three parameters, namely $\text{Nd/Yb}_{\text{MUQ}}$, La/La^* and Y/Ho , can be used to gauge the extent of seawater influence relevant to the formation of the BIF at Meadowbank (e.g., Kamber, 2010; Thurston et al., 2012). The ratios are all defined by Lawrence and Kamber (2006): (1) La/La^* is a measure of the strength of the La anomaly caused by seawater precipitation; (2) Y/Ho is a measure of the enrichment or depletion of Y from chondritic values, again a measure of hydrogenous processes; (3) Nd/Yb is used as a measure of HREE fractionation in BIF geochemistry, as it uses only elements not affected by seawater or hydrothermal processes. The $\text{Nd/Yb}_{\text{MUQ}}$ values for the West BIF (0.042-2.170) are greater in average than those for the East BIF (0.142-0.484) and the Central BIF (0.135-0.484), thus, it can be inferred that the West BIF likely formed in deeper water than either the Central or the East BIF which show similar values. The positive- to moderately negative $\text{Nd/Yb}_{\text{MUQ}}$ values and associated chondritic Y/Ho ratio indicate a hydrogenous sedimentary signature (e.g., Thurston et al., 2012). Most samples in this

study also show weakly positive values for Eu/Eu^* (1.24-5.12), which provide an indication of the relative influence of high-temperature hydrothermal fluids and thus proximity of chert deposition relative to fluid vents (i.e., the more positive the Eu anomaly the closer the hydrothermal fluid source). In this context, it is noted that the positive Eu anomaly for the Meadowbank BIF is not as high as that recorded for the BIFs which occur above the Deloro assemblage (e.g., 30+) in the Abitibi greenstone belt (Thurstion et al., 2012). Finally, the West BIF and East BIF show similar REE patterns, which means that the two units could be folded equivalents of the same unit with the western unit perhaps representing deeper water based on Nd/Yb values listed above (Kamber, 2010).

2.7.2 Implications for the nature of gold mineralization in BIF at Meadowbank

The use of the REE+Y geochemistry of chert within BIFs at the Meadowbank mine has been effective in terms of recognizing processes (i.e., seawater, hydrothermal fluids, and contamination) relevant to their formation; however, there appears to be no difference in the geochemistry of barren versus mineralized BIFs in the Meadowbank area. The study has not, however, examined the potential influence of other factors that may be relevant in the context of the gold mineralizing event; these include the influence of organic processes on BIF development (Posth et al., 2013), the effects of early versus late-stage sulfide formation, the geochemistry of the sulfides, and the overall oxidation state of the BIF on the mineralizing processes. Furthermore, and also important, is that the absence of comparable data sets to that presented here precludes the possibility of assessing the results in a broader context; however, it is the intent of this project to further evaluate the application of the methods presented here to other auriferous BIF settings (i.e., Meliadine, NWT; Musselwhite and Beardmore-Geraldton deposits, Ontario). Moreover, Meadowbank has discontinuous outcrop exposure of BIFs and this

precluded, unfortunately, assessing the on-strike variability of the chert chemistry. Better continuity of exposure is found at Beardmore-Geraldton and Meliadine deposits where this aspect will be addressed in the context of evaluating the hydrothermal footprint in the context of both chemistry and extent.

2.7.3 Implications of the results for BIFs

The foregoing discussion has emphasized several important and significant contributions from this study which are relevant to studying BIFs in general: (1) The LA ICP-MS analyses done in traverse mode on carefully selected chert bands within BIFs using appropriate analytical protocols can provide quantitatively meaningful data at both low detection limits (i.e., to 0.0001 to 0.001 shale-normalized values; see Fig. 2.7) and sufficiently high resolution (200 μm beam diameter); (2) The data produced in this study, when shale-normalized, indicate repeatedly that internally consistent and regular shale-normalized patterns can be achieved and reproduced. The data reflect and are consistent with the well-known and established geochemical behavior of the REEs as a group, in particular within a marine setting, which allow them to be routinely used as petrogenetic indicators for a wide variety of processes; (3) The consistency of the patterns noted in this study indicate, importantly, that potentially primary chemical signatures have been retained within the chert samples used despite several post-formation deformation and metamorphic events, in some cases to amphibolite facies; and (4) The previous conclusions provide, therefore, the opportunity to interpret, as has been done previously but with a high degree of confidence, the geochemical signals in the context of processes relevant to chert formation, these being contributions from ambient seawater, hydrothermal fluids, and detrital contamination. Given the robust behavior of the REEs and other elements not easily volatilized, these elements can be used in conjunction with easily volatilized elements to define the extent of

the hydrothermal footprint of the gold mineralizing event in settings where continuity of exposure may allow this.

2.8 Acknowledgements

The authors gratefully acknowledge the staff of Agnico Eagle Mines Ltd. and Goldcorp Ltd. and more particularly the Meadowbank regional exploration crews. The LA-ICP-MS analyses were done in the Geochemical Fingerprinting Laboratory at Laurentian University with the capable assistance of Dr. J. Petrus. Finally, we sincerely acknowledge the contribution of Drs. B. Dubé, S. Pehrsson, S. Castonguay and P. Mercier-Langevin of the Geological Survey of Canada for their input and continued support. The study is supported by both TGI-4 funding from Natural Resources Canada and funding through a Natural Sciences and Engineering Research Council Collaborative Research and Development agreement with participation by Agnico Eagle Mines Ltd and Goldcorp.

2.9 Figures and captions

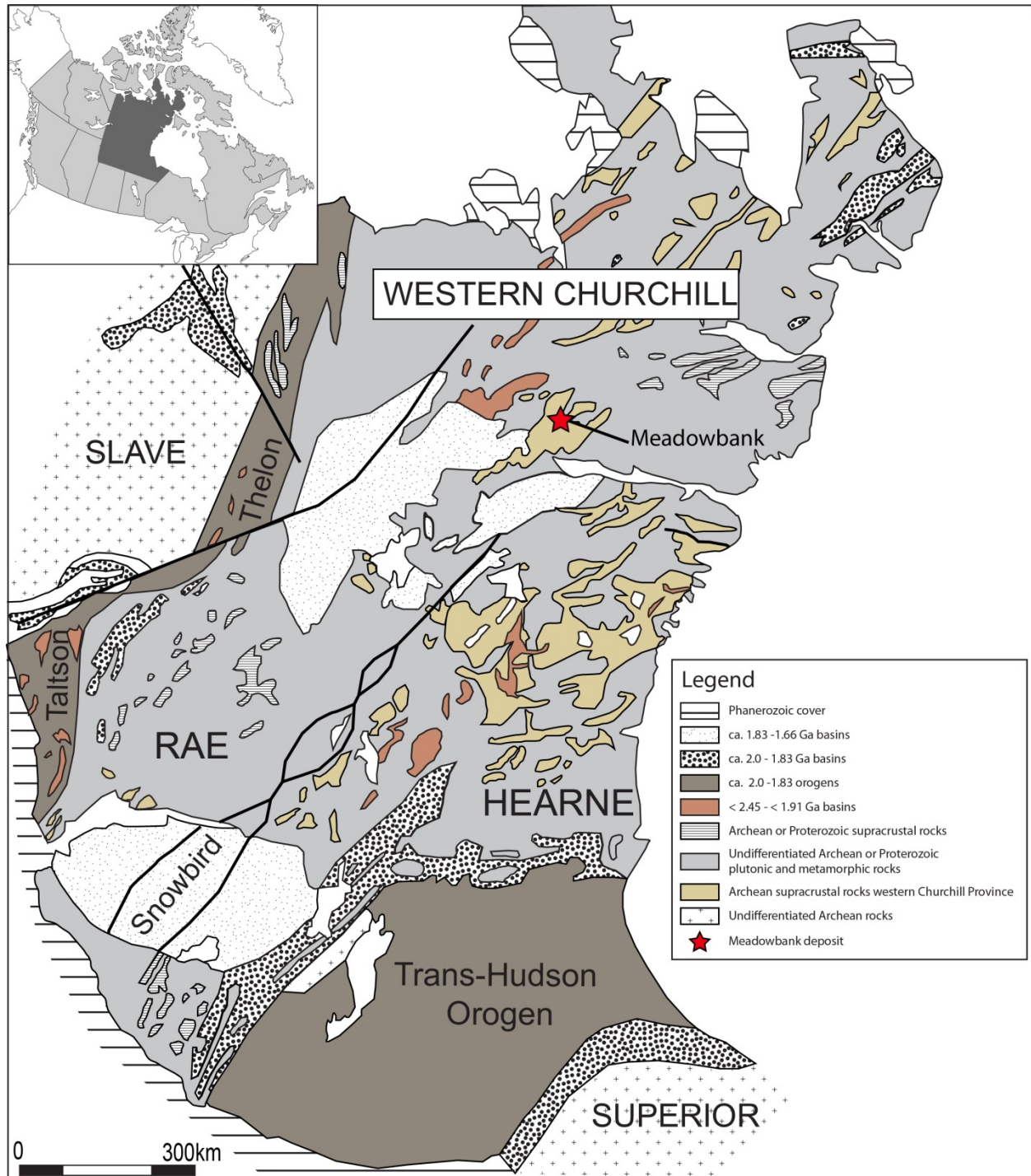


Figure 2.1: Simplified regional geological map of the Rae and Hearne Domains (modified from Hrabí et al., 2003).

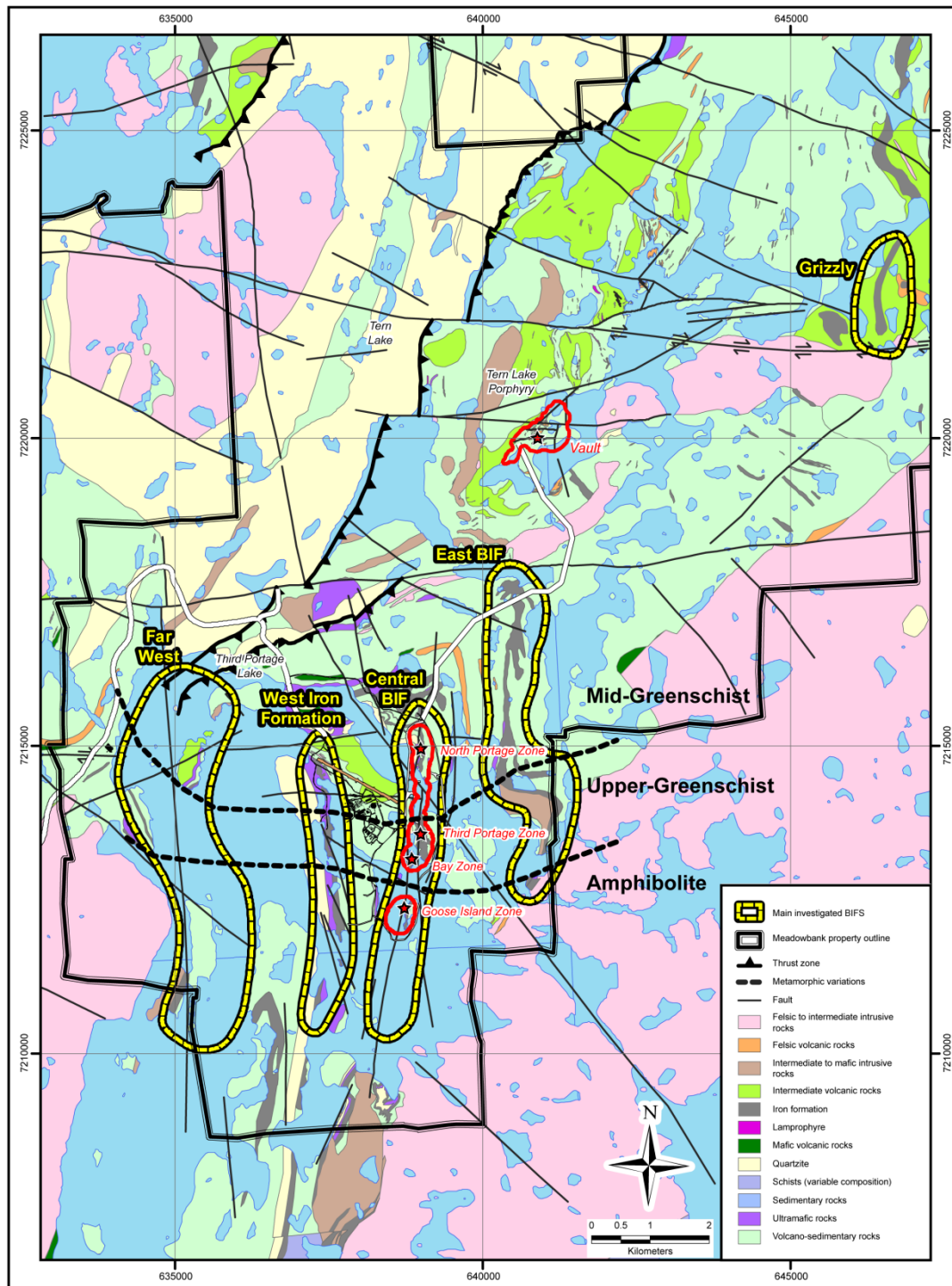


Figure 2.2: Geological map of the Meadowbank deposit area showing the location of the main BIFs which have been sampled for this study (modified after Agnico-Eagle Mines Ltd.).



Figure 2.3: Photographs of drill core (5 cm in length) and corresponding scanned polished-thin sections for samples from the BIFs used in this study: A, B) Sample AMB-216236 from the Far West; C, D) Sample AMB-126234 from the West IF; E, F) Sample AMB-126224 from the Central BIF; G, H) Sample AMB-126242 from the East BIF; I, J) Sample AMB-1268335 from the Grizzly zone. For the polished-thin sections, the clear transparent material is chert, whereas the remaining dark material is a mixture of oxides, silicates and sulfide material, as discussed in the text for each BIF.

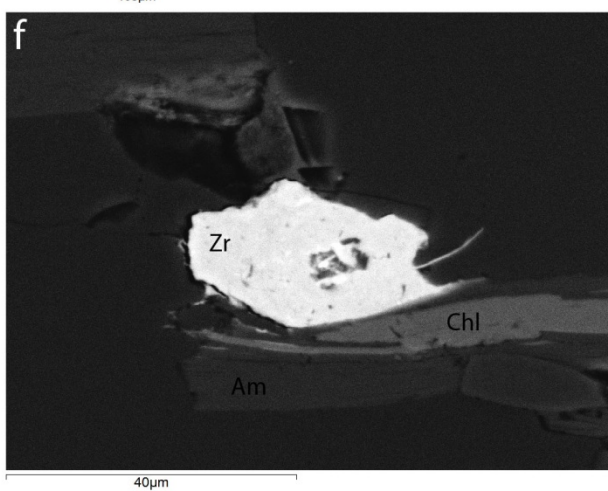
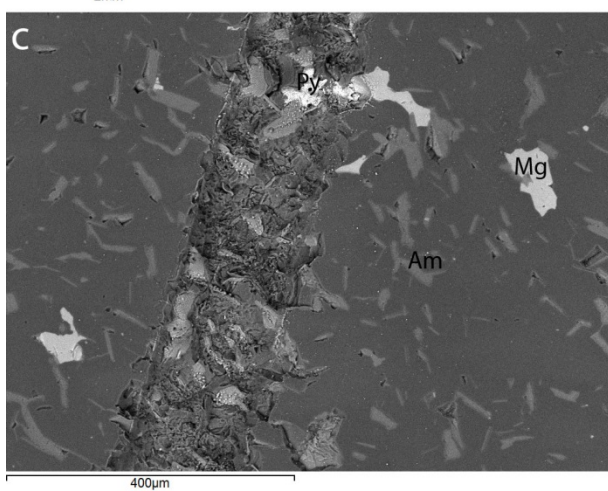
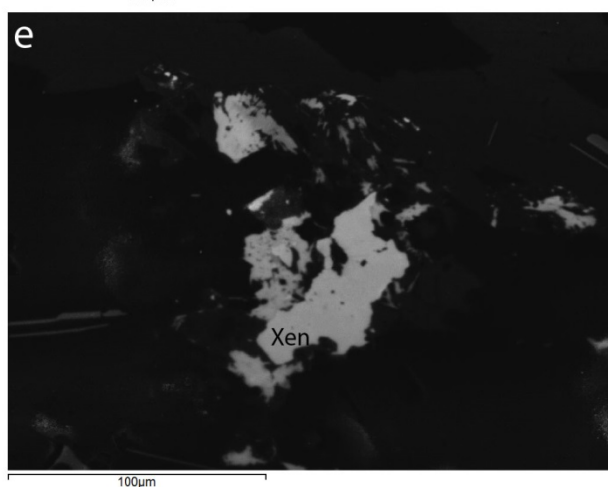
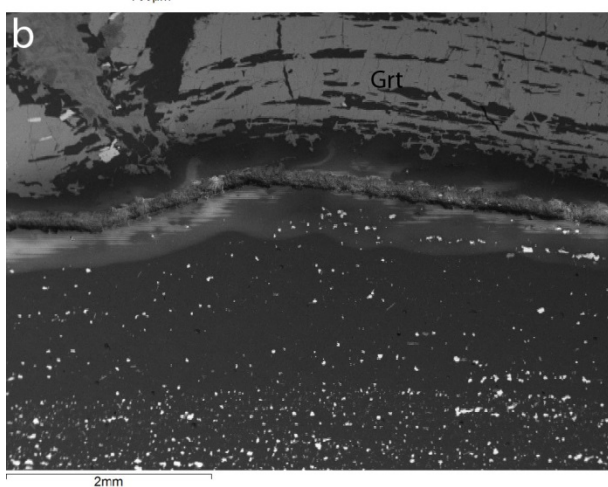
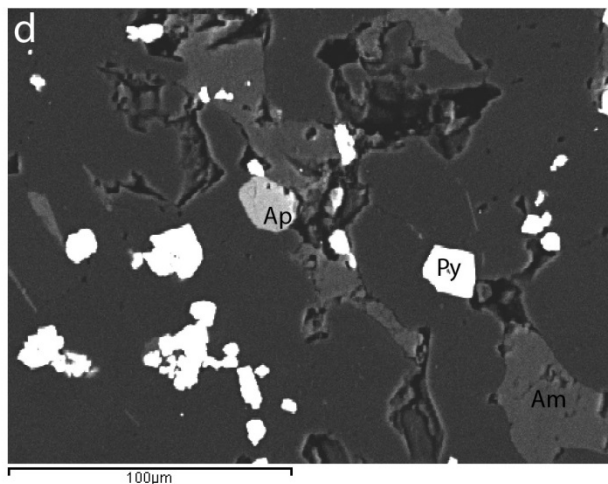
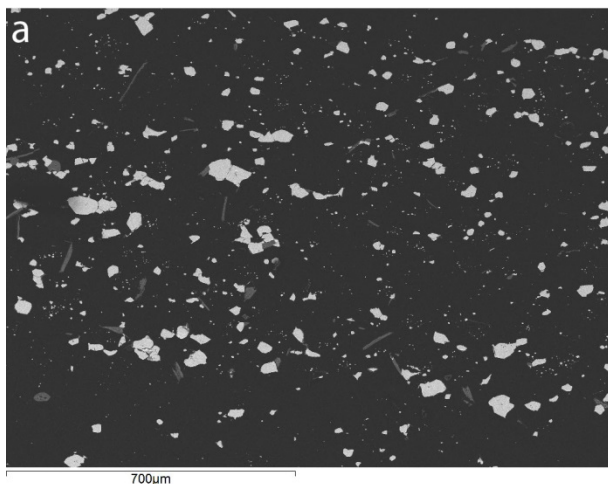


Figure 2.4: Back-scattered electron image from the SEM for different samples from the Meadowbank BIFs: A) chert bands with heterogeneities (e.g., magnetite and amphiboles grains); B) example of traverse line done in chert bands in edge of garnet band (from AMB-126232); C) zoom-in of traverse line in chert bands (from AMB-126223). Example of heterogeneities in chert bands: D) apatite grain in chert bands (from AMB-126247); E) xenotime grains disseminated in chert bands (from AMB-126231); and F) zircon grains disseminated in chert bands (from AMB-126231).

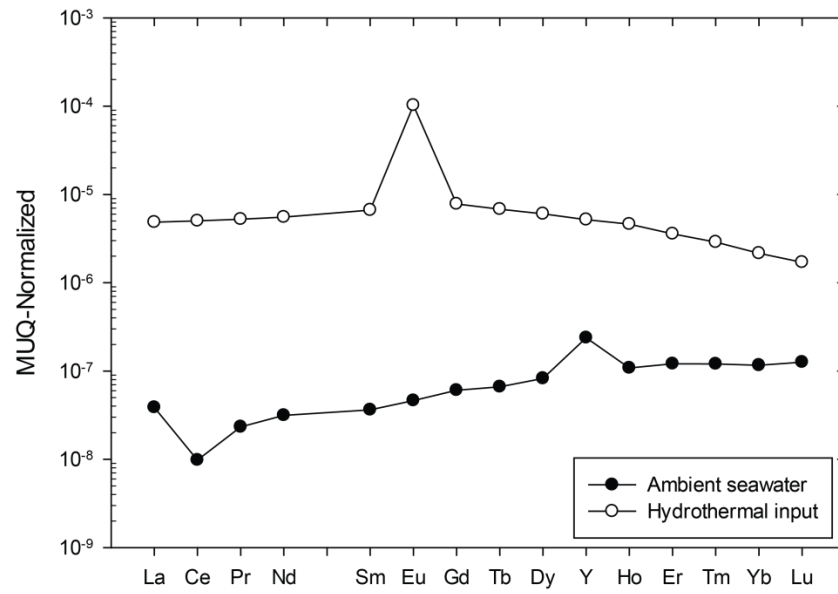


Figure 2.5: Shale (MUQ)-normalized REE+Y patterns illustrating the chemical signatures of the modern ambient seawater and hydrothermal vent fluid (after Bau and Dulski, 1999).

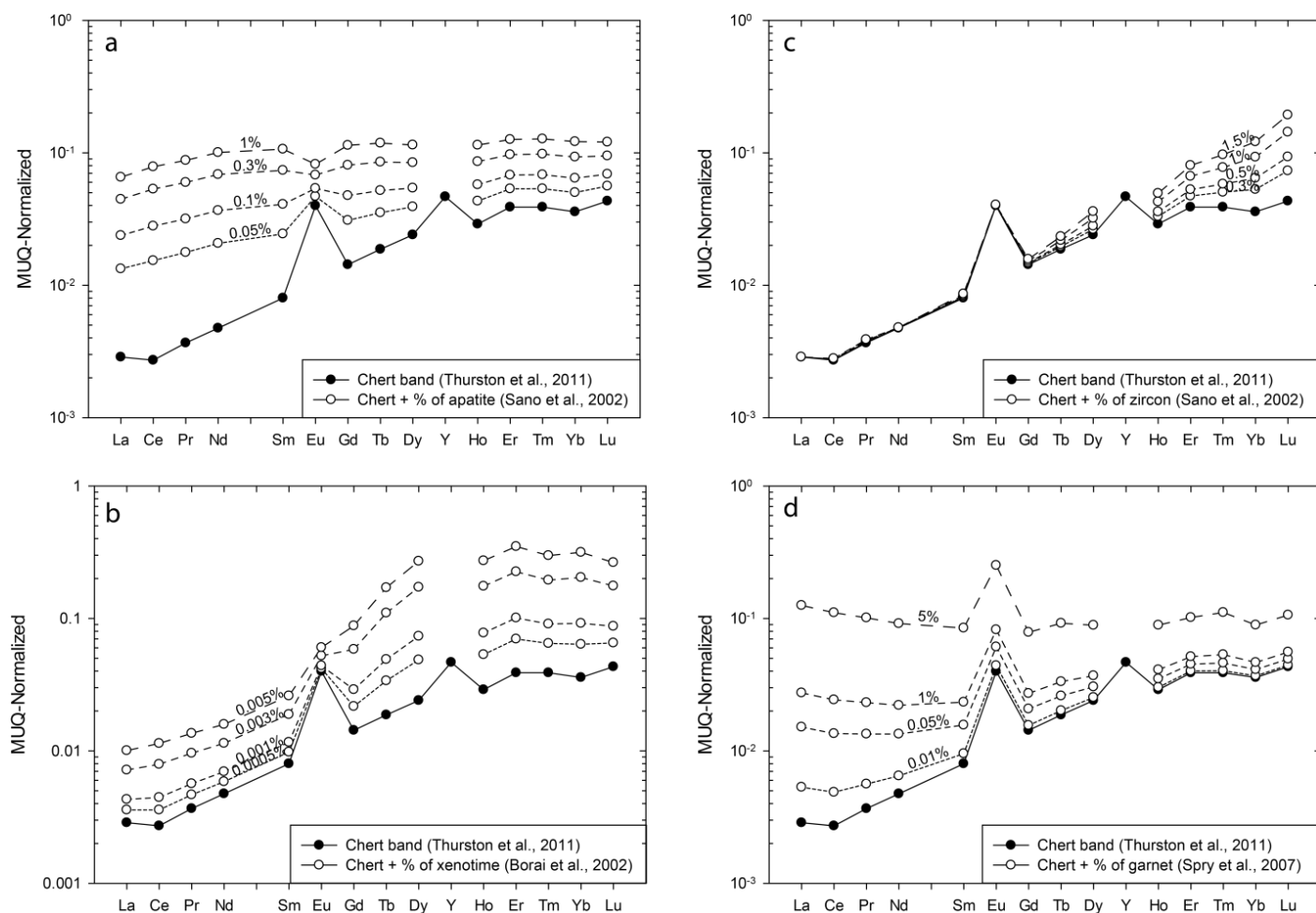


Figure 2.6: Shale (MUQ) - normalized REE+Y patterns of chert sample (black circle) from Thurston et al. (2011), affected by variable concentration of residual contamination: A) apatite (data from Sano et al. (2002)); B) xenotime (data from Borai et al. (2002)); C) zircon (data from Sano et al. (2002)); and D) garnet (data from Spry et al. (2007)).

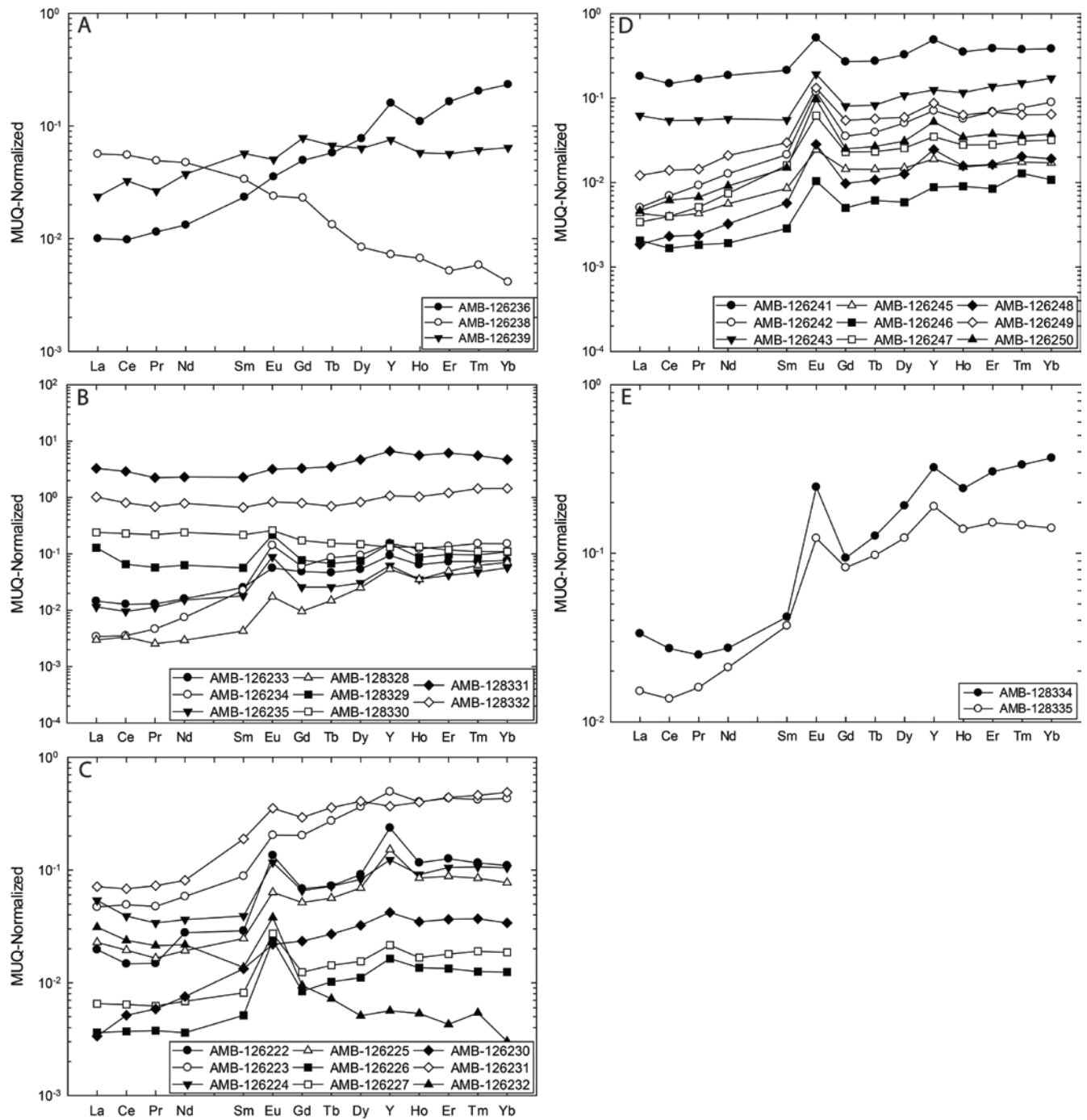


Figure 2.7: Shale (MUQ) - normalized REE+Y patterns for chert samples from the different BIFs sampled at Meadowbank: A) Far West; B) West IF; C) Central BIF; D) East BIF; and E) Grizzly area.

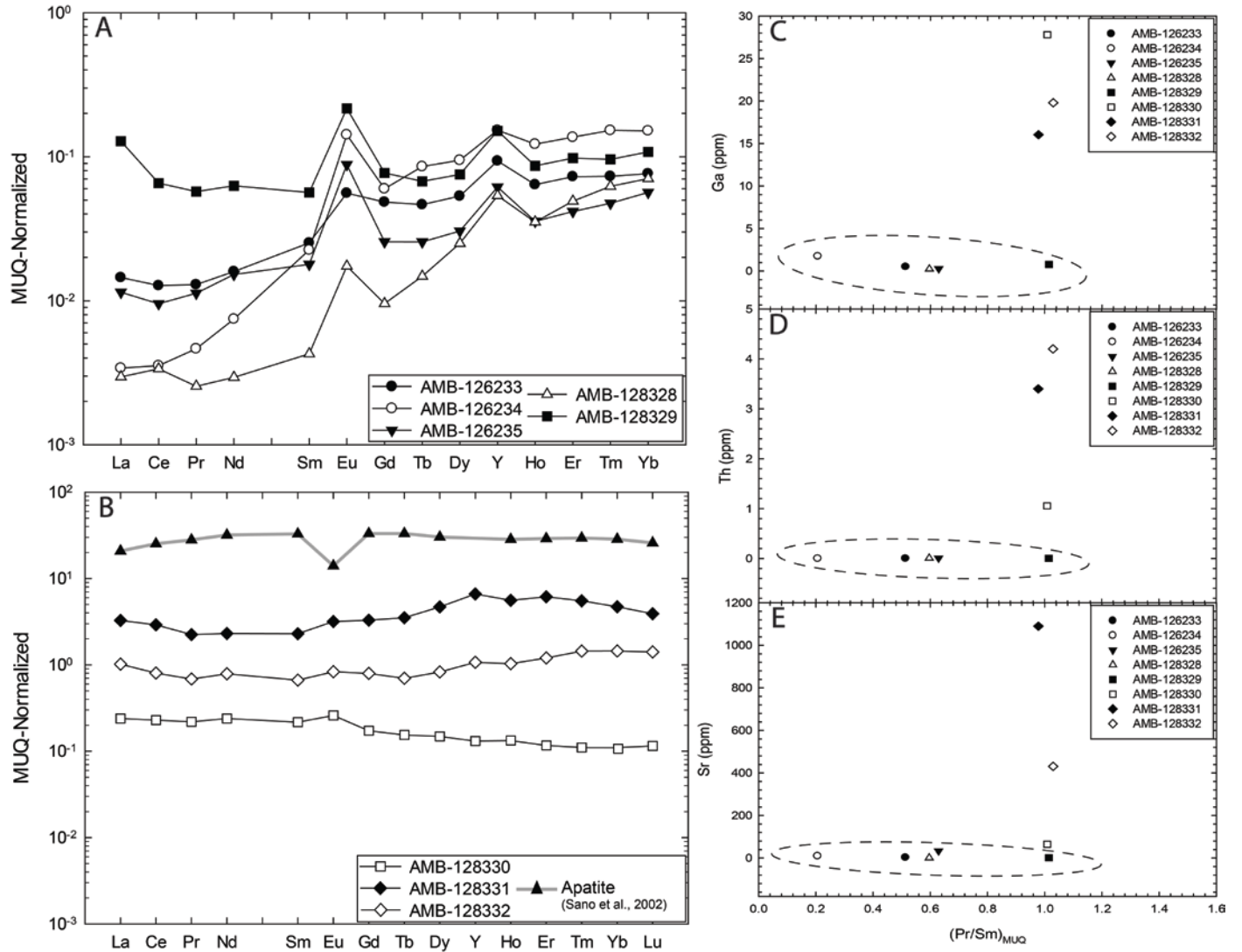


Figure 2.8: Geochemical data for chert samples from the West BIF at Meadowbank: A, B) Shale (MUQ) - normalized REE patterns reflecting the influence of ambient seawater and hydrothermal fluids. Note that in Fig. 2.8B is also shown the profile for an apatite for comparison to samples from Meadowbank, as discussed in the text; C) Ga vs. Pr/Sm_{MUQ} ; D) Th vs. Pr/Sm_{MUQ} ; and E) Sr vs. Pr/Sm_{MUQ} .

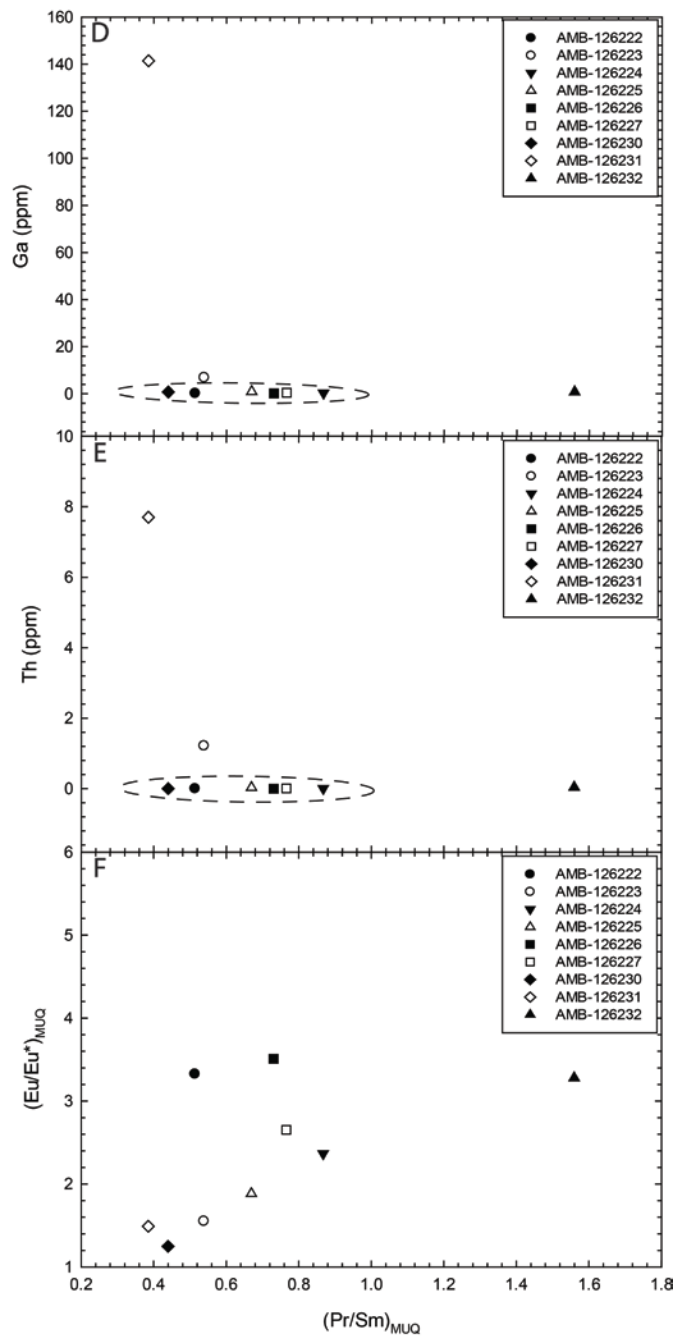
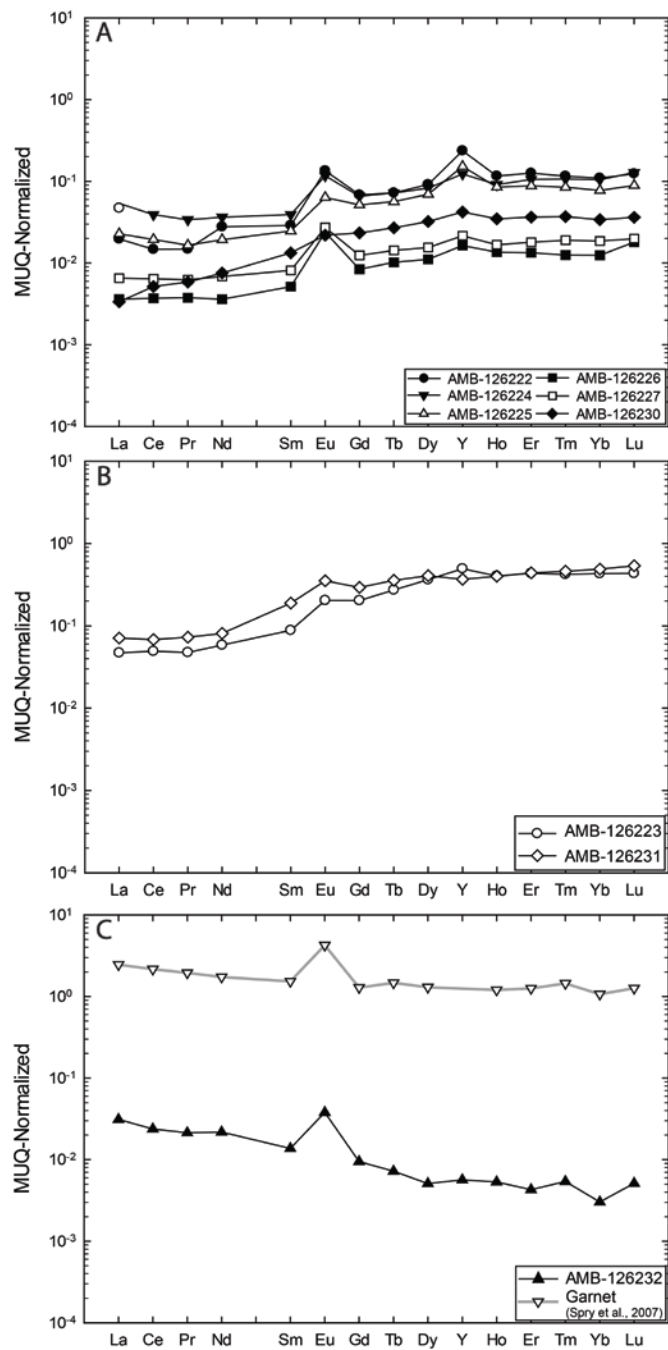


Figure 2.9: Geochemical data for chert samples from the Central BIF at Meadowbank: A, B, C) Shale (MUQ) - normalized REE patterns reflecting the influence of ambient seawater and hydrothermal fluids. Also note that in Figure 2.9C is shown the profile for a garnet-rich sample from Mt. Isa, Australia (from Spry et al., 2007) for comparison to one of the profiles from Meadowbank, as discussed in the text; D) Ga vs. $\text{Pr}/\text{Sm}_{\text{MUQ}}$; E) Th vs. $\text{Pr}/\text{Sm}_{\text{MUQ}}$; and F) $\text{Eu}/\text{Eu}^*_{\text{MUQ}}$ vs. $\text{Pr}/\text{Sm}_{\text{MUQ}}$.

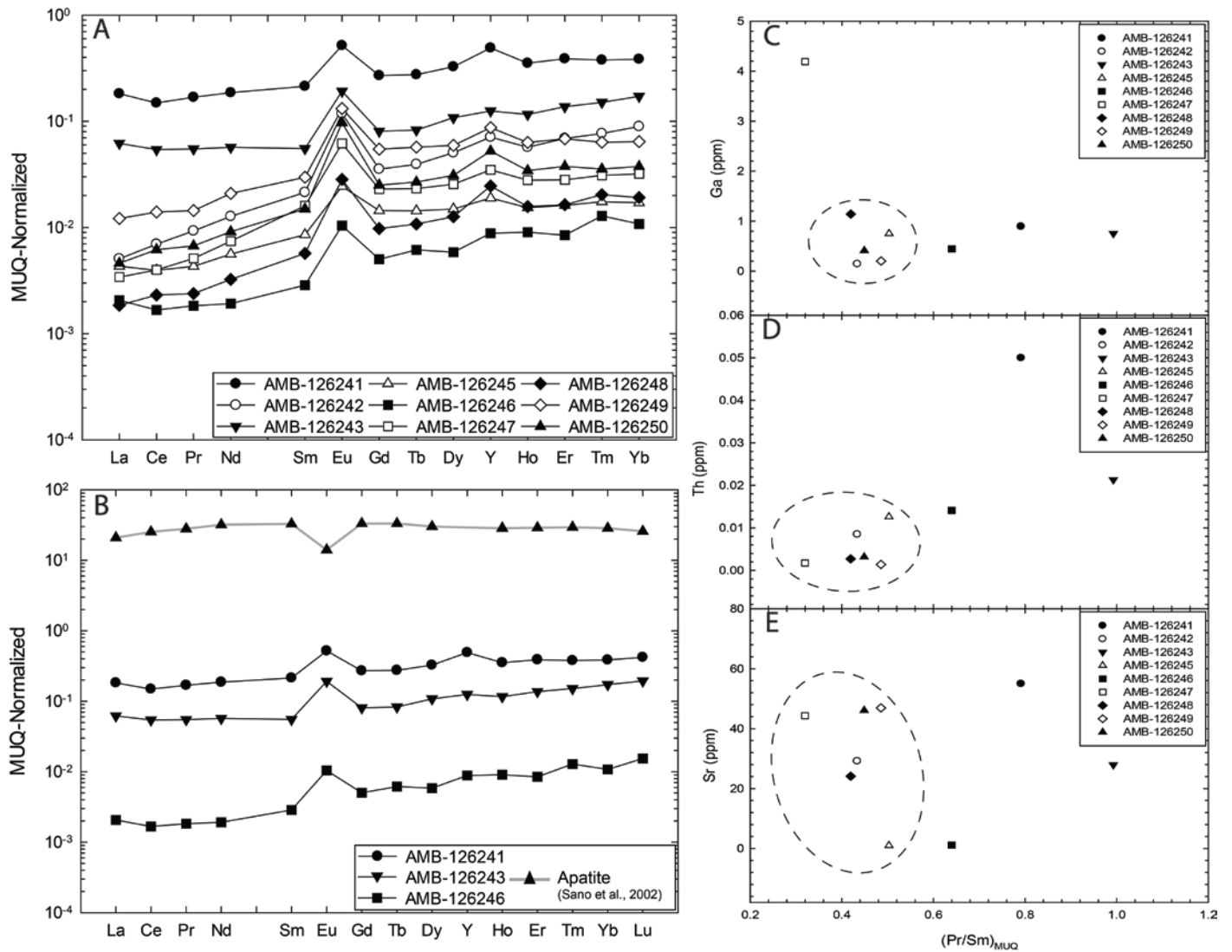


Figure 2.10: Geochemical data for chert samples from the East BIF at Meadowbank: A,B) Shale (MUQ) - normalized REE patterns reflecting the influence of ambient seawater and hydrothermal fluids; C) Ga vs. $(Pr/Sm)_{MUQ}$; D) Th vs. $(Pr/Sm)_{MUQ}$; and E) Sr vs. $(Pr/Sm)_{MUQ}$.

2.10 Tables and captions

Table 2.1: Deformation events in the Meadowbank area

Deformation events	Generation of structure	Description	Age
D4	L4	Crenulation lineation	1835-1760 Ma
	S4	Steeply dipping axial surfaces, and local crenulation cleavages	
	F4	Upright, open- to tight folds. Moderately to shallowly plunging, with NNE-trending, steeply dipping ($>60^\circ$) axial surfaces	
D3	L3	Shallowly plunging to subhorizontal crenulation lineation, itself subparallel to F3 fold axes	1790 Ma
	F3	Southeast-verging minor fold set with shallowly to moderately northwest-dipping ($<40^\circ$) axial surfaces	
D2	Shear zone	West-directed, reverse shear zones	1800-1900 Ma
	L2	Strong crenulation or intersection lineations	
	S2	Axial-planar foliations with variable orientation. Vary from schistosity, to crenulation, to a transposition foliation	
	F2	Tight- to isoclinal, generally intrafolial folds. The folds are doubly plunging shallowly to the north or south, NE- to E-verging in the Third Portage area, and NW- to N-verging in the North Portage area	
D1	L1	Clast elongation lineations	2620-2590 Ma and 1835 Ma
	S1	Schistosity largely sub-parallel to bedding and layers. Indicated by phyllosilicate and chlorite alignment	
	F1	Shallowly plunging, isoclinal folds	

Table 2.2: Metamorphic events in the Meadowbank area

Metamorphic events	Facies assemblage	Description	Age
M3	Mid-upper greenschist to amphibolite	Characterized by a new generation of biotite, garnet, cummingtonite and actinolite overprinting D2 structures and is contained in S3 fabrics. The mineral assemblage suggests a temperature near 450°C and a pressure of 3 kbars (Pehrsson et al., 2000)	post-mineralization, 1.8 Ga
M2	Amphibolite grade	Located in the south part of the property, in the Goose Island zone (Fig. 3). Characterized by an assemblages of biotite-staurolite-muscovite-garnet suggesting temperatures near 550°C and a pressure at least 3.0 kbars	Coeval with D2
	Upper greenschist	Located in the central part of the Meadowbank area; characterized by an assemblages of epidote amphibolites suggesting temperature of about 450°C at lower pressures	
	Mid-greenschist	Located in the north of the Meadowbank area; composed of kyanite in the quartzite unit and grunerite-chlorite in the BIF suggesting a temperature near 400°C and pressure of at least 2.5 kbars (Armitage et al., 1996)	
M1	Greenschist	Unknown pressure. Interpreted to predate D2 structures and postdates the 2.60 Ga granites	< 2.60 Ga- > 1.8-1.9 Ga

Table 2.3: Abundances of elements and REE+Y for samples from Central BIF

Samples	AMB-126222	AMB-126223	AMB-126224	AMB-126225	AMB-126226	AMB-126227	AMB-126230	AMB-126231	AMB-126232
Si (ppm)	331200	250600	313200	366000	357800	326800	329400	155600	381400
Li (ppm)	0.310	4.630	0.760	1.760	0.077	0.055	0.455	16.610	0.974
Be (ppm)	0.560	0.254	0.480	0.240	0.067	0.187	0.144	6.370	0.000
Sc (ppm)	4.551	10.140	4.252	5.295	3.903	3.437	3.524	27.180	3.054
Ti (ppm)	4.210	1358.000	5.100	27.100	2.101	6.980	5.270	2780.000	35.900
V (ppm)	0.324	9.360	0.118	1.565	0.049	0.386	0.445	188.900	3.330
Cr (ppm)	6.800	46.600	5.500	17.100	4.880	2.890	5.900	201.400	5.880
Mn (ppm)	540	616	353.716	239	96	39.500	33.500	34.700	7.370
Fe (ppm)	82.660	63.400	33100	30600	2050	25600	30800	12450	2140
Co (ppm)	0.553	0.870	1.730	0.509	0.235	0.203	1.000	1.943	0.177
Ni (ppm)	13.200	74.430	14.000	11.000	4.190	2.600	6.200	7.310	4.900
Cu (ppm)	475.635	151.568	13.000	13.900	15.400	6.900	12.900	2.750	8.700
Zn (ppm)	41.400	132.100	26.800	33.000	7.600	13.400	15.600	13.000	14.500
Ga (ppm)	0.176	6.830	0.320	0.924	0.178	0.417	0.758	141.400	0.839
As (ppm)	2.446	4.300	0.761	0.630	1.310	0.923	0.860	0.479	1.380
Rb (ppm)	0.208	3.460	0.652	1.630	0.220	0.675	1.645	364.000	0.273
Sr (ppm)	1.460	20.400	18.400	5.650	21.800	3.830	13.500	95.200	10.930
Y (ppm)	7.790	16.300	4.050	5.000	0.539	0.710	1.384	12.100	0.186
Zr (ppm)	0.153	104.900	0.205	8.800	0.233	0.146	0.199	183.000	2.250
Nb (ppm)	0.031	4.170	0.050	0.180	0.016	0.053	0.064	7.900	0.022
Mo (ppm)	0.107	0.166	0.062	0.088	0.078	0.038	0.171	0.125	0.134
Ag (ppm)	0.270	0.117	3.000	0.054	0.054	0.026	0.043	0.058	0.069
Cd (ppm)	0.292	0.213	1.500	0.408	0.700	0.316	0.429	0.150	0.676
In (ppm)	0.024	0.049	0.027	0.026	0.012	0.022	0.015	0.142	0.020
Sn (ppm)	1.087	3.082	1.470	2.600	0.620	1.940	0.373	19.800	0.338
Sb (ppm)	0.702	0.736	0.760	0.388	0.148	0.348	0.000	0.137	0.140
Cs (ppm)	0.088	1.607	0.227	0.505	0.083	0.187	1.104	10.190	0.121
Ba (ppm)	0.394	3.280	1.430	3.580	0.598	1.140	2.820	1480.000	1.600
La (ppm)	0.733	1.750	2.000	0.850	0.135	0.243	0.125	2.650	1.160
Ce (ppm)	1.190	3.970	3.150	1.570	0.299	0.518	0.416	5.500	1.920
Pr (ppm)	0.141	0.451	0.322	0.157	0.036	0.059	0.056	0.690	0.203
Nd (ppm)	1.010	2.120	1.320	0.700	0.131	0.249	0.274	2.940	0.790
Sm (ppm)	0.213	0.650	0.288	0.182	0.038	0.060	0.098	1.390	0.101
Eu (ppm)	0.217	0.328	0.188	0.102	0.038	0.044	0.035	0.568	0.061
Gd (ppm)	0.455	1.350	0.437	0.343	0.056	0.083	0.156	1.950	0.063
Tb (ppm)	0.074	0.281	0.074	0.058	0.011	0.015	0.028	0.368	0.007
Dy (ppm)	0.556	2.220	0.503	0.423	0.068	0.094	0.197	2.480	0.031
Ho (ppm)	0.145	0.503	0.114	0.106	0.017	0.021	0.043	0.500	0.007
Er (ppm)	0.438	1.510	0.366	0.306	0.047	0.063	0.127	1.530	0.015
Tm (ppm)	0.060	0.219	0.055	0.044	0.007	0.010	0.019	0.239	0.003
Yb (ppm)	0.366	1.439	0.349	0.258	0.042	0.062	0.113	1.630	0.010
Lu (ppm)	0.062	0.217	0.064	0.045	0.009	0.010	0.018	0.268	0.003
Hf (ppm)	0.004	1.591	0.002	0.170	0.002	0.002	0.004	4.610	0.058
Ta (ppm)	0.002	0.430	0.003	0.013	0.001	0.003	0.005	0.604	0.003
W (ppm)	0.258	0.993	0.080	0.234	0.042	0.053	0.710	11.390	0.091
Au (ppm)	0.004	0.012	0.022	0.004	0.002	0.003	0.007	0.013	0.004
Tl (ppm)	0.006	0.020	0.019	0.013	0.007	0.011	0.032	3.045	0.029
Pb (ppm)	17.363	9.748	940.000	4.500	3.340	1.079	2.150	11.740	5.380
Th (ppm)	0.006	1.220	0.005	0.035	0.002	0.012	0.003	7.700	0.043
U (ppm)	0.007	0.930	0.043	0.045	0.012	0.021	0.023	6.320	0.021
Y/Ho	53.724	32.406	35.526	47.170	31.706	33.971	31.889	24.200	27.886
Eu/Eu*	3.327	1.553	2.366	1.883	3.511	2.652	1.249	1.490	3.280
La/La*	4.648	1.494	1.819	1.875	0.887	1.265	0.954	1.215	1.508
Y/Y*	1.956	1.184	1.253	1.758	1.214	1.242	1.180	0.875	1.175
Ce/Ce*	1.860	1.273	1.234	1.371	0.945	1.132	1.134	1.045	1.132
Gd/Gd*	1.246	1.065	1.088	1.166	0.987	1.002	1.055	1.001	1.011
Pr/Sm	0.514	0.538	0.867	0.669	0.731	0.765	0.440	0.385	1.559
Nd/Yb	0.254	0.135	0.348	0.249	0.290	0.369	0.222	0.166	7.191

Table 2.4: Abundances of elements and REE+Y for samples from the East BIF

Samples	AMB-126241	AMB-126242	AMB-126243	AMB-126245	AMB-126246	AMB-126247	AMB-126248	AMB-126249	AMB-126250
Si (ppm)	488400	832000	784800	714600	746000	670600	639600	569600	657400
Li (ppm)	1.907	0.406	0.282	0.061	2.150	0.536	0.576	0.249	0.680
Be (ppm)	3.720	0.215	0.206	0.096	0.099	0.148	0.058	0.000	0.040
Sc (ppm)	5.466	4.041	3.514	2.986	3.516	2.821	2.617	2.907	2.872
Ti (ppm)	8.570	3.050	12.100	12.250	13.400	5.030	4.830	1.368	4.070
V (ppm)	0.601	0.185	1.770	0.529	1.047	0.245	0.188	0.085	0.205
Cr (ppm)	16.900	6.100	15.500	5.800	7.600	5.820	5.200	9.100	6.630
Mn (ppm)	1602	1030	265	89	78.500	222	105	677	482
Fe (ppm)	28800	13490	12890	54700	31800	9790	6720	12200	17020
Co (ppm)	0.340	0.471	0.661	1.140	0.389	0.129	0.189	0.165	0.372
Ni (ppm)	2.770	2.750	6.500	2.750	5.600	2.750	2.790	3.500	2.450
Cu (ppm)	5.100	2.970	4.700	5.200	5.300	37.400	7.300	6.400	4.660
Zn (ppm)	15.600	10.870	10.350	12.000	12.840	6.670	11.300	7.800	7.560
Ga (ppm)	0.894	0.144	0.751	0.751	0.444	4.190	1.140	0.201	0.412
As (ppm)	0.514	0.142	1.790	0.624	2.140	0.558	0.055	0.567	0.553
Rb (ppm)	1.550	0.019	0.069	0.026	0.774	1.940	0.909	0.078	1.150
Sr (ppm)	55.000	29.200	27.900	0.998	1.120	44.300	24.100	46.900	46.100
Y (ppm)	16.190	2.340	4.120	0.624	0.291	1.150	0.810	2.870	1.730
Zr (ppm)	2.170	0.461	0.970	0.550	0.860	0.224	1.120	0.178	0.425
Nb (ppm)	0.169	0.026	0.048	0.102	0.053	0.078	0.035	0.014	0.024
Mo (ppm)	0.124	0.138	0.460	0.034	0.134	0.079	0.081	29.000	0.111
Ag (ppm)	0.043	0.028	0.045	0.016	0.044	0.133	0.030	0.047	0.088
Cd (ppm)	0.296	0.422	0.331	0.198	0.407	0.308	0.321	0.314	0.327
In (ppm)	0.083	0.012	0.036	0.008	0.030	0.010	0.010	0.017	0.009
Sn (ppm)	0.870	0.261	1.560	0.226	2.200	0.209	0.148	1.840	0.200
Sb (ppm)	-0.029	0.030	0.075	0.687	0.725	0.000	0.000	0.152	0.000
Cs (ppm)	0.279	0.008	0.029	0.017	0.062	0.062	0.053	0.041	0.060
Ba (ppm)	11.860	0.293	0.555	0.384	2.460	85.000	18.100	1.260	3.990
La (ppm)	6.790	0.189	2.310	0.161	0.077	0.127	0.069	0.453	0.172
Ce (ppm)	12.030	0.562	4.380	0.319	0.135	0.322	0.187	1.130	0.499
Pr (ppm)	1.605	0.088	0.522	0.041	0.017	0.049	0.023	0.137	0.064
Nd (ppm)	6.770	0.463	2.070	0.204	0.070	0.270	0.118	0.760	0.332
Sm (ppm)	1.574	0.158	0.408	0.063	0.021	0.118	0.042	0.219	0.110
Eu (ppm)	0.834	0.191	0.309	0.039	0.017	0.100	0.046	0.212	0.156
Gd (ppm)	1.800	0.236	0.537	0.096	0.033	0.153	0.065	0.364	0.167
Tb (ppm)	0.283	0.041	0.085	0.015	0.006	0.024	0.011	0.059	0.028
Dy (ppm)	1.990	0.309	0.660	0.091	0.036	0.156	0.077	0.362	0.189
Ho (ppm)	0.441	0.071	0.145	0.019	0.011	0.035	0.020	0.079	0.043
Er (ppm)	1.354	0.240	0.478	0.056	0.030	0.098	0.057	0.238	0.131
Tm (ppm)	0.197	0.040	0.079	0.009	0.007	0.016	0.011	0.033	0.019
Yb (ppm)	1.285	0.299	0.574	0.057	0.036	0.107	0.064	0.215	0.125
Lu (ppm)	0.210	0.060	0.097	0.010	0.008	0.020	0.013	0.040	0.024
Hf (ppm)	0.036	0.009	0.013	0.015	0.010	0.004	0.009	0.003	0.009
Ta (ppm)	0.003	0.002	0.004	0.007	0.005	0.003	0.004	0.001	0.001
W (ppm)	0.215	0.076	0.085	0.120	0.136	0.249	0.095	0.060	0.084
Au (ppm)	0.002	0.002	0.003	0.001	0.003	0.004	0.002	0.002	0.001
Tl (ppm)	0.023	0.015	0.015	0.008	0.022	0.014	0.018	0.009	0.012
Pb (ppm)	2.030	1.133	2.970	1.010	2.850	3.860	1.570	2.170	1.273
Th (ppm)	0.050	0.009	0.021	0.013	0.014	0.002	0.003	0.001	0.003
U (ppm)	0.255	0.015	0.212	0.040	0.027	0.006	0.006	0.004	0.011
Y/Ho	36.712	32.819	28.414	32.500	25.752	32.951	41.117	36.329	40.233
Eu/Eu*	2.198	4.359	2.949	2.292	2.672	3.272	3.833	3.449	5.122
La/La*	1.312	1.025	1.213	1.706	1.237	1.408	1.431	1.773	1.272
Y/Y*	1.325	1.128	0.988	1.202	1.009	1.245	1.531	1.325	1.458
Ce/Ce*	0.973	1.027	1.024	1.197	0.956	1.132	1.317	1.407	1.252
Gd/Gd*	1.055	1.066	1.085	1.141	0.998	1.075	1.068	1.154	1.094
Pr/Sm	0.791	0.434	0.993	0.503	0.640	0.320	0.419	0.485	0.449
Nd/Yb	0.484	0.142	0.332	0.328	0.178	0.233	0.170	0.325	0.243

Table 2.5: Abundances of elements and REE+Y for samples from the West IF

Samples	AMB-126233	AMB-126234	AMB-126235	AMB-128328	AMB-128329	AMB-128330	AMB-128331	AMB-128332
Si (ppm)	302600	249000	328200	593400	611000	393600	305800	457600
Li (ppm)	0.146	0.213	0.130	0.316	0.226	65.100	9.790	11.100
Be (ppm)	0.063	0.990	0.213	0.012	0.316	1.154	1.570	1.980
Sc (ppm)	2.980	3.530	3.234	3.241	2.538	15.610	7.340	7.780
Ti (ppm)	7.510	7.550	2.380	2.249	1.910	1840.000	474.000	630.000
V (ppm)	0.211	0.465	0.131	0.162	0.133	27.200	11.090	4.610
Cr (ppm)	4.710	172.000	6.700	5.250	3.590	39.100	49.300	22.600
Mn (ppm)	210.0	226.0	159.0	126.1	264.0	658.0	268.6	158.0
Fe (ppm)	38800	61500	31100	78600	39100	67800	51400	15900
Co (ppm)	1.080	0.740	0.397	0.479	0.314	11.980	2.120	1.710
Ni (ppm)	12.000	7.400	6.700	2.690	2.790	44.100	13.050	12.100
Cu (ppm)	25.000	2.800	3.900	2.360	19.400	18.800	3.780	9.010
Zn (ppm)	11.200	22.900	11.600	14.670	12.300	141.000	13.760	16.500
Ga (ppm)	0.517	1.753	0.264	0.237	0.773	27.800	16.040	19.800
As (ppm)	0.528	0.128	0.406	-0.193	0.307	0.168	168.400	12.300
Rb (ppm)	2.460	8.400	0.335	0.366	2.130	116.000	30.800	34.300
Sr (ppm)	3.410	10.000	33.100	1.016	1.880	64.900	1090.000	431.000
Y (ppm)	3.080	5.030	2.030	1.767	4.980	4.320	218.300	35.200
Zr (ppm)	5.800	0.111	0.790	0.319	0.300	19.100	43.400	20.100
Nb (ppm)	0.038	0.157	0.041	0.072	0.049	3.430	1.590	1.840
Mo (ppm)	0.051	0.060	0.065	0.025	0.043	0.736	0.054	0.084
Ag (ppm)	0.034	0.370	0.038	0.009	0.050	0.033	0.068	0.043
Cd (ppm)	0.160	0.166	0.491	0.139	0.118	0.131	0.275	0.221
In (ppm)	0.012	0.021	0.015	0.007	0.016	0.093	0.017	0.021
Sn (ppm)	0.500	0.670	0.520	0.550	0.192	4.200	0.610	0.485
Sb (ppm)	0.275	0.124	0.260	0.000	0.098	0.000	0.027	0.095
Cs (ppm)	1.010	6.100	0.242	0.089	1.027	7.970	4.830	2.050
Ba (ppm)	2.370	19.800	1.870	3.040	11.310	234.000	304.000	365.000
La (ppm)	0.540	0.127	0.427	0.110	4.780	8.920	122.000	38.000
Ce (ppm)	1.030	0.286	0.770	0.272	5.290	18.520	235.000	65.000
Pr (ppm)	0.123	0.044	0.107	0.024	0.544	2.080	21.300	6.500
Nd (ppm)	0.580	0.271	0.553	0.107	2.280	8.690	84.000	28.600
Sm (ppm)	0.186	0.166	0.132	0.032	0.416	1.600	16.900	4.900
Eu (ppm)	0.090	0.229	0.142	0.028	0.349	0.418	5.120	1.340
Gd (ppm)	0.323	0.399	0.171	0.064	0.514	1.149	21.900	5.300
Tb (ppm)	0.048	0.088	0.026	0.015	0.070	0.159	3.620	0.720
Dy (ppm)	0.325	0.577	0.186	0.153	0.459	0.906	28.600	5.050
Ho (ppm)	0.080	0.153	0.045	0.044	0.108	0.166	6.990	1.290
Er (ppm)	0.253	0.476	0.145	0.171	0.340	0.406	21.400	4.190
Tm (ppm)	0.038	0.079	0.025	0.032	0.050	0.057	2.870	0.750
Yb (ppm)	0.255	0.505	0.189	0.236	0.361	0.367	15.740	4.830
Lu (ppm)	0.049	0.095	0.035	0.039	0.069	0.058	1.958	0.706
Hf (ppm)	0.060	0.003	0.012	0.007	0.003	0.579	1.133	0.630
Ta (ppm)	0.002	0.006	0.002	0.004	0.003	0.330	0.124	0.230
W (ppm)	0.064	0.051	0.068	0.023	0.050	1.020	1.227	0.463
Au (ppm)	0.003	0.002	0.002	0.000	0.001	0.004	0.003	0.002
Tl (ppm)	0.011	0.011	0.017	0.005	0.012	0.476	0.157	0.190
Pb (ppm)	0.970	1.620	1.680	0.401	0.407	5.880	20.470	8.860
Th (ppm)	0.004	0.002	0.006	0.007	0.003	1.055	3.400	4.200
U (ppm)	0.043	0.007	0.017	0.003	0.014	0.465	2.170	2.080
Y/Ho	38.500	32.876	45.618	40.159	46.111	26.024	31.230	27.287
Eu/Eu*	1.745	3.916	4.203	2.558	3.516	1.318	1.215	1.226
La/La*	1.701	1.895	1.857	1.541	2.689	1.304	1.552	1.972
Y/Y*	1.368	1.179	1.596	1.273	1.643	1.052	1.129	0.956
Ce/Ce*	1.215	1.226	1.144	1.523	1.254	1.144	1.338	1.353
Gd/Gd*	1.237	1.062	1.087	0.932	1.180	0.980	1.091	1.153
Pr/Sm	0.513	0.206	0.629	0.596	1.014	1.009	0.978	1.029
Nd/Yb	0.209	0.049	0.269	0.042	0.581	2.177	0.491	0.544

Table 2.6: Abundances of elements and REE+Y for samples from the Far West and Grizzly

	Far West			Grizzly	
Samples	AMB-126236	AMB-126238	AMB-126239	AMB-128334	AMB-128335
Si (ppm)	317200	549200	495200	271600	523400
Li (ppm)	0.72	0.09	0.21	0.67	0.15
Be (ppm)	0.33	0.00	0.06	1.00	0.20
Sc (ppm)	3.89	2.98	4.66	3.53	4.31
Ti (ppm)	19.20	7.90	27.00	49.06	1.98
V (ppm)	1.58	0.32	3.79	11.41	0.79
Cr (ppm)	7.00	8.20	7.00	25.90	5.53
Mn (ppm)	236.00	23.50	336.00	2539.00	747.00
Fe (ppm)	39700	890	10900	506100	10090
Co (ppm)	1.69	0.21	0.84	2.67	0.47
Ni (ppm)	3.71	6.24	5.10	46.08	11.00
Cu (ppm)	8.00	11.10	8.00	3.47	3.14
Zn (ppm)	28.30	11.60	29.30	230.10	10.49
Ga (ppm)	1.28	0.19	1.18	0.77	0.25
As (ppm)	0.33	1.25	0.69	0.68	7.80
Rb (ppm)	0.10	0.17	0.50	1.05	0.17
Sr (ppm)	3.12	1.45	2.25	127.00	37.10
Y (ppm)	5.24	0.24	2.48	10.61	6.24
Zr (ppm)	0.50	0.53	16.00	17.30	48.30
Nb (ppm)	0.08	0.03	0.23	0.28	0.02
Mo (ppm)	0.09	0.22	0.22	0.05	0.09
Ag (ppm)	0.06	0.05	0.09	0.02	0.03
Cd (ppm)	0.59	0.45	0.55	0.57	0.28
In (ppm)	0.04	0.03	0.02	0.01	0.01
Sn (ppm)	0.38	1.52	0.72	0.13	0.20
Sb (ppm)	0.06	0.04	0.15	1.60	0.34
Cs (ppm)	0.05	0.12	0.11	0.71	0.23
Ba (ppm)	0.46	0.51	3.69	0.77	3.20
La (ppm)	0.373	2.1	0.88	1.246	0.567
Ce (ppm)	0.79	4.46	2.63	2.2	1.107
Pr (ppm)	0.109	0.467	0.251	0.237	0.1519
Nd (ppm)	0.48	1.72	1.36	0.996	0.765
Sm (ppm)	0.172	0.248	0.42	0.309	0.274
Eu (ppm)	0.0569	0.0384	0.081	0.398	0.198
Gd (ppm)	0.33	0.153	0.52	0.625	0.548
Tb (ppm)	0.0594	0.0137	0.069	0.1306	0.1003
Dy (ppm)	0.471	0.0512	0.385	1.168	0.752
Ho (ppm)	0.137	0.00837	0.0722	0.303	0.174
Er (ppm)	0.571	0.018	0.197	1.06	0.528
Tm (ppm)	0.106	0.00303	0.0318	0.1742	0.0765
Yb (ppm)	0.777	0.0138	0.214	1.229	0.471
Lu (ppm)	0.163	0.00268	0.0382	0.1914	0.0708
Hf (ppm)	0.0149	0.011	0.249	0.245	0.289
Ta (ppm)	0.00759	0.00319	0.0148	0.01262	0.00172
W (ppm)	0.0414	0.1129	0.089	0.2389	0.151
Au (ppm)	0.00439	0.00268	0.0049	0.00227	0.00182
Tl (ppm)	0.0241	0.0239	0.0311	0.0057	0.0151
Pb (ppm)	2.09	2.13	1.56	2.11	3.17
Th (ppm)	0.00414	0.0228	0.055	0.0141	0.00666
U (ppm)	0.029	0.0561	0.196	0.176	0.123
Y/Ho	38.25	28.43	34.35	35.02	35.86
Eu/Eu*	1.082	0.931	0.813	3.964	2.329
La/La*	1.156	1.063	1.794	1.618	1.650
Y/Y*	1.163	1.218	1.317	1.178	1.303
Ce/Ce*	0.982	1.082	1.746	1.200	1.129
Gd/Gd*	1.126	1.218	1.197	1.045	1.134
Pr/Sm	0.492	1.461	0.464	0.595	0.430
Nd/Yb	0.057	11.459	0.584	0.075	0.149

Table 2.7: Estimated LOD values for the analyzed elements.

Analyte	Estimated LOD [ppm]		Analyte	Estimated LOD [ppm]
Li7	0.015		Sb121	0.004
Be9	0.028		Cs133	0.001
Si29	40		Ba137	0.018
Sc45	0.033		La139	0.002
Ti47	0.143		Ce140	0.002
V51	0.027		Pr141	0.002
Cr52	0.077		Nd146	0.012
Mn55	0.069		Sm147	0.012
Fe57	0.238		Eu153	0.004
Co59	0.005		Gd157	0.015
Ni60	0.052		Tb159	0.002
Cu65	0.024		Dy163	0.010
Zn66	0.035		Ho165	0.002
Ga69	0.009		Er166	0.007
As75	0.193		Tm169	0.002
Rb85	0.003		Yb172	0.011
Sr88	0.001		Lu175	0.003
Y89	0.001		Hf178	0.009
Zr90	0.002		Ta181	0.003
Nb93	0.001		W182	0.008
Mo95	0.006		Au197	0.004
Ag107	0.002		Tl205	0.002
Cd111	0.017		Pb208	0.003
In115	0.001		Th232	0.005
Sn118	0.004		U238	0.003

2.11 References

- Alexander, B.W., Bau, M., Andersson, P. and Dulski, P. 2008. Continentially-derived solutes in shallow Archean sea water; rare earth element and Nd isotope evidence in iron formation from the 2.9 Ga Pongola Supergroup, South Africa; *Geochimica et Cosmochimica Acta* 72, p. 378-394.
- Allwood, A.C., Kamber, B.S., Walter, M.R., Burch, I.W. and Kanik, I. 2010: Trace element record depositional history of an Early Archean stromatolitic carbonate platform; *Chemical Geology*, v. 270, p. 148-163.
- Armitage, A.E., James, R.S. and Goff, S.P. 1996. Gold mineralization in Archean banded iron formation, Third Portage Lake area, Northwest Territories, Canada; *Exploration and Mining Geology*, v. 5, no. 1, p. 1-15.
- Ashton, K.E. 1985. Archean orthoquartzites from the Churchill Structural Province near Baker Lake, N.W.T.; Geological Association of Canada, Mineralogical Association of Canada, Program with Abstracts, v. 10, p. A2.
- Aspler, L.B. and Chiarenzelli, J.R., 1996a. Stratigraphy, sedimentology and physical volcanology of the Henik Group, central Ennadai-Rankin greenstone belt, Northwest Territories, Canada: Late Archean paleogeography of the Hearne Province and tectonic implications; *Precambrian Research*, v. 77, p. 59-89.
- Agnico Eagle Mines Ltd. 2012. Technical Report on the Mineral Resources and Mineral Reserves, Meadowbank gold Project, Nunavut, Canada. Prepared for Agnico Eagle Mines Ltd. By Ruel, M., Proulx, A., Muteb, P.N. and Connell, L., February 15, 2012, 190 p.

- Agnico Eagle Mines Ltd. 2008. Technical Report on the Mineral Resources and Mineral Reserves, Meadowbank gold Project, Nunavut, Canada. Prepared for Agnico Eagle Mines Ltd. By Connell, L., Doucet, D., Fortin, A., Hettinger, J., Lamontagne, E. and Perron, B., Septembre 30, 2008, 169 p.
- Agnico Eagle Mine Ltd., 2012. Meadowbank project exploration compilation and best targets in the mine area. Prepared by Côté-Mantha, O., scale 1:20 000.
- Bau, M. and Alexander, B. W. 2009. Distribution of high field strength elements (Y, Zr, REE, Hf, Ta, Th, U) in adjacent magnetite and chert bands and in reference standards FeR-3 and FeR-4 from the Temagami iron-formation, Canada, and the redox level of the Neoproterozoic ocean; *Precambrian Research*, v. 174, p. 337-346.
- Bau, M. and Dulski, P. 1996. Distribution of Y and rare-earth elements in the Penge and Kuruman Iron Formations, Transvaal Supergroup, South Africa; *Precambrian Research*, v. 79, p. 37-55.
- Bekker, A., Slack, J.F., Planavsky, N., Krapez, B., Hofmann, A., Konhauser, K.O. and Rouxel, J., 2010. Iron formation: the sedimentary product of a complex interplay among mantle, tectonic, oceanic and biospheric processes; *Economic Geology*, v. 105, p. 467-508.
- Biczok, J., Hollings, P., Klipfel, P., Heaman, L., Maas, R., Hamilton, M., Kamo, S. and Friedman, R., 2012. Geochronology of the North Caribou greenstone belt, Superior Province Canada: Implications for tectonic history and gold mineralization at the Musselwhite mine; *Precambrian Research*, v. 192-195, p. 209-230.
- Bleeker, W., 2006. The Slave Craton: Geological and Metallogenic Evolution. In Goodfellow,

W.D. (Ed.), Mineral Resources of Canada: A Synthesis of Major Deposit-types, District Metallogeny, the Evolution of Geological Provinces, and Exploration Methods", Geological Survey of Canada.

Bolhar, R., Van Kranendonk, M.J. and Kamber, B.S. 2005. A trace element study of siderite-jasper banded iron formation in the 3.45 Ga Warrawoona Group, Pilbara craton-Formation from hydrothermal fluids and shallow seawater; Precambrian Research, v. 137, p. 93-114.

Borai, E.H., Eid, M.A. and Aly, H.F. 2002. Determination of REEs distribution in monazite and xenotime minerals by iron chromatography and ICP-AES; Anal Bional Chemical, v. 372, p. 537-541.

Castonguay, S., Janvier, V., Mercier-Langevin, P., Dubé, B., McNicoll, V., Malo, M., Pehrsson, S. and Bécu, V., 2012. Recognizing optimum banded-iron formation-hosted gold environments in ancient, deformed and metamorphosed terranes: Preliminary results from the Meadowbank deposit, Nunavut: 40th Annual Yellowknife Geoscience Forum, Yellowknife, NWT, November 15-17.

Danielson, A., Moeller, P. and Dulski, P. 1992. The europium anomalies in banded iron formations and the thermal history of the oceanic crust; Chemical Geology, v. 97, p. 89-100.

Davis, W.J. and Zaleski, E. 1998. Geochronological investigations of the Woodburn Lake group, Western Churchill province, Northwest Territories: Preliminary results; Radiogenic Age and Isotopic Studies: Report 11; in Current Research 1998-F, Geological Survey of Canada Research, p. 89-97.

Goldfarb, R.J., Baker, T., Dubé, B., Groves, D.I., Hart, C.J.R. and Gosselin, P., 2005.

- Distribution, character and genesis of gold deposits in metamorphic terranes. In: Economic Geology 100th Anniversary Volume, J.W. Hedenquist, J.F.H. Thompson, R.J. Goldfarb, and J.P. Richards (eds.), p. 407-450. Goldfarb, R.J., Groves, D.I. and Gardoll, S. 2001, Orogenic gold and geologic time: A global synthesis: Ore Geology Reviews, v. 18, p. 1–75.
- Goodwin, A.M., 1973. Archean iron-formations and tectonic basins of the Canadian Shield; Economic Geology, v. 68, p. 915-933.
- Gourcerol, B., Thurston, P.C., Kontak, D.J. and Côté-Mantha, O., 2014, Interpretations and implications of preliminary LA ICP-MS analysis of chert for the origin of geochemical signatures in banded iron formations (BIFs) from the Meadowbank gold deposit, Western Churchill Province, Nunavut: Geological Survey of Canada, Current research 2014-1, 26 p.
- Hanor, J.S. and Duchac, K.C. 1990. Isovolumetric silicification of early Archean komatiites; geochemical mass balances and constraints on origin; Journal of Geology, v. 98, p. 863-877.
- Henderson, J.R. and Henderson, M.N. 1994. Geology of the Whitehills-Tehek Lakes area, District of Keewatin, Northwest Territories (parts of 56D, 56E, 66A and 66H); Geological Survey of Canada, Open File 2923, scale 1:100 000.
- Henderson, J.R., Henderson, M.N., Pryer, L.L. and Cresswell, R.G. 1991. Geology of the Whitehills-Tehek area, District of Keewatin: An Archean supracrustal belt with iron-formation hosted gold mineralization in the central Churchill province; In Current Research, 1991-2001C, Geological Survey of Canada, p. 149-156.
- Hrabi, R.B., Barclay, W.A., Fleming, D. and Alexander, R.B. 2003. Structural evolution of the Woodburn Lake group in the area of the Meadowbank gold deposit, Nunavut; in Current

- Research 2003-C27, Geological Survey of Canada, 10 p.
- James, H.L., 1954. Sedimentary facies iron-formation; *Economic Geology*, v. 49, p. 235-293.
- Kamber, B.S., 2010. Archean mafic-ultramafic volcanic landmasses and their effect on ocean-atmosphere chemistry; *Chemical Geology*, v. 274, p. 19-28.
- Kamber, B.S. and Webb, G.E. 2007. Transition metal abundances in microbial carbonate: a pilot study based on in-situ LA-ICP-MS analysis; *Geobiology*, v. 5, p. 375-389.
- Kamber, B.S., Greig, A. and Collerson, K.D., 2005. A new estimate for the composition of weathered young upper continental crust from alluvial sediments, Queensland, Australia. *Geochimica et Cosmochimica Acta*, v. 69, p. 1041-1058.
- Kamber, B.S., Bolhar, R. and Webb, G.E. 2004. Geochemistry of late Archean stromatolites from Zimbabwe: evidence for microbial life in restricted epicontinental seas; *Precambrian Research*, v. 132, p. 379-399.
- Klein, C., 2005. Some Precambrian banded iron-formation (BIFs) from around the world: Their age, geologic settings, mineralogy, metamorphism, geochemistry, and origin; *American Mineralogist*, v. 90, p. 1473-1499.
- Kerswill, J.A. 2000. Iron-formation-hosted gold deposits: a view from Nunavut with emphasis on “Lupin-like” deposits; [extended abstract with maps]; In Abstract Volume, Short Course on Geology and Mineral Deposits of Nunavut Territory; Society of Economic Geologists, London Student Chapter, March 3, 2000, 10 p.
- Kerswill, J.A., Goff, S.P., Kjarsgaard, B.A., Jenner, G.A. and Wilkinson, L. 2000. Highlights of

recent metallogenic investigations in western Churchill province, Nunavut, Canada:
Implications for mineral exploration in Archean greenstone belts; in GeoCanada 2000 —
The Millennium Geoscience Summit CD-ROM, Calgary, Abstract 736.

Kerswill, J.A., Goff, S.P., Wilkinson, L., Jenner, G.A., Kjarsgaard, B.A., Bretzlaff, R. and
Samaras, C. 1998. An update on the metallogeny of the Woodburn Lake group, western
Churchill province, Northwest Territories; In Current Research 1998-C, Geological Survey
of Canada, p. 29-41.

Lawrence, M. G. and Kamber, B. S., 2005. The behavior of the rare earth elements during
estuarine mixing- revisited; Marine Chemistry, v. 100, p.147-161.

Longerich, H. P., Jackson, S. E. and Gunther, D. 1996. Laser ablation inductively coupled
plasma mass spectrometric transient signal data acquisition and analyte concentration
calculation; Journal of Analytical Atomic Spectrometry, v. 11, p. 899-904.

Lowe, D.R. 1999. Petrology and sedimentology of cherts and related silicified sedimentary rocks
in the Swaziland Supergroup; Special Paper - Geological Society of America, v. 329, p. 83-
114.

Pehrsson, S., Wilkinson, L., Zaleski, E., Kerswill, J. and Alexander, R.B. 2000. Structural
geometry of the Meadowbank deposit area, Woodburn Lake group—implications for a
major gold deposit in the western Churchill province; in GeoCanada 2000—The Millennium
Geoscience Summit CD-ROM, Calgary.

Pehrsson, S.J., Wilkinson, L. and Zaleski, E. 2004. Geology of the Meadowbank gold deposit
area, Nunavut; Geological Survey of Canada, Open File 4269, scale 1:20 000.

- Phillips, G.N., Groves, D.I. and Martyn, J.E., 1984. An epigenetic origin for Archean banded iron-formation-hosted gold deposits; *Economic Geology and the Bulletin of the Society of Economic Geologists* 79, p. 162-171.
- Planavsky, N., Bekker, A., Rouxel, O.J., Kamber, B.S., Hofmann, A.W., Knudsen, A. and Lyons, T.W. 2010. Rare Earth Element and yttrium compositions of Archean and Paleoproterozoic Fe formations revisited: New perspectives on the significance and mechanisms of deposition; *Geochimica et Cosmochimica Acta* 74.
- Posth, N.R., Kohler, I., Swanner, E.D., Schroder, C., Wellmann, E., Binder, B., Konhauser, K.O., Neumann, U., Berthold, C., Nowak, M. and Kappler, A. 2013. Simulating Precambrian banded iron formation diagenesis; *Chemical Geology*, in press, 8 p.
- Roddick, J.C., Henderson, J.R. and Chapman, H.J. 1992. U-Pb ages from the Archean Whitehills-Tehek Lakes Supracrustal Belt, Churchill Province, District of Keewatin, Northwest Territories; in *Radiogenic Age and Isotopic Studies: Report 6*. Geological Survey of Canada, Paper 1992-2, p. 31-40.
- Sano, Y., Terada, K. and Fukuoka, T. 2002. High mass resolution ion microprobe analysis of rare earth element in silicate glass, apatite and zircon: lack of matrix dependency; *Chemical Geology*, v. 184, p. 217-230.
- Sherlock, R.L., Pehrsson, M.S., Logan, A.V., Hrabi, R.B. and Davis, W.J. 2004. Geological Setting of the Meadowbank Gold Deposits, Woodburn Lake Group, Nunavut; *Exploration and Mining Geology*, v. 13, no. 1-4, p. 67-107.
- Sherlock, R.L., Alexander, R.B., March, R. and Barclay, W.A. 2001a. Geologic setting of the

Meadowbank iron formation-hosted gold deposits; in Current Research 2001-C11, Geological Survey of Canada, 23 p.

Sherlock, R.L., Alexander, R.B., March, R. and Barclay, W.A. 2001b. Geologic setting of the Meadowbank iron formation-hosted gold deposits; Geological Survey of Canada, Open File 3149, scale 1:10 000.

Spry, P.G., Messerly, J.D. and Houk, R.S. 2007. Discrimination of metamorphic and metasomatic processes at the Broken Hill Pb-Zn-Ag deposit, Australia: rare earth element signature of garnet-rich rocks; *Economic Geology*, v. 102, p. 471-494.

Thurston, P.C., Kamber, B.S. and Whitehouse, M. 2012. Archean cherts in banded iron formation: Insight into Neoarchean ocean chemistry and depositional processes; *Precambrian Research*, v. 214-215, p. 227-257.

Zaleski, E., Duke, N.L., L'Heureux, R. and Wilkinson, L. 1999a. Geology, Woodburn Lake group, Amarulik Lake to Tehek Lake, Kivalliq Region, Nunavut; Geological Survey of Canada, Open File 3743, scale 1:50 000.

Zaleski, E., L'Heureux, R., Duke, N., Wilkinson, L. and Davis, W.J. 1999b. Komatiitic and felsic volcanic rocks overlain by quartzite, Woodburn Lake group, Meadowbank River Area, western Churchill province, Northwest Territories (Nunavut); in Current Research 1999-C, Geological Survey of Canada, p. 9-18.

Zaleski, E., Corrigan, D., Kjarsgaard, B.A., Kerswill, J.A., Jenner, G.A. and Henderson, J.R. 1997a. Geology, Woodburn Lake group, Meadowbank River to Tehek Lake (66H/1, 56E/4), District of Keewatin (Nunavut), Northwest Territories; Geological Survey of Canada, Open

File 3461, scale 1:50 000.

Zaleski, E., Corrigan, D., Kjarsgaard, B.A., Kerswill, J.A., Jenner, G.A. and Henderson, J.R.
1997b. Preliminary results of mapping and structural interpretation from the Woodburn
project, western Churchill province, Northwest Territories; in Current Research 1997-C,
Geological Survey of Canada, p. 91-100.

Chapter 3: Depositional setting of Algoma-type BIF

3.1 Abstract

Algoma-type banded iron formations (BIF) are chemical sedimentary rocks characterized by alternating layers of iron-rich minerals and chert that are generally interstratified with bimodal submarine volcanic rocks and/or sedimentary sequences in Archean greenstone belts. However, the geological setting for Algoma-type BIF deposition remains equivocal due to the effects of post-depositional deformation and metamorphism and absence of modern analogues for comparative studies. It is commonly accepted that the abundance of rare earth element and yttrium (REE+Y) in chert bands may retain a primary geochemical signature and therefore constrain their geological setting. In order to explore the latter, a geochemical study using the laser ablation-inductively coupled plasma-mass spectrometry (LA-ICP-MS) methodology was done using cherts from four Canadian BIF-hosted gold deposits. These results suggest that chert bands record: (1) interaction of seawater with Fe-oxyhydroxides, as suggested by their heavy REE enrichment coupled with La and Y enrichments; (2) contributions from high-temperature (>250°C) hydrothermal fluids, as suggested by positive Eu excursions; and (3) detrital contamination, which is suggested by relatively consistent REE concentrations and a chondritic Y/Ho ratio (i.e., $Y/Ho \approx 27$). Water-column pH conditions at the time of BIF deposition are evaluated using Ce/Ce*: a positive Ce/Ce* anomaly suggests relatively acidic conditions (i.e., $pH \leq 5$) for most of the chert samples, but more alkaline conditions (i.e., $pH \geq 5$) for samples showing Fe-oxyhydroxide precipitation within chert bands. Finally, *in-situ* secondary ion mass spectrometry (SIMS) analysis ($n = 73$) of chert from Meliadine show the $\delta^{18}O$ of primary amorphous silica (+27‰) was modified to values of around +8 to +20‰ during diagenesis at

temperatures $>100^{\circ}\text{C}$ with a fluid having $\delta^{18}\text{O}_{\text{H}_2\text{O}} = 0$ to 5‰. Thus, whereas there has been O isotopic exchange during diagenesis, the REEs and trace elements are not modified in the chert due to the low concentrations of these elements in the reacting fluid of sea water origin.

3.2 Introduction

Algoma-type BIFs are thinly bedded, chemical sedimentary rocks comprising alternating layers of iron-rich minerals and chert. These rocks are typically intercalated with Eoarchean to late Paleoproterozoic volcano-sedimentary sequences within greenstone belts (Goodwin, 1973; Bekker et al., 2010). They differ from Superior-type BIFs which represent extensive units, mainly Proterozoic in age, located in passive margin sedimentary successions and showing no specific association with volcanic units (e.g., Gross, 1980; Bekker et al., 2010). Based on their sedimentary and geochemical features, a restricted basin model, equivalent to the modern Red Sea, corresponding to closed to semi-closed basins where volcanic and hydrothermal activities were extensive represents one potential BIF depositional model (e.g., Barrett et al., 1988a; Bolhar et al., 2005; Ohmoto et al., 2006; Bekker et al., 2010). In this scenario, iron-rich minerals precipitated contemporaneously with hydrothermal vent fluids to form various iron oxyhydroxides, such as ferrihydrite. These primary minerals were subsequently transformed during diagenesis to hematite, magnetite and siderite depending in part on the microbial biomass concentration (Posth et al., 2013). Where metamorphosed, the Fe-rich assemblage may comprise more complex mineral assemblages that include a variety of silicate phases (e.g., amphibole, garnet and plagioclase). The interbedded chert horizons are considered to reflect: (1) direct seawater precipitation (e.g., Bolhar et al., 2005; Thurston et al., 2012); (2) hydrothermal precipitation from vent fluids (Allwood et al., 2010; Thurston et al., 2012); and/or (3) the

products of secondary replacement (Hanor and Duchac, 1990) as confirmed by their shale-normalized chemical signature (e.g., Thurston et al., 2011; Gourcerol et al., 2015a).

In this study, we explore the chert geochemistry at four Canadian BIF-hosted gold deposits (the ~4 Moz Au Meadowbank deposit, hosted by the 2.71 Ga Woodburn Lake greenstone belt; the ≥ 2.8 Moz Au Meliadine district, hosted by the 2.6 Ga Rankin Inlet greenstone belt; the ~6 Moz Au Musselwhite deposit, hosted by the 2.9-3 Ga North Caribou greenstone belt; and the ~4 Moz Au Beardmore-Geraldton district, hosted by the 2.7 Ga eponymous greenstone belt) that are either intercalated with mafic to ultramafic volcanic rocks or associated interflow sediments. These four gold deposits were selected in order to validate the restricted-basin model (e.g., Barrett et al., 1988a) as a depositional setting for Algoma-type BIFs by using the geochemical signature of the chert bands as a proxy for the primary signature of ocean water chemistry and hydrothermal vent fluids. The chert chemistry was characterized by using *in-situ* LA-ICP-MS analysis following the protocol outlined in our earlier contributions (Gourcerol et al., 2015a, b). In addition, we have also analyzed the cherts *in-situ* using secondary ion mass spectrometry (SIMS) to determine their $\delta^{18}\text{O}$ signature in order to assess their post depositional exchange with later fluids (e.g., diagenetic, metamorphic). As far as we are aware, this is the first study that integrates these two data sets, that is chert trace element chemistry, in particular the rare earth elements (REEs), and $\delta^{18}\text{O}$. An indirect intent of this study was also to examine if chert beds in these settings retain a geochemical signature that may relate to the gold mineralizing event. In detail, these hypotheses were tested by: (1) defining the role of chemical reservoirs (i.e., seawater, hydrothermal fluids, and terrestrial detritus) in chert deposition; and (2) using Ce behavior to assess the oxygenation state of the water column during chert precipitation.

3.3 Geological setting of the selected BIFs

3.3.1 The Meadowbank gold deposit

Located in the Rae Domain of the Churchill Province, the Meadowbank deposit is hosted by the Woodburn Lake greenstone belt (ca. 2.71 Ga), which consists of tholeiitic and komatiitic metavolcanic rocks with minor calc-alkaline felsic tuffs and flows with intercalated BIF and clastic metasedimentary rocks (Armitage et al., 1996; Sherlock et al., 2001a, b, 2004; Hrabí et al., 2003; Pehrsson et al., 2004). The regional metamorphic grade ranges from middle greenschist to amphibolite facies (Pehrsson et al., 2004) and the sequence was deformed by at least six regional-scale deformation events (e.g., Pehrsson et al., 2013; Janvier et al., 2015).

Numerous units of oxide-, silicate- and locally sulfide-facies Algoma-type BIF have been identified, which include the West IF, Central BIF and East BIF; all of the BIFs are generally interlayered with ultramafic to felsic volcanic rocks and locally with a quartzite unit (Gourcerol et al., 2015a; Sherlock et al., 2001a, b, 2004). The BIF display cm- to mm-thick, laminated magnetite and white- to grey chert with associated layers (0.2 to 5 cm thick) of grunerite/biotite, cummingtonite/biotite or garnet/biotite combinations that are related to metamorphic variation on the property (e.g., Gourcerol et al., 2015a). Moreover, minor chlorite, sericite, ankerite, siderite, stilpnomelane and apatite grains are observed either as layers interbedded with chert and magnetite or as inclusions in chert bands (Armitage et al., 1996; Hrabí et al., 2003; Sherlock et al., 2004; Gourcerol et al., 2015a). These BIFs are described more in detail in Gourcerol et al. (2015a).

3.3.2 The Meliadine gold district

The Meliadine deposit is hosted by the 2.6 to 2.7 Ga Rankin Inlet greenstone belt (Wright, 1967; Aspler and Chiarenzelli, 1996a), which lies along the boundary between the Central and the North Western Hearne domains of the Churchill Province (Tella et al., 2007; Davis et al., 2008). The Rankin Inlet greenstone belt consists of polydeformed massive and pillowed mafic volcanic rocks, felsic pyroclastic rocks and associated interflow sedimentary units, gabbro sills and oxide-facies BIFs; all of these units are intruded by minor granite, undeformed biotite lamprophyre, as well as late gabbro and diabase dykes of Archean and Proterozoic age. These rocks have been metamorphosed from lower greenschist to lower-middle amphibolite facies (Carpenter, 2004; Carpenter, et al., 2005; Lawley et al., 2015).

Several Algoma-type BIFs are recognized along the structural hanging wall of the regional-scale Pyke Fault, including the Pump, F-Zone and Discovery (e.g., Lawley et al., 2015). These BIFs consist of continuous, subparallel, medium-grey cherty beds interbedded with massive, mm- to cm-thick beds of magnetite BIF with some chert-grunerite units and local sulfide-facies. Minor cm- to mm-thick layers of chlorite are reported mainly in the Discovery BIF.

3.3.3 The Musselwhite gold deposit

Located in the North Caribou terrane of the Superior Province, the Musselwhite deposit is hosted by the North Caribou greenstone belt dominated by mafic to ultramafic metavolcanic rocks of the 2973 to <2967 Ma Opapimiskan-Markop metavolcanic assemblage and tholeiitic basalts and minor felsic volcanics of the 2980 to 2982 Ma South Rim metavolcanic assemblage (Biczok et al., 2012; McNicoll et al., 2013). These rocks have been metamorphosed from lower greenschist to lower-mid amphibolite facies (Breaks et al., 2001) and deformed by three

deformation events (e.g., Hall and Rigg, 1986; Breaks et al., 2001; Oswald et al., 2015; McNicoll et al., 2016). The Opapimiskan-Markop metavolcanic assemblage consists, from the structural base to the top, of the “Lower Basalt” unit, the Southern Iron Formation, “Basement Basalt” unit and the Northern Iron Formation (Otto, 2002; Moran, 2008; Biczok et al., 2012).

The “Basement Basalt” unit is a thick sequence of massive- and pillowed tholeiitic basalt (Moran, 2008). The “Lower Basalt” unit is composed of basalt and ultramafic rocks, but includes extensive andesite (Hollings and Kerrich, 1999; Otto, 2002). The North Iron Formation is subdivided, from the structural base to top, into: pyrrhotite-rich mudstone (4H), chert-grunerite (4A), chert-magnetite (4B), clastic-chert-magnetite (“clastic”4B), garnet-grunerite-chert (4EA), garnetiferous amphibolite (4E) and garnet-biotite schist (4F) (e.g., Otto, 2002; Moran, 2008; Biczok et al., 2012). The Southern Iron Formation consists of two sub-parallel BIF horizons (Biczok et al., 2012). These BIFs are described more in detail in Gourcerol et al. (2015b).

3.3.4 The Beardmore-Geraldton gold district

The Beardmore-Geraldton gold district is hosted by the 2.7 Ga Beardmore-Geraldton Greenstone Belt located (BGGB) within the southern margin of the Wabigoon Subprovince (Lafrance et al., 2004). The BGGB consists of three east-trending shear-bounded units of metasedimentary and metavolcanic rocks. The southern assemblage is characterized by massive and pillowed basalt and andesite with thin sedimentary and tuffaceous beds (Shanks, 1993; Tomlinson et al., 1996) interbedded with wacke, conglomerate, siltstone and oxide-facies BIF in which the presence of jasper is notable. The central assemblage reflects felsic to mafic calc-alkaline and tholeiitic volcanic units that are associated with feldspathic sandstone, siltstone, argillite and minor BIF overlain by polymictic conglomerate (Lafrance et al., 2004). The

occurrence of the pyroclastic rocks and large amygdules in the volcanic rocks suggest shallow-water or subaerial volcanism (Kresz and Zayachivsky, 1991). Lastly, the northern assemblage consists of massive and amygdaloidal pillowed tholeiitic basalt and andesite interbedded with polymictic conglomerate and minor sandstone (e.g., Mackasey et al., 1976). These rocks have been metamorphosed to greenschist facies and deformed by four events of deformation (Tóth et al., 2015).

The BIFs occur high in the stratigraphy of the southern metasedimentary belt and can be divided into three types (Fralick and Pufahl, 2006): (1) an iron oxide-rich type referred to as “a-type” which is a dominantly iron oxide-rich (i.e., magnetite and/or hematite) sediment interbedded with mm- to cm-scale graded or ungraded siltstone; (2) a siltstone-rich type (i.e., “b-type”) which is characterized by cm-scale graded to sharply bounded siltstone layers separated by mm-thick iron oxide-rich laminae; and (3) a sandstone-rich type (i.e., “c-type”) which corresponds to sandstone beds separated by mm- to cm-scale iron oxide-rich bands. Hematitic chert laminae or bands (i.e., jasper) are common in the three types of BIF and are interbedded with either sediments or iron oxide-rich layers.

A braided fluvial system was proposed as the depositional environment for these BIFs (e.g., Barrett and Fralick 1989; Fralick and Pufahl, 2006) in which the BIFs occur mainly on flooding surfaces separating the offshore and the fluvial systems. The BIF and iron oxide-rich material were deposited during transgression whereas the interbedded siliciclastic sedimentary rocks reflect regression.

3.4 Analytical Methods and data treatment

The BIF samples collected for this study included: (1) thirty-three samples from drill core

and outcrops (Fig. 3.1A) from the Meadowbank deposit (i.e., West IF, Central BIF, East BIF); (2) forty samples in the Meliadine district (i.e., Pump, F-Zone and Discovery); (3) twenty-three samples from the Musselwhite deposit (i.e., chert-magnetite (4B), garnet-grunerite-(chert) (4EA), garnetiferous amphibolite (4E), and garnet-biotite schist (4F) facies); and (4) twenty seven samples from the Beardmore-Geraldton district (i.e., a-, b- and c-types BIF).

3.4.1 Scanning electron microscopy and *in-situ* LA-ICP-MS analysis

The chert material was analyzed by micro-sampling using laser ablation followed by ICP-MS analysis. The advantage of this protocol over bulk analysis is that it excludes any influence of later veining, sulfides or deformation-related metamorphic recrystallization-precipitation (e.g., Kamber and Webb, 2007). In order to select areas for analysis, polished thin sections (100 μm thick; Fig. 3.1B) were prepared and examined, using both transmitted and reflected light microscopy; and selected material was studied in more detail using the scanning electron microscopy (SEM) coupled with an energy dispersive spectrometer (EDS) to select the most suitable chert bands with minimal amounts of detrital mineral inclusions and other contaminants related to alteration, diagenesis, metamorphic or ore-forming events (e.g., clastic grains, volcanic ash, phosphates). The SEM used was a JEOL 6400 SEM with an INCA energy dispersive spectrometer (EDS) system housed in the Central Analytical Facilities (CAF) at Laurentian University, Sudbury, Ontario. Operating conditions were accelerating voltage of 20 keV, 1.005 nA beam current, acquisition count times of 10 seconds, and a working distance of 15 mm.

The trace element chemistry was determined using a Thermo Scientific XSERIES II ICP-MS Laurin Technic two-volume sample cell using a pulsed ArF excimer laser (RESolution M-50) emitting at 193 nm and a repetition rate of 10 Hz. The instrument operated with a forward

power of 1450 W. Gas flows were 800 ml/min for argon, 650 ml/min for He and 6 ml/min for N. Dwell times for elements analysed were 10 ms. As chert bands have very low concentration of REEs, spot analyses may be below the limit of detection for many elements, hence, in order to circumvent this issue, line traverses using both 140 and 190 μm beam diameters were made with a repetition rate of 10 Hz and an energy density of 7 J/cm² (Fig. 3.1C). No pre-ablation was done as virtually any non microcrystalline quartz present would substantially modify the REE+Y patterns from their primary abundances. However, as the line traverse method increases the influence of any detrital contaminants, either as inclusions or minerals disseminated along the traverse line, the Queensland alluvial shale composite (MUQ) was used to normalize the REE+Y values to minimize the influence of potential terrigenous input. The MUQ composition represents a mixed bimodal felsic and mafic volcanic provenance (Kamber et al., 2005), which acts as a proxy for the expected average terrigenous input from a typical bimodal greenstone belt into the Archean ocean (e.g., Bolhar et al., 2005; Thurston et al., 2012).

The elemental concentrations reported in this study (Tables 1, 2, 3 and 4) represent the integrated signal over the length of the line traverses, which measured about 6500 μm . The element list used for each analysis included the 14 REEs (¹³⁹La, ¹⁴⁰Ce, ¹⁴¹Pr, ¹⁴⁶Nd, ¹⁴⁷Sm, ¹⁵³Eu, ¹⁵⁷Gd, ¹⁵⁹Tb, ¹⁶³Dy, ¹⁶⁵Ho, ¹⁶⁶Er, ¹⁶⁹Tm, ¹⁷²Yb and ¹⁷⁵Lu), in addition to ⁷Li, ⁹Be, ²⁹Si, ⁴⁵Sc, ⁴⁷Ti, ⁵¹V, ⁵²Cr, ⁵⁵Mn, ⁵⁶Fe, ⁵⁹Co, ⁶⁰Ni, ⁶⁵Cu, ⁶⁶Zn, ⁶⁹Ga, ⁷⁵As, ⁸⁵Rb, ⁸⁸Sr, ⁸⁹Y, ⁹⁰Zr, ⁹³Nb, ⁹⁵Mo, ¹⁰⁷Ag, ¹¹¹Cd, ¹¹⁵In, ¹¹⁸Sn, ¹²¹Sb, ¹³³Cs, ¹³⁷Ba, ¹⁷⁸Hf, ¹⁸¹Ta, ¹⁸²W, ¹⁹⁷Au, ²⁰⁵Tl, ²⁰⁸Pb, ²³²Th and ²³⁸U. The detection limits for the analyzed elements vary based on a variety of factors, such as the volume of inclusions within chert. The detection limits were calculated using the relationship described in Longerich et al. (1996) and range from 0.01 to 0.002 ppm for the REE and Y (Table 2.7). The NIST 612 glass was used as an external standard and analyzed at the beginning and at the end of

each line traverse and for the internal standard, the silica content of the analyzed chert was used. It is noticed that presence of minor impurities (such as garnets, amphiboles) on a random basis in chert will have the effects of creating large RSD %.values. Furthermore, the La, Ce, Eu, Gd, and Y anomalies discussed below are calculated (Equations (1) to (5)) following the procedure of Lawrence and Kamber (2006):

$$\text{La/La}^*_{\text{MUQ}} = \text{La}_{\text{MUQ}} / (\text{Pr}_{\text{MUQ}} * (\text{Pr}_{\text{MUQ}}/\text{Nd}_{\text{MUQ}})^2) \quad (1)$$

$$\text{Ce/Ce}^*_{\text{MUQ}} = \text{Ce}_{\text{MUQ}} / (\text{Pr}_{\text{MUQ}} * (\text{Pr}_{\text{MUQ}}/\text{Nd}_{\text{MUQ}})) \quad (2)$$

$$\text{Eu/Eu}^*_{\text{MUQ}} = \text{Eu}_{\text{MUQ}} / (\text{Sm}_{\text{MUQ}}^2 * \text{Tb}_{\text{MUQ}})^{1/3} \quad (3)$$

$$\text{Gd/Gd}^*_{\text{MUQ}} = \text{Gd}_{\text{MUQ}} / (\text{Tb}_{\text{MUQ}}^2 * \text{Sm}_{\text{MUQ}})^{1/3} \quad (4)$$

$$\text{Y/Y}^*_{\text{MUQ}} = \text{Y}_{\text{MUQ}} / (0.5\text{Er}_{\text{MUQ}} * 0.5\text{Ho}_{\text{MUQ}}) \quad (5)$$

3.4.2 Oxygen isotopes

The oxygen isotopic compositions of selected chert samples from Meliadine (i.e., MEL-006, MEL-008 and MEL-033) were determined by Secondary Ion Mass Spectrometry (SIMS) analysis using the CAMECA 7f ion microprobe at the University of Manitoba (Winnipeg, Canada).

Prior to analysis, each polished thin section was cleaned with ethanol and polished with a 1-mircon diamond-cleaning compound to remove carbon coating that was used for the SEM analyses. They were then cleaned with soap and immersed in a dilute soap solution in an ultrasonic cleaner for 10 minutes. The protocol followed was immersion of the sections three times each for 10 minutes in the ultrasonic cleaner, successively using tap water, purified water and finally ethanol.

Fragments of John Valley Metamorphic Quartz (JValleyQtz) were used as a standard to determine instrumental mass fractionation. The standard was analysed at the beginning and at the end of each sample analysis. Looking at the acquisition method, a ≈ 2 nA primary beam of Cs^+ was accelerated at 10 kV and focused to a $15 \times 20 \mu\text{m}$ spot. An offset of 300-volts was used to eliminate molecular ion interferences. Ions were detected with a Balzers SEV 1217 electron multiplier coupled with an ion-counting system using an overall dead time of 28ns. Isotopes of ^{16}O and ^{18}O were detected by switching the magnetic field and analysis comprised 70 cycles for a total analytical time of 10 minutes. Over the four days of analyses, the external reproducibility (1σ) obtained on John Valley standard varied respectively from $\pm 0.6\text{‰}$, $\pm 0.4\text{‰}$, $\pm 0.6\text{‰}$ and $\pm 0.5\text{‰}$ (Table 5).

Ten analyses were performed on MEL-008, whereas thirty analyses were obtained for each of samples MEL-016 and MEL-033 (Table 5). In the latter two samples, the data are divided into three different domains (e.g., B, C and D for MEL-033) to study the variability of the $\delta^{18}\text{O}$ values in different chert bands from the same thirty centimeter sample. We also note that the analyzed cherts were carefully selected to exclude any influence of accessory minerals (e.g., amphiboles, silicates, phosphate, carbonates).

Oxygen isotope compositions are reported in this study as per mil (‰) deviations (Table 5) from the Vienna Standard Mean Ocean Water (V-SMOW) using the conventional notation:

$$\delta^{18}\text{O} = [(^{18}\text{O}/^{16}\text{O}_{\text{sample}}) / (^{18}\text{O}/^{16}\text{O}_{\text{V-SMOW}}) - 1] \times 1000 \quad (6)$$

3.5 Background

3.5.1 Rare earth element and yttrium systematics

The presence and abundance of REE+Y in chert bands may represent their primary signature, which can be influenced by one or more processes: (1) precipitation from marine water either in isolated basins or basins well connected to the open ocean (e.g., Bau and Dulski, 1996, Kamber et al., 2014); (2) precipitation from vent-sourced hydrothermal fluids (e.g., Danielson et al., 1992; Allwood et al., 2010); and (3) chemical inheritance due to replacement by silicification of precursor volcanic units (e.g., Hanor and Duchac, 1990). Chert geochemistry is also strongly dependent on the extent of contamination by terrigenous detritus (e.g., Alexander et al., 2008), volcanic ash (e.g., Klein, 2005) and oceanographic processes (e.g., phosphate and oxyhydroxide circulation and precipitation) (e.g., Alibo and Nozaki, 1999; Bau, 1999; Konhauser et al., 2005). Moreover, elements such as Sr, Ga, Sc, Zr and Th are excellent monitors of hydrogenous contamination such as detrital or volcanic input (Gourcerol et al., 2015a).

Several studies have shown that the REE+Y systematics of Archean seawater are analogous to the modern ocean with slight to moderate influence of hydrothermal vent fluids (Fig. 2.5; e.g., Bau and Dulski, 1996; Lawrence and Kamber, 2006; Thurston et al., 2012; Gourcerol et al., 2015a). It follows, therefore, that the shale (i.e., MUQ) normalized REE+Y pattern for the Archean seawater will be characterized by: (1) a depletion in light rare earth elements (LREE) relative to heavy rare earth elements (HREE); (2) a super-chondritic Y/Ho ratio (i.e., $Y/Ho > 27$), yielding a positive Y/Y^*_{MUQ} anomaly, commonly between 40-90; and (3) a slightly positive La anomaly (La/La^*_{MUQ} between 1.15 and 1.3). These features illustrate fractionation of REE and Y in the water column resulting in preferential removal onto Mn-Fe-

oxyhydroxides, organic matter, and clay particles (e.g., Kawabe et al., 1999; Bau and Koschinsky, 2009). Moreover, as the chemistry of Archean seawater was also influenced by volcanism, water-rock interaction (e.g., Veizer, 1988), and the contribution of high-temperature (>250°C) hydrothermal fluids (Fig. 2.5; e.g., Danielson et al., 1992; Bau and Dulski, 1999; Kamber et al., 2004; Allwood et al., 2010), these processes are characterized by variable, but well-developed positive Eu anomalies which are a product of hydrothermal processes (Fig. 2.5; Kamber et al., 2004). Previously, several authors also referred to a positive Gd anomaly as a seawater feature (e.g., Bau and Dulski, 1996; Lawrence and Kamber, 2006; Thurston et al., 2012) however, it has been shown that Gd is extremely sensitive to interaction of seawater with oxyhydroxides in which case it may show negative values (e.g., Alibo and Nosaki, 1999). Therefore, a positive Gd anomaly is not used in this article as an indicator of precipitation from seawater (Gourcerol et al., 2015a).

3.5.2 Oxygen isotopes

Cherts regardless of age are considered to have precipitated from Si-rich water initially as opal-A, then converted into opal-CT, and then finally converted to chert as a final product of dissolution-(re-)precipitation reactions during diagenesis (e.g., Knauth, 1994; Knauth and Lowe, 2003; Marin Carbonne et al., 2014) despite limited evidence of the preservation of the precursor phases (e.g., Marin-Carbonne et al., 2014; Westall et al., 2015). These aforementioned reactions involve the conversion of opal to microcrystalline chert in either in a closed (i.e., metamorphic) or open (i.e., seawater interaction) system. Marin et al. (2010) have argued for a closed system conversion based on the observed large range of $\delta^{18}\text{O}$ values (up to +14‰) for chert from the 1.8 Ga Superior-type Gunflint iron formation (Canada). These authors suggest that the amorphous silica precursor ($\delta^{18}\text{O} \approx +27\text{‰}$; from Marin et al., 2010), which precipitated at equilibrium with

seawater in warm Archean ocean waters, was dissolved during diagenesis by high temperature fluids in a closed system such that the initial chert records low $\delta^{18}\text{O}$ values (e.g., ca. +14‰) but the later chert record increasingly heavier values (i.e., ca. +24 to +26‰) as a result of closed system diagenesis (i.e., a Rayleigh process). Consequently, these authors have suggested a model in which the $\delta^{18}\text{O}$ values of chert are predicted to increase continuously through the dissolution-precipitation process due to the closed nature of the system.

3.6 Results

3.6.1 Rare earth and yttrium systematics characteristics

3.6.1.1 Meadowbank area

Data for line traverse analyses on chert samples from the Central BIF, East BIF and West IF within the Meadowbank area (Gourcerol et al., 2015a) show relatively uniform REE+Y patterns (Fig. 3.2; table 1), with three notable exceptions (samples AMB-126232, AMB-128330 and AMB-128332 in Fig. 3.2A and 3.2C), that include a slight to moderate enrichment in HREE relative to LREE and MREE ($\text{Nd/Yb}_{\text{MUQ}} = 0.04\text{-}0.58$) that are associated with slight to moderate positive La, Y and Eu anomalies ($\text{La/La}^*_{\text{MUQ}} = 0.89\text{-}4.65$, $\text{Y/Y}^*_{\text{MUQ}} = 0.88\text{-}1.96$, $\text{Eu/Eu}^*_{\text{MUQ}} = 1.25\text{-}5.12$) and chondritic to super-chondritic Y/Ho values ($\text{Y/Ho} = 24.2\text{-}53.72$) (Table 1).

A group of samples from the East BIF (AMB-126241 and AMB-126243; Fig. 3.2B) and the West IF (AMB-128330, AMB-128331 and AMB-128332; Fig. 3.2C) show relatively flat REE patterns ($\text{Pr/Sm}_{\text{MUQ}} = 0.79\text{-}1.03$) associated with chondritic to super-chondritic Y/Ho values ($\text{Y/Ho} = 26.02\text{-}36.71$). Enrichments in Sr (i.e., 27.9-55 ppm; and 64.9-1090 ppm), Zr (i.e., 0.97-2.17 ppm; and 19.1-43.4 ppm) and variable amounts of Th (i.e., 1.055-4.2 ppm) and Ga (i.e.,

16.04-27.8 ppm) relative to the bulk of the samples is illustrated for most material from the West IF. Two samples from the Central BIF (AMB-126223 and AMB-126231; Fig. 3.2A) show depletion in LREE relative to the HREE, but moderate to flat patterns for the MREE and HREE that are associated with chondritic to super-chondritic Y/Ho values ($Y/Ho = 24.2-32.41$), enrichment in Zr (i.e., 104.9-183 ppm), Ga (i.e., 6.83-141.4 ppm), Sr (i.e., 20.4-95.2 ppm) and Th (i.e., 1.22-7.7 ppm) relative to other samples.

Two samples from the south of the property (i.e., AMB-128330 from West IF and AMB-126232 from Central BIF; Gourcerol et al., 2015a) show depletion in HREE relative to LREE ($Nd/Yb_{MUQ} = 2.18-7.19$) that are associated with positive La, Y and Eu anomalies (Fig. 3.2A,C).

Lastly, with respect to these cherts, it is noted that Ce exhibits a slight to moderate positive anomaly in the samples ($Ce/Ce^*_{MUQ} = 0.94-1.86$).

3.6.1.2 Meliadine gold district

Data for chert samples from the Pump, F-Zone and Discovery deposits within the Meliadine gold district yield variable REE+Y patterns (Fig. 3.3; Table 2). Chert samples from the Pump deposit (Fig. 3.3A) are all very uniform in their chemistry and are characterized by LREE depletion ($Nd/Yb_{MUQ} = 0.06-0.75$), chondritic to sub-chondritic Y/Ho values ($Y/Ho = 11.44-32.53$), variable La and Y anomalies ($La/La^*_{MUQ} = 0.02-1.11$, $Y/Y^*_{MUQ} = 0.54-1.13$) and positive Eu anomalies ($Eu/Eu^*_{MUQ} = 2.17-6.13$) (Fig. 3.3A). The Y/Ho ratios for most of the samples are lower than chondritic values (i.e., 27) and correlate with negative La and Y anomalies despite a depletion in LREE which is typical of seawater input.

All chert samples from the F-Zone, except for two (MEL-015 and MEL-017), show relatively LREE-depleted patterns ($Nd/Yb_{MUQ} = 0.16-0.61$). In contrast, samples MEL015 and

MEL017 show the opposite trends with slight HREE depletion ($\text{Nd/Yb}_{\text{MUQ}} = 1.19\text{-}7.21$). Overall, samples show negative to positive La anomalies associated with slight- to strong relative enrichment in Y and Eu ($\text{La/La}^*_{\text{MUQ}} = 0.42\text{-}1.43$, $\text{Y/Y}^*_{\text{MUQ}} = 1.05\text{-}1.35$, $\text{Eu/Eu}^*_{\text{MUQ}} = 2.12\text{-}8.14$) (Fig. 3.3B). In addition, all samples yield chondritic to super-chondritic Y/Ho values ($\text{Y/Ho} = 25.25\text{-}36.34$) and Sr enrichment (i.e., 6.5-30.6 ppm). Moderate enrichment in Zr is notable in MEL-013 and MEL-018 (i.e., 2.14-4.93 ppm).

Chert samples from the Discovery deposit show relative LREE depletion ($\text{Nd/Yb}_{\text{MUQ}} = 0.11\text{-}1.18$) except for MEL-025 ($\text{Nd/Yb}_{\text{MUQ}} = 11$; Fig. 3.3C). Slight to moderate enrichment for La, Y and Eu occur ($\text{La/La}^*_{\text{MUQ}} = 0.68\text{-}2.1$, $\text{Y/Y}^*_{\text{MUQ}} = 0.80\text{-}1.28$, $\text{Eu/Eu}^*_{\text{MUQ}} = 1.05\text{-}7.46$) for most samples, the exception being for MEL-038 ($\text{La/La}^*_{\text{MUQ}} = 0.47$, $\text{Y/Y}^*_{\text{MUQ}} = 0.85$, $\text{Eu/Eu}^*_{\text{MUQ}} = 2.13$) (Fig. 3.3C). The Y/Ho ratios vary from sub-chondritic to super-chondritic with $\text{Y/Ho} = 18.23\text{-}37.48$. In addition, most of the samples exhibit chondritic Y/Ho values associated with Sr enrichment (i.e., 0.3-177 ppm) and moderate Ga enrichment (i.e., 1.32-7.04 ppm). In contrast, samples MEL-038, MEL-039 and MEL-040 yield trace element concentrations (\pm elevated Ga). Sample MEL-038 yield low Y/Ho ratios that correlate with depletion in La and Y concentrations, which was also reported for some chert samples from the Pump deposit (Fig. 3.3C).

Chert samples from the Meliadine gold district show variable Ce anomalies: (1) $\text{Ce/Ce}^*_{\text{MUQ}} = 0.15\text{-}1.01$ for chert samples from the Pump deposit; (2) $\text{Ce/Ce}^*_{\text{MUQ}} = 0.65\text{-}1.22$ for the F-Zone deposit; and finally (3) $\text{Ce/Ce}^*_{\text{MUQ}} = 0.64\text{-}2.01$ for the Discovery deposit.

3.6.1.3 Musselwhite area

Data for chert samples from the chert-magnetite (4B; Fig. 3.4A, Table 3), the garnetiferous amphibolite (4E; Fig. 3.4B, Table 3), the garnet-grunerite-(chert) (4EA; Fig. 3.4C, Table 3), and the garnet-biotite schist (4F; Fig. 3.4D, Table 3) within the Musselwhite area were reported by Gourcerol et al. (2015b). It should be noted that sample E599656 from the 4B facies, samples E599660, E599665 and sample E599666 from 4EA are not illustrated in Figure 3.4 due to their erratic patterns that reflect some REE values approaching the limit of detection. However, these samples will be reviewed here in regard to elements lying above the detection limit.

Samples exhibit relatively uniform REE+Y patterns except for chert in the 4F facies (Fig. 3.4D). Most chert sampled from the 4B facies show HREE enrichment ($Nd/Yb_{MUQ} = 0.04-0.66$), yield slight to moderate positive La, Y and Eu anomalies ($La/La^*_{MUQ} = 0.8-2.35$, $Y/Y^*_{MUQ} = 0.87-1.52$, $Eu/Eu^*_{MUQ} = 2.6-3.61$) and sub-chondritic to super-chondritic Y/Ho values ($Y/Ho = 22.13-44.01$) (Fig. 3.4A). Sample E599656 differs from the majority of samples by its negative La and Y anomalies ($La/La^*_{MUQ} = 0.24$, $Y/Y^*_{MUQ} = 0.51$; $Eu/Eu^*_{MUQ} = 3.70$) and very low Y/Ho value (i.e., 9.79). It is also noted that samples E599655 and E599668 are Sr enriched (i.e., 848.8 ppm and 150.8 ppm respectively).

The two samples from the 4E show minor LREE depletion ($Nd/Yb_{MUQ} = 0.39-0.7$), are slightly to moderately La, Y and Eu enriched ($La/La^*_{MUQ} = 0.7-1.66$, $Y/Y^*_{MUQ} = 0.98-1.22$, $Eu/Eu^*_{MUQ} = 2.43-2.6$), and yield chondritic to super-chondritic Y/Ho values ($Y/Ho = 25.71-32.8$) (Fig. 3.4B).

The chert samples from the 4EA facies are characterized by relatively flat to slightly fractionated patterns with LREE depletion relative to HREE ($Nd/Yb_{MUQ} = 0.15-0.7$), except for

samples E599654 and E599659 showing enrichment in LREE versus HREE (i.e., $\text{Nd/Yb}_{\text{MUQ}} = 2.34\text{-}2.98$). All these samples are associated with positive Eu anomalies ($\text{Eu/Eu}^*_{\text{MUQ}} = 2.34\text{-}3.97$) (Fig. 3.4C). Considering the La and Y anomalies along with the Y/Ho values, two groups of samples are present: (1) E599654, E599659 and E599667 show positive La and Y anomalies ($\text{La/La}^*_{\text{MUQ}} = 1.51\text{-}3.02$, $\text{Y/Y}^*_{\text{MUQ}} = 1.2\text{-}2.07$) and chondritic to super-chondritic Y/Ho ratios ($\text{Y/Ho} = 29.86\text{-}55.91$) (Fig. 3.4C); and (2) E599660, E599665 and E599666, which are not shown in the figure (see above), show negative La and Y anomalies ($\text{La/La}^*_{\text{MUQ}} = 0.04\text{-}0.16$, $\text{Y/Y}^*_{\text{MUQ}} = 0.22\text{-}0.73$) and very low Y/Ho ratios ($\text{Y/Ho} = 4.11\text{-}16.52$) (Fig. 3.4C).

The chert bands within the garnet-biotite schist (4F) facies are geochemically anomalous compared to chert from all the other studied deposits. The former samples show variable, but elevated LREE and MREE enrichments ($\text{Pr/Sm}_{\text{MUQ}} = 0.18\text{-}0.83$; $\text{Nd/Yb}_{\text{MUQ}} = 1.17\text{-}5.75$) and only moderately positive Eu anomalies ($\text{Eu/Eu}^*_{\text{MUQ}} = 1.08\text{-}1.94$) are noted (Fig. 3.4D). This facies is distinguished from the others by its REE+Y signature and, furthermore, is similar to the argillite studied by Thurston et al. (2012), which documented only a weak hydrothermal fluid influence.

Chert samples from the Musselwhite area exhibit variable Ce anomalies: (1) $\text{Ce/Ce}^*_{\text{MUQ}} = 0.40\text{-}1.96$ for chert samples from the 4B facies; (2) $\text{Ce/Ce}^*_{\text{MUQ}} = 0.40\text{-}1.96$ for the 4E facies; (3) $\text{Ce/Ce}^*_{\text{MUQ}} = 0.18\text{-}1.50$ for the 4EA facies; and finally (4) $\text{Ce/Ce}^*_{\text{MUQ}} = 0.74\text{-}1.25$ for the 4F facies.

3.6.1.4 Beardmore-Geraldton gold district

Data for chert and jasper samples from the a-type (i.e., iron oxide-rich type), b-type (i.e., siltstone-rich type) and c-type (i.e., sandstone-rich type) BIF within the Beardmore-Geraldton

gold district yield variable REE+Y patterns (Fig. 3.5, Table 4). Some samples exhibit both chert (named BG-0XX-C) and jasper (named BG-0XX-J) features, which allow a comparative study of their REE+Y systematics. However, most of the traverses are done on jasper bands as layers of pure chert are rare in this gold district.

Most of chert and jasper samples from the a-type BIF yield LREE depleted patterns ($\text{Nd/Yb}_{\text{MUQ}} = 0.23\text{-}0.97$) except for the BG001-J and BG002-J samples that exhibit weak depletion in HREE relative to LREE ($\text{Nd/Yb}_{\text{MUQ}} = 1.40\text{-}1.62$) (Fig. 3.5A). However, all chert and jasper samples show chondritic to super-chondritic Y/Ho values ($\text{Y/Ho} = 28.19\text{-}38.86$), variable La and Y anomalies ($\text{La/La}^*_{\text{MUQ}} = 0.85\text{-}4.00$, $\text{Y/Y}^*_{\text{MUQ}} = 1.12\text{-}1.45$) and positive Eu anomalies ($\text{Eu/Eu}^*_{\text{MUQ}} = 1.81\text{-}4.40$) (Fig. 3.5A).

Chert and jasper samples from the b-type BIF show depletion in LREE relative to HREE ($\text{Nd/Yb}_{\text{MUQ}} = 0.28\text{-}0.55$) except for sample BG006B-J, which exhibits the largest LREE enrichment and consequent depletion in HREE relative to LREE ($\text{Nd/Yb}_{\text{MUQ}} = 1.91$) with associated slight enrichment in Th (i.e., 1.16 ppm) and Ga (i.e., 24.3 ppm) relative to other samples (Fig. 3.5B). However, all chert and jasper samples show chondritic to super-chondritic Y/Ho values ($\text{Y/Ho} = 27.65\text{-}39.75$) and positive La, Y and Eu anomalies ($\text{La/La}^*_{\text{MUQ}} = 1.38\text{-}2.59$, $\text{Y/Y}^*_{\text{MUQ}} = 1.08\text{-}1.35$, $\text{Eu/Eu}^*_{\text{MUQ}} = 1.50\text{-}2.69$) (Fig. 3.5B).

Chert and jasper samples from the c-type BIF show relatively flat patterns and they may be divided in two distinct groups (Fig. 3.5C): (1) samples that exhibit depletion in LREE relative to HREE ($\text{Nd/Yb}_{\text{MUQ}} = 0.41\text{-}0.89$) that are associated with weak Sr and Sc concentrations (i.e., BG004-J, BG017-J and BG018J) relative to other samples (i.e., respectively 6.21-11.37 ppm and 3.35-4.88 ppm); and (2) samples that show depletion in the HREE relative to LREE ($\text{Nd/Yb}_{\text{MUQ}}$

= 1.37-2.98) and associated with enrichment in Sr and Sc (i.e., BG004-C, BG014-J, BG016-C, BG016-J, BG019-J and BG022-J) relative to other samples (i.e., respectively 13.6-31.46 ppm and 3.0-7.2 ppm). All the samples show chondritic to super-chondritic values for Y/Ho (Y/Ho = 24.24-37.71), associated with positive La, Y and Eu anomalies ($La/La^*_{MUQ} = 1.11-2.14$, $Y/Y^*_{MUQ} = 0.97-1.45$, $Eu/Eu^*_{MUQ} = 1.07-3.05$) (Fig. 3.5C).

It is noted that chert and jasper samples from the three types of BIF exhibit slight to moderate positive Ce anomalies ($Ce/Ce^*_{MUQ} = 0.75-2.11$).

3.6.2 Oxygen isotopes

The $\delta^{18}O$ values for sample MEL-008 show a range from +6.6 to +19.1‰ with a mean of +14.1‰ (Fig. 3.6A), whereas in MEL-016, the values range from +7 to +17.3‰ and have a mean of +12.2‰ (Fig. 3.6B), and for sample MEL-033, values range from +11 to +16.3‰ with a mean of +14‰ (Fig. 3.6C). Importantly, none of the samples have values close to +27‰ which is the inferred precursor $\delta^{18}O$ value of amorphous silica predicted by Marin et al. (2010), instead, they are significantly lower by 20.4 to 7.9‰.

3.7 Discussion

3.7.1 Rare earth element and yttrium systematics

Most of the chert and jasper samples (i.e., corresponding to line traverse; Fig. 3.7A) from the four deposits yield similar shale-normalized systematic patterns showing depletion in LREE relative to HREE associated with positive La and Y anomalies as well as positive Eu anomalies. These observations record the influence of ambient seawater and high-temperature (>250°C) hydrothermal fluids during chert deposition.

Detrital contamination is commonly observed in several chert samples from the four deposits especially enrichments in particular elements such as Sr, Th, Ga, Sc and Zr combined with petrographic evidences and SEM-EDS analysis. Thus, presence of apatite in a chert band (Fig. 3.7B) may account for elevated Sr and Th values, the presence of carbonates may account for the elevated Sr values, the presence of clay minerals may account for elevated Ga and Th values, as well zircon may account for the enrichment in Zr and monazite for Th (Fig. 3.7C, D) (Gourcerol et al., 2015a). These enrichments may represent variable detrital inputs during deposition of the contained chert (Gourcerol et al., 2015a) and will significantly affect the REE+Y systematic patterns by yielding flatter patterns (compared to samples without detrital contamination), as well as chondritic values of the Y/Ho ratios (Gourcerol et al., 2015a). It is noted that no specific distinction between primary versus secondary apatite has been established in this study.

Secondary (versus primary) chemical features of few chert samples can also be pointed out by study of the REE+Y patterns as demonstrated by: (1) a depletion in HREE relative to LREE associated with positive La, Y and Eu anomalies (e.g., AMB-128330 and AMB-126232 from the Meadowbank area) due to presence of garnet (Fig. 3.7E) associated with the amphibolite facies assemblages confirmed petrographically (Gourcerol et al., 2015a); as well as (2) a pronounced depletion in LREE relative to HREE suggesting presence of late carbonates (Gourcerol et al., 2015a) such as ankerite illustrated in the Musselwhite area by samples E599655 and E599668 and confirmed petrographically (Fig. 3.7F).

Some samples from the Meliadine district (i.e., most of samples from Pump, Mel-038 from Discovery) as well as the Musselwhite area (i.e., E599656 from the 4B, E599660, E599665 and E599666 from the 4EA) show depletion in LREE relative to HREE associated with positive Eu

anomalies but differ from the bulk of samples by a lower Y/Ho ratios than chondritic values (i.e., 27) correlated with negative La and Y anomalies. Thus, this may likely reflect precipitation from high-temperature (T) (>250°C) hydrothermal vent fluid with mixing of seawater with another influence such as Fe-oxyhydroxides.

The comparison of chert and adjacent jasper bands from the Beardmore-Geraldton district does not show a notable difference from other BIF samples in this study which suggests therefore the same type of process (i.e., seawater interaction with high-T hydrothermal fluids and variable detrital contamination) during jasper deposition. In detail, jasper bands exhibit, in general, higher Fe, Ti and V and lower Si contents than chert bands which is consistent with the presence of hematite within “chert groundmass” as confirmed by petrographic study. In addition, it is noticed that on average, the associated chert bands show higher Eu anomalies than the jasper bands which suggest a greater influence of high-T hydrothermal vent fluids during its deposition.

3.7.2 Assessing the influence of high-temperature hydrothermal fluids

The REE+Y patterns, for all the chert samples from the Meadowbank, Meliadine, Musselwhite and Beardmore-Geraldton gold districts record the influence of high-temperature hydrothermal vent fluids (>250°C). In this section, we explore the relative importance of the hydrothermal input during chert precipitation in part by calculating binary mixing lines between a modern seawater composition from the North Pacific (Alibo and Nozaki, 1999) and a hydrothermal fluid. Shibuya et al. (2010) suggested Archean greenstone belt hydrothermal fluids were SiO₂-rich, Fe-poor, and highly alkaline in character which contrasts with the Fe-rich and acidic nature of modern hydrothermal fluids. Consequently, to more accurately constrain the Archean conditions, a 2.7 Ga brecciated chert sample (i.e., 06PCT001M; Thurston et al., 2012)

characterized by an overall hydrogeneous REE+Y signature associated with a strong positive Eu anomaly ($\text{Eu}/\text{Eu}^*_{\text{MUQ}} = 30.01$) was chosen over modern high-T hydrothermal fluids to illustrate the hydrothermal influence in an Archean greenstone belt. This sample suggests a very close linkage of this chert with a hydrothermal source (Thurston et al., 2012). Note that this high Eu/Eu^* sample does not display the most likely contaminating phases based on geochemical filtering for sulfides, felsic ash and phosphates (Thurston et al., 2012). The Eu/Sm and Sm/Yb ratios are quantitative measures of the strength of the positive Eu anomaly and the flatness of the pattern that characterizes the hydrothermal fluid (Fig. 2.5).

According to Shibuya et al. (2010), Archean hydrothermal fluid was highly alkaline due to presence of calcite in the sea floor alteration minerals based on a high- CO_2 concentration in seawater/hydrothermal fluid. Among other factors, the hydrothermal fluid chemistry is controlled by oceanic crust composition, pH and redox conditions. The Great Oxygenation Event at ca. 2.4 Ga would have rendered seawater more oxic (e.g., van Kranendonk et al., 2012).

Most of the samples in this study fall on the mixing line despite some exhibiting high Sm/Yb ratios (Fig. 3.8). The Sm/Yb ratio is particularly sensitive to the presence of high-pressure residual metamorphic phases, such as amphiboles and garnets, which may overprint the primary geochemical signature of the BIFs. For example, in the Meadowbank area (Fig. 3.8A), three samples are located above the mixing line (i.e., AMB-126231 from Central BIF; AMB-128330, AMB-128331 and AMB-128332 from West IF) and correspond to samples selected in the southern part of the property affected by amphibolite-facies metamorphism. In the Musselwhite area (Fig. 3.8C), samples from the 4F and 4EA facies also lie above the mixing line and are explained by presence of garnets. For most of the samples, the position of samples along the mixing line reflects the strength of the seawater signature.

In the Meadowbank area, samples from the Central BIF suggest an input from the high-T fluid of 1-11%, versus 3-16% for the East BIF and 0-16% for the West IF (Fig. 3.8A). It is noted that samples from the southern part of the West IF show a very low component of hydrothermal fluid based on their flat REE patterns. In the Meliadine gold district, most samples record a moderate hydrothermal influence (2-3% for the Discovery zone, 4-28% for the F-Zone, 3-22% for the Pump deposit) during chert precipitation (Fig. 3.8B). In the Musselwhite area, input from the high-T fluid was generally low during chert formation at 0-15% for the 4B facies, 4-7% for the 4E facies, 2-11% for the 4EA facies, and 0-5% for the 4F facies (Fig. 3.8C). The 4F samples seem to record more restricted influence of hydrothermal fluids, which is consistent with a slightly more positive Eu anomaly. And finally, in the Beardmore-Geraldton gold district, the a-type BIF characterized by an iron oxide-rich character suggests 2-12.5% of high-T hydrothermal fluid whereas the b-type (i.e., siltstone-rich BIF) and c-type (i.e., sandstone-rich BIF) record respectively 0-5% and 0-6% (Fig. 3.8D).

These mixing diagrams may provide an indication of the locus of the depositional site relative to the hydrothermal source vent: when the depositional site is near the hydrothermal source vent, samples will be qualitatively closer to the high-temperature hydrothermal fluid end-member whereas when the depositional site is more distal, the samples will be qualitatively closer to the seawater end-member. In this study, most of the studied samples have values that reflect between ≈ 0 to 20% of a high-temperature hydrothermal fluid input which may define a general lateral distance for the depositional site for Algoma-type BIF from the hydrothermal source vent. Kamber et al., (2014) have used the slope of the REE+Y plot (Pr/Yb) as a proxy for water depth but given the lack of persistent along-strike sampling, we do not attempt this sort of analysis.

3.7.3 Sources and influence of detrital contamination

Most chert samples from the Meadowbank, Meliadine, Musselwhite and Beardmore-Geraldton areas show the influence of detrital contamination, as illustrated by flatter MUQ normalized REE patterns ($\text{Pr}/\text{Sm}_{\text{MUQ}} \approx 1$), chondritic Y/Ho ratios (i.e., $\text{Y}/\text{Ho} \approx 27$) and variations of REE+Y concentration. Despite normalization to MUQ, which is used to minimize the detrital influence in chert, some samples clearly still reflect a detrital component, which indicates therefore, that an important part of chert genesis and its study is a key to understanding the depositional setting for Algoma-type BIF. Detrital contamination may be present in chert as single mineral phases, such as phosphates, clays, and/or resistant minerals (e.g., zircon, xenotime, etc.), all of which induce a range of effects on the REE+Y patterns depending on their modal abundances (Gourcerol et al., 2015a). In order to assess the various sources of detrital contamination, a combination of ternary (La-Th-Sc) and binary element (Cr/V and Y/Ni) plots are used (Fig. 3.8). The La-Th-Sc ternary diagram was introduced by Bhatia and Crook (1986) to distinguish different provenances for turbidite sequences, the metabasic contamination represented by higher Sc, and felsic volcanic and clastic contamination by higher La and Th. The Cr/V ratio reflects enrichment of Cr over other oxides, whereas Y/Ni reflects the level of ferromagnesian input compared to HREE. Ultramafic and tholeiitic sources tend to have higher Cr/V and lower Y/Ni ratios, whereas felsic- to mafic sources of calc-alkaline rocks in general have lower and higher values, respectively. In order to assess these diagrams, representative data for komatiitic and andesitic volcanic rocks are shown in the binary plots in Figure 3.8 for reference.

In the Meadowbank area, the La-Th-Sc plot suggests most samples represent a metabasic source for the detrital contamination (Fig. 3.8A). For samples AMB-128330, AMB-128331 and

AMB-128332 from West IF, the flatter MUQ-normalized REE patterns suggest more felsic to mixed (i.e., felsic to mafic) sources. It should also be noted that sample AMB-126241 from East BIF is close to the mixed source domain and could also reflect bimodal contamination. Samples AMB-126223 and AMB-126231 from the Central BIF are located within or beyond the metabasic domain and could reflect metabasic clastic contamination associated with an external source and could reflect addition of volcanic ash during deposition. This hypothesis is supported by the high Zr concentration in these samples and also the positive correlation between Th and Zr in the Central BIF ($r^2 = 0.85$). The Cr/V and Y/Ni plot confirms the presence of ultramafic clastic contamination for the bulk of samples from the Meadowbank area and a mixed source for AMB-126241, AMB-128330 and AMB-128332 and felsic to intermediate calc-alkaline source for sample AMB-128331 (Fig. 3.8B). For AMB-126231, which is also located in the mixed source region of the plot, this confirms the presence of volcanic ash in chert bands affected by ultramafic clastic contamination and suggests that the lower content of Zr in AMB-126223 was not enough to overprint the ultramafic clastic contamination.

In the Meliadine gold district, the La-Th-Sc plot suggests a metabasic clastic contamination (Fig. 3.8C) for all the samples which is confirmed by the Cr/V and Y/Ni plot (Fig. 3.8D).

In the Musselwhite area, the La-Th-Sc plot suggests a metabasic clastic contamination for all the samples except for one sample (E599667) which may reflect some felsic clastic contamination (Fig. 3.8E). It should also be noticed that a group of 4B samples differs from the majority of the other samples by their moderate La values. The Cr/V and Y/Ni plot confirms ultramafic clastic contamination for most of these samples and a felsic calc-alkaline clastic source for E599667 (Fig. 3.8F). However, for samples E599655 and E599668 from unit 4B, which exhibit moderate La enrichment in the La-Th-Sc plot, they show high Y/Ni ratios which

could suggest contamination by a mafic calc-alkaline source, such as basalt or gabbro, rather than ultramafic contamination for these two samples.

In the Beardmore-Geraldton gold district, the La-Th-Sc plot suggests a metabasic contamination for most of the samples (Fig. 3.8G), with some exceptions: (1) sample BG004-C from the c-type BIF, which may reflect either granitic gneiss contamination or a mixed source of detrital contamination in the chert band. This observation is consistent with the enrichment in Th and Zr observed in this sample (cf. REE+Y systematics section); and (2) sample BG006B-J from the b-type BIF shows higher La and Th concentrations than other samples from this BIF and may reflect either a mixed source of detrital contamination which is consistent with Th and Ga enrichments in this sample or a metabasic source with high La (cf. REE+Y systematics study). However, these observations are not illustrated in the Cr/V and Y/Ni plot (Fig. 3.8H) which confirms a mixed source of detrital contamination for BG004-C, in which the felsic influence is much lower than the mafic contamination, and probably a metabasic source for BG006B-J with its high La, Th and Ga values.

In general, a component of ultramafic clastic contamination is illustrated for the four deposits and is consistent with the Keewatin Stratigraphy (e.g., Lawson, 1885; Thurston and Chivers, 1990) for Algoma-type BIF deposition and therefore the most important clastic contamination is likely komatiite and tholeiitic material. Moreover, local volcanic ash and some felsic to intermediate calc-alkaline clastic material in addition to felsic to mafic calc-alkaline clastic contamination are suggested for the Meadowbank and Musselwhite samples, respectively.

3.7.3.1 Assessing the detrital contamination input

To estimate the degree of influence of the detrital component within BIFs, a conservative mixing line was calculated using seawater samples selected in the North Pacific from Alibo and Nozaki (1999) and the MUQ composite as end-members and using the $(\text{Pr}/\text{Nd})_{\text{MUQ}}$ ratios as a measure of the flatness of the pattern and chondritic values of Y/Ho ratio characteristic of detrital contamination (Fig. 11). The MUQ end member represents a perfect example of the influence of detrital contamination within an Archean greenstone belt as the mud represents a basaltic provenance with minor felsic volcanic input. Before discussing these plots, it is noted that the bulk of the samples lie just below the calculated mixing line, which represents the high-temperature hydrothermal input to the samples. In the following discussion, the percentage values should be considered to represent the relative influence of the end members rather than quantitative measures.

In the Meadowbank area, samples from the Central BIF suggest $\approx 8\text{-}100\%$, the East BIF $\approx 50\text{-}100\%$ and the West IF $\approx 30\text{-}100\%$ detrital influence during chert precipitation suggesting that East BIF and West IF are the BIFs most affected by detrital contamination in the Meadowbank area (Fig. 3.10A). The East BIF shows more hydrothermal influence than the Central BIF and West IF samples, which is consistent with where samples plotted in Figure 3.8A. All these samples are located either on the mixing line or below it, which suggests the influence of a detrital component, a seawater influence and also a high-temperature hydrothermal fluid input during precipitation of the chert bands.

In the Meliadine gold district, some samples differ from those from Meadowbank by their lower Y/Ho ratios, which are mainly observed in the Pump samples and MEL-025 and MEL-038

from Discovery (Fig. 3.10B). Considering only samples located on or directly below the mixing line, Discovery samples suggests 60-100%, F-Zone samples 65-100% and the Pump samples \approx 85-95% detrital influence during chert precipitation. All the samples from the F-Zone and most from Discovery (except MEL-025 and MEL-038) are located either on or below the mixing line which suggests the significant influence of a detrital component, seawater influence and high-temperature hydrothermal fluid input during precipitation of chert bands.

In the Musselwhite area, as in the Meliadine gold district, some samples differ by their low Y/Ho ratios mainly observed in the 4B, 4EA and 4F facies. Considering only samples located on or directly below the mixing line, the detrital influence during chert precipitations is estimated at 40-100% for 4B, 80-100% for 4E, and 0-85% for 4EA (Fig. 3.10C). Based on these observations, the 4EA seems to be “relatively less affected” by detrital contamination than the other facies and 4B the most influence of hydrothermal fluids.

In the Beardmore-Geraldton gold district, samples from the a-type BIF suggest 60-90% detrital contamination, samples from the b-type BIF indicate 58-100% and finally samples from the c-type BIF suggest 65-100% detrital influence during chert and jasper precipitation (Fig. 3.10D). The a-type BIF appears the least affected by detrital contamination and is consistent with the nature of b- and c-type BIF which are intercalated, respectively, with siltstone and sandstone layers.

The percentage of detrital contamination discussed is indicative of the general degree of contamination allowing a comparison of the different chert samples as most of the samples showing \approx 100% MUQ contamination on the mixing trends also show a seawater signature based on their positive La and Y anomalies and REE fractionation patterns. Thus, this treatment

confirms that a small amount of clastic detritus in the chert bands is sufficient to dominate the bulk REE signature of the cherts as proposed by Gourcerol et al. (2015a). We also note that we have previously documented the effects of small amounts of detrital apatite, xenotime, zircon, and garnet on REE+Y plots (Gourcerol et al., 2015a).

Focusing on samples from the Meliadine gold district and Musselwhite area that show low Y/Ho ratios (Figs. 3.10B, C), it is suggested that another factor and/or environmental control may be involved which is not considered in the mixing model above. In this case, we note that the fractionation between Y and Ho during particle scavenging by Fe-oxyhydroxides (rather than Mn-oxyhydroxides in an Archean context) may explain the Y/Ho ratios lower than chondritic values based on the experimental observations of Bau (1999). In this latter work it was shown that scavenging of REE+Y can occur in a restricted environment and Fe-oxyhydroxide REE+Y patterns can display less positive or even negative La and Y anomalies associated with a M-type lanthanide tetrad effect (Masuda et al., 1987). These observations are consistent with the good correlation noted in this study between the low Y/Ho and negative La and Y anomalies observed in the chert samples. Therefore, it is suggested the REE and trace element chemistry of the studied chert samples may illustrate the influence of coeval precipitation of Fe-oxyhydroxides in a restricted basin isolated from recharge from an open ocean. In such a case, the isolation of such a basin from open seawater influence is reflected in the chert chemistry that inherits a chemical signature which in part is due to scavenging of REE+Y by contemporaneous Fe-oxyhydroxides (e.g., Kawabe et al., 1999; Bau, 1999; Minami et al., 1998).

3.7.4 Mechanical versus biological processes controlling chert precipitation

As previously suggested, some of the Meliadine and Musselwhite samples may reflect a

primary signature derived by scavenging by Fe-oxyhydroxide particulate matter in a restricted basin isolated from seawater influence (i.e., low Y/Ho ratio associated with negative La and Y anomalies; Bau, 1999). The precipitation of Fe-oxyhydroxides in Archean seawater can be explained both by mechanical and biological processes considering that seawater was devoid of free oxygen (e.g., Konhauser et al., 2005; Shibuya et al., 2010; Fig. 3.11). In the mechanical-process model of Shibuya et al. (2010), a dynamic pH modification during the mixing of alkaline, SiO₂-rich and Fe-poor hydrothermal fluids with acidic to neutral, silica-saturated, Fe-rich Archean seawater causes precipitation of Fe³⁺ from Fe²⁺-rich seawater as well as silica under anoxic conditions (Figs. 3.11A, 3.12). This process is illustrated by reaction 7:

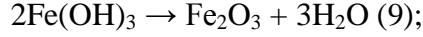


In contrast to the former model, the biological-process model (Fig. 3.11B) of Konhauser et al. (2005) refers to biological oxidation of Fe²⁺ which occurs in ocean bottom waters near the seafloor by photoautotrophic bacteria. This model can be divided into two stages (i.e., photoautotrophic activity and sedimentation), described below.

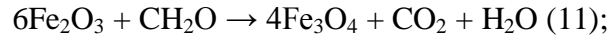
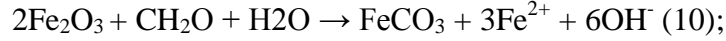
Initially, photoautotrophic Fe²⁺ is oxidized by bacteria, which results in formation of Fe-hydroxide (reaction 8; Posth et al., 2013):



Sedimentation of these Fe-hydroxides (e.g., ferrihydrite) occurs at the bottom of the water column and during formation of the oxide bands, the Fe:C ratio changes and produces an excess of Fe(III) in the sediments, which leads to preferential mobilization of fermentation products relative to Fe(III) and results in precipitation of hematite (reaction 9; Posth et al., 2013):



Moreover, if a biomass is present in the environment, the hematite is transformed to siderite or magnetite through the reactions below (10) and (11):



In order to explore the potential role played by the presence of Fe-oxyhydroxides on chert geochemistry, mixing lines were calculated based on the Alibo and Nozaki (1999) seawater composition, Fe-oxyhydroxide precipitates, and graphitic mudstone from the Meliadine gold district (i.e., the KMG unit) as end members using the $\text{La}/\text{La}^*_{\text{MUQ}}$ and $\text{Y}/\text{Y}^*_{\text{MUQ}}$ ratios as their polarity reflects respectively seawater-dominated or Fe-oxyhydroxide-dominated precipitation. The results are summarized in Figure 3.13. In detail, Fe-oxyhydroxide precipitates produced under experimental conditions in both a restricted environment from acidic seawater (Bau, 1999) and from alkaline solutions (Kawabe et al., 1999) are used for comparison. The KMG samples are graphitic mudstones and may represent a carbon reservoir that reflects biological oxidation of Fe^{2+} and which shows low Y/Ho ratios associated with negative La and Y anomalies, hence having a chemistry consistent with formation in a restricted basin (Table 6).

The distribution of samples from the Meadowbank area (Fig. 3.13A) illustrates the domination of a primary seawater signature despite the fact that interaction with Fe-oxyhydroxides is highlighted by positive variations of La and Y anomalies along the mixing lines. Within an open seawater system, it is difficult to attribute formation of Fe-oxyhydroxides to either pH variation or biological oxidation in an environment devoid of oxygen. Nonetheless,

pH variation is strongly suggested as a result of seawater and hydrothermal mixing (i.e., acidic versus alkaline; Figs. 3.8A, 3.12A). In contrast, the biological influence, as illustrated by the presence of a carbonaceous argillite (i.e., the KMG samples), appears to have generated weak Y enrichment. Therefore, samples from Central BIF and East BIF suggest a combination of pH variation and biological processes, whereas the West IF suggests mainly pH variation for Fe-oxyhydroxide precipitation.

In the Meliadine gold district, the bulk of samples are also located in the seawater domain of Figure 3.13B (blue dashed box) except for samples showing negative La and Y anomalies (i.e., from Pump and MEL-025 and MEL-028), for which Fe-oxyhydroxide dominates the primary signature. In detail, three trends are observed: (1) interaction along or slightly below the mixing line with samples from Bau (1999), which reflects acidic pH with variable biological influence (i.e., mainly F-Zone); (2) interaction along a mixing line with samples from Kawabe et al., (1999) which reflect slightly-neutral to alkaline pH (i.e., Discovery); and (3) interaction along the mixing line with KMG samples in the purple dashed box (Fig. 3.13B). Thus, two mechanisms for precipitation of Fe-oxyhydroxide are proposed for these samples: (1) influence of dynamic pH between alkaline hydrothermal fluids and acidic-neutral seawater; and (2) biological oxidation of Fe^{2+} . Moreover, samples associated with group (3) suggest deposition in a restricted basin under a biological influence.

In the Musselwhite area, three groups are illustrated in Figure 3.13C: (1) a group of samples reflecting interaction of seawater with Fe-oxyhydroxides (i.e., positive La and Y anomalies); (2) a group of samples illustrating domination of Fe-oxyhydroxides on the primary signature (i.e., E599656 from 4B; E599660, E599665 and E599666 from 4EA) and which are closely associated with the KMG-seawater mixing line; and (3) a group of samples showing weak negative La and

Y anomalies associated with low Y/Ho ratios and which are similar to Fe-oxyhydroxide samples from Bau (1999) (i.e., E599670 and E599671 from 4B; E599657 and E599658 from 4F and E599652 from 4E). The first group of samples reflects interaction of seawater with Fe-oxyhydroxide and domination of the primary signature by seawater as previously seen for Meadowbank and Meliadine and may reflect variable pH conditions. The second group of samples reflects domination of Fe-oxyhydroxide on the primary signature associated with biological oxidation. Finally, the third group of samples may represent domination of the primary signature by Fe-oxyhydroxides precipitated under conditions similar to those described by Bau (1999) and involving acidic pH.

Samples from the Beardmore-Geraldton gold district, in which hematitic inclusions in jasper bands are presumed to reflect Fe-oxyhydroxide precipitation in chert bands, show interaction of seawater with Fe-oxyhydroxides (Fig. 3.13D) and domination of the seawater influence on the primary signature of chert and jasper. Most of these samples show correlation with the Fe-oxyhydroxides from Bau (1999), which were obtained experimentally from acidic seawater. It is noted that three samples from the a- and b-type BIF fall below the mixing line of seawater with KMG which may reflect interaction of seawater with Fe-oxyhydroxide precipitated under biological influence.

3.7.4.1 pH condition relationships

In modern hydrothermal systems, pH and redox conditions of high temperature hydrothermal fluids are strongly buffered by the mineral assemblage of plagioclase + epidote + anhydrite. This process maintains the value of pH around 5 (as confirmed by *in-situ* pH measurements of deep-sea high temperature hydrothermal fluid) (e.g., Ding et al., 2005). In the

Archean, it appears that calcite (rather than anhydrite) and igneous plagioclase precipitated due to extremely low sulfate concentration in the seawater (Kump and Seyfried, 2005) suggesting that CO₂ concentration in the Archean hydrothermal fluid was high enough to precipitate calcite compared to modern basalt-hosted hydrothermal fluids which have CO₂ up to 0.02 mol/kg.

By calculation, Shibuya et al. (2010) demonstrated that, in this mineral-buffered system, the minimum pH *in-situ* depends on CO₂, and the CO₂ of a hydrothermal fluid in the early Archean is considered to be at least 0.2 mol/kg. This condition gives highly alkaline pH *in-situ* (>10) because the presence of calcite keeps Ca²⁺ very low in the hydrothermal fluid as opposed to the modern equivalent.

In parallel to what has been already discussed, several related studies have suggested that given the anoxic character of Archean seawater, the shale-normalized REE+Y patterns for Archean seawater differ from the modern seawater based on the behavior of Ce which shows a well-developed, negative Ce anomaly in the latter due to oxidation of Ce⁺³ to Ce⁺⁴ in the stratified water column resulting in preferential removal onto Mn-Fe-oxyhydroxides, organic matter, and clay particles (e.g., Kawabe et al., 1999; Bau and Koschinsky, 2009; Planavsky et al., 2010). However, Bau (1999) experimented with the scavenging of dissolved REE+Y by precipitating Fe-oxyhydroxide in a restricted environment at pH values ranging from 3.6 to 6.2 and ambient oxygen content (i.e., oxic conditions) and demonstrated that pH has a more important effect on Ce than oxygen in presence of Fe-oxyhydroxides. Thus, at a pH ≤5 oxidative scavenging of Ce is favored in the presence of Fe-oxyhydroxide and generates a positive Ce anomaly (Fig. 3.14) and in pH ≥5, REE+Y systematics shows a negative Ce anomaly associated with an M-type lanthanide tetrad effect (Fig. 3.14). Therefore, we only consider Ce anomalies to be significant with respect to oxygenation status when open basin conditions prevail.

Based on the above, samples for Pump, MEL-025, MEL-028 and the second group of samples from Musselwhite (previously described in this section) reflect deposition in a restricted environment, and show negative Ce anomalies that may reflect precipitation at a pH >5. As the KMG samples also show negative Ce anomalies ($Ce/Ce^*_{MUQ} = 0.14-0.47$), this suggests their formation at pH >5 and, therefore, that samples from Pump, MEL-025, MEL-028 and the second group of sample from Musselwhite may reflect domination of the primary signature by Fe-oxyhydroxides formed by biological processes. It is noted, however, that in an open system the Ce anomaly has to be used with some caution as biological processes appears to drive the binary mixing lines of pH variation to the right on Fig. 14, which suggests Y enrichment.

3.7.5 Influence of post-depositional events on primary isotopic and trace element signature of the chert

It is now recognized that post-depositional processes (i.e., diagenesis, metamorphism, hydrothermal fluids) have negligible influence on the REE+Y composition in BIF (e.g., Bau, 1993; Bau and Dostal, 1996; Bolhar et al., 2004; Webb et al., 2009; Thurston et al., 2012), which is further supported by the results of this study. However, in contrast to this stability, the results of recent microanalysis of the oxygen isotopic signature of chert from BIF using *in-situ* SIMS measurements (e.g., Marin et al., 2010; Marin-Carbonne et al., 2011, 2012, 2013, 2014; Robert and Chaussidon, 2012) have demonstrated that post-depositional perturbation of the primary $\delta^{18}O$ signal is variably developed in samples. In order to further evaluate such modification, we have also undertaken similar *in-situ* SIMS $\delta^{18}O$ analysis of certain of our chert samples used for the trace element work to track such modification and assess its relevance to the present study.

For the purpose of also assessing the influence of post-depositional processes on cherts, the

$\delta^{18}\text{O}$ values were determined on three selected chert samples from the Meliadine area. The results of the oxygen isotopic study suggest: (1) modification of the $\delta^{18}\text{O}$ values caused by oxygen isotopic fractionation due to dissolution of precursor amorphous silica during diagenesis; and (2) an open system until sealing of the chert-system occurred which avoids an increase of the $\delta^{18}\text{O}$ chert through the combined effects of dissolution-precipitation and isotopic fractionation (as discussed earlier in this section).

The fractionation of oxygen isotopes is temperature-sensitive and thus it may be used as a means to assess the temperature of the fluids mediating the reaction process whereby opal is converted to chert. Thus, in order to address the potential influence of post-depositional fluids and to define the intensive parameters associated with the replacement process, we have undertaken modeling using the equations of Taylor (1998). For this, we have assumed the primary amorphous silica had a $\delta^{18}\text{O} = +27\text{‰}$ (Marin et al., 2010) and that it reacted to form chert with final $\delta^{18}\text{O}$ values between +6.6 to +19.1‰ by interacting with fluids. For the latter, we use four different reacting fluids (i.e., $\delta^{18}\text{O}_{\text{H}_2\text{O}} = 0, 5, 10$ and 15‰) to represent seawater through to metamorphic fluid values at variable temperature (30° to 400°C ; Hoefs, 2009). These results are summarized in Figure 3.15 and form the basis of the following discussion.

For a fluid with $\delta^{18}\text{O}_{\text{H}_2\text{O}} = 0\text{‰}$ (i.e., ocean water), the modelling suggests high-temperature ($>100^\circ\text{C}$) interaction of fluid with amorphous silica is required to obtain the observed chert $\delta^{18}\text{O}$ values (i.e., +6.6 to +19.1‰). It is accepted that the Archean oceanic temperature was around 70°C (e.g., Knauth and Lowe, 1978, 2003), but higher values are not realistic. Thus, for the parameters discussed above, it is unlikely that Archean seawater interacting with original opal could produce the observed $\delta^{18}\text{O}$ values in the chert samples (Fig. 3.15A).

For a fluid with $\delta^{18}\text{O}_{\text{H}_2\text{O}}$ values of +5 and +10‰, the modelling suggests that temperatures $>200^\circ\text{C}$ and $>250^\circ\text{C}$, respectively (Figs. 3.15B, C) are required to account for the observed $\delta^{18}\text{O}$ chert values of between +11 to +19‰, which represent 80% of the dataset. These temperatures would equate to the onset of metamorphic conditions (i.e., zeolite facies) and require deep burial.

Finally, for a fluid with $\delta^{18}\text{O}_{\text{H}_2\text{O}} = +15\text{‰}$, the parameters used in the modelling do not provide any plausible scenarios to explain the observed $\delta^{18}\text{O}_{\text{chert}}$ values (Fig. 3.15D). The higher temperature (i.e., $\geq 300^\circ\text{C}$) and isotopic parameters ($\delta^{18}\text{O}_{\text{H}_2\text{O}} = +15\text{‰}$) equate to a typical metamorphic fluid, as documented for regional metamorphism or orogenic gold mineralization (e.g., Taylor, 1974; Goldfarb et al., 2005), which has been implicated by Marin et al. (2010) where chert has the appropriate $\delta^{18}\text{O}$ values.

In summary, although the lower $\delta^{18}\text{O}$ values recorded by cherts (i.e., from +6.6 to +11‰) may be interpreted as evidence for a hot Archean seawater, it is unlikely that such fluids could penetrate the crust and be heated to the necessary temperatures (i.e., 100° to 400°C) and not exchange with the host rocks and thus have their $\delta^{18}\text{O}$ signature modified to higher values. For these reasons, such a singular fluid model is not considered a viable explanation for the observed ranges in the $\delta^{18}\text{O}_{\text{chert}}$. At the other extreme, a singular model using $\delta^{18}\text{O}_{\text{H}_2\text{O}} = +15\text{‰}$ would require very high temperatures. A compromise is therefore found for a fluid of $\delta^{18}\text{O}_{\text{H}_2\text{O}} = +5\text{‰}$ which may represent fluid present during diagenesis, essentially an isotopically modified downwelling and heated sea water sourced fluid with an original $\delta^{18}\text{O}_{\text{H}_2\text{O}} = 0\text{‰}$. In this model, the $\delta^{18}\text{O}_{\text{chert}}$ records both a change in the reacting fluid as it interacts with the crust and also as it heats up. This fluid chert interaction would proceed until the system was essentially sealed. This hypothesis is also supported by the fact that REEs and trace element concentrations in chert bands do not show resetting of their primary signature (as seen previously in this paper)

suggesting that a fluid with very low concentration of REEs and trace elements was responsible for conversion of opal to chert. The chemical data for the ambient seawater, which show a range of REE concentration normalized to MUQ between 10^{-7} to 10^{-8} (Fig. 2.5), would therefore satisfy this requirement and is why the $\delta^{18}\text{O}$ values for chert change whereas their REE+Y systematic do not.

3.8 Conclusions

Chert bands sampled from BIF horizons in four gold deposit settings in Canada (Meadowbank, Meliadine, Musselwhite and Beardmore Geraldton) were used to validate the restricted basin model for BIF proposed by Barrett et al. (1988a) in which seawater is not considered to have been of uniform chemistry. The use of *in-situ* LA ICP-MS analyses obtained via a traverse mode on carefully selected chert bands within the BIF using appropriate analytical protocols provide quantitatively meaningful data at low detection limits (i.e., to 0.0001 to 0.001 shale-normalized values). The consistency of the patterns noted in this study indicates, importantly, that primary chemical signatures have been retained within the selected chert material despite several post-formation deformation and metamorphic events, in some cases to amphibolite facies. In contrast to the trace element chemistry, *in-situ* analysis of $\delta^{18}\text{O}$ indicates the cherts record extensive oxygen isotopic exchange during conversion of primary opal to microcrystalline silica. Based on detailed REE+Y geochemistry and petrographic studies, the chert bands are interpreted to reflect the following:

1. Most samples from the four deposits record the influence of seawater during precipitation, as illustrated by depletion in the LREE relative to the MREE and HREE with associated positive La and Y anomalies. These chemical features

suggest deposition in either a partially closed basin under the constant influence of seawater or within an open seawater system.

2. The influence of high-temperature (>250°C) hydrothermal vent fluid during deposition is reflected by a positive Eu anomaly. Importantly, it is suggested here that this anomaly may provide indirect information about proximity to the vent and thus important information about the deposition site for BIF; thus, the stronger the Eu anomaly, the closer to the vent site. The influence of a detrital input is illustrated from petrographic and SEM-EDS imaging by the presence of apatite, xenotime and zircon grains that occur disseminated in chert bands, in addition to the enrichment in the REE, elevated chondritic Y/Ho values and variably elevated values for Th, Ga, Zr, Sc and Sr. Furthermore, an evaluation of chemical contamination from ultramafic (i.e., komatiite or tholeiite) and minor volcanic ash and felsic to intermediate calc-alkaline clastic material is consistent with the stratigraphic proportions in a Keewatin sequence model for Algoma-type BIF deposition (e.g., Thurston et al., 2008).

3. Domination of the primary signature by particle scavenging by Fe-oxyhydroxide phases, as revealed by negative La, Gd and Y anomalies in some samples from the Meliadine and Musselwhite areas, suggest BIF deposit occurred in a restricted basin environment, involving no REE+Y recharge from the open ocean to re-equilibrate the REE+Y budget. The Fe-oxyhydroxides, rather than Mn-oxyhydroxides, are favoured due to the presumably anoxic deep Archean seawater setting, as Mn-oxyhydroxides precipitate in the presence of oxygen and dissolve through the anoxic water column; the latter is common in modern oceans which are

more oxic than their Archean precursors (e.g., Kawabe et al., 1999; Bau and Koschinsky, 2009).

4. The negative Ce anomalies in some of the chert samples indicates precipitation of Fe-oxyhydroxide occurred at a pH >5, most of the cherts from the four deposits studied have positive Ce anomalies and may reflect precipitation at a pH <5. This conclusion suggests that Archean high-temperature hydrothermal vent fluids from which oxyhydroxides originate may represent an alkaline hydrothermal fluid, as proposed by Shibuya et al. (2010).

5. Lastly, an *in-situ* detailed study of $\delta^{18}\text{O}$ for three chert samples from the Meliadine gold district suggests the influence of a fluid $\delta^{18}\text{O}_{\text{H}_2\text{O}} = 0$ to 5‰ at high-temperature (>100°C) during diagenesis within an open system, as illustrated by modification of the precursor amorphous silica $\delta^{18}\text{O}$ value caused by oxygen isotopic fractionation due to dissolution-precipitation processes. However, it is noted that contrary to the $\delta^{18}\text{O}$ values, the REEs and trace elements are not modified as the reacting fluid, of sea water origin, is characterized by very low-REE concentrations.

3.9 Acknowledgements

The authors gratefully acknowledge the staff of Agnico Eagle Mines Ltd., Goldcorp Ltd. and Premier Gold. The authors also thank Dr. Matthew Leybourne, Dr. Sally Pehrsson, Dr. Olivier Côté-Mantha, and John Biczok for discussions regarding the geochemistry and regional geological setting of the study areas. The LA-ICP-MS analyses were done in the Geochemical Fingerprinting Laboratory at Laurentian University with the assistance of Dr. J. Petrus and the oxygen isotope analyses were performed at the University of Manitoba (Winnipeg) with the capable assistance of R. Sharp. Finally, we sincerely acknowledge the contribution of Dr. Benoit

Dubé, Dr. Sebastien Castonguay and Dr. Patrick Mercier-Langevin of the Geological Survey of Canada for their input and continued support. The study is supported by both TGI-4 funding from Natural Resources Canada and funding through a Natural Sciences and Engineering Research Council Collaborative Research and Development agreement with participation by Agnico Eagle Mines Ltd and Goldcorp Ltd. We thank also Drs. L. Brengman and an anonymous reviewer for their constrictive comments that helped to substantially improve the manuscript.

3.10 Figures and captions

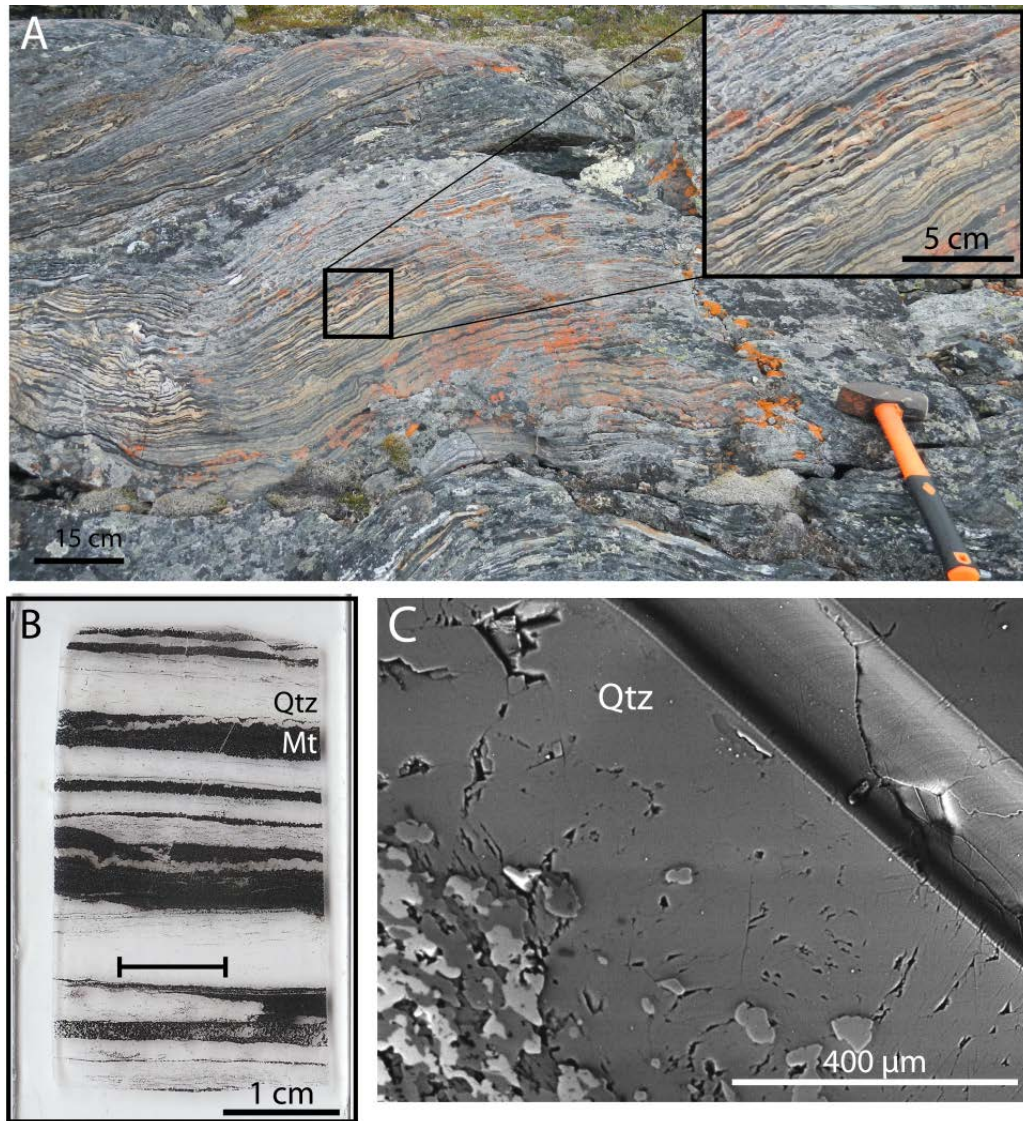


Figure 3.1:
Field and
laboratory
photographs of
BIF to show
the nature of
sampling used
in the study:

(A) Outcrop of
BIF in the
Meadowbank
gold area. The
inset is a close
up to illustrate
the nature of
the chert and

magnetite layering; (B) Polished thin section of chert (Qtz) and magnetite (Mt) layers made from the previous sample. The black solid line represents the line traverse done during LA ICP-MS study; and (C) Back-scattered electron image from the SEM illustrating the line traverse (upper right corner) done in the chert (Qtz) band.

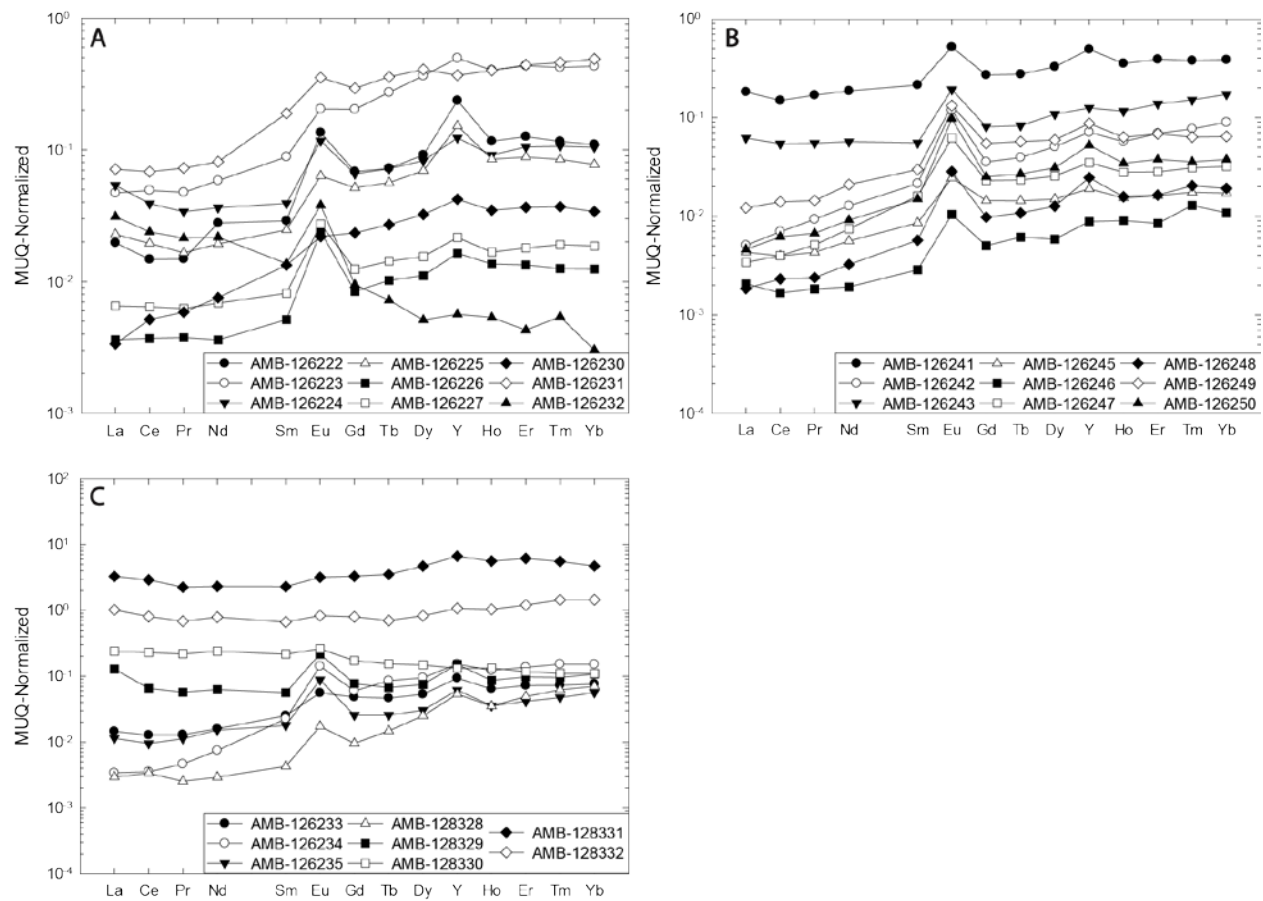


Figure 3.2: MUQ - normalized REE+Y patterns for BIF-hosted cherts from samples in different parts of the Meadowbank area: (A) Central BIF, (B) East BIF, and (C) West IF.

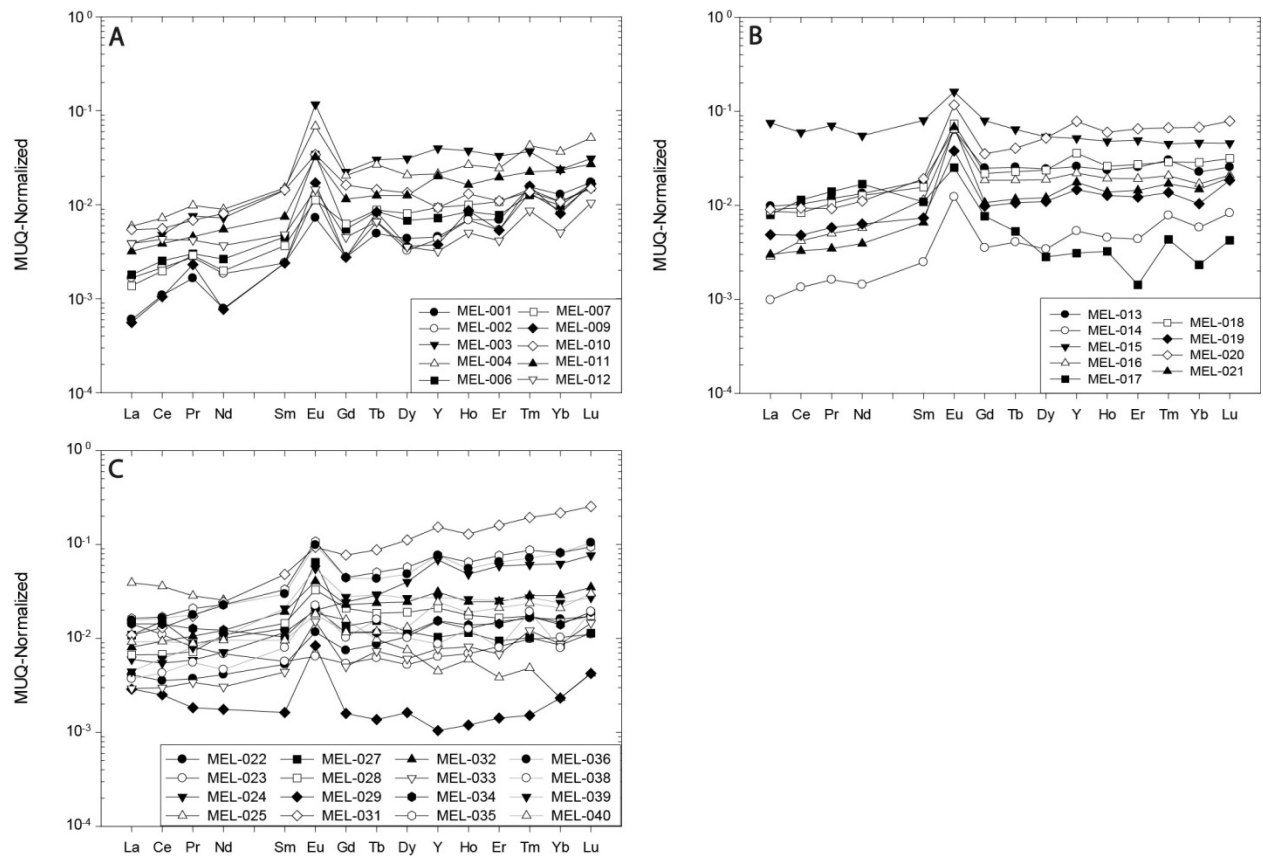


Figure 3.3: MUQ - normalized REE+Y patterns for BIF-hosted cherts from samples in different parts of the Meliadine gold district: (A) Pump, (B) F-Zone, and (C) Discovery.

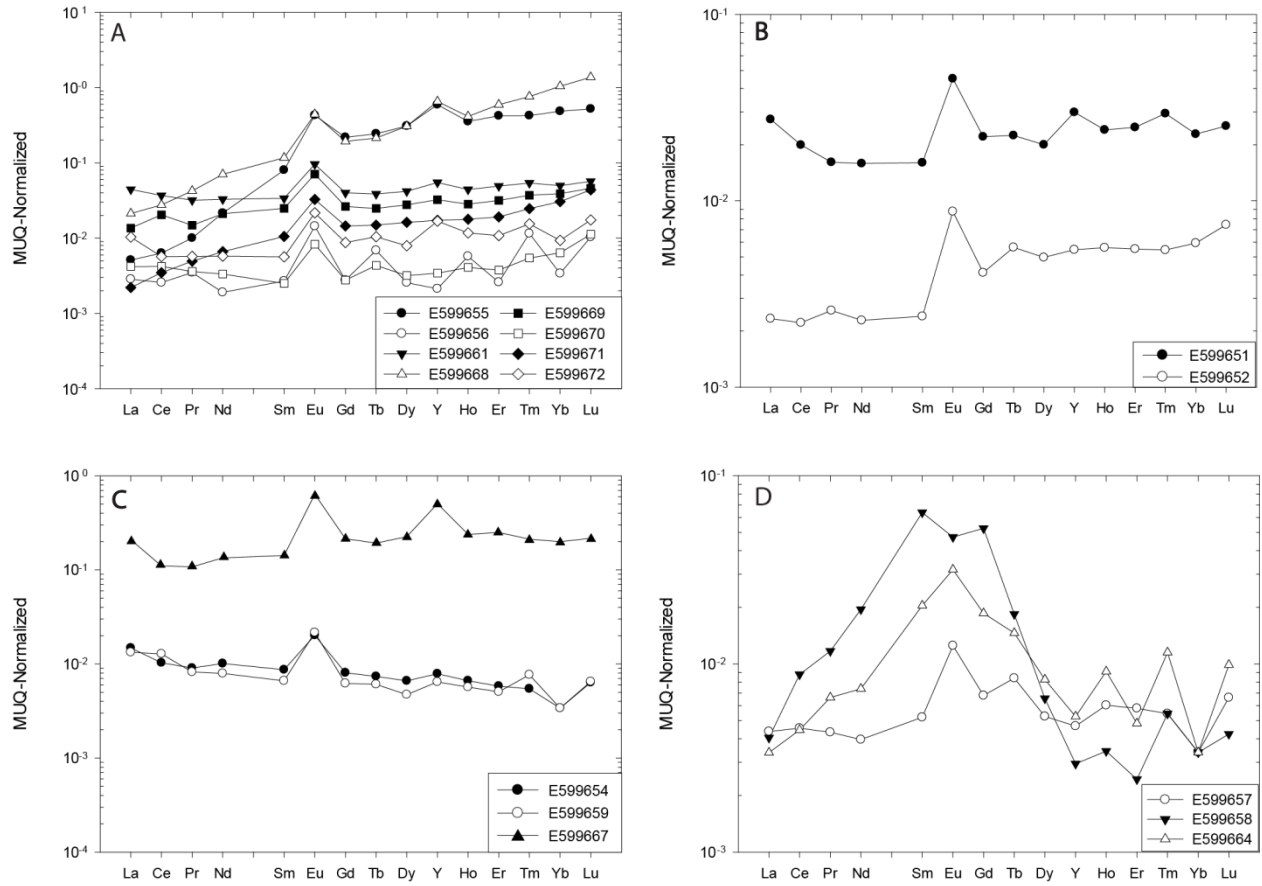


Figure 3.4: MUQ - normalized REE+Y patterns for BIF-hosted chert from samples in different parts of the Musselwhite area: (A) 4B - Oxide dominant facies excluding sample E599656, (B) 4E - garnetiferous amphibolite samples, (C) 4EA - garnet-grunerite samples excluding samples E599660, E599665 and E599666, and (D) 4F - biotite-garnet schist samples.

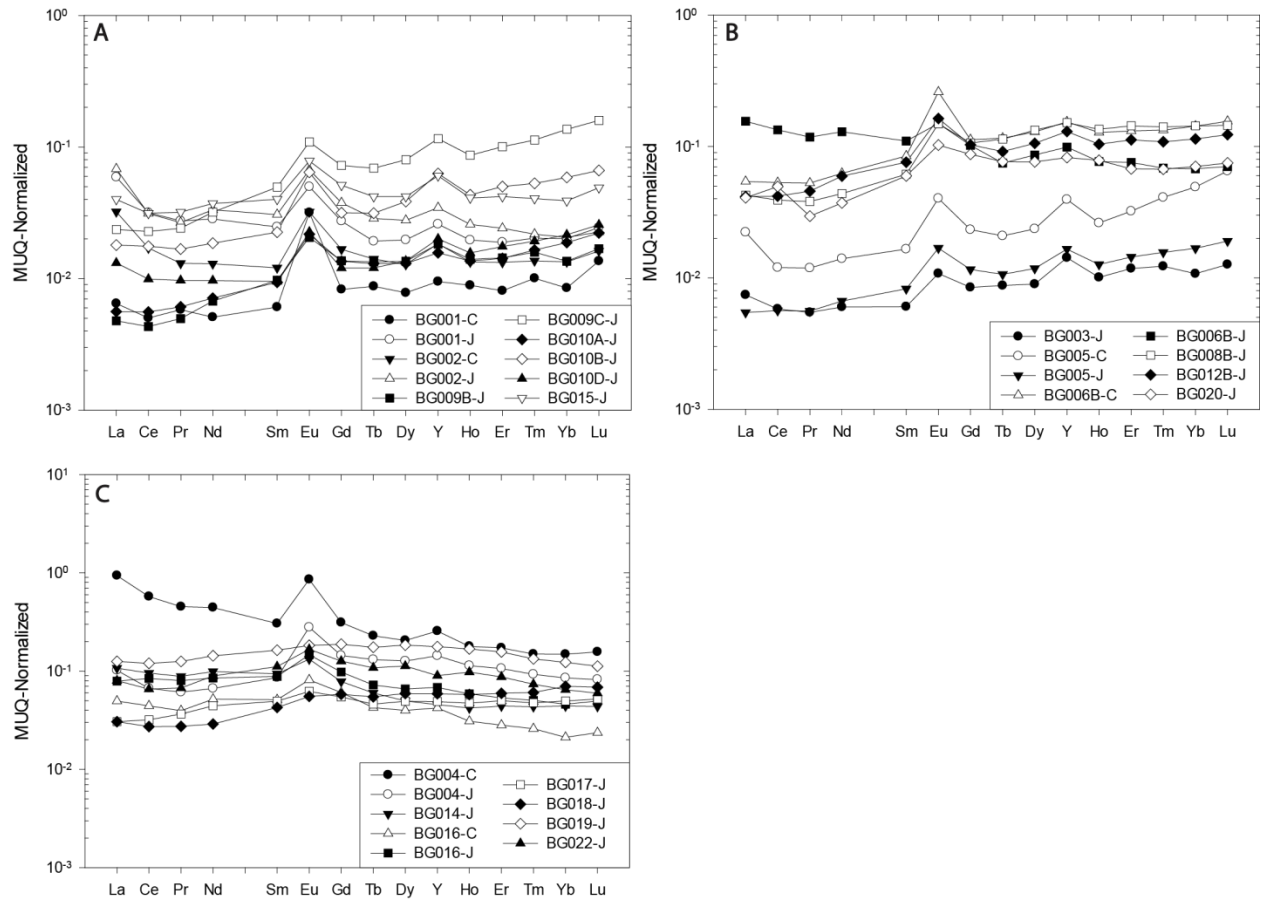


Figure 3.5: MUQ - normalized REE+Y patterns for BIF-hosted chert from samples in different parts of the Beardmore-Geraldton gold district: (A) a-type - iron oxide-rich type, (B) b-type - siltstone-rich type, and (C) c-type - sandstone-rich type. Note that the lettering refers to chert (C) and jasper (J) types of silica layers.

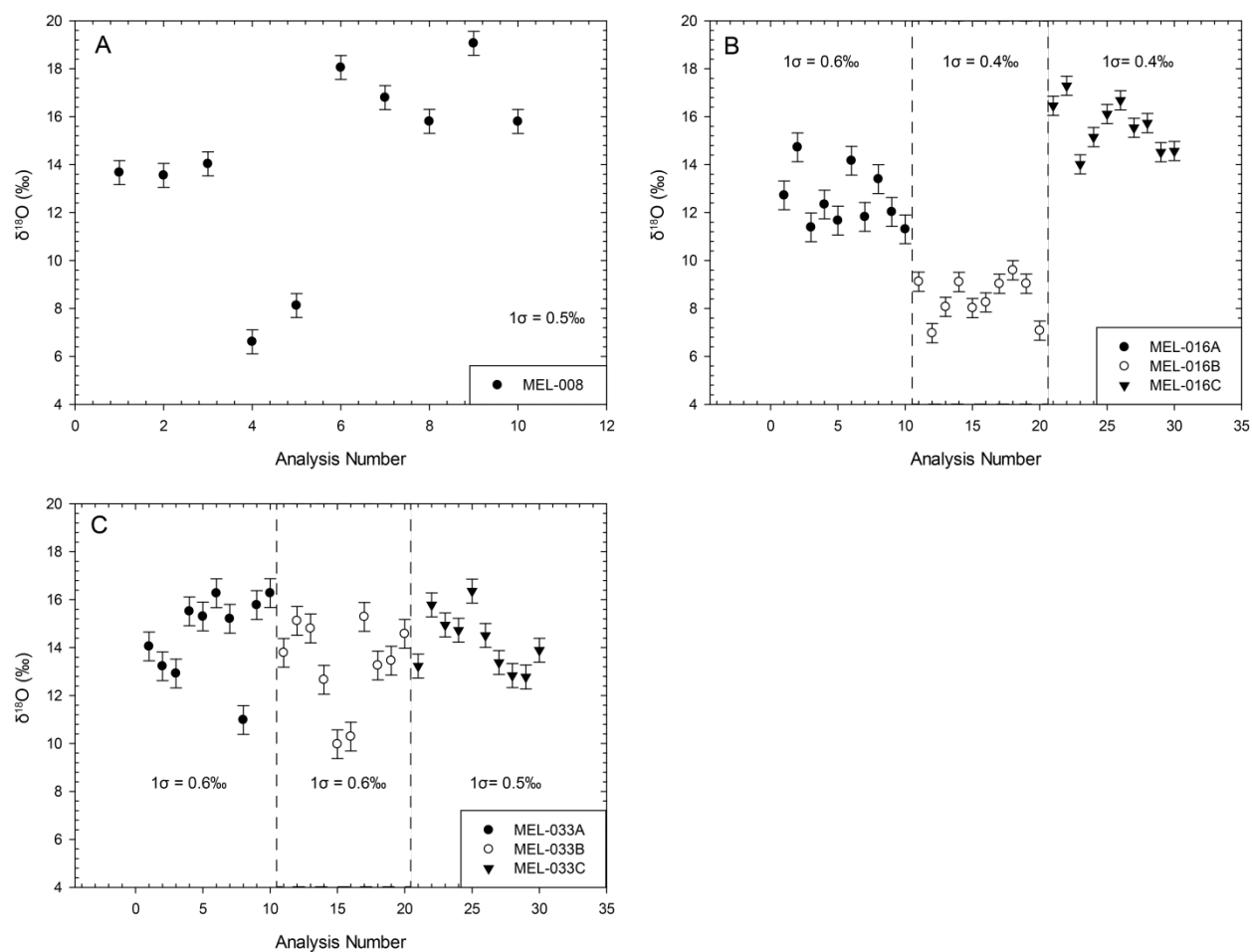


Figure 3.6: Variation in the $\delta^{18}\text{O}$ values versus analysis number for chert samples from Meliadine gold district: (A) MEL-008, (B) MEL-016, and (C) MEL-033.

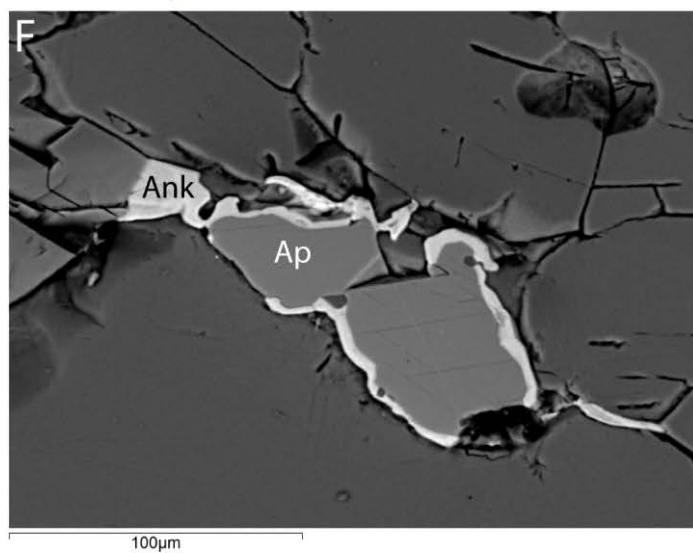
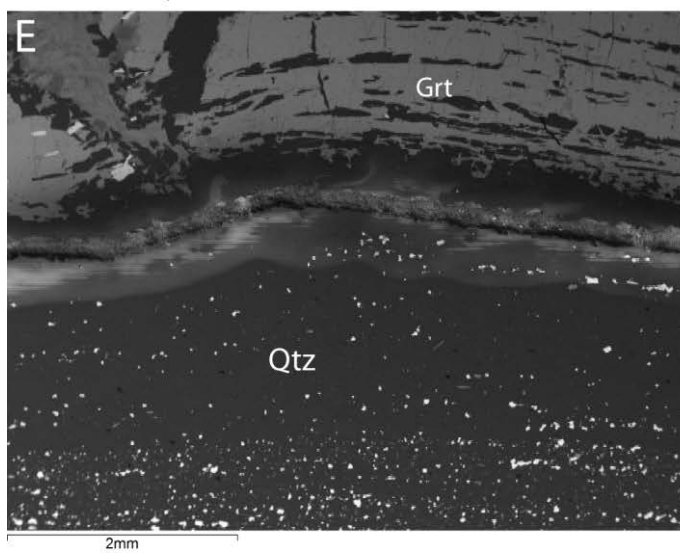
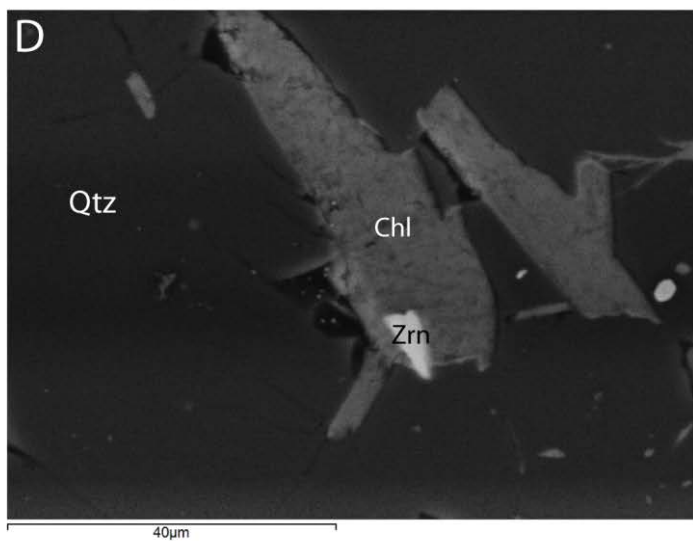
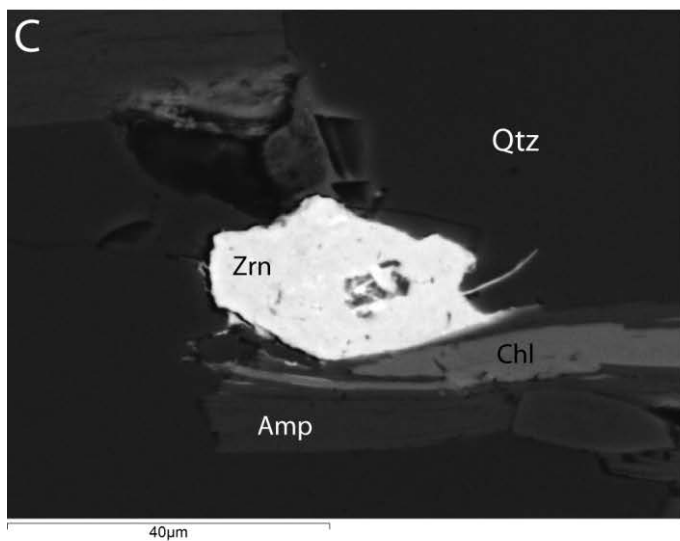
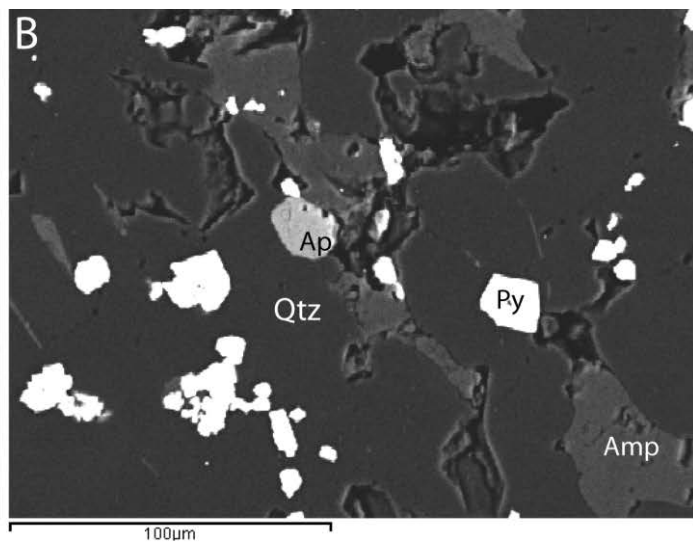
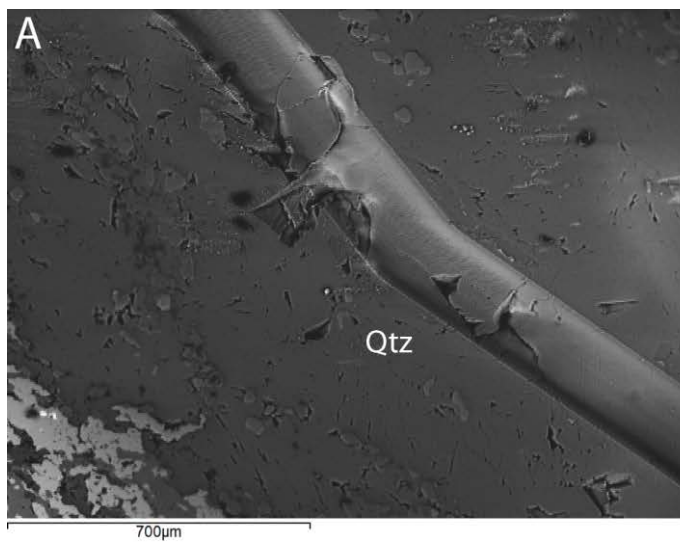


Figure 3.7: Back-scattered electron image from the SEM for different BIF-hosted chert samples from the Meadowbank and Musselwhite: (A) an example of line traverse done in a chert band during LA ICP-MS analysis (from E599668); (B) example of mineral inclusions in a chert band which includes anhedral apatite (Ap), euhedral pyrite (Py) and variable subhedral to anhedral amphibole (Amp) (from AMB-126247); (C) subhedral chlorite (Chl) and amphibole (Amp) grains surrounding subhedral to euhedral zircon (Zrn) grains in chert band (from AMB-126231); (D) subhedral to euhedral grains of chlorite (Chl) with an inclusion of euhedral zircon (Zrn) in chert band (from AMB-126223); (E) traverse line in centre of the image done in a chert band at the edge of a garnet (Gr) band (from AMB-126232); and (F) ankerite (Ank) surrounding subhedral apatite (Ap) grains in a chert band (from E599655).

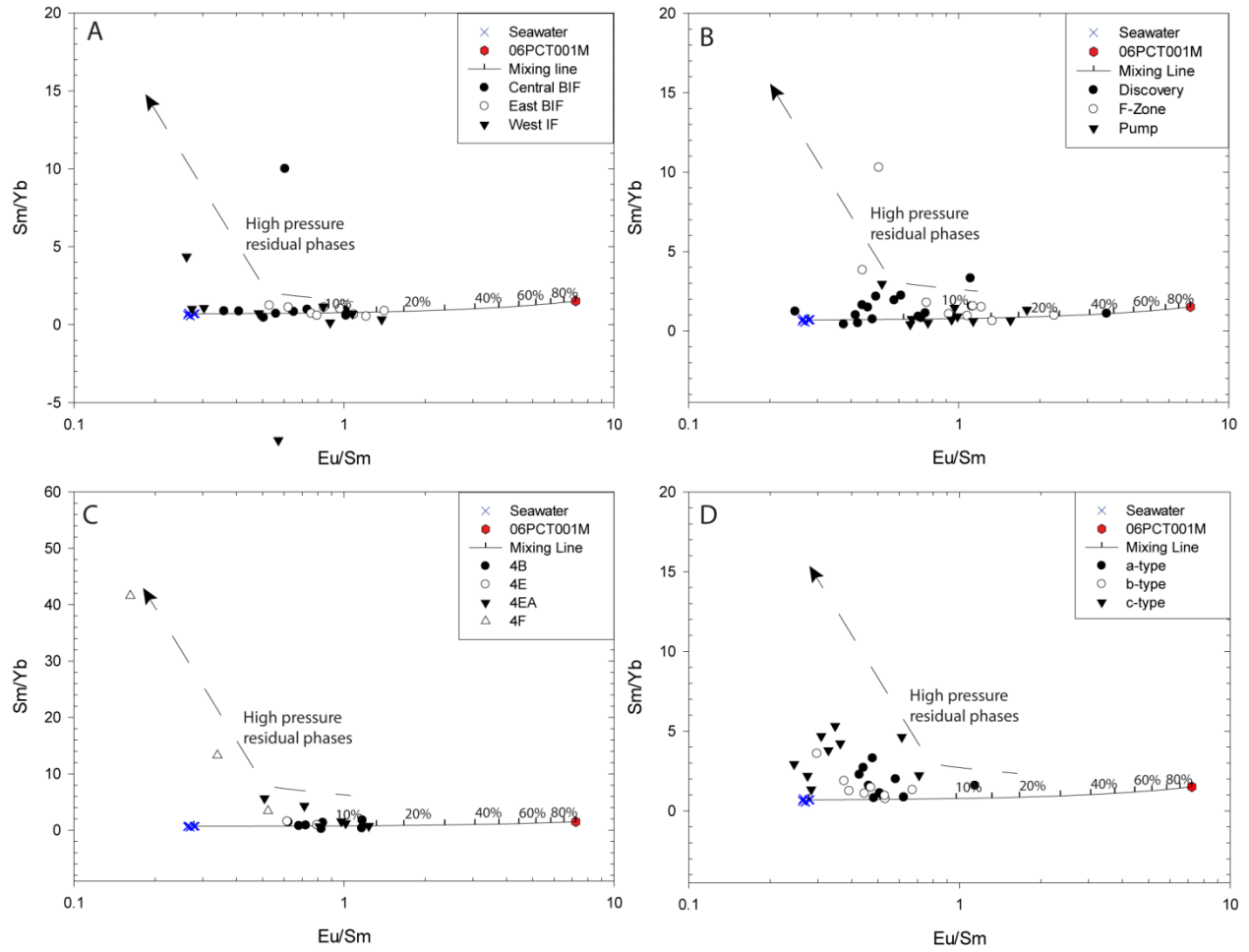


Figure 3.8: Binary plots of elemental ratio data (Eu/Sm and Sm/Yb) for chert samples in BIFs from Meadowbank (A), Meliadine (B), Musselwhite (C), and Beardmore-Geraldton (D). These plots are used to assess the potential influence of high-T hydrothermal fluids on the chert chemistry, as illustrated with the conservative mixing line. The data for the high-T hydrothermal fluid is from Thurston et al., (2012) and data for seawater is from Alibo and Nozaki (1999).

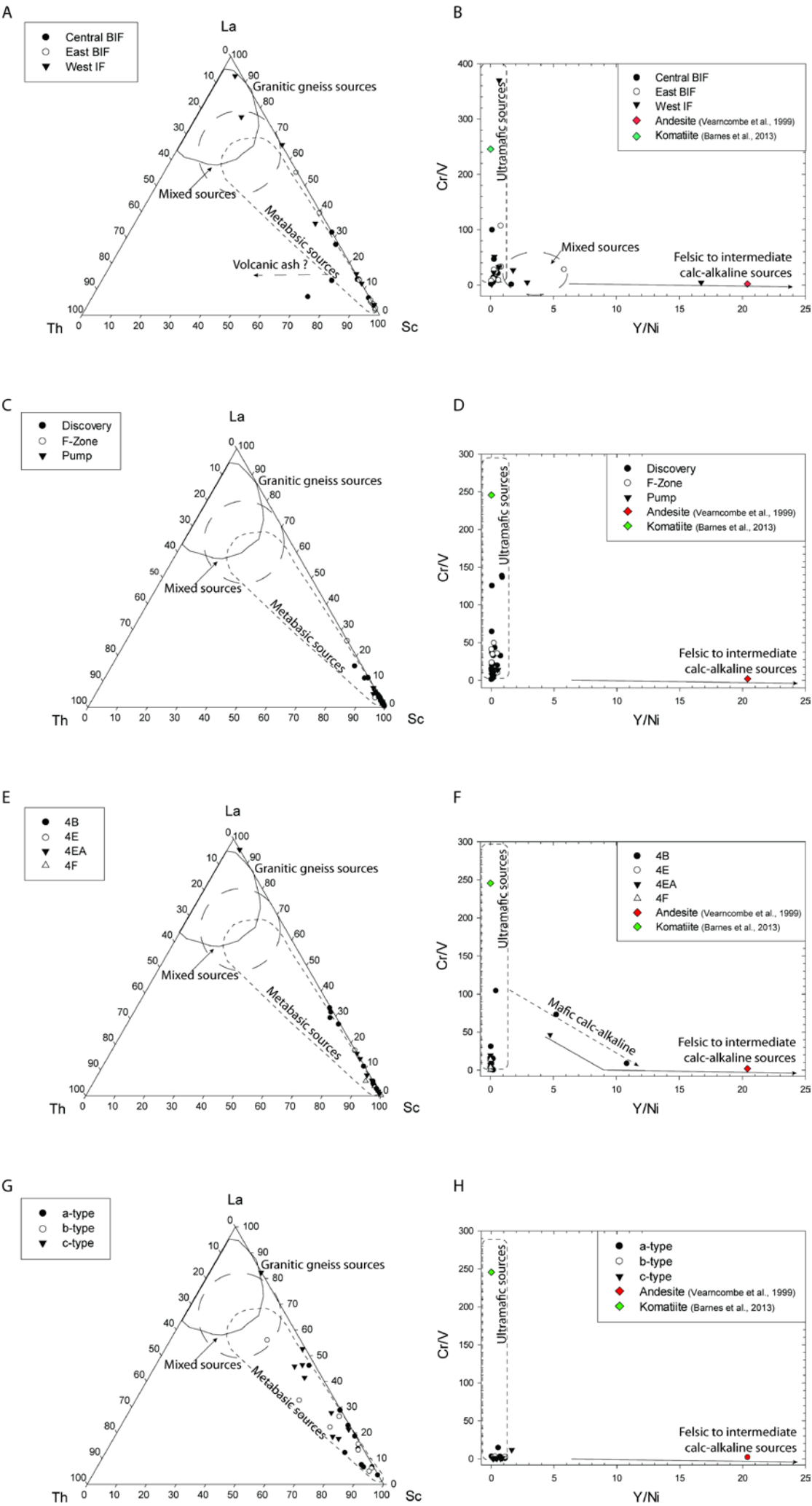


Figure 3.9: Trace element plots (La-Th-Sc and Cr/V and Y/Ni) used to constrain the provenance of detrital contamination in chert bands from the BIF localities (respectively modified from Bhatia and Crook, 1986; and modified from McLennan et al., 1993): (A) and (B) from the Meadowbank area, (C) and (D) from Meliadine gold district, (E) and (F) from the Musselwhite area, and (G) and (H) from the Beardmore-Geraldton gold district.

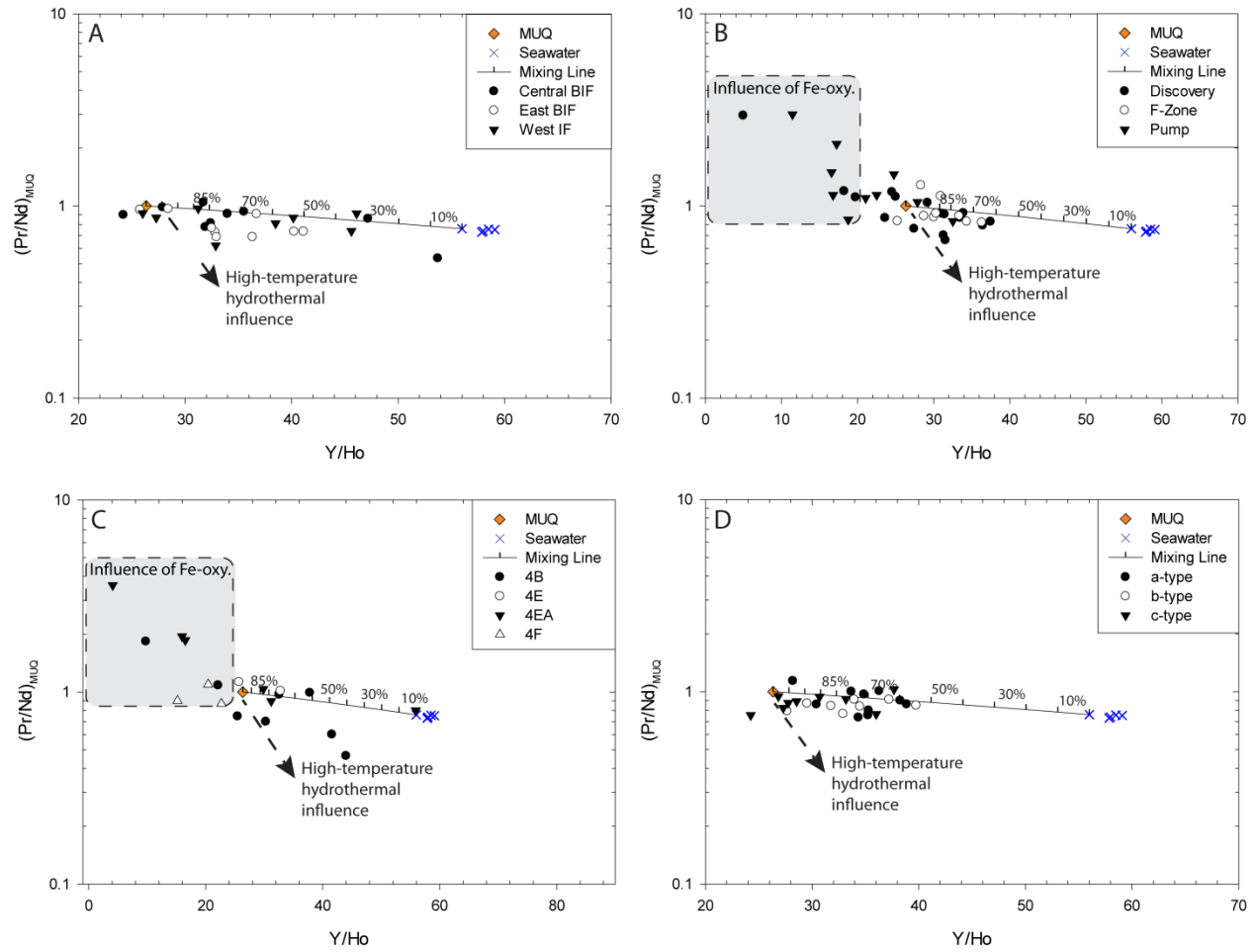


Figure 3.10: Binary plots of Y/Ho versus and $(Pr/Sm)_{MUQ}$ for chert samples from the Meadowbank area (A), the Meliadine gold district (B), the Musselwhite area (C) and the Beardmore-Geraldton gold district (D) BIFs. These plots are used to assess the potential influence of detrital contamination in the chert layers, as illustrated with the conservative mixing line. The data for the MUQ and seawater are from Kamber et al. (2005) and Alibo and Nozaki (1999), respectively. The dashed arrow represents the influence of a high-T hydrothermal fluid and the grey square presented in Meliadine and Musselwhite represents the influence of Fe-oxyhydroxides.

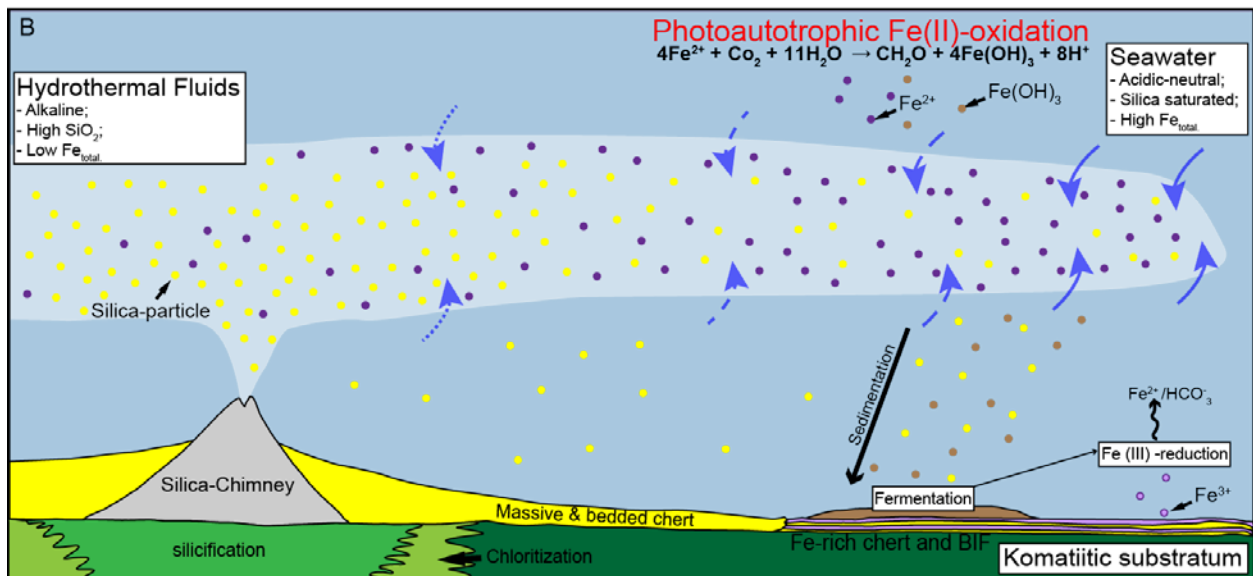
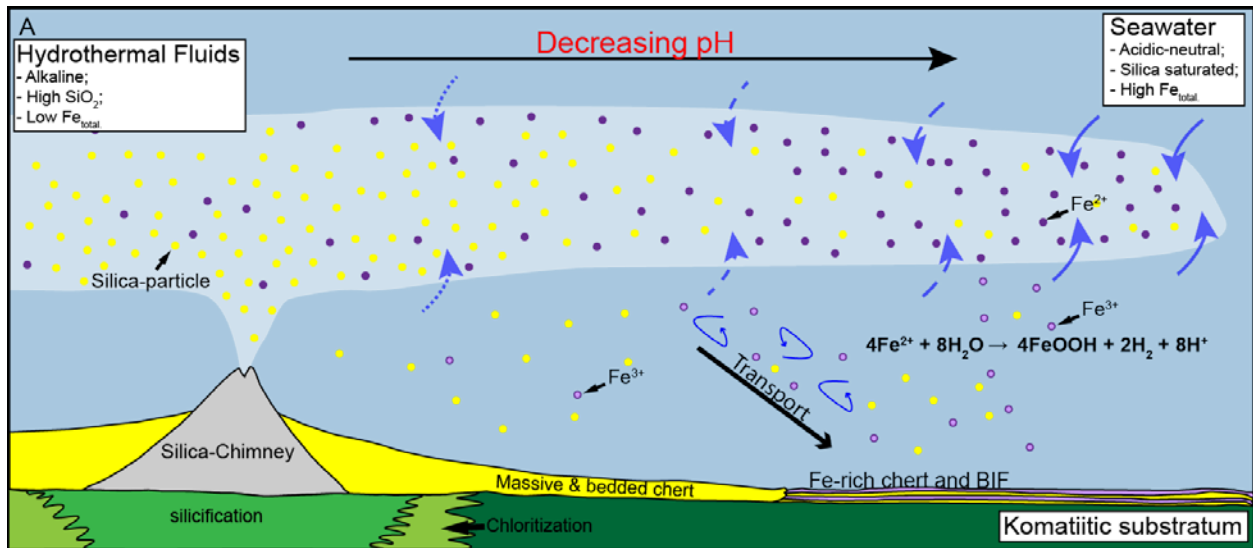


Figure 3.11: Model of Algoma-type BIF deposition on Archean seafloor: a) the mechanical-process model illustrated by progressive decrease of pH from the silica-chimney through the seawater column; b) the biological-process model illustrated by oxidation of photoautotrophic produced Fe(II) followed by sedimentation of Fe-hydroxide leading to fermentation and release of Fe(III). Several meters away from the vents, the emissions become white and turbid by precipitation of the oversaturated silica; while with increasing distance from the vent, a cloud of reddish brown particles of iron oxyhydroxides dominates hydrothermal plumes. In the vicinity of the hydrothermal vent systems, the silica particles are predominant in the hydrothermal sediments, but the iron oxyhydroxides are abundant with increasing distance from the vent systems (modified from Konhauser et al., 2005 and Shibuya et al., 2010).

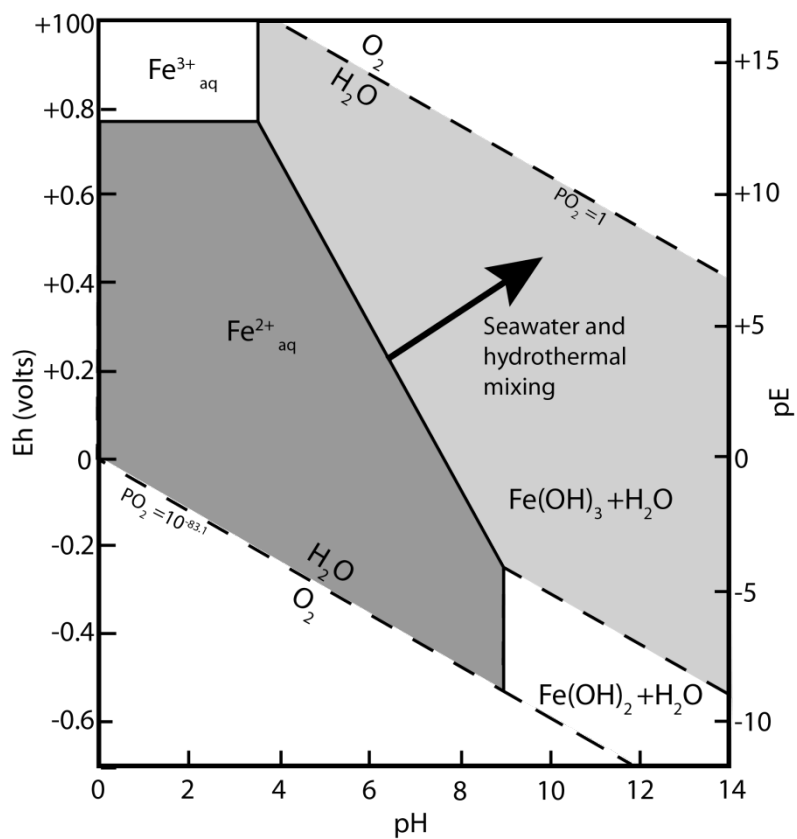
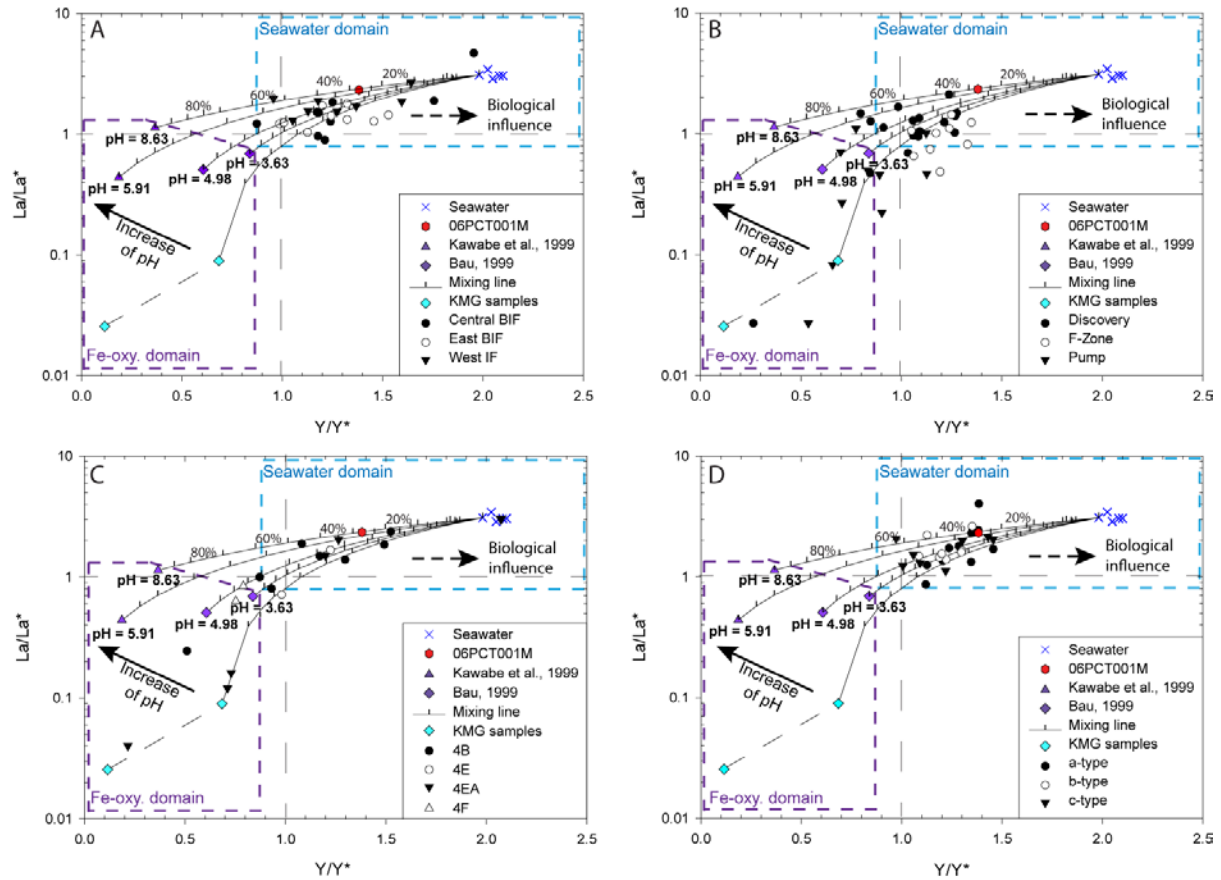


Figure 3.12: Redox path for precipitation of Fe-oxyhydroxide by mixing of acidic to neutral seawater and alkaline hydrothermal fluids in a low temperature seawater setting. The black arrow represents the mixing of acidic seawater with Fe^{2+} in solution with alkaline hydrothermal fluids which leads to precipitation of Fe(OH)_3 (modified from Pufahl et al., 2013).



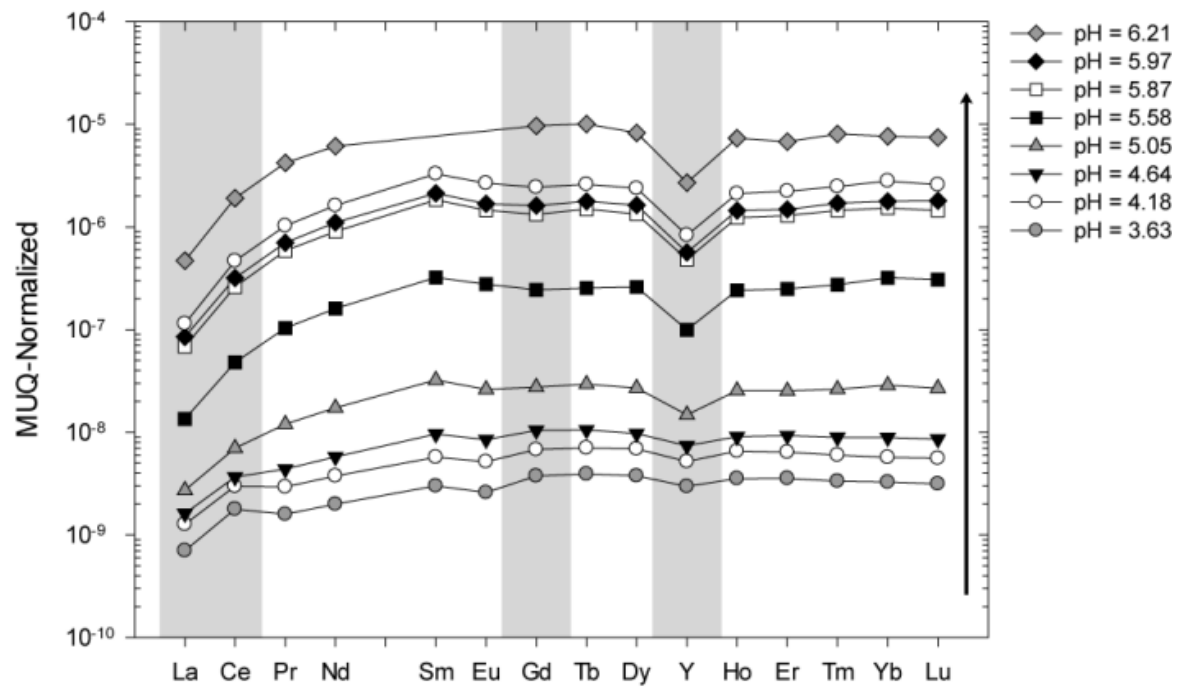


Figure 3.14: Plot of MUQ - normalized REE+Y patterns for experimentally produced Fe-oxyhydroxide precipitates at variable pH values (data from Bau, 1999). The black arrow indicates the increasing pH values.

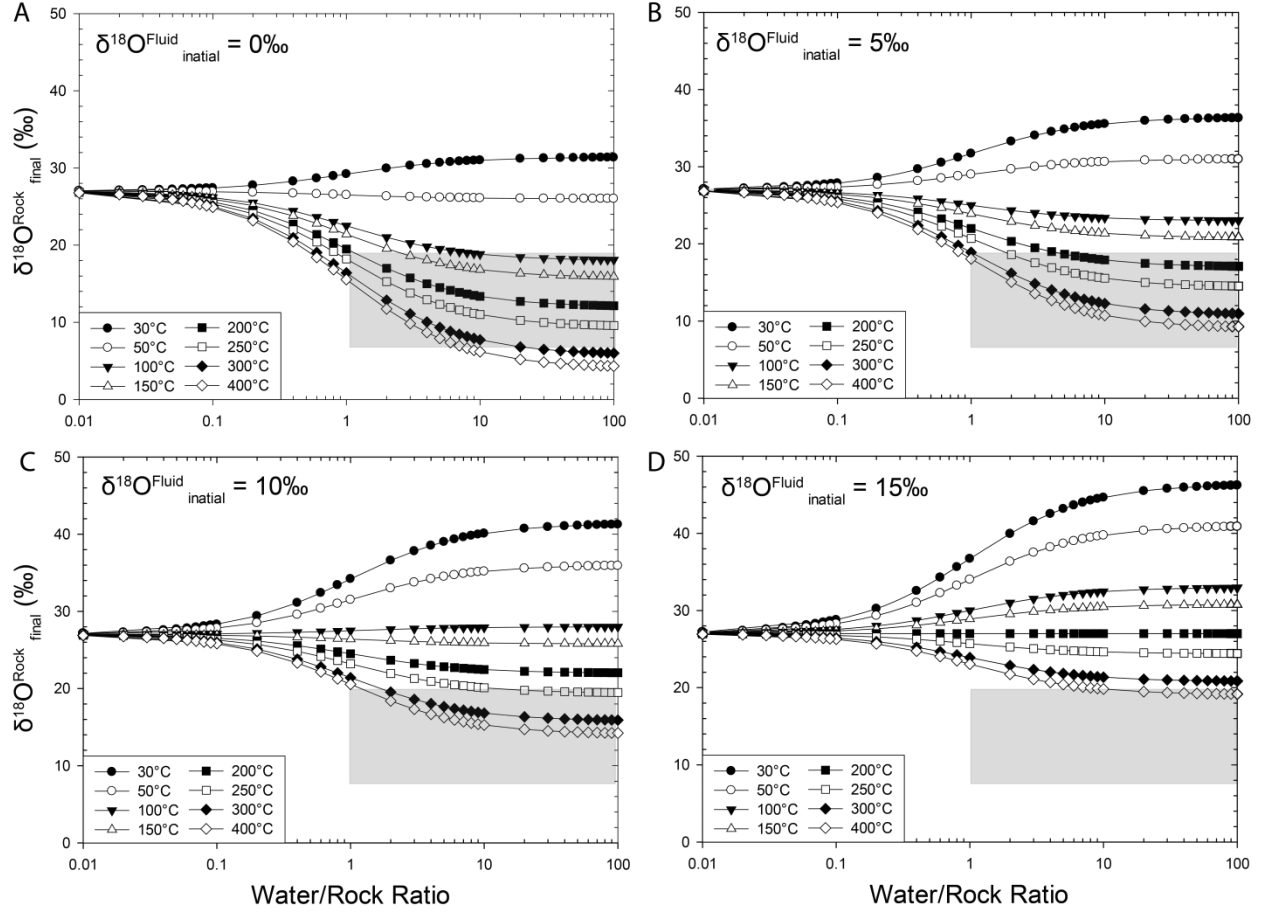


Figure 3.15: Diagram summarizing the variation of calculated values of $\delta^{18}\text{O}_{\text{chert}}$, using the equations of Taylor (1978) and variety of appropriate silica- H_2O ^{18}O fractionation factors (Kawabe, 1978; Matsuhisa et al., 1979; Kita et al., 1985), as a function of temperature (30° to 300°C) and water/rock ratios for four reacting fluids having $\delta^{18}\text{O}_{\text{H}_2\text{O}} = 0, +5, +10$ and $+15\text{‰}$ (respectively A, B, C, and D). The shaded area represents the range of $\delta^{18}\text{O}$ values (i.e., $+6.6$ to $+19.1\text{‰}$) obtained for chert from the Meliadine gold district. Note that the value of the initial $\delta^{18}\text{O}_{\text{chert}}$ was assumed to be $+27\text{‰}$, which is the value of precursor amorphous silica in Archean BIF settings (Marin et al., 2010).

3.11 Tables and captions

Table 3.1: Abundances of elements and REE+Y for samples from Pump in the Meliadine gold district

Samples	MEL001	MEL002	MEL003	MEL004	MEL006	MEL007	MEL008	MEL009	MEL010	MEL011	MEL012
Si (ppm)	346900	397500	401100	338500	341200	430500	380800	395100	409800	330700	410800
Li (ppm)	0.114	0.219	0.564	0.433	0.233	0.219	0.377	0.205	0.110	0.405	0.261
Be (ppm)	0.019	0.026	0.033	0.048	0.023	0.028	0.025	0.021	0.000	0.066	0.024
Sc (ppm)	3.072	3.425	2.909	2.733	3.030	2.643	2.390	2.259	2.488	2.158	2.187
Ti (ppm)	6.900	3.170	4.770	2.920	3.040	2.720	4.030	2.590	2.430	3.480	2.660
V (ppm)	0.394	0.333	0.299	0.440	0.436	0.223	0.601	0.189	0.209	0.285	0.365
Cr (ppm)	2.750	3.470	4.100	4.730	4.650	4.130	3.020	2.550	3.880	4.130	6.670
Mn (ppm)	333	540	629	566	108	48.200	9.470	172	217	647	234
Fe (ppm)	5710	5690	5140	8450	2330	1240	335	402	1100	19240	1860
Co (ppm)	0.434	0.301	0.235	0.256	0.387	0.630	0.317	0.198	0.415	0.225	0.191
Ni (ppm)	10.000	7.200	2.520	3.110	5.900	10.100	9.400	7.900	6.900	3.800	2.780
Cu (ppm)	22.000	25.400	13.800	12.500	22.800	23.200	19.800	19.200	19.100	8.500	10.800
Zn (ppm)	40.600	54.600	46.800	64.300	72.000	48.400	37.300	37.400	32.000	34.500	39.800
Ga (ppm)	0.119	0.182	0.321	0.219	0.196	0.201	0.468	0.118	0.188	0.147	0.161
As (ppm)	78.400	68.980	48.890	52.170	30.640	19.100	8.880	12.700	7.780	5.600	6.690
Rb (ppm)	0.061	0.162	0.062	0.074	0.058	0.069	1.830	0.076	0.049	0.035	0.037
Sr (ppm)	0.407	0.418	4.560	6.270	3.460	0.390	0.343	2.180	9.300	0.995	0.430
Y (ppm)	0.150	0.142	1.310	0.699	0.238	0.308	0.106	0.124	0.306	0.663	0.105
Zr (ppm)	3.970	0.160	0.492	0.173	0.394	4.960	6.280	2.640	0.561	0.381	0.342
Nb (ppm)	0.031	0.035	0.059	0.055	0.027	0.033	0.059	0.045	0.024	0.025	0.025
Mo (ppm)	0.085	0.165	0.143	0.146	0.111	0.192	0.169	0.169	0.760	0.095	0.123
Ag (ppm)	0.109	0.138	0.168	0.193	0.083	1.800	0.332	0.540	0.320	0.280	0.192
Cd (ppm)	0.747	1.285	1.536	1.490	0.933	1.630	1.041	1.830	0.830	0.552	0.834
In (ppm)	0.067	0.090	0.121	0.138	0.082	0.100	0.059	0.115	0.053	0.050	0.068
Sn (ppm)	0.192	0.276	0.274	0.278	0.237	0.339	1.203	0.271	0.245	0.262	1.070
Sb (ppm)	0.294	0.454	0.339	0.403	0.267	0.490	0.404	0.492	0.347	0.226	0.350
Cs (ppm)	0.040	0.066	0.068	0.093	0.036	0.049	0.108	0.060	0.025	0.022	0.038
Ba (ppm)	0.136	0.278	0.162	0.172	0.384	0.168	2.370	0.207	0.524	0.191	0.155
La (ppm)	0.022	0.062	0.145	0.220	0.067	0.051	0.024	0.021	0.203	0.119	0.144
Ce (ppm)	0.088	0.173	0.386	0.582	0.204	0.159	0.123	0.085	0.450	0.312	0.346
Pr (ppm)	0.016	0.026	0.072	0.093	0.029	0.028	0.014	0.022	0.065	0.043	0.040
Nd (ppm)	0.029	0.067	0.263	0.325	0.096	0.072	0.024	0.028	0.293	0.199	0.134
Sm (ppm)	0.018	0.018	0.105	0.111	0.034	0.027	0.018	0.018	0.106	0.055	0.036
Eu (ppm)	0.012	0.020	0.188	0.110	0.054	0.018	0.014	0.028	0.055	0.052	0.023
Gd (ppm)	0.018	0.018	0.149	0.136	0.037	0.042	0.018	0.018	0.108	0.077	0.030
Tb (ppm)	0.005	0.007	0.031	0.028	0.009	0.009	0.005	0.009	0.015	0.013	0.007
Dy (ppm)	0.027	0.020	0.189	0.126	0.042	0.049	0.015	0.022	0.082	0.077	0.022
Ho (ppm)	0.009	0.009	0.047	0.033	0.011	0.012	0.006	0.011	0.016	0.020	0.006
Er (ppm)	0.024	0.019	0.115	0.085	0.027	0.038	0.016	0.019	0.038	0.068	0.014
Tm (ppm)	0.008	0.007	0.019	0.022	0.007	0.008	0.006	0.008	0.007	0.012	0.004
Yb (ppm)	0.043	0.029	0.079	0.123	0.033	0.036	0.035	0.027	0.036	0.078	0.017
Lu (ppm)	0.009	0.008	0.016	0.026	0.008	0.008	0.008	0.008	0.007	0.014	0.005
Hf (ppm)	0.035	0.008	0.014	0.008	0.008	0.065	0.027	0.041	0.008	0.008	0.012
Ta (ppm)	0.006	0.008	0.011	0.014	0.005	0.005	0.005	0.011	0.003	0.002	0.006
W (ppm)	0.131	0.176	0.179	0.223	0.105	0.184	0.205	0.260	0.217	0.142	0.135
Au (ppm)	0.011	0.019	0.017	0.011	0.011	0.319	0.630	0.291	0.168	0.093	0.079
Tl (ppm)	0.078	0.097	0.105	0.126	0.061	0.106	0.250	0.121	0.055	0.030	0.068
Pb (ppm)	2.540	2.840	3.400	3.420	2.190	4.280	4.940	3.490	2.690	2.240	2.510
Th (ppm)	0.007	0.006	0.017	0.012	0.004	0.007	0.011	0.012	0.011	0.036	0.012
U (ppm)	0.047	0.050	0.064	0.082	0.044	0.065	0.059	0.115	0.035	0.024	0.032
Y/Ho	17.241	16.573	27.872	21.054	22.517	24.779	17.755	11.439	18.773	32.532	16.778
Eu/Eu*	2.249	3.499	6.131	3.598	5.728	2.175	2.705	4.440	2.276	3.456	2.568
La/La*	0.083	0.270	0.468	0.499	0.460	0.222	0.089	0.027	1.106	1.012	0.709
Y/Y*	0.658	0.705	1.126	0.833	0.892	0.903	0.685	0.537	0.774	1.123	0.698
Ce/Ce*	0.314	0.519	0.602	0.668	0.737	0.466	0.472	0.152	0.960	1.019	0.896
Gd/Gd*	0.673	0.558	0.917	0.891	0.756	0.906	0.721	0.475	1.077	1.041	0.721
Pr/Sm	0.689	1.150	0.532	0.652	0.662	0.790	0.610	0.961	0.476	0.612	0.872
Nd/Yb	0.061	0.215	0.305	0.244	0.269	0.184	0.064	0.095	0.752	0.235	0.729

Table 3.2: Abundances of elements and REE+Y for samples from F-Zone in the Meliadine gold district

Samples	MEL013	MEL014	MEL015	MEL016	MEL017	MEL018	MEL019	MEL020	MEL021
Si (ppm)	402400	418400	387500	426200	449000	347900	373100	383800	393000
Li (ppm)	0.250	0.154	0.271	0.131	0.122	0.139	0.178	0.475	0.295
Be (ppm)	0.045	0.018	0.068	0.058	0.018	0.040	0.018	0.018	0.052
Sc (ppm)	8.849	8.554	8.112	8.366	7.716	8.093	8.414	7.729	7.536
Ti (ppm)	5.620	5.330	6.580	4.990	4.731	6.550	4.563	6.740	5.780
V (ppm)	0.327	0.160	0.591	0.227	0.097	0.265	0.119	0.618	0.368
Cr (ppm)	5.350	3.740	5.830	3.700	3.960	13.100	4.110	22.100	5.460
Mn (ppm)	370	365	569	622	8.110	752	557	1990	1000
Fe (ppm)	1770	2560	7940	2980	84	10690	1440	5040	3320
Co (ppm)	0.286	0.206	0.764	0.148	0.153	0.351	0.135	0.266	0.183
Ni (ppm)	4.730	5.240	3.390	3.930	5.230	5.640	4.320	5.400	5.120
Cu (ppm)	9.820	11.100	7.290	6.310	9.140	23.600	6.900	8.330	8.150
Zn (ppm)	44.200	60.500	104.000	32.800	31.900	42.900	21.900	60.600	33.700
Ga (ppm)	0.178	0.175	0.356	0.187	0.260	0.158	0.136	0.381	0.539
As (ppm)	54.100	46.100	34.500	29.200	34.500	20.200	20.400	27.200	21.400
Rb (ppm)	0.063	0.056	0.065	0.059	0.041	0.037	0.035	0.064	0.305
Sr (ppm)	11.500	0.750	6.500	6.360	1.480	15.300	8.500	30.600	16.200
Y (ppm)	0.850	0.175	1.700	0.724	0.102	1.181	0.482	2.570	0.577
Zr (ppm)	2.140	0.549	0.175	0.373	0.027	4.930	0.213	0.416	0.436
Nb (ppm)	0.031	0.024	0.041	0.032	0.026	0.035	0.024	0.035	0.028
Mo (ppm)	0.253	0.274	0.232	0.181	0.211	0.277	0.340	0.219	0.229
Ag (ppm)	0.640	0.470	0.380	0.450	0.360	0.150	0.292	0.390	0.300
Cd (ppm)	1.794	1.390	0.928	1.512	1.065	0.776	1.146	1.222	1.080
In (ppm)	0.067	0.062	0.093	0.063	0.048	0.067	0.050	0.057	0.063
Sn (ppm)	0.189	0.368	0.618	0.178	0.297	0.196	0.112	0.257	0.370
Sb (ppm)	0.658	0.398	0.280	0.463	0.519	0.514	0.333	0.622	0.276
Cs (ppm)	0.041	0.034	0.020	0.041	0.040	0.025	0.032	0.026	0.040
Ba (ppm)	0.334	0.355	0.234	0.155	0.970	0.172	0.141	0.630	3.880
La (ppm)	0.365	0.037	2.800	0.106	0.295	0.323	0.181	0.337	0.112
Ce (ppm)	0.828	0.108	4.800	0.338	0.920	0.672	0.388	0.752	0.264
Pr (ppm)	0.112	0.015	0.670	0.048	0.133	0.099	0.055	0.087	0.033
Nd (ppm)	0.483	0.052	2.000	0.208	0.610	0.461	0.230	0.402	0.142
Sm (ppm)	0.134	0.018	0.590	0.084	0.080	0.115	0.054	0.141	0.048
Eu (ppm)	0.102	0.020	0.260	0.102	0.041	0.118	0.061	0.188	0.109
Gd (ppm)	0.165	0.024	0.530	0.123	0.051	0.145	0.065	0.235	0.071
Tb (ppm)	0.026	0.004	0.066	0.019	0.005	0.024	0.011	0.042	0.012
Dy (ppm)	0.148	0.021	0.326	0.114	0.017	0.144	0.067	0.316	0.073
Ho (ppm)	0.030	0.006	0.060	0.024	0.004	0.033	0.016	0.075	0.017
Er (ppm)	0.088	0.015	0.171	0.067	0.005	0.094	0.043	0.226	0.050
Tm (ppm)	0.016	0.004	0.023	0.011	0.002	0.015	0.007	0.035	0.009
Yb (ppm)	0.076	0.019	0.154	0.056	0.008	0.095	0.035	0.226	0.049
Lu (ppm)	0.013	0.004	0.023	0.010	0.002	0.016	0.009	0.039	0.010
Hf (ppm)	0.021	0.013	0.006	0.006	0.006	0.071	0.006	0.006	0.010
Ta (ppm)	0.005	0.003	0.006	0.004	0.005	0.005	0.004	0.004	0.004
W (ppm)	0.540	0.550	0.183	0.212	0.550	0.840	0.116	0.390	0.250
Au (ppm)	2.400	3.700	3.800	0.580	2.200	0.440	0.380	3.400	0.500
Tl (ppm)	0.113	0.094	0.055	0.108	0.074	0.079	0.074	0.060	0.082
Pb (ppm)	3.000	1.610	2.310	2.120	2.480	2.690	1.251	4.840	2.530
Th (ppm)	0.020	0.011	0.011	0.004	0.138	0.019	0.004	0.004	0.007
U (ppm)	0.046	0.030	0.023	0.055	0.034	0.048	0.029	0.049	0.032
Y/Ho	28.716	30.919	28.333	30.042	25.248	36.339	30.315	34.358	33.353
Eu/Eu*	3.000	3.946	2.117	4.535	2.809	3.971	4.361	4.585	8.136
La/La*	1.056	0.482	0.649	0.741	0.813	1.233	1.003	1.431	1.100
Y/Y*	1.052	1.195	1.063	1.145	1.331	1.350	1.174	1.251	1.241
Ce/Ce*	0.981	0.738	0.658	0.954	0.976	0.972	0.907	1.223	1.065
Gd/Gd*	1.052	0.968	1.123	1.128	1.085	1.042	0.995	1.083	1.060
Pr/Sm	0.648	0.649	0.881	0.440	1.290	0.668	0.790	0.480	0.530
Nd/Yb	0.588	0.246	1.194	0.340	7.210	0.446	0.611	0.164	0.264

Table 3.3: Abundances of elements and REE+Y for samples from Discovery in the Meliadine gold district

Samples	MEL022	MEL023	MEL024	MEL025	MEL027	MEL028	MEL029	MEL031	MEL032	MEL033	MEL034	MEL035	MEL036	MEL038	MEL039	MEL040
Si (ppm)	288500	454000	358400	374700	337500	363000	327200	472800	431200	458300	375400	426300	409400	444700	369200	409100
Li (ppm)	0.135	0.129	0.194	0.180	0.163	0.170	10.370	1.399	0.340	0.159	0.136	0.211	0.356	1.260	1.780	1.970
Be (ppm)	0.066	0.018	0.018	0.018	0.018	0.018	0.018	0.047	0.065	0.018	0.018	0.033	0.030	0.031	0.076	0.038
Sc (ppm)	6.008	8.897	7.210	7.512	7.985	6.503	6.145	10.760	7.231	5.832	4.148	4.744	4.581	5.093	10.990	9.191
Ti (ppm)	20.030	5.330	4.630	6.100	19.600	4.140	44.600	9.000	15.630	4.080	5.560	3.710	4.500	4.790	24.700	8.160
V (ppm)	0.908	0.074	0.109	0.129	4.180	0.094	4.640	0.199	1.010	0.137	0.230	0.310	0.247	0.190	1.488	0.216
Cr (ppm)	7.670	9.300	14.900	8.330	6.410	4.060	5.450	27.600	7.850	4.980	4.940	6.120	8.010	4.410	5.430	7.100
Mn (ppm)	117.800	22.700	102.700	4.450	40.800	21.100	129	378.000	81.100	25.600	21.800	450	270	15.800	92.000	46.500
Fe (ppm)	21210	1360	4270	2420	1030	1770	7280	9540	14200	3620	16500	5140	11520	640	10200	4200
Co (ppm)	0.207	0.125	0.111	0.086	0.456	0.071	2.540	0.410	0.288	0.250	0.226	0.307	0.345	0.399	0.260	0.187
Ni (ppm)	2.550	3.740	2.590	3.370	5.720	2.450	12.450	5.900	4.370	4.770	3.800	5.300	3.410	4.620	4.790	4.810
Cu (ppm)	3.250	7.900	5.460	6.770	13.600	4.280	4.120	22.000	15.200	15.300	11.100	10.400	9.200	9.110	19.300	11.600
Zn (ppm)	17.800	43.000	16.100	13.400	27.600	10.210	37.100	88.000	53.000	46.000	49.000	70.000	64.000	64.000	111.000	50.400
Ga (ppm)	0.656	0.397	0.288	0.391	2.420	0.203	6.770	1.710	0.476	0.613	0.486	0.264	0.299	1.320	1.200	7.040
As (ppm)	10.500	12.000	10.080	13.400	17.400	9.720	6.070	168.200	127.800	104.700	86.000	161.000	98.000	134.000	55.900	37.700
Rb (ppm)	0.057	0.195	0.177	0.216	2.250	0.141	3.210	1.820	0.513	0.084	0.151	0.160	0.162	1.170	4.220	4.940
Sr (ppm)	0.838	0.307	92.500	3.130	11.400	5.150	0.800	177.000	15.800	64.000	30.500	71.000	72.000	5.800	66.600	9.640
Y (ppm)	0.500	0.211	2.260	0.148	0.340	0.697	0.035	5.040	1.027	0.255	0.508	2.520	2.520	0.288	0.900	0.800
Zr (ppm)	0.294	0.120	0.145	0.910	0.164	0.110	0.168	0.148	0.500	0.168	0.215	0.162	0.274	0.075	1.140	0.242
Nb (ppm)	0.476	0.078	0.038	0.031	0.047	0.013	0.099	0.099	0.077	0.036	0.054	0.072	0.051	0.085	0.191	0.026
Mo (ppm)	0.118	0.167	0.072	0.161	0.190	0.350	0.062	2.500	0.445	0.910	0.211	1.050	0.266	0.460	0.860	0.355
Ag (ppm)	0.096	0.193	0.082	0.118	0.105	0.099	0.121	4.400	0.930	1.730	0.660	1.180	0.650	1.320	1.050	0.450
Cd (ppm)	0.415	0.662	0.714	0.591	0.566	0.792	0.352	2.900	1.700	1.508	1.081	3.110	1.650	2.910	1.659	1.059
In (ppm)	0.024	0.032	0.030	0.026	0.025	0.030	0.022	0.120	0.068	0.068	0.072	0.177	0.094	0.185	0.103	0.055
Sn (ppm)	0.106	0.115	0.101	0.107	0.147	0.082	0.156	0.389	0.247	0.268	0.134	0.309	0.246	0.329	0.241	0.152
Sb (ppm)	0.321	0.137	0.109	0.200	0.136	0.245	0.112	0.703	0.456	0.365	0.257	0.687	0.419	0.700	0.424	0.306
Cs (ppm)	0.034	0.049	0.046	0.089	0.092	0.083	0.093	0.458	0.180	0.046	0.071	0.136	0.108	0.279	0.575	3.530
Ba (ppm)	1.830	2.050	2.320	1.840	19.500	0.331	41.300	17.700	0.425	3.010	0.249	0.417	1.270	10.600	10.400	90.300
La (ppm)	0.153	0.533	0.223	1.460	0.405	0.249	0.108	0.405	0.301	0.109	0.535	0.609	0.581	0.139	0.166	0.343
Ce (ppm)	0.287	0.890	0.441	2.900	1.230	0.544	0.203	1.049	0.753	0.242	1.150	1.370	1.330	0.346	0.494	0.751
Pr (ppm)	0.036	0.077	0.056	0.270	0.083	0.069	0.017	0.163	0.101	0.032	0.121	0.198	0.169	0.053	0.076	0.084
Nd (ppm)	0.150	0.249	0.259	0.930	0.366	0.396	0.064	0.886	0.443	0.111	0.445	0.830	0.817	0.169	0.382	0.348
Sm (ppm)	0.039	0.042	0.086	0.008	0.094	0.107	0.012	0.354	0.142	0.032	0.076	0.244	0.219	0.059	0.154	0.070
Eu (ppm)	0.019	0.010	0.032	0.030	0.104	0.053	0.014	0.066	0.024	0.034	0.077	0.173	0.159	0.036	0.089	0.029
Gd (ppm)	0.050	0.036	0.163	0.105	0.090	0.140	0.011	0.514	0.152	0.033	0.077	0.295	0.292	0.068	0.184	0.077
Tb (ppm)	0.009	0.006	0.030	0.010	0.016	0.019	0.001	0.090	0.025	0.008	0.012	0.052	0.045	0.016	0.030	0.012
Dy (ppm)	0.064	0.032	0.244	0.046	0.072	0.116	0.010	0.681	0.149	0.037	0.069	0.349	0.295	0.062	0.164	0.080
Ho (ppm)	0.016	0.009	0.060	0.008	0.014	0.022	0.002	0.161	0.031	0.010	0.017	0.081	0.069	0.016	0.033	0.024
Er (ppm)	0.053	0.029	0.206	0.013	0.033	0.057	0.005	0.557	0.086	0.024	0.050	0.265	0.227	0.028	0.088	0.074
Tm (ppm)	0.009	0.005	0.032	0.003	0.005	0.009	0.001	0.101	0.015	0.006	0.009	0.045	0.037	0.010	0.014	0.012
Yb (ppm)	0.054	0.034	0.208	0.008	0.028	0.049	0.008	0.723	0.096	0.029	0.047	0.273	0.270	0.027	0.080	0.070
Lu (ppm)	0.009	0.006	0.038	0.002	0.006	0.009	0.002	0.127	0.018	0.007	0.010	0.047	0.052	0.010	0.014	0.015
Hf (ppm)	0.006	0.006	0.006	0.021	0.006	0.006	0.010	0.006	0.006	0.006	0.009	0.010	0.006	0.009	0.023	0.006
Ta (ppm)	0.011	0.004	0.002	0.004	0.005	0.002	0.010	0.010	0.007	0.006	0.007	0.014	0.008	0.016	0.015	0.007
W (ppm)	0.198	0.200	0.079	0.055	0.180	0.136	0.113	0.190	0.105	0.128	0.174	0.238	0.158	0.190	3.700	0.910
Au (ppm)	1.400	0.300	0.310	0.064	0.099	0.070	0.038	29.500	23.800	19.900	14.800	23.000	19.100	19.600	2.800	3.200
Tl (ppm)	0.036	0.059	0.049	0.052	0.053	0.069	0.048	0.173	0.099	0.087	0.072	0.191	0.128	0.233	0.171	0.118
Pb (ppm)	0.888	1.098	1.090	0.838	1.060	0.790	4.200	6.480	2.280	3.720	1.570	3.730	2.200	4.400	2.970	1.296
Th (ppm)	0.026	0.042	0.005	0.222	0.009	0.007	0.007	0.021	0.025	0.018	0.008	0.078	0.013	0.011	0.039	0.013
U (ppm)	0.065	0.036	0.015	0.033	0.011	0.014	0.011	0.047	0.049	0.057	0.062	0.115	0.071	0.098	0.067	0.034
Y/Ho	31.427	24.535	37.479	19.733	23.611	31.539	23.000	31.304	33.453	25.000	29.195	31.111	36.469	18.228	27.439	33.898
Eu/Eu*	1.775	1.048	1.219	7.460	4.553	2.001	5.109	1.543	1.891	2.760	1.853	2.731	2.836	2.127	2.274	1.690
La/La*	1.341	1.261	1.476	1.118	1.653	2.098	1.463	1.279	1.014	0.688	1.042	0.942	1.400	0.470	0.962	1.239
Y/Y*	1.091	0.849	1.278	0.913	0.986	1.239	0.799	1.060	1.267	1.035	1.093	1.086	1.270	0.847	1.061	1.215
Ce/Ce*	1.051	1.150	1.116	1.138	2.010	1.404	1.320	1.076	1.016	0.787	1.075	0.892	1.170	0.645	1.005	1.150
Gd/Gd*	0.969	0.851	1.109	3.113	0.894	1.181	1.027	1.048	0.988	0.772	0.986	0.980	1.113	0.772	1.015	1.007
Pr/Sm	0.703	1.426	0.509	24.686	0.685	0.498	1.125	0.357	0.549	0.776	1.232	0.630	0.599	0.694	0.383	0.925
Nd/Yb	0.257	0.669	0.115	10.992	1.185	0.737	0.757	0.113	0.424	0.352	0.870	0.280	0.278	0.586	0.439	0.455

Table 3.4: Abundances of elements and REE+Y for samples from the 4B and 4E facies in the Musselwhite area

	4B								4E	
Samples	E599655	E599656	E599661	E599668	E599669	E599670	E599671	E599672	E599651	E599652
Si (ppm)	4170	436900	379900	170300	122700	314200	196400	342100	430300	443600
Li (ppm)	0.068	1.084	1.052	0.158	0.379	0.199	1.853	0.249	0.569	1.259
Be (ppm)	0.061	0.061	0.293	0.301	0.061	0.061	0.107	0.061	0.061	0.000
Sc (ppm)	0.489	3.757	3.382	1.514	1.124	2.584	1.627	2.950	4.745	4.295
Ti (ppm)	11.600	3.250	55.300	1.850	17.200	2.011	1.356	4.660	11.000	15.400
V (ppm)	1.330	0.240	5.300	0.176	1.490	0.146	0.054	0.229	0.860	0.940
Cr (ppm)	11.570	3.760	2.290	12.850	22.390	4.540	5.630	2.000	6.260	3.150
Mn (ppm)	3355	16	1308	3470	2090	467.400	628.100	159.000	129	39
Fe (ppm)	6330	216	19600	10180	45500	22480	38270	4920	3170	1000
Co (ppm)	0.340	0.514	4.490	0.441	0.769	0.587	1.126	0.193	2.060	2.330
Ni (ppm)	1.800	21.000	7.700	4.100	5.000	3.100	1.290	5.900	47.800	26.800
Cu (ppm)	3.870	81.000	33.300	12.300	10.200	7.300	3.730	28.700	106.000	328.000
Zn (ppm)	10.100	131.000	63.100	21.300	28.700	22.200	18.700	50.600	189.000	72.000
Ga (ppm)	0.186	0.252	0.924	0.644	0.627	0.136	0.056	0.161	0.387	0.148
As (ppm)	0.233	3.590	1.570	0.625	1.480	0.352	0.301	0.838	5.600	1.850
Rb (ppm)	0.028	0.124	5.820	0.055	0.584	0.024	0.039	0.085	0.089	0.140
Sr (ppm)	848.800	1.570	8.160	150.800	2.270	0.196	0.191	4.200	13.200	1.380
Y (ppm)	19.500	0.070	1.800	21.500	1.066	0.112	0.565	0.552	0.984	0.180
Zr (ppm)	0.104	0.202	0.323	0.086	0.339	0.065	0.103	0.059	0.620	0.477
Nb (ppm)	0.018	0.042	0.179	0.033	0.074	0.021	0.027	0.039	0.075	0.023
Mo (ppm)	0.016	1.280	0.165	0.096	0.072	0.058	0.038	0.134	0.460	0.950
Ag (ppm)	0.012	0.321	0.105	0.067	0.070	0.028	0.018	0.128	0.457	0.414
Cd (ppm)	0.499	2.330	0.925	1.123	0.374	0.245	0.220	1.470	3.120	0.871
In (ppm)	0.009	0.198	0.098	0.053	0.033	0.027	0.023	0.087	0.202	0.059
Sn (ppm)	0.140	0.476	0.262	0.143	0.281	0.196	0.078	0.200	0.486	0.435
Sb (ppm)	0.099	1.550	0.594	0.244	0.297	0.386	0.591	0.980	1.681	0.503
Cs (ppm)	0.002	0.057	1.042	0.039	0.254	0.013	0.019	0.046	0.038	0.016
Ba (ppm)	2.354	0.523	5.900	7.440	1.770	0.204	0.230	0.196	0.529	0.444
La (ppm)	0.190	0.106	1.650	0.792	0.506	0.156	0.082	0.383	1.020	0.087
Ce (ppm)	0.510	0.207	2.970	2.228	1.650	0.339	0.280	0.460	1.610	0.179
Pr (ppm)	0.095	0.033	0.302	0.402	0.141	0.034	0.047	0.054	0.153	0.025
Nd (ppm)	0.782	0.069	1.190	2.554	0.767	0.121	0.240	0.209	0.576	0.083
Sm (ppm)	0.591	0.020	0.249	0.861	0.183	0.018	0.077	0.042	0.118	0.018
Eu (ppm)	0.689	0.023	0.154	0.711	0.114	0.013	0.053	0.035	0.073	0.014
Gd (ppm)	1.451	0.018	0.266	1.285	0.175	0.018	0.097	0.058	0.147	0.027
Tb (ppm)	0.251	0.007	0.040	0.220	0.026	0.004	0.015	0.011	0.023	0.006
Dy (ppm)	1.881	0.016	0.255	1.870	0.169	0.019	0.099	0.048	0.122	0.030
Ho (ppm)	0.443	0.007	0.055	0.517	0.035	0.005	0.022	0.015	0.030	0.007
Er (ppm)	1.467	0.009	0.171	2.060	0.110	0.013	0.067	0.038	0.086	0.019
Tm (ppm)	0.221	0.006	0.028	0.394	0.019	0.003	0.013	0.008	0.015	0.003
Yb (ppm)	1.621	0.011	0.166	3.470	0.130	0.021	0.102	0.031	0.076	0.020
Lu (ppm)	0.260	0.005	0.028	0.685	0.023	0.006	0.022	0.009	0.013	0.004
Hf (ppm)	0.008	0.008	0.011	0.008	0.008	0.008	0.008	0.008	0.019	0.008
Ta (ppm)	0.003	0.009	0.013	0.005	0.003	0.003	0.003	0.008	0.008	0.004
W (ppm)	0.060	0.387	0.339	0.178	0.582	0.079	0.078	2.187	1.030	0.630
Au (ppm)	0.004	0.076	0.030	0.011	0.011	0.011	0.011	0.025	0.082	0.035
Tl (ppm)	0.011	0.226	0.125	0.053	0.036	0.020	0.017	0.096	0.291	0.121
Pb (ppm)	7.290	12.500	4.820	14.800	1.680	1.590	0.725	3.340	18.450	6.280
Th (ppm)	0.004	0.008	0.038	0.008	0.035	0.004	0.006	0.007	0.007	0.008
U (ppm)	0.005	0.054	0.076	0.035	0.031	0.014	0.010	0.053	0.042	0.023
Y/Ho	44.008	9.790	32.550	41.586	30.284	22.126	25.450	37.808	32.800	25.714
Eu/Eu*	3.608	3.705	2.622	3.031	2.751	2.599	2.651	2.975	2.426	2.595
La/La*	2.358	0.242	1.482	1.384	1.868	0.990	0.800	1.836	1.660	0.710
Y/Y*	1.526	0.512	1.173	1.299	1.084	0.874	0.932	1.493	1.225	0.983
Ce/Ce*	1.358	0.401	1.194	1.084	1.965	1.076	0.940	1.007	1.221	0.761
Gd/Gd*	1.274	0.521	1.047	1.085	1.022	0.724	1.047	0.981	1.061	0.920
Pr/Sm	0.125	1.297	0.941	0.362	0.597	1.442	0.470	1.013	1.006	1.075
Nd/Yb	0.044	0.561	0.660	0.068	0.542	0.521	0.217	0.618	0.697	0.385

Table 3.5: Abundances of elements and REE+Y for selected samples from the 4EA and 4F facies
in the Musselwhite area

	4EA						4F		
Samples	E599654	E599659	E599660	E599665	E599666	E599667	E599657	E599658	E599664
Si (ppm)	362400	381200	328600	395600	364100	1760	418000	423500	450200
Li (ppm)	1.477	0.277	1.361	0.920	0.132	0.098	4.290	3.390	1.189
Be (ppm)	0.061	0.061	0.104	0.061	0.061	0.061	0.061	0.061	0.061
Sc (ppm)	3.257	2.519	2.258	2.765	2.677	0.340	3.499	3.542	3.251
Ti (ppm)	9.370	3.150	17.100	5.460	3.470	4.000	43.000	185.000	15.200
V (ppm)	0.920	0.178	1.660	0.220	0.323	0.233	5.530	11.300	2.770
Cr (ppm)	2.920	2.810	4.020	2.750	2.380	11.140	2.770	6.200	2.840
Mn (ppm)	31.400	8.900	105.000	11.100	23.900	6890	59.600	7.400	30.500
Fe (ppm)	1920	173	4250	710	1380	9654	1840	3030	1020
Co (ppm)	1.330	0.265	0.930	0.440	0.407	0.346	1.630	4.300	1.730
Ni (ppm)	19.800	9.800	16.100	11.200	7.700	3.550	13.700	46.000	15.300
Cu (ppm)	115.000	95.000	42.400	46.500	34.900	12.500	55.000	82.000	45.800
Zn (ppm)	280.000	141.000	82.000	94.300	87.000	17.400	125.000	59.000	83.800
Ga (ppm)	0.404	0.590	0.664	0.144	0.233	0.791	0.763	1.610	1.036
As (ppm)	3.160	1.320	3.220	1.301	1.170	1.260	1.205	1.190	1.740
Rb (ppm)	0.080	0.049	3.070	0.141	0.122	0.059	3.140	8.100	1.410
Sr (ppm)	2.700	12.200	1.620	0.374	1.030	783.400	1.600	1.380	0.730
Y (ppm)	0.259	0.212	0.340	0.020	0.095	16.650	0.154	0.097	0.173
Zr (ppm)	0.123	0.084	0.166	0.111	0.164	0.070	0.164	0.156	0.142
Nb (ppm)	0.027	0.019	0.185	0.049	0.038	0.016	0.084	0.275	0.114
Mo (ppm)	0.320	0.249	0.445	0.224	0.190	0.560	0.210	0.330	3.900
Ag (ppm)	0.255	0.127	0.374	0.154	0.144	0.117	0.182	1.000	0.187
Cd (ppm)	2.170	0.864	2.780	1.263	1.095	0.880	0.993	0.900	1.333
In (ppm)	0.126	0.081	0.375	0.122	0.098	0.074	0.084	0.063	0.162
Sn (ppm)	0.490	0.389	0.645	0.318	0.273	0.308	0.665	0.990	0.422
Sb (ppm)	0.833	0.442	1.318	0.571	0.703	0.570	0.775	0.880	1.260
Cs (ppm)	0.026	0.020	1.228	0.083	0.066	0.022	0.118	0.234	0.144
Ba (ppm)	0.553	8.600	5.680	0.462	1.190	15.070	2.160	13.600	2.030
La (ppm)	0.550	0.497	0.199	0.045	0.025	7.800	0.163	0.151	0.126
Ce (ppm)	0.830	1.030	0.456	0.128	0.121	8.900	0.368	0.710	0.360
Pr (ppm)	0.086	0.078	0.083	0.022	0.015	1.023	0.041	0.111	0.063
Nd (ppm)	0.366	0.288	0.163	0.024	0.031	4.883	0.144	0.710	0.268
Sm (ppm)	0.064	0.049	0.047	0.009	0.012	1.048	0.038	0.470	0.150
Eu (ppm)	0.033	0.035	0.047	0.011	0.010	1.025	0.020	0.076	0.051
Gd (ppm)	0.054	0.041	0.054	0.007	0.018	1.428	0.045	0.350	0.124
Tb (ppm)	0.008	0.006	0.019	0.004	0.004	0.199	0.009	0.019	0.015
Dy (ppm)	0.040	0.029	0.053	0.009	0.014	1.373	0.032	0.040	0.050
Ho (ppm)	0.008	0.007	0.021	0.005	0.006	0.298	0.008	0.004	0.011
Er (ppm)	0.020	0.018	0.039	0.006	0.012	0.869	0.020	0.008	0.017
Tm (ppm)	0.003	0.004	0.018	0.005	0.005	0.110	0.003	0.003	0.006
Yb (ppm)	0.011	0.011	0.038	0.011	0.018	0.666	0.011	0.011	0.011
Lu (ppm)	0.003	0.003	0.014	0.004	0.005	0.108	0.003	0.002	0.005
Hf (ppm)	0.008	0.008	0.015	0.008	0.008	0.008	0.008	0.008	0.008
Ta (ppm)	0.004	0.004	0.027	0.010	0.008	0.003	0.008	0.020	0.014
W (ppm)	0.510	0.360	0.584	0.304	0.238	0.234	0.300	0.470	0.374
Au (ppm)	0.108	0.061	0.062	0.042	0.035	0.011	0.035	2.700	0.034
Tl (ppm)	0.206	0.090	0.328	0.125	0.093	0.029	0.105	0.104	0.135
Pb (ppm)	8.760	5.600	11.100	4.040	3.380	21.000	5.720	14.300	6.810
Th (ppm)	0.004	0.004	0.022	0.007	0.005	0.004	0.006	0.007	0.014
U (ppm)	0.034	0.025	0.211	0.053	0.046	0.017	0.024	0.065	0.093
Y/Ho	31.205	29.859	15.962	4.113	16.522	55.910	20.424	22.558	15.175
Eu/Eu*	2.341	3.191	3.106	3.488	2.546	3.971	1.944	1.085	1.669
La/La*	2.035	1.510	0.161	0.040	0.120	3.025	0.842	0.962	0.631
Y/Y*	1.264	1.199	0.730	0.216	0.712	2.073	0.790	1.002	0.753
Ce/Ce*	1.269	1.505	0.332	0.189	0.510	1.277	0.960	1.252	0.748
Gd/Gd*	0.986	0.945	0.606	0.364	0.835	1.209	0.904	1.822	1.094
Pr/Sm	1.042	1.240	1.385	2.026	0.954	0.757	0.832	0.183	0.325
Nd/Yb	2.982	2.340	0.397	0.192	0.158	0.674	1.170	5.757	2.178

Table 3.6: Abundances of elements and REE+Y for samples from the a-type facies in the Beardmore-Geraldton gold district

	a-type BIF									
Samples	BG001-C	BG001-J	BG002-C	BG002-J	BG009B-J	BG009C-J	BG010A-J	BG010B-J	BG010D-J	BG015-J
Si (ppm)	302700	243700	259200	122300	122900	162500	130000	210600	293800	258600
Li (ppm)	19.800	0.172	1.101	0.712	0.132	7.960	0.828	1.270	1.700	1.430
Be (ppm)	0.424	0.145	0.158	0.119	0.115	1.674	0.358	0.580	0.255	0.078
Sc (ppm)	6.480	5.435	5.200	2.855	2.395	5.790	2.455	4.116	6.750	5.011
Ti (ppm)	11.400	10.020	18.180	39.770	47.270	197.600	57.830	70.300	16.770	23.600
V (ppm)	1.480	3.705	1.253	3.507	4.332	3.429	3.562	2.004	1.842	1.735
Cr (ppm)	4.700	1.470	1.560	2.417	2.714	49.800	3.839	6.060	3.250	1.990
Mn (ppm)	98	80	54.200	5.730	13.500	57.700	7.750	227	61	69.500
Fe (ppm)	19500	67420	38500	83970	72620	38900	64200	62390	47200	65200
Co (ppm)	2.030	0.665	0.284	0.070	0.132	0.784	0.234	0.623	0.540	0.231
Ni (ppm)	9.400	2.610	3.030	1.030	1.360	6.800	1.530	2.910	4.580	3.790
Cu (ppm)	86.000	27.700	51.000	2.150	15.100	6.700	14.700	10.800	65.000	32.000
Zn (ppm)	72.000	18.200	35.600	3.390	6.120	6.660	7.400	10.010	47.500	16.900
Ga (ppm)	14.400	3.040	3.400	0.716	3.150	54.700	11.460	17.360	2.268	0.577
As (ppm)	37.900	21.900	28.400	6.800	10.170	10.390	5.470	11.560	33.300	14.300
Rb (ppm)	9.900	4.000	6.130	0.112	2.253	56.100	9.350	6.030	7.830	0.085
Sr (ppm)	6.910	2.850	2.220	2.730	1.927	30.000	3.740	26.300	3.700	17.100
Y (ppm)	0.313	0.854	0.606	1.140	0.601	3.810	0.517	2.070	0.660	1.990
Zr (ppm)	0.312	0.533	0.430	1.321	1.378	29.600	2.280	2.220	0.660	0.662
Nb (ppm)	0.053	0.065	0.135	0.096	0.122	0.151	0.151	0.072	0.080	0.086
Mo (ppm)	0.232	0.778	0.441	0.089	0.318	11.850	0.129	0.216	0.279	0.422
Ag (ppm)	0.215	0.066	0.094	0.010	0.024	0.032	0.016	0.027	0.231	0.041
Cd (ppm)	0.750	0.252	0.463	0.036	0.045	0.067	0.024	0.333	0.485	0.221
In (ppm)	0.030	0.015	0.015	0.003	0.006	0.016	0.005	0.006	0.029	0.017
Sn (ppm)	0.790	0.427	0.410	0.135	0.194	0.500	0.114	0.170	0.850	0.324
Sb (ppm)	6.430	13.670	7.340	8.120	10.530	10.530	7.680	13.740	11.750	5.140
Cs (ppm)	0.619	0.236	0.517	0.037	0.123	3.550	0.683	0.360	0.416	0.089
Ba (ppm)	183.000	39.900	44.000	3.000	34.230	539.000	145.000	248.500	30.800	3.600
La (ppm)	0.241	2.200	1.200	2.540	0.178	0.880	0.209	0.670	0.490	1.490
Ce (ppm)	0.405	2.560	1.380	2.520	0.349	1.840	0.450	1.420	0.800	2.530
Pr (ppm)	0.055	0.261	0.124	0.253	0.047	0.229	0.058	0.159	0.092	0.304
Nd (ppm)	0.185	1.030	0.470	1.210	0.245	1.160	0.258	0.675	0.351	1.350
Sm (ppm)	0.045	0.182	0.089	0.226	0.072	0.365	0.069	0.166	0.070	0.295
Eu (ppm)	0.051	0.080	0.052	0.108	0.033	0.176	0.035	0.103	0.036	0.126
Gd (ppm)	0.055	0.182	0.111	0.251	0.091	0.481	0.090	0.210	0.080	0.341
Tb (ppm)	0.009	0.020	0.015	0.030	0.014	0.071	0.013	0.032	0.012	0.043
Dy (ppm)	0.048	0.120	0.078	0.169	0.083	0.488	0.079	0.235	0.083	0.256
Ho (ppm)	0.011	0.025	0.017	0.032	0.018	0.108	0.017	0.054	0.020	0.051
Er (ppm)	0.028	0.066	0.046	0.084	0.050	0.350	0.050	0.174	0.061	0.146
Tm (ppm)	0.005	0.011	0.007	0.011	0.008	0.059	0.009	0.028	0.010	0.021
Yb (ppm)	0.028	0.067	0.045	0.069	0.045	0.455	0.063	0.196	0.072	0.130
Lu (ppm)	0.007	0.012	0.008	0.011	0.008	0.080	0.011	0.033	0.013	0.025
Hf (ppm)	0.010	0.011	0.013	0.036	0.038	0.760	0.056	0.051	0.019	0.018
Ta (ppm)	0.011	0.003	0.006	0.006	0.008	0.028	0.012	0.008	0.006	0.004
W (ppm)	5.210	15.700	19.200	18.400	29.100	9.160	24.600	8.580	26.700	2.970
Au (ppm)	0.058	0.019	0.028	0.007	0.022	0.012	0.010	0.017	0.067	0.016
Tl (ppm)	0.091	0.032	0.051	0.002	0.012	0.226	0.035	0.025	0.054	0.014
Pb (ppm)	10.800	10.200	9.900	0.490	1.663	10.050	1.010	2.599	7.800	2.390
Th (ppm)	0.013	0.023	0.020	0.113	0.090	0.492	0.101	0.082	0.033	0.034
U (ppm)	0.034	0.070	0.037	0.025	0.030	0.229	0.047	0.051	0.039	0.026
Y/Ho	28.198	34.857	36.287	35.294	34.343	35.245	30.412	38.262	33.673	38.867
Eu/Eu*	4.402	2.117	2.419	2.161	1.817	1.920	1.988	2.461	2.101	1.864
La/La*	0.859	2.287	2.423	4.001	1.782	1.718	1.242	1.323	1.351	1.684
Y/Y*	1.121	1.349	1.383	1.386	1.287	1.237	1.127	1.348	1.207	1.458
Ce/Ce*	0.759	1.191	1.298	1.465	1.186	1.252	1.062	1.166	1.020	1.137
Gd/Gd*	1.018	1.258	1.193	1.242	1.085	1.137	1.109	1.083	1.032	1.201
Pr/Sm	0.954	1.113	1.081	0.868	0.510	0.487	0.652	0.743	1.020	0.799
Nd/Yb	0.601	1.407	0.967	1.622	0.498	0.234	0.379	0.317	0.448	0.955

Table 3.7: Abundances of elements and REE+Y for samples from the b-type facies in the Beardmore-Geraldton gold district

	b-type BIF							
Samples	BG003-J	BG005-C	BG005-J	BG006B-C	BG006B-J	BG008B-J	BG012B-J	BG020-J
Si (ppm)	242300	236700	183200	153300	39800	75200	130700	368500
Li (ppm)	0.153	16.230	0.964	0.611	0.849	1.790	0.938	0.683
Be (ppm)	0.080	0.230	0.203	0.768	0.923	0.253	0.827	0.145
Sc (ppm)	4.147	5.290	3.756	5.510	3.390	2.695	4.953	8.180
Ti (ppm)	22.740	97.300	41.270	25.400	591.000	1072.000	402.000	25.100
V (ppm)	2.596	2.341	4.417	1.360	21.690	31.910	10.220	3.110
Cr (ppm)	1.512	5.920	2.371	3.490	15.500	19.290	16.870	9.900
Mn (ppm)	9	261	19.600	2339	42.400	53.500	73.800	551
Fe (ppm)	51820	42000	54180	36200	118000	94100	117900	9990
Co (ppm)	0.109	1.727	0.176	18.900	2.892	4.016	2.190	1.260
Ni (ppm)	2.130	6.630	1.520	4.550	12.480	16.860	10.700	8.820
Cu (ppm)	7.400	49.000	16.700	94.000	8.170	9.400	13.800	314.000
Zn (ppm)	6.700	38.500	8.400	43.200	13.710	17.700	35.300	78.000
Ga (ppm)	1.835	1.990	7.120	4.700	24.300	3.499	4.360	1.990
As (ppm)	11.320	17.600	11.400	28.000	5.260	5.840	6.110	28.300
Rb (ppm)	2.407	2.500	3.690	6.190	26.100	0.134	8.320	2.920
Sr (ppm)	1.139	4.080	2.310	295.000	10.490	23.880	32.400	94.000
Y (ppm)	0.469	1.300	0.545	5.070	3.260	4.990	4.280	2.710
Zr (ppm)	0.705	3.750	1.020	0.504	11.540	16.070	13.850	0.550
Nb (ppm)	0.068	0.097	0.118	0.134	1.404	2.420	0.805	0.116
Mo (ppm)	0.194	0.239	0.142	0.270	0.215	0.296	0.560	0.313
Ag (ppm)	0.019	0.055	0.029	0.111	0.019	0.017	0.044	0.181
Cd (ppm)	0.075	0.536	0.073	0.359	0.016	0.021	0.071	0.664
In (ppm)	0.006	0.017	0.008	0.024	0.016	0.011	0.055	0.027
Sn (ppm)	0.270	0.650	0.269	0.343	1.090	0.935	1.008	0.396
Sb (ppm)	9.649	11.080	12.810	0.908	1.418	9.270	1.356	2.320
Cs (ppm)	0.153	0.270	0.285	0.279	0.999	0.054	2.194	0.205
Ba (ppm)	20.330	22.600	92.000	72.900	275.000	5.620	39.300	26.500
La (ppm)	0.277	0.830	0.203	2.020	5.800	1.590	1.550	1.520
Ce (ppm)	0.468	0.970	0.455	4.290	10.800	3.150	3.380	4.000
Pr (ppm)	0.052	0.113	0.053	0.501	1.120	0.362	0.434	0.280
Nd (ppm)	0.218	0.509	0.242	2.270	4.700	1.590	2.160	1.350
Sm (ppm)	0.045	0.122	0.061	0.624	0.810	0.453	0.559	0.440
Eu (ppm)	0.017	0.065	0.027	0.418	0.241	0.240	0.263	0.165
Gd (ppm)	0.056	0.155	0.077	0.751	0.680	0.708	0.686	0.580
Tb (ppm)	0.009	0.022	0.011	0.119	0.077	0.117	0.094	0.079
Dy (ppm)	0.055	0.144	0.072	0.787	0.525	0.811	0.645	0.466
Ho (ppm)	0.013	0.033	0.016	0.160	0.096	0.169	0.130	0.098
Er (ppm)	0.041	0.112	0.050	0.457	0.263	0.500	0.391	0.235
Tm (ppm)	0.006	0.021	0.008	0.069	0.036	0.073	0.057	0.035
Yb (ppm)	0.036	0.164	0.056	0.477	0.226	0.479	0.381	0.235
Lu (ppm)	0.006	0.033	0.010	0.078	0.035	0.072	0.062	0.037
Hf (ppm)	0.021	0.095	0.028	0.013	0.306	0.389	0.336	0.015
Ta (ppm)	0.004	0.011	0.008	0.004	0.102	0.140	0.057	0.006
W (ppm)	30.210	16.550	38.000	9.800	4.240	8.350	25.500	0.507
Au (ppm)	0.007	0.023	0.011	0.026	0.006	0.011	0.011	0.059
Tl (ppm)	0.012	0.030	0.020	0.042	0.119	0.002	0.073	0.042
Pb (ppm)	1.394	3.970	2.270	5.200	1.028	1.939	2.890	5.450
Th (ppm)	0.042	0.116	0.093	0.135	1.160	0.591	0.485	0.065
U (ppm)	0.022	0.073	0.062	0.064	0.174	0.210	0.180	0.035
Y/Ho	37.222	39.755	34.494	31.767	33.958	29.527	32.898	27.653
Eu/Eu*	1.504	2.165	1.789	2.699	1.513	1.926	1.972	1.536
La/La*	1.641	2.597	1.384	1.442	1.589	1.476	1.541	2.199
Y/Y*	1.303	1.353	1.223	1.189	1.299	1.087	1.201	1.128
Ce/Ce*	1.165	1.189	1.201	1.193	1.245	1.176	1.192	2.119
Gd/Gd*	1.043	1.158	1.131	1.058	1.172	1.121	1.169	1.202
Pr/Sm	0.905	0.719	0.678	0.623	1.073	0.620	0.602	0.494
Nd/Yb	0.558	0.285	0.397	0.438	1.912	0.305	0.521	0.528

Table 3.8: Abundances of elements and REE+Y for samples from the b-type facies in the Beardmore-Geraldton gold district

	c-type BIF								
Samples	BG004-C	BG004-J	BG014-J	BG016-C	BG016-J	BG017-J	BG018-J	BG019-J	BG022-J
Si (ppm)	257100	147400	42900	366000	375100	194200	115000	103500	117500
Li (ppm)	34.200	5.660	5.910	4.580	1.940	3.720	2.700	0.596	0.359
Be (ppm)	0.273	0.043	0.125	0.089	0.496	0.210	0.387	0.336	0.233
Sc (ppm)	5.890	3.350	4.260	6.738	7.262	4.880	4.510	5.920	3.061
Ti (ppm)	209.500	86.500	581.000	50.300	122.300	525.000	406.000	528.000	216.400
V (ppm)	3.640	4.950	41.620	9.120	6.520	26.870	37.680	75.100	32.080
Cr (ppm)	40.150	5.340	12.400	5.870	7.840	9.710	17.150	14.760	8.290
Mn (ppm)	161	120.500	70.200	46	12.900	23.500	60	267	57.800
Fe (ppm)	18920	75400	149400	15230	30420	72300	144600	138900	165100
Co (ppm)	1.670	1.384	0.660	0.595	0.270	1.103	1.927	3.260	1.004
Ni (ppm)	11.800	5.370	8.480	9.120	5.940	11.410	15.140	12.940	3.990
Cu (ppm)	28.500	29.500	8.000	53.000	41.000	24.300	12.400	22.300	5.900
Zn (ppm)	25.200	15.800	23.700	36.400	18.300	15.670	7.440	43.800	29.500
Ga (ppm)	8.700	1.201	3.191	1.880	15.260	7.890	38.300	8.450	2.399
As (ppm)	21.600	15.200	5.760	20.100	14.870	10.700	5.770	3.880	5.930
Rb (ppm)	3.390	0.575	0.567	0.113	5.080	5.610	22.010	1.265	0.486
Sr (ppm)	23.700	8.140	19.800	13.600	15.910	6.210	11.370	31.460	24.890
Y (ppm)	8.410	4.710	1.502	1.390	2.250	1.610	1.940	5.830	2.960
Zr (ppm)	19.000	3.320	8.350	3.450	7.290	8.990	9.170	8.390	5.960
Nb (ppm)	0.248	0.415	0.748	0.096	0.350	2.050	1.054	1.036	0.665
Mo (ppm)	0.440	0.495	0.154	0.418	0.531	0.180	0.950	1.000	0.680
Ag (ppm)	0.060	0.040	0.014	0.074	0.043	0.032	0.010	0.056	0.013
Cd (ppm)	0.220	0.170	0.031	0.317	0.177	0.122	0.036	0.060	0.026
In (ppm)	0.016	0.013	0.022	0.023	0.012	0.011	0.016	0.024	0.013
Sn (ppm)	0.617	0.933	1.840	0.730	0.600	0.485	1.251	0.941	0.723
Sb (ppm)	4.820	5.320	6.960	3.120	4.684	7.670	8.450	3.079	3.307
Cs (ppm)	0.274	0.085	0.086	0.134	0.339	0.581	1.944	0.296	0.094
Ba (ppm)	170.000	4.630	6.380	12.300	280.500	97.400	498.000	88.400	6.860
La (ppm)	35.000	3.800	4.000	1.850	2.950	1.140	1.140	4.670	2.980
Ce (ppm)	46.300	5.400	7.700	3.580	6.800	2.580	2.200	9.700	5.300
Pr (ppm)	4.300	0.580	0.840	0.376	0.760	0.347	0.260	1.190	0.640
Nd (ppm)	16.100	2.420	3.600	1.880	3.090	1.610	1.050	5.200	3.240
Sm (ppm)	2.250	0.633	0.690	0.377	0.650	0.364	0.314	1.200	0.820
Eu (ppm)	1.380	0.449	0.213	0.131	0.236	0.100	0.089	0.294	0.269
Gd (ppm)	2.080	0.960	0.521	0.403	0.653	0.363	0.387	1.250	0.841
Tb (ppm)	0.236	0.135	0.062	0.044	0.075	0.048	0.056	0.180	0.111
Dy (ppm)	1.249	0.773	0.303	0.243	0.401	0.301	0.361	1.120	0.687
Ho (ppm)	0.223	0.142	0.053	0.039	0.073	0.059	0.072	0.210	0.122
Er (ppm)	0.599	0.369	0.154	0.098	0.186	0.174	0.207	0.545	0.304
Tm (ppm)	0.078	0.048	0.023	0.014	0.026	0.025	0.032	0.069	0.038
Yb (ppm)	0.496	0.284	0.147	0.071	0.154	0.166	0.234	0.410	0.216
Lu (ppm)	0.078	0.041	0.022	0.012	0.025	0.026	0.034	0.056	0.030
Hf (ppm)	0.516	0.078	0.214	0.076	0.184	0.232	0.246	0.201	0.163
Ta (ppm)	0.030	0.018	0.080	0.007	0.021	0.053	0.065	0.067	0.037
W (ppm)	5.670	53.000	6.120	1.920	24.420	0.887	53.000	12.400	8.960
Au (ppm)	0.019	0.019	0.008	0.025	0.023	0.013	0.007	0.015	0.007
Tl (ppm)	0.022	0.010	0.002	0.020	0.034	0.031	0.070	0.007	0.004
Pb (ppm)	3.880	2.200	1.290	3.290	2.230	1.600	1.557	1.589	1.018
Th (ppm)	1.800	0.076	0.363	0.100	0.396	0.407	0.485	0.668	0.464
U (ppm)	0.181	0.083	0.255	0.066	0.146	0.231	0.462	0.905	0.312
Y/Ho	37.713	33.169	28.555	36.010	30.696	27.288	26.833	27.762	24.242
Eu/Eu*	3.050	2.756	1.598	1.641	1.732	1.247	1.157	1.076	1.483
La/La*	1.988	1.987	1.524	2.143	1.118	1.232	1.246	1.306	2.079
Y/Y*	1.457	1.302	1.058	1.430	1.219	1.006	1.004	1.091	0.972
Ce/Ce*	1.240	1.195	1.208	1.464	1.119	1.061	1.051	1.096	1.290
Gd/Gd*	1.222	1.239	1.095	1.297	1.237	1.119	1.120	1.080	1.131
Pr/Sm	1.483	0.711	0.944	0.774	0.907	0.740	0.642	0.769	0.605
Nd/Yb	2.984	0.783	2.247	2.441	1.845	0.892	0.413	1.166	1.379

Table 3.9: Oxygen isotope compositions of microquartz determined by ion microprobe on chert from the Meliadine gold district

Sample	Mineral	$\delta^{18}\text{O}_{\text{V-SMOW}}(\text{‰})$	1σ	Sample	Mineral	$\delta^{18}\text{O}_{\text{V-SMOW}}(\text{‰})$	1σ
MEL-008-1	Chert	13.7	0.5	MEL-016C-6	Chert	16.7	0.4
MEL-008-2	Chert	13.6	0.5	MEL-016C-7	Chert	15.5	0.4
MEL-008-3	Chert	14.0	0.5	MEL-016C-8	Chert	15.7	0.4
MEL-008-4	Chert	6.6	0.5	MEL-016C-9	Chert	14.5	0.4
MEL-008-5	Chert	8.1	0.5	MEL-016C-10	Chert	14.6	0.4
MEL-008-6	Chert	18.1	0.5	MEL-033A-1	Chert	14.0	0.6
MEL-008-7	Chert	16.8	0.5	MEL-033A-2	Chert	13.2	0.6
MEL-008-8	Chert	15.8	0.5	MEL-033A-3	Chert	12.9	0.6
MEL-008-9	Chert	19.1	0.5	MEL-033A-4	Chert	15.5	0.6
MEL-008-10	Chert	15.8	0.5	MEL-033A-5	Chert	15.3	0.6
MEL-016A-1	Chert	12.7	0.6	MEL-033A-6	Chert	16.3	0.6
MEL-016A-2	Chert	14.7	0.6	MEL-033A-7	Chert	15.2	0.6
MEL-016A-3	Chert	11.4	0.6	MEL-033A-8	Chert	11.0	0.6
MEL-016A-4	Chert	12.3	0.6	MEL-033A-9	Chert	15.8	0.6
MEL-016A-5	Chert	11.7	0.6	MEL-033A-10	Chert	16.3	0.6
MEL-016A-6	Chert	14.2	0.6	MEL-033B-1	Chert	13.8	0.6
MEL-016A-7	Chert	11.8	0.6	MEL-033B-2	Chert	15.1	0.6
MEL-016A-8	Chert	13.4	0.6	MEL-033B-3	Chert	14.8	0.6
MEL-016A-9	Chert	12.0	0.6	MEL-033B-4	Chert	12.7	0.6
MEL-016A-10	Chert	11.3	0.6	MEL-033B-5	Chert	10.0	0.6
MEL-016B-1	Chert	9.1	0.4	MEL-033B-6	Chert	10.3	0.6
MEL-016B-2	Chert	7.0	0.4	MEL-033B-7	Chert	15.3	0.6
MEL-016B-3	Chert	8.1	0.4	MEL-033B-8	Chert	13.3	0.6
MEL-016B-4	Chert	9.1	0.4	MEL-033B-9	Chert	13.5	0.6
MEL-016B-5	Chert	8.0	0.4	MEL-033B-10	Chert	14.6	0.6
MEL-016B-6	Chert	8.3	0.4	MEL-033C-1	Chert	13.2	0.5
MEL-016B-7	Chert	9.0	0.4	MEL-033C-2	Chert	15.8	0.5
MEL-016B-8	Chert	9.6	0.4	MEL-033C-3	Chert	14.9	0.5
MEL-016B-9	Chert	9.0	0.4	MEL-033C-4	Chert	14.7	0.5
MEL-016B-10	Chert	7.1	0.4	MEL-033C-5	Chert	16.4	0.5
MEL-016C-1	Chert	16.5	0.4	MEL-033C-6	Chert	14.5	0.5
MEL-016C-2	Chert	17.3	0.4	MEL-033C-7	Chert	13.4	0.5
MEL-016C-3	Chert	14.0	0.4	MEL-033C-8	Chert	12.8	0.5
MEL-016C-4	Chert	15.1	0.4	MEL-033C-9	Chert	12.8	0.5
MEL-016C-5	Chert	16.1	0.4	MEL-033C-10	Chert	13.9	0.5

Table 3.10: Abundances of elements and REE+Y for KMG samples from the Meliadine gold district

Sample	KMG1	KMG2
Si (ppm)	378400	380800
Li (ppm)	2.090	0.377
Be (ppm)	0.146	0.025
Sc (ppm)	3.185	2.390
Ti (ppm)	6.190	4.030
V (ppm)	0.212	0.601
Cr (ppm)	3.340	3.020
Mn (ppm)	19.200	9.470
Fe (ppm)	1050	335
Co (ppm)	0.262	0.317
Ni (ppm)	5.300	9.400
Cu (ppm)	9.600	19.800
Zn (ppm)	41.400	37.300
Ga (ppm)	3.360	0.468
As (ppm)	29.850	8.880
Rb (ppm)	3.530	1.830
Sr (ppm)	1.650	0.343
Y (ppm)	0.017	0.106
Zr (ppm)	0.131	6.280
Nb (ppm)	0.176	0.059
Mo (ppm)	0.125	0.169
Ag (ppm)	0.212	0.332
Cd (ppm)	1.790	1.041
In (ppm)	0.157	0.059
Sn (ppm)	5.000	1.203
Sb (ppm)	0.565	0.404
Cs (ppm)	0.464	0.108
Ba (ppm)	65.800	2.370
La (ppm)	0.026	0.024
Ce (ppm)	0.098	0.123
Pr (ppm)	0.025	0.014
Nd (ppm)	0.029	0.024
Sm (ppm)	0.018	0.018
Eu (ppm)	0.022	0.014
Gd (ppm)	0.018	0.018
Tb (ppm)	0.007	0.005
Dy (ppm)	0.009	0.015
Ho (ppm)	0.008	0.006
Er (ppm)	0.008	0.016
Tm (ppm)	0.007	0.006
Yb (ppm)	0.010	0.035
Lu (ppm)	0.006	0.008
Hf (ppm)	0.013	0.027
Ta (ppm)	0.025	0.005
W (ppm)	0.210	0.205
Au (ppm)	0.011	0.630
Tl (ppm)	0.263	0.250
Pb (ppm)	25.300	4.940
Th (ppm)	0.015	0.011
U (ppm)	0.085	0.059
Y/Ho	2.115	17.755
Eu/Eu*	3.889	2.705
La/La*	0.026	0.089
Y/Y*	0.115	0.685
Ce/Ce*	0.144	0.472
Gd/Gd*	0.550	0.721
Pr/Sm	1.080	0.610
Nd/Yb	0.256	0.064

3.12 References

- Alexander, B.W., Bau, M., Andersson, P. and Dulski, P., 2008. Continentally-derived solutes in shallow Archean sea water; rare earth element and Nd isotope evidence in iron formation from the 2.9 Ga Pongola Supergroup, South Africa; *Geochimica et Cosmochimica Acta*, v. 72, p. 378-394.
- Alibo, D. S. and Nozaki, Y., 1999. Rare earth elements in seawater: particle association, shale-normalization, and Ce oxidation; *Geochimica et Cosmochimica Acta*, v. 63, p. 363-372.
- Allwood, A.C., Kamber, B.S., Walter, M.R., Burch, I.W. and Kanik, I., 2010. Trace element record depositional history of an Early Archean stromatolitic carbonate platform; *Chemical Geology*, v. 270, p. 148-163.
- Armitage, A.E., James, R.S. and Goff, S.P., 1996. Gold mineralization in Archean banded iron formation, Third Portage Lake area, Northwest Territories, Canada; *Exploration and Mining Geology*, v. 5, no. 1, p. 1-15.
- Aspler, L.B. and Chiarenzelli, J.R. 1996a. Stratigraphy, sedimentology and physical volcanology of the Henik Group, central Ennadai-Rankin greenstone belt, Northwest Territories, Canada: Late Archean paleogeography of the Hearne Province and tectonic implications; *Precambrian Research*, v. 77, p. 59-89.
- Barnes, S.J, Heggie, G.J and Fiorentini, M.L., 2013. Spatial variation in platinum group element concentrations in ore-bearing komatiite at the Long-Victor deposit, Kambalda Dome, Western Australia: enlarging the footprint of nickel sulfide orebodies; *Economic Geology*, v. 108, p. 913-933

- Barrett, T.J., Fralick, P.W. and Jarvis, I., 1988a. Rare-earth-element geochemistry of some Archean iron formations north of Lake Superior, Ontario: *Canadian Journal of Earth Sciences*, v. 25, p. 570–580.
- Bau, M. 1993. Effects of syn- and post-depositional processes on the rare-earth element distribution in Precambrian iron-formations; *European Journal of Mineralogy*, v. 5, p. 257-267.
- Bau, M. and Dulski, P., 1996. Distribution of Y and rare-earth elements in the Penge and Kuruman Iron Formations, Transvaal Supergroup, South Africa; *Precambrian Research*, v. 79, p. 37-55.
- Bau, M. and Dulski, P., 1999. Comparing yttrium and rare earths in hydrothermal fluids from the Mid-Atlantic Ridge: implications for Y and REE behavior during near-vent mixing and for the Y/Ho ratio of the Proterozoic seawater; *Chemical Geology*, v. 155, p. 70-90.
- Bau, M., 1999. Scavenging of dissolved yttrium and rare-earths by precipitating iron oxyhydroxide: Experimental evidence for Ce oxidation, Y-Ho fractionation, and lanthanide tetrad effect; *Geochimica et Cosmochimica Acta*, v. 63, no. 1, p.67-77.
- Bau, M. and Koschinsky, A., 2008. Oxidative scavenging of cerium on hydrous Fe oxide: Evidence from distribution of rare earth elements and yttrium between Fe oxides and Mn oxides in hydrogenetic ferro manganeses crusts; *Geochemical Journal*, v. 43, p. 37-47.
- Bekker, A., Slack, J.F., Planavsky, N., Krapez, B., Hofmann, A., Konhauser, K.O. and Rouxel, J., 2010. Iron formation: the sedimentary product of a complex interplay among mantle, tectonic, oceanic and biospheric processes; *Economic Geology*, v. 105, p. 467-508.

- Bhatia, M.R. and Crook, K.A.W., 1986. Trace elements characteristics of graywackes and tectonic setting discrimination of sedimentary basins; *Contributions to Mineralogy and Petrology*, v. 92, p. 181-193.
- Biczok, J., Hollings, P., Klipfel, P., Heaman, L., Maas, R., Hamilton, M., Kamo, S. and Friedman, R., 2012. Geochronology of the North Caribou greenstone belt, Superior Province Canada: Implications for tectonic history and gold mineralization at the Musselwhite mine; *Precambrian Research*, v. 192-195, p. 209-230.
- Bolhar, R., Van Kranendonk, M.J. and Kamber, B.S., 2005. A trace element study of siderite-jasper banded iron formation in the 3.45 Ga Warrawoona Group, Pilbara craton-Formation from hydrothermal fluids and shallow seawater; *Precambrian Research*, v. 137, p. 93-114.
- Breaks, F.W., Osmani, I.A. and DeKemp, E.A., 2001. Geology of the North Caribou Lake area, northwestern Ontario; Ontario Geological Survey, Open File Report 6023, 80 p.
- Carpenter, R.L., 2004. Relative and absolute timing of supracrustal deposition, tectonothermal activity and gold mineralization, West Meliadine region, Rankin Inlet greenstone belt, Nunavut, Canada; PhD. Thesis, Faculty of Graduate Studies, University of Western Ontario, 62 p.
- Carpenter, R.L., Duke, N.A., Sandeman, H.A. and Stern, R., 2005. Relative and absolute timing of gold mineralization along the Meliadine Trend, Nunavut, Canada; evidence for Paleoproterozoic gold hosted in an Archean greenstone belt.; *Economic Geology and the Bulletin of the Society of Economic Geologists*, v. 100, p. 567-576.
- Danielson, A., Moeller, P. and Dulski, P., 1992. The europium anomalies in banded iron

- formations and the thermal history of the oceanic crust; *Chemical Geology*, v. 97, p. 89-100.
- Davis, W.J., Ryan, J.J., Sandeman, H.A. and Tella, S., 2008. A Paleoproterozoic detrital zircon age for a key conglomeratic horizon within the Rankin Inlet area, Kivalliq region, Nunavut: implications for Archean and Proterozoic evolution of the area; *In Current research 2008-8*, Geological Survey of Canada, 10 p.
- DeBaar, H.J.W, Bacon, M.P. and Brewer, P.G., 1985. Rare earth elements in the Pacific and Atlantic Oceans; *Geochemica et Cosmochimica Acta*, v. 49, p. 1943-1959.
- Ding, K., Seyfried Jr., W.E., Zhang, Z., Tivey, M.K., Von Damm, K.L. and Bradley, A.M., 2005. The in-situ pH of hydrothermal fluids at mid-ocean ridge; *Earth and Planetary*, v. 237, p. 167-174.
- Fralick, P. and Pufahl, P.K., 2006. Iron formation in Neoproterozoic deltaic successions and the microbially mediated deposition of transgressive systems tracts; *Journal of Sedimentary Research*, v. 76, p. 1057-1066.
- Goodwin, A.M., 1973. Archean iron-formations and tectonic basins of the Canadian Shield; *Economic Geology*, v. 68, p. 915-933.
- Gourcerol, B., Thurston, P.C., Kontak, D.J. and Côté-Mantha, O., 2015a. Interpretations and implications of preliminary LA ICP-MS analysis of chert for the origin of geochemical signatures in banded iron formations (BIFs) from the Meadowbank gold deposit, Western Churchill Province, Nunavut; *Chemical Geology*, v. 410, p. 89-107.
- Gourcerol, B., Thurston, P.C., Kontak, D.J., Côté-Mantha, O. and Biczok, J. 2015b. The

- geochemistry of chert from the Banded Iron Formation-type Musselwhite and Meadowbank gold deposits: Distinguishing primary and mineralization-related signatures of chert: Geological Survey of Canada, Current Research 2015-1, 24 p.
- Gross, G.A., 1980. A classification of iron-formations based on depositional environments; Canadian Mineralogist, v. 100, p.1511-1527.
- Hall, R.S. and Rigg, D.M., 1986. Geology of the West Anticline Zone, Musselwhite Prospect, Opapimiskan Lake, Ontario, Canada, *In*: Macdonald, A.J. (Ed.), Gold '86; an international symposium on the geology of gold deposits; proceedings volume; GOLD '86, Toronto, ON, Canada, p. 124-136.
- Hanor, J.S. and Duchac, K.C., 1990. Isovolumetric silicification of early Archean komatiites; geochemical mass balances and constraints on origin; Journal of Geology, v. 98, p. 863-877.
- Hoefs, J., 2009. Stable isotope geochemistry; 6th Edition Springer Berlin, Heidelberg, 293p.
- Holland, H.D., 2003. The geologic history of seawater; *In* Treatise on Geochemistry *Edited* by H.D. Holland and K.K. Turekian. Pergamon, Oxford, p. 583-625.
- Hollings, P. and Kerrich, R., 1999. Trace element systematics of ultramafic and mafic volcanic rocks from the 3 Ga North Caribou greenstone belt, northwestern Superior Province. Precambrian Research, v. 93, p. 257-279.
- Hrabi, R.B., Barclay, W.A., Fleming, D. and Alexander, R.B., 2003. Structural evolution of the Woodburn Lake group in the area of the Meadowbank gold deposit, Nunavut; *In* Current Research 2003-C27, Geological Survey of Canada, 10 p.

- James, H.L., 1954. Sedimentary facies iron-formation; *Economic Geology*, v. 49, p. 235-293.
- Janvier, V., Castonguay, S., Mercier-Langevin, P., Dubé, B., McNicoll, V., Pehrsson, S., Malo, M., De Chavigny, B. and Côté-Mantha, O., 2015a. Preliminary results of geology of the Portage deposit, Meadowbank gold mine, Churchill Province, Nunavut, Canada; *Geological Survey of Canada, Current Research 2015-2*, 18 p. doi:10.4095/295532
- Kamber, B.S., Bolhar, R. and Webb, G.E., 2004. Geochemistry of late Archean stromatolites from Zimbabwe: evidence for microbial life in restricted epicontinental seas; *Precambrian Research*, v. 132, p. 379-399.
- Kamber, B.S., Greig, A. and Collerson, K.D., 2005. A new estimate for the composition of weathered young upper continental crust from alluvial sediments, Queensland, Australia; *Geochimica et Cosmochimica Acta*, v. 69, p. 1041-1058.
- Kamber, B.S. and Webb, G.E., 2007. Transition metal abundances in microbial carbonate: a pilot study based on in-situ LA-ICP-MS analysis; *Geobiology*, v. 5, p. 375-389.
- Kamber, B.S., Webb, G.E. and Gallagher, M., 2014. The rare earth element signal in Archaean microbial carbonate: information on ocean redox and biogenicity; *Journal of the Geological Society, London* v. 171, p. 745-763.
- Kappler, A., Pasquero, C., Konhauser, K.O. and Newman D.K., 2005. Deposition of banded iron formations by anoxygenic phototrophic Fe(II)-oxidizing bacteria; *Geology*, v. 33, p. 865-868.
- Kawabe, I., Ohta, A., Ishii, S., Tokumura, M. and Miyauchi, K., 1999b. REE partitioning

between Fe-Mn oxyhydroxide precipitates and weakly acid NaCl solutions: Convex tetrad effect and fractionation of Y and Sc from heavy lanthanides; *Geochemical Journal*, v. 33, p. 167-179.

Kawabe, I., 1978. Calculation of oxygen isotope fractionation in quartz-water system with special reference to the low temperature fractionation. *Geochimica et Cosmochimica Acta*, v.42, p. 613-621.

Kita, I., Taguchi, S. and Matsubaya, O., 1985. Oxygen isotope fractionation between amorphous silica and water at 34-93°C. *Nature*, v. 314, p. 83-84.

Klein, C., 2005. Some Precambrian banded iron-formation (BIFs) from around the world: Their age, geologic settings, mineralogy, metamorphism, geochemistry, and origin; *American Mineralogist*, v. 90, p. 1473-1499.

Knauth L. P. and Lowe D. R., 1978. Oxygen isotope geochemistry of cherts from Onverwacht Group (3.4 billion years), Transvaal, South-Africa, with implications for secular variations in isotopic composition of cherts; *Earth Planetary Science Letter*, v. 41, p. 209-222.

Knauth, L.P., 1994. Petrogenesis of chert, *In*: Heaney, P.J.P., Prewitt, C.T., Gibbs, G.V. (Eds.), *Silica: Physical Behavior, Geochemistry and Materials Applications*; Mineralogical Society of America, p. 233-258.

Knauth, L.P. and Lowe, D.R., 2003. High Archean climatic temperature inferred from oxygen isotope geochemistry of chert in the 3.5 Ga Swaziland Supergroup; *Geological Society of America Bulletin*, v. 115, p. 566-580.

- Konhauser, O.K., Newman, D.K. and Kappler, A., 2005. The potential significance of microbial Fe(III) reduction during deposition of Precambrian banded iron formations; *Geobiology*, v. 3, p. 167-177.
- Kresz, D.U. and Zayachivsky, B., 1991. Precambrian Geology, northern Long Lac area; Ontario Geological Survey, Report 273.
- Kump, L.R. and Seyfried Jr., W.E., 2005. Hydrothermal Fe fluxes during the Precambrian: effect of low oceanic sulfate concentrations and low hydrostatic pressure on the composition of black smokers; *Earth and Planetary Science Letters*, v. 235, p. 654-662.
- Lafrance, B., DeWolfe, J.C. and Stott, G M., 2004. A structural reappraisal of the Beardmore-Geraldton Belt at the southern boundary of the Wabigoon subprovince, Ontario, and implications for gold mineralization; *Canadian Journal Earth Sciences*, v. 41, p. 217-235.
- Lawley, C.J.M., Dubé, B., Mercier-Langevin, P., Kjarsgaard, B., Knight R. and Vaillancourt, D., 2015a. Defining and mapping hydrothermal footprints at the BIF-hosted Meliadine gold district, Nunavut, Canada; *Journal of Geochemical Exploration*, v.155, p. 33-55.
- Lawrence, M. G. and Kamber, B. S., 2006. The behavior of the rare earth elements during estuarine mixing- revisited; *Marine Chemistry*, v. 100, p. 147-161.
- Lawson, A.C., 1885. Report on the geology of the Lake of the Woods region, with special reference to the Keewatin (Huronian?) belt of the Archean rocks; Geological Survey of Canada, Annual Report (new series), v.I, Report CC, 151 p.
- Lécuyer, C. and Allemand, P., 1999. Modelling of the oxygen isotopes evolution of seawater:

- implications for the climate interpretation of the $\delta^{18}\text{O}$ of marine sediments; *Geochimica et Cosmochimica Acta*, v. 63, p. 351-361.
- Longerich, H. P., Jackson, S. E. and Gunther, D., 1996. Laser ablation inductively coupled plasma mass spectrometric transient signal data acquisition and analyte concentration calculation; *Journal of Analytical Atomic Spectrometry*, v. 11, p. 899-904.
- Mackasey, W.O., Edwards, G.R. and Cape, D.F., 1976. Legault Township, District of Thunder Bay; Ontario Division of Mines, Preliminary Map P-1191, scale 1:15 840.
- Marin, J., Chaussidon, M. and Robert, F., 2010. Microscale oxygen isotope variations in 1.9 Ga Gunflint cherts: assessments of diagenesis effects and implications for oceanic paleo-temperature reconstructions; *Geochimica et Cosmochimica Acta*, v. 74, p. 116-130.
- Marin-Carbonne, J., Chaussidon, M., Boiron, M.C. and Robert, F., 2011. A combined in-situ oxygen, silicon isotopic and fluid inclusion study of a chert sample from Onverwacht Group (3.35 Ga, South Africa): new constraints on fluid circulation; *Chemical Geology*, v. 286, p. 59-71.
- Marin-Carbonne, J., Chaussidon, M. and Robert, F., 2012. Micrometer-scale chemical and isotopic criteria (O and Si) on the origin and history of Precambrian cherts: implications for paleo-temperature reconstructions; *Geochimica et Cosmochimica Acta*, v. 92, p. 129-147.
- Marin-Carbonne, J., Faure, F., Chaussidon, M., Jacob, D. and Robert, F., 2013. A petrographic and isotopic criterion of the state of preservation of Precambrian cherts based on the characterization of the quartz veins; *Precambrian Research*, v. 231, p. 290-300.

- Marin-Carbonne, J., Robert, F. and Chaussidon, M., 2014. The silicon and oxygen isotope compositions of Precambrian cherts: A record of oceanic paleo-temperatures? ; *Precambrian Research*, v. 247, p. 223-234.
- Masuda, A. and Ikeuchi, Y., 1979. Lanthanide tetrad effect observed in marine environment; *Geochemical Journal*, v. 13, p. 19-22.
- Masuda, A., Kawakami, O., Dohmoto, Y. and Takenaka, T., 1987. Lanthanide tetrad effects in nature: two mutually opposite types, W and M; *Geochemical Journal*, v. 21, p. 119-124.
- Matsuhisa, Y., Goldsmith, J.R. and Clayton, R.N., 1979. Oxygen isotopic fractionation in the system quartz-albite-anorthite-water. *Geochimica et Cosmochimica Acta*, v. 43, p. 1131-1140.
- McLennan, S.M., Hemming, S., McDaniel, D.K. and Hanson, G.N., 1993. Geochemical approaches to sedimentation, provenance and tectonics; *Geological Society of America, Special Papers 1993*, v. 284, p. 21-40.
- McNicoll, V., Dubé, B., Biczok, J., Castonguay, S., Oswald, W., Mercier-Langevin, P., Skulski, T. and Malo, M., 2013. The Musselwhite gold deposit, North Caribou greenstone belt, Ontario: new high-precision U-Pb ages and their impact on the geological and structural setting of the deposit; Abstract, Geol. Assoc. of Canada annual meeting, Winnipeg.
- Minami, M., Masuda, A., Takahashi, K., Adachi, M. and Shimizu, H., 1998. Y-Ho fractionation and lanthanide tetrad effect observed in cherts; *Geochemical Journal*, v. 32, p. 405-419.
- Moran, P., 2008. Lithogeochemistry of the sedimentary stratigraphy and metasomatic alteration

in the Musselwhite gold deposit. North Caribou Lake metavolcanic-metasedimentary belt, Superior Province, Canada: implications for deposition and mineralization; Unpublished Master's Thesis, Lakehead University, 351 p.

Ohmoto, H., Watanabe, Y., Yamaguchi, K.E., Naraoka, H., Haruna, M., Kakegawa, T., Hayashi, K. and Kato, Y., 2006. Chemical and biological evolution of early Earth: Constraints from banded iron formations: Geological Society of America Memoire, v. 198, p. 291-331.

Oswald, W., Castonguay, S., Dubé, B., McNicoll, V.J., Biczok, J., Malo, M. and Mercier-Langevin, P., 2015. Geological setting of the world-class Musselwhite gold Mine, Superior Province, northwestern Ontario, and implications for exploration, In: Targeted Geoscience Initiative 4: Contributions to the Understanding of Precambrian Lode Gold Deposits and Implications for Exploration, (ed.) B. Dubé and P. Mercier-Langevin; Geological Survey of Canada, Open File 7852, p. 69-84.

Otto, A., 2002. Ore forming processes in the BIF-hosted gold deposit Musselwhite Mine, Ontario, Canada. Unpublished Master's Thesis, Freiberg Institute of Mining and Technology, 86 p.

Pehrsson, S.J., Wilkinson, L. and Zaleski, E., 2004. Geology of the Meadowbank gold deposit area, Nunavut; Geological Survey of Canada, Open File 4269, scale 1:20 000.

Pehrsson, S.J., Berman, R.G. and Davis, W.J., 2013. Paleoproterozoic orogenesis during Nuna aggregation: a case study of reworking of the Rae craton, Woodburn Lake, Nunavut; Precambrian Research, v. 232, p. 167-188.

Planavsky, N., Bekker, A., Rouxel, O.J., Kamber, B.S., Hofmann, A.W., Knudsen, A. and

- Lyons, T.W., 2010. Rare Earth Element and yttrium compositions of Archean and Paleoproterozoic Fe formations revisited: New perspectives on the significance and mechanisms of deposition; *Geochimica et Cosmochimica Acta*, v. 74, p. 6387-6405.
- Posth, N.R., Kohler, I., Swanner, E.D., Schroder, C., Wellmann, E., Binder, B., Konhauser, K.O., Neumann, U., Berthold, C., Nowak, M. and Kappler, A., 2013. Simulating Precambrian banded iron formation diagenesis; *Chemical Geology*, v. 362, p. 66-73.
- Pufahl, P.K., Pirajno, F. and Hiatt, E.E., 2013. Riverine mixing and fluvial iron formation: A new type of Precambrian biochemical sediment; *Geology*, v. 41, n. 12, p. 1235-1238.
- Robert, F. and Chaussidon, M., 2006. A palaeo-temperature curve for the Precambrian oceans based on silicon isotopes in cherts; *Nature*, v. 443, p. 969-972.
- Shanks, W.S., 1993. Geology of Eva and Summer Townships, District of Thunder Bay; Ontario Geological Survey, Open File Report 5821.
- Sherlock, R., Pehrsson, S., Logan, A.V., Hrabi, R.B. and Davis, W.J., 2004. Geologic setting of the Meadowbank gold deposits, Woodburn Lake group, Nunavut; *Exploration Mining Geology*, v. 13 (1-4), p. 67-107.
- Sherlock, R.L., Alexander, R.B., March, R. and Barclay, W.A., 2001a. Geologic setting of the Meadowbank iron formation-hosted gold deposits; *In Current Research 2001-C11*, Geological Survey of Canada, 23 p.
- Sherlock, R.L., Alexander, R.B., March, R. and Barclay, W.A., 2001b. Geologic setting of the Meadowbank iron formation-hosted gold deposits; Geological Survey of Canada, Open File

3149, scale 1:10 000.

Shibuya, T., Komiya, T., Nakamura, K., Takai, K. and Maruyama, S., 2010. Highly alkaline, high-temperature hydrothermal fluids in the early Archean ocean; *Precambrian Research*, v. 182, p. 230-238.

Taylor, H.P., 1974. The application of oxygen and hydrogen isotope studies to problems of hydrothermal alteration and ore deposition; *Economic Geology*, v. 69, p. 843-883.

Taylor, H.P., 1978. Oxygen and hydrogen isotope studies of plutonic granitic rocks; *Earth Planetary Science Letter*, v. 38, p. 177-210.

Tella, S., Paul, D., Berman, R.G., Davis, W.J., Peterson, T.D., Pehrsson, S.J. and Kerswill, J.A., 2007. Bedrock geology compilation and regional synthesis of parts of Hearne and Rae domains, western Churchill Province, Nunavut-Manitoba; Geological Survey of Canada, Open File 5441, scale 1:550 000 (3 sheets and a CD-ROM).

Tóth, Z., Lafrance, B., Dube, B., McNicoll, V.J., Mercier-Langevin, P. and Creaser, R.A., 2015. Banded iron formation-hosted gold mineralization in the Geraldton area, northwestern Ontario: Structural setting, mineralogical characteristics, and geochronology, In: *Targeted Geoscience Initiative 4: Contributions to the Understanding of Precambrian Lode Gold Deposits and Implications for Exploration*, (ed.) B. Dube and P. Mercier-Langevin; Geological Survey of Canada, Open File 7852, p. 85-97.

Thurston, P.C. and Chivers, K.M., 1990. Secular variation in greenstone sequence development emphasizing Superior Province, Canada; *Precambrian Research*, v.46, p.21-58.

Thurston, P.C., Ayer, J.A., Goutier, J. and Hamilton, M.A., 2008. Depositional gaps in Abitibi greenstone belt stratigraphy: a key to exploration for syngenetic mineralization; *Economic geology*, v. 103, p. 1097-1134.

Thurston, P.C., Kamber, B.S. and Whitehouse, M., 2012. Archean cherts in banded iron formation: Insight into Neoproterozoic ocean chemistry and depositional processes; *Precambrian Research*, v. 214-215, p. 227-257.

Tomlinson, K.Y., Hall, R.P., Hughes, D.J. and Thurston, P.C., 1996. Geochemistry and assemblage accretion of metavolcanic rocks in the Beardmore-Geraldton greenstone belt, Superior Province; Canadian Journal of Earth Sciences, v. 33, p. 1520-1533.

Melezhik, V.A., Nutman, A.P., Papineau, D. and Pirajno, F. 2012. A chronostratigraphic division of the Precambrian ; possibilities and challenges; *In* Gradstein, F.M, Ogg, J.G., Schmitz, M.D., Ogg, G.J. (Eds.), The Geologic Time Scale 2012; Elsevier, Boston, USA, p. 299-39.

Vearncombe, S. and Kerrich, R., 1999. Geochemistry and Geodynamic setting of volcanic and plutonic rocks associated with early Archean volcanogenic massive sulphide mineralization, Pilbara Craton; *Precambrian Research*, v. 98, p. 243-270.

Veizer, J., 1988. The evolving exogenic cycle; *In* Chemical cycles in the evolution of the Earth
Edited by B.C. Gregor, R.M. Garrels, F.T. Mackenzie and B.J. Maynard. Wiley-
Interscience, New York, p. 175-218.

[illegible]

- Grassineau, N. and Guido, D.M., 2015. Archean (3.33 Ga) microbe-sediment systems were diverse and flourished in a hydrothermal context; *Geology*, v. 43, p. 615-618.
- Webb, G.E., Nothdurft, L.D., Kamber, B.S., Klopogge, J.T. and Zhao, J.X., 2009. Rare earth element geochemistry of scleractinian coral skeleton during meteoric diagenesis: A sequence through neomorphism of aragonite to calcite; *Sedimentology*, v. 56, p. 1433-1463.
- Wright, G.M., 1967. Geology of the southeastern barren grounds, Parts of the Districts of Mackenzie and Keewatin. Geological Survey of Canada, Memoire 350, 91 p.

Chapter 4: Gold and trace element distribution in sulfides from mineralized Algoma-type BIFs; Implications for nature of mineralizing fluids, metal sources and deposit models

4.1 Abstract

Quantitative laser ablation inductively coupled plasma mass spectrometry (LA-ICP-MS) element distribution maps combined with traverse and spot analyses have been performed on various sulfides (i.e., pyrite, pyrrhotite, arsenopyrite) from three Canadian Algoma-type BIF-hosted gold deposits (i.e., the ~4 Moz Au Meadowbank deposit and the ≥ 2.8 Moz Au Meliadine district, and the ~6 Moz Au Musselwhite deposit) in order to examine trace element zoning, evaluate gold distribution, and identify element associations characterizing gold event(s) in these Algoma-type BIFs. These data demonstrate that the main gold event in the three deposits is characterized by a coupling of elements, namely As-Se-Te-Ag, which establishes the trace metal association for this mineralization associated with intense stratabound sulfide-replacement of the Fe-rich material. Furthermore, the data reveal the presence of a later remobilization event responsible for upgrading of gold tenor along fracture networks due to ingress by a subsequent generation of base metal-bearing fluids (mainly Pb-Bi-rich) assumed to be metamorphic in origin based on their paragenesis and the element association.

This study confirms the epigenetic origin of BIF-hosted gold mineralization and supports a model whereby metamorphic/hydrothermal orogenic processes were responsible for the devolatilization of a common source area. The latter process resulted in the source rock liberating gold-bearing fluid along with a specific element suite noted above which was channelled into Algoma-type BIF at higher crustal levels via major crustal faults and/or shear

zones. Due to the high iron content, BIF acts as a favorable chemical trap reducing the gold-bearing fluid via sulfidation of a pre-existing Fe-rich material to generate iron-bearing sulfides. Moreover, the data reveal that stratigraphy contributes to the fluid chemistry and may influence the nature of the sulfide (e.g., arsenopyrite versus pyrite). In addition, the enrichment of gold, as either nonrefractory or refractory type, along networks of fractures suggests a role for later deformation and metamorphic events on gold remobilization and hence upgrading in the deposits consistent with the deformation history of the deposits.

4.2 Introduction

Algoma-type BIFs, which are thinly bedded, chemical sedimentary rocks comprising alternating layers of iron-rich minerals and chert, represent a significant host-rock for gold mineralization in Precambrian terranes (e.g., Homestake and Musselwhite deposits; Frei et al., 2009; Oswald et al., 2015). The timing of the mineralizing event (syngenetic versus epigenetic) and the origin of gold within BIF-hosted gold deposits have been subject of research and genetic debates over the last few decades (e.g., Groves et al. 1998; Goldfarb et al., 2001, 2005; Dubé et al., 2015). In the 1970s, some authors suggested a syngenetic model whereby gold was concentrated in arsenian pyrite within the host BIFs by hydrothermal fluids during chemical sedimentation and/or early diagenesis (e.g., Fripp et al., 1976; Kerswill, 1993, 1996). However, recent work on the depositional setting of Algoma-type BIFs establishing their primary signature using REE+Y systematics (e.g., Bolhar et al., 2005; Thurston et al., 2012; Gourcerol et al., 2015c) combined with the presence of replacement features (e.g., sulfide facies) and the discordant nature of veining systems typically observed in BIF-hosted gold deposits do not support the syngenetic model. Lately, the consensus has been that gold mineralization is epigenetic, produced by potential metamorphic/hydrothermal processes in which the BIF

represents an efficient chemical trap by virtue of its high iron content and thus potential reactivity for metal- and H₂S-rich fluids migrating via structural channels into favorable structural traps (e.g., fold hinges, shear zones) (e.g., Poulsen et al., 2000; Dubé et Gosselin, 2007; Phillips and Powell, 2010). This latter scenario is therefore more representative of an orogenic model for the gold mineralization (e.g., Phillips et al., 1984; Phillips and Powell, 2010; Poulsen et al., 2000; Goldfarb et al. 2001, 2005). However, the initial source of the gold and nature of the mineralizing fluids are still debated with components of magmatic, metamorphic and diagenetic sources suggested (e.g., Phillips and Powell, 2010; Large et al., 2011).

In recent years Large et al. (2007, 2009, 2011), based on detailed LA-ICP-MS mapping studies, suggested that gold in sediment-hosted gold deposits (e.g., the Sukhoi Log in Siberia, Bendigo in Victoria, Spanish Mountain in British Columbia, North Carlin Trend in Nevada) likely originated from the mobilization of gold out of syn-sedimentary to early-diagenetic, fine-grained and/or framboidal pyrite hosted by carbonaceous sediments such as black shales. These sulfides originally precipitated at the bottom of basins as a result of oxygen depletion (Scholtz and Neuman, 2007) combined with the mediating influence of sulfate-reducing bacteria (e.g., Schieber, 2002; Folk, 2005; Large et al., 2014) and in doing so, were enriched in a specific suite of trace elements present in Archean seawater (As, Mo, Co, Ni, Pb, Zn, Te, V, Se). The subsequent effects of deformation and metamorphism, (likely greenschist facies) and/or intrusive activity, resulted in recrystallization of the host sulfide and conversion to coarse-grained pyrite and/or pyrrhotite with commensurate release of any contained gold and other metals into the fluid phase. The transport and structural focusing of these metalliferous fluids is considered to then result in the formation of a variety of quartz-sulfide veins and disseminated sediment-hosted gold deposits (e.g., Wagner et al., 2007; Large et al., 2011, Cook et al., 2013; Bull et al., 2015).

In this context, an important question is whether the gold mineralization in BIF-hosted gold deposits originates from similar source rocks (e.g., black shale) with early metal enrichment in diagenetic sulfide phases which is released into an ore forming fluid that is responsible for the ore, in much the same manner as discussed above (e.g., Steadman et al., 2014; Gao et al., 2015).

In this study, we examine the textures and trace-element zoning of various sulfides such as pyrite, pyrrhotite and arsenopyrite in order to identify element associations characterizing gold event(s) and evaluate the source of sulfides and metals within three Canadian BIF-hosted gold deposits (Fig. 4.1): (1) the ~4 Moz Au Meadowbank deposit, hosted by the 2.71 Ga Woodburn Lake greenstone belt; (2) the ≥ 2.8 Moz Au Meliadine district, hosted by the 2.6 Ga Rankin Inlet greenstone belt; and (3) the ~6 Moz Au Musselwhite deposit, hosted by the 2.9-3 Ga North Caribou greenstone belt. These deposits are hosted by Algoma-type BIFs within moderately to strongly deformed and metamorphosed (i.e., greenschist to amphibolite facies) greenstone belts and are considered to best fit with the orogenic gold deposit model (e.g., Dubé et al., 2015). In detail, this study investigates: (1) the distribution of gold and various trace elements structurally bound within the sulfide phases in order to identify similarities and differences in gold mineralization from the three deposits; and (2) compares these features to other orogenic deposits, such as clastic sediment-hosted gold deposits, in order to examine the potential for a similar source for the gold and associated elements.

4.3 Geological setting of the selected BIFs

4.3.1 The Meadowbank deposit

Located in the Rae Domain of the Churchill Province (Fig. 4.1), the Meadowbank deposit is hosted by the Pipedream-Third Portage area of the Woodburn Lake greenstone belt (ca. 2.71 Ga)

consisting of tholeiitic and komatiitic metavolcanic rocks with minor calc-alkaline, intermediate to felsic tuffs and flows with intercalated BIF and clastic metasedimentary rocks that include quartzite and conglomerates (Armitage et al., 1996; Sherlock et al., 2001a, b, 2004; Hrabí et al., 2003; Pehrsson et al., 2004; Janvier et al., 2015). The regional metamorphic grade ranges from middle greenschist to amphibolite facies (Pehrsson et al., 2004) and rocks were deformed by at least by six regional-scale deformation events during the Proterozoic Trans-Hudson orogeny (e.g., Pehrsson et al., 2013; Janvier, et al., 2015).

Numerous units of oxide-, silicate- and locally sulfide-facies Algoma-type BIF have been identified in the deposit area. These BIFs include the West IF, Central BIF and East BIF which are all interlayered with the volcanic rocks and locally with a quartzite unit (Gourcerol et al., 2015a; Sherlock et al., 2001a, b; 2004). The BIFs display cm- to mm-thick laminated magnetite and white- to grey chert with associated layers (0.2 to 5 cm thick) of various assemblages of grunerite/biotite or cummingtonite/biotite or garnet/biotite which reflect variable metamorphic grades in the deposit area. Moreover, minor chlorite, sericite, ankerite, siderite, stilpnomelane and apatite form layers interbedded with the chert and magnetite or as inclusions in chert bands (Armitage et al., 1996; Hrabí et al., 2003; Sherlock et al., 2004; Gourcerol et al., 2015a). Further details of these BIFs are provided in detail in Gourcerol et al. (2015a).

Despite their mineralogical and textural similarities, only the Central BIF contains economic gold concentrations (i.e., the Portage and Goose deposits; e.g., Janvier et al., 2015, Gourcerol et al., 2015a). Ore-bearing BIFs are characterized by high-strain zones associated with intense stratabound sulfide-rich replacement (e.g., pyrrhotite and pyrite with local chalcopyrite and arsenopyrite) of pre-existing magnetite bands and/or transposed quartz-sulfide stockworks in magnetite and chert bands (e.g., Janvier et al., 2015). The gold mineralization, which occurs

mainly as fracture-fills or as inclusions in sulfides with an elemental association, as determined by bulk ICP-MS analyses, of anomalous As, Cu, Pb, Ni, Co and Te, is considered to have been introduced into the BIF by a pre-D2 event (i.e., prior to 1.85 Ga; Janvier et al., 2015).

4.3.1.1 Sulfide paragenesis at the Meadowbank deposit

The Meadowbank deposit illustrates a complex sulfide paragenetic sequence characterized by several pyrite events and formation of metamorphic pyrrhotite in addition to minor chalcopyrite and arsenopyrite that are seen as inclusions and/or disseminated grains either in magnetite bands or in metamorphic pyrrhotite (Fig. 4.2). Pyrite mainly occurs as one of three types in the paragenetic sequence, from pyrite 1 (py1) to pyrite 3 (py3). The earliest pyrite (py1) consists of aggregates (<100 μm) of sooty, fine-grained “framboidal-like” texture (Fig. 4.3A, B, C, D) that suggests an early-diagenetic origin (e.g., Large et al., 2007). This pyrite is overgrown by coarser-grained (<200 μm), subhedral to euhedral pyrite (py2) characterized by its sieve-texture due to abundant inclusions (Fig. 4.3D) that are oriented along the foliation. Pyrite 2 may have fine-grained internal domains and be zoned, which suggests that inclusions of py1 may be completely incorporated within py2 (Fig. 4.3A, B). It is noted that distinctive inclusions of py1 in py2 are named py1' (Fig. 4.3B). Finally, the latest pyrite (py3) is euhedral to subhedral and texturally “clean” compared to py1 and py2 and overprint locally previous pyrites. Coarse-grained (>200 μm) metamorphic pyrrhotite appears to replace pre-existing magnetite bands and thereby has incorporated py1 and py2 as inclusions. Py3 overprints metamorphic pyrrhotite (Fig. 4.3E) and appears to mimic a late magnetite event illustrated by euhedral disseminated grains. Moreover, local fine-grained anhedral to subhedral chalcopyrite and arsenopyrite occur as inclusions or disseminated grains in the margins of pyrrhotite grains, which suggests these phases are coeval with this event (Fig. 4.3F). It is notable that only samples from Central BIF

show combination of py1 and py2 grains.

4.3.2 The Meliadine gold district

The Meliadine deposit is hosted by the 2.6-2.7 Ga Rankin Inlet greenstone belt (Wright, 1967; Aspler and Chiarenzelli, 1996a), which lies along the boundary between the Central and the Northwestern Hearne domains of the Churchill Province (Fig. 4.1; Tella et al., 2007; Davis et al., 2008). The Rankin Inlet greenstone belt consists of polydeformed massive and pillowed mafic flows, felsic pyroclastic rocks and associated interflow sedimentary units, gabbroic sills and oxide-facies BIFs. All of the aforementioned units are intruded by minor granite, undeformed biotite lamprophyre, as well as late gabbro and diabase dykes of Archean and Proterozoic age. These rock units have been metamorphosed from lower greenschist to lower-middle amphibolite facies (Carpenter, 2004; Carpenter, et al., 2005).

Several gold hosting Algoma-type BIFs are recognized along the structural hanging wall of the regional-scale Pyke Fault and include the Pump and F-Zone BIF. These mineralized BIFs are oxide-facies that are interbedded with mafic volcanic and volcanoclastic rocks. The BIFs are characterized by continuous, subparallel, medium-grey cherty beds interbedded with variable amounts of massive, mm- to cm-thick beds of magnetite and Fe-silicate minerals (e.g., grunerite, hornblende, chlorite), the latter of which are located at the margins of magnetite bands and radiate towards the chert bands (Lawley et al., 2015a,b).

Gold mineralization in the Meliadine district consists of BIF-hosted replacement-style mineralization in addition to auriferous quartz-ankerite veins and their alteration selvages. In contrast to the Meadowbank area, the BIF hosted-gold mineralization here represents only a part of the mineralization and is characterized by intense stratabound sulfide-rich replacement (e.g.,

pyrite, arsenopyrite and pyrrhotite) of pre-existing magnetite along with strong sericite-carbonate alteration. Lawley et al. (2015a) have shown that the gold mineralization occurs in two forms, as inclusions within and fracture fills cutting arsenopyrite. Furthermore, they suggest that the gold was introduced at either 2.27 Ga and/or 1.90 Ga, the latter time representing possible upgrading of the early gold event during the Trans-Hudson Orogeny. Furthermore, an elemental association of anomalous As, Te, Bi and Sb associated with the gold-mineralized BIF was proposed by Lawley et al. (2015a, b, c) based on whole-rock geochemical analyses coupled with LA-ICP-MS element mapping.

4.3.2.1 Sulfide paragenesis at the Meliadine gold district

The Meliadine gold district shows a complex paragenetic sequence with two generations arsenopyrite that are mainly associated with gold mineralization (Fig. 4.4). In addition, pyrrhotite and pyrite with lesser chalcopyrite, galena and rare sphalerite occur as inclusions or disseminated grains (Fig. 4.5). These sulfide phases all occur within quartz-carbonate veins or as randomly-oriented grains within vein-selvages (Lawley et al., 2015a). In particular, two types of arsenopyrite can be distinguished, identified as aspy1 and aspy2. Aspy1 occurs as strongly fractured, coarse euhedral that have a sieve-texture (along main fabric) and is considered to represent the primary hydrothermal event in the area (Fig. 4.5A, B, C, D, E). In contrast, aspy2 is fine- to medium grained and is unfractured and inclusion-free. The latter features suggest aspy2 may represent a later remobilization (Fig. 4.5F). Anhedral to subhedral and locally sieve-textured grains of pyrrhotite, pyrite, chalcopyrite, galena and minor sphalerite, as well as native gold, occur mainly in low-strain micro-textural sites in aspy1 and as fracture-fillings. These phases appear to locally overgrow aspy1 and thereby suggest a post-aspy1 and pre-aspy2 time of crystallization (Fig. 4.5A, B, C, D, E). Moreover, a minor sulfide-rich event may occur before

precipitation of aspy1, as some pyrrhotite and pyrite inclusions have been noted to occur in aspy1 (e.g., Carpenter, 2004).

Elemental mapping of arsenopyrite grains (Carpenter, 2004; Lawley et al., 2015c) confirmed the above paragenetic interpretation. In assessing the timing of gold mineralization, Lawley et al. (2015c) suggested the early sulfide phases pre-date the regional 1.86 Ga deformation event and that this later event caused release of gold during progressive deformation and fluid-assisted recrystallization of sulfides. This latter process resulted in remobilization and precipitation of the paragenetically later gold, during the Trans-Hudson orogeny, in low-strain microstructures or as clusters at aspy1/aspy2 crystals boundaries (Fig. 4.4). Importantly, the timing of this later gold event was constrained by the proximity of gold to hydrothermal xenotime grains that were dated using *in-situ* LA ICP-MS at 1.86 Ga.

4.3.3 The Musselwhite deposit

Located in the North Caribou terrane of the Superior Province (Fig. 4.1), the Musselwhite deposit is hosted by the North Caribou greenstone belt, which is dominated by mafic to ultramafic metavolcanic rocks of the 2973<2967 Ma Opapimiskan-Markop metavolcanic assemblage and tholeiitic basalts and minor felsic volcanics of the 2980-2982 Ma South Rim Metavolcanic assemblage (Biczok et al., 2012; McNicoll et al., 2013). These rocks have been metamorphosed from lower greenschist to low-mid amphibolite facies (Breaks et al., 2001) and deformed by three deformation events (Hall and Rigg, 1986; Breaks et al., 2001). The Opapimiskan-Markop metavolcanic assemblage is composed, from the structural base to the top, of the “Lower Basalt” unit, the Southern Iron Formation, “Basement Basalt” unit and the Northern Iron Formation (Otto, 2002; Moran, 2008; Biczok et al., 2012).

The “Basement Basalt” unit lying between the Northern and Southern Iron Formations is a thick sequence of massive- and pillowed tholeiitic basalt (Moran, 2008). The “Lower Basalt” unit is composed of basalt and ultramafic rocks but includes extensive andesite (Hollings and Kerrich, 1999).

The North Iron Formation, which is the main host to mineralization, is subdivided, from the structural base to top, into: pyrrhotite-rich mudstone (4H), chert-grunerite (4A), chert-magnetite (4B), clastic-chert-magnetite (“clastic”4B), garnet-grunerite-chert (4EA), garnetiferous amphibolite (4E) and garnet-biotite schist (4F) (e.g., Otto, 2002; Moran, 2008; Biczok et al., 2012, Oswald et al., 2015, Gourcerol et al., 2015c). The Southern Iron Formation consists of two sub-parallel BIF horizons (Biczok et al., 2012).

Gold mineralization is mainly confined to BIF, more particularly in silicate-facies (i.e., 4EA, 4E and 4F) BIF within high-strain zones mainly along and immediately adjacent to the lower pressure areas such as steep limbs of the folded iron formation (Biczok et al., 2012). Ore-bearing BIF is characterized by intense stratabound sulfide-rich replacement (e.g., mainly pyrrhotite) of pre-existing Fe-rich minerals, such as grunerite and garnets, spatially related to zones of silica flooding with local discordant quartz-pyrrhotite veinlets (e.g., Oswald et al., 2015). Gold occurs mainly within pyrrhotite-filled fractures in coarse-grained, subhedral to euhedral almandine garnet porphyroblasts and/or in pressure-shadows developed along garnet crystals formed during the 2788 to 2703 Ga D₂ event which is the dominant deformation style in the deposit (e.g., Oswald et al., 2015; Biczok et al., 2012; Kelly and Schneider, 2015). Oswald et al. (2015) proposed an elemental association of anomalous Ag, Cu, Se and Te with the Au mineralized BIFs based on bulk ICP-MS analyses of sulfide grains, whereas elemental mapping of pyrite nodules (Gao et al., 2015) from a carbonaceous argillite unit within the deposit vicinity provides

striking evidence for generation of Au-rich fluids during recrystallization along with As, Mo, Ag, Sb, Te, W, Tl, Pb, and Bi. Furthermore, Gao et al. (2015) also suggested that this unit may represent a possible source of gold for the deposit based on analogies with the model of Large et al., (2011).

4.3.3.1 Sulfide paragenesis at the Musselwhite deposit

The Musselwhite deposit illustrates a complex sulfide paragenetic sequence characterized by several generations of pyrite and formation of metamorphic pyrrhotite in addition to the presence of inclusions of minor amounts of chalcopyrite and arsenopyrite (Fig. 4.6). Two types of pyrite are recognized in the paragenetic sequence: (1) py1 is seen as very fine-grained (<25 μm), anhedral to subhedral annealed grains in metamorphic pyrrhotite (Fig. 4.7A, B); and (2) py2 occurs as coarser-grained (>100 μm), euhedral grains overprinting pyrrhotite (Fig. 4.7C, D). Coarse- (>100 μm) to fine-grained (<100 μm) aggregates of metamorphic pyrrhotite appear to replace pre-existing Fe-rich material, such as magnetite or possibly also pyrite, and may also form veinlets and/or filling fractures in coarse-grained, almandine garnet porphyroblasts (Fig. 4.7C). The relationship between annealed py1 and pyrrhotite suggest that pyrrhotite formed in response to increasing in metamorphic grade along with recrystallization of py1 rather than metamorphic conversion of pyrite to pyrrhotite (Tomkins, 2010), that is growth of new pyrrhotite. Chalcopyrite and rare arsenopyrite occur as inclusions in pyrrhotite (Fig. 4.7B, D). Notable, the presence of arsenopyrite inclusions do not correlate with gold mineralization (Oswald et al., 2015).

4.4 Analytical methods and data treatment

4.4.1 LA-ICP-MS sulfide trace element chemistry

Sulfide compositions were determined in the Geochemical Fingerprinting Lab at Laurentian University by LA ICP-MS using a 193 nm wavelength Resonetics RESolution M-50 ArF excimer laser ablation system coupled to a Thermo X Series II quadrupole ICP-MS. A series of spot, traverse and map analyses were conducted on pyrite, pyrrhotite and arsenopyrite grains in thick sections. Beam diameters were typically chosen based on grain sizes of the selected minerals, thus this parameter varied from 9 to 40 μm . Traverse and map scan rates were approximately 1/3 the beam diameter per second. The laser pulse rate was 7 and 6 Hz for traverses and spots, respectively. In all cases, a fluence of $\sim 5 \text{ J/cm}^2$ was used. Ablation took place in ultra-pure He flowing at a rate of 650 ml/min, which was combined after the sample cell with Ar (750 ml/min) and N_2 (6 ml/min; for added sensitivity). The RESolution M-50 employs a Laurin Technic two-volume sample cell with excellent washout characteristics (Müller et al., 2009), and therefore provides good spatial resolution for traverses and maps. For all analysis types, 30 seconds of washout/background was collected before each analysis and reference materials were typically analyzed bracketing and between every several unknowns. The maps were acquired by rastering the laser over the region of interest with successive lines offset by the beam diameter. The ICP-MS was operated with a forward power of 1450 W and oxide production rate of $<0.5\%$ as determined from ThO^+/Th^+ while ablating NIST 612. Dwell times were 10 ms for each analyte except Au, which was 30 ms. All data acquisition was done in time-resolved mode to understand the spatial relationships between elements and mineral growth.

Data quantification was carried out using the trace elements data reduction scheme of Iolite

(Paton et al., 2011) with NIST 610 and Fe acting as the external and internal references, respectively. Secondary reference materials BHVO2-G and Po725 (Sylvester et al., 2005) were also analyzed to verify the reasonable reproduction of known compositions. Considering the differences in ablation between silicate glass (NIST 610) and sulfides, it is expected that melting and fractionation limits the accuracy of the quantified data to ~20% (Wohlge-muth-Ueberwasseret al., 2015). The limits of detection for integrated data were calculated according to Longerich et al. (1996) and Howell et al. (2013) (for analytes with no background counts) and were typically 0.01 to 1 ppm for trace elements depending primarily on beam diameter and the analyte background signal. The time-slice (i.e. not averaged) data used in binary plots and profiles are subject to higher detection limits, but were not quantified as it is the elemental associations that are of interest in these plots. Maps were originally stitched together using Iolite (e.g. Woodhead et al., 2007), but were also subjected to bilinear interpolation between adjacent lines and 3x3 mean pixel smoothing. This improves the visualization of the data, but can also reduce or eliminate spikes resulting from the ablation of tiny inclusions (e.g., Rittner and Müller, 2012). The traverse and spot data used for all bivariate plots included herein were not smoothed in any way.

4.4.2 Electron Backscattered Diffraction analysis

Selected pyrite grains from the Meadowbank area were analyzed by electron backscattered diffraction (EBSD) using a JEOL JSM-6400 scanning electron microscope coupled to an energy dispersive spectrometer (EDS) housed in the Central Analytical Facilities (CAF) at Laurentian University, Sudbury, Ontario. This technique allows generation of diffraction patterns forming Kikuchi bands which correspond to each of the lattice diffracting crystal planes and identification of crystallographic orientation (Bestmann and Prior, 2003; Prior et al., 2002).

Pyrite samples were polished prior to analysis to remove any surface damage and covered by a thin carbon coat in order to reduce charging effects and maintain a strong crystallographic signal. Operating conditions were accelerating voltage of 20 keV, 3 nA beam current.

4.5 Results and interpretation

Based on using data from three Algoma-type BIF-hosted gold deposits (e.g., the Meadowbank, Meliadine and Musselwhite deposits), this study aims to evaluate the sources of metals present in sulfides and to establish similarities or differences between potential processes of gold enrichment. Due to the highly variable level of knowledge and analyses available on these deposits (e.g., Janvier et al., 2015; Lawley et al., 2015c; Oswald et al., 2015), a combination of LA-ICP-MS mapping and traverse analyses were performed on pyrite and pyrrhotite for the Meadowbank deposit, whereas only LA-ICP-MS traverse analyses were performed on arsenopyrite and pyrrhotite from the Meliadine gold district, and LA-ICP-MS traverse and spot analyses on pyrrhotite and pyrite from the Musselwhite deposit.

4.5.1 The Meadowbank deposit

In order to evaluate gold distribution in variable sulfides (i.e., pyrite and pyrrhotite) and its relationship with other elements in the mineralized BIF (i.e., the Central BIF) and characterize gold event(s) within the Meadowbank deposit, LA-ICP-MS mapping of pyrite samples (py1, py2 and py3) combined with LA-ICP-MS traverse analyses on metamorphic pyrrhotite were performed. EBSD analyses were performed on samples selected for LA-ICP-MS mapping in order to identify different domains and therefore to attribute element associations to variable pyrite domains.

4.5.1.1 LA-ICP-MS trace element chemistry

Sample AMB-126223 from the Central BIF (e.g., Gourcerol et al., 2015a) was selected for elemental mapping of py1, py1 and py2 occurrences in local sulfide-facies BIF representing intense stratabound sulfide-rich replacement of pre-existing magnetite bands by late metamorphic pyrrhotite. In this sample, py1, which reflects an-early diagenetic origin (i.e., sooty, porous aspect, fine-grained and “framboidal” texture) is overgrown and locally incorporated as py1’ in a coarser-grained, sieve-textured py2 (Fig. 4.8). The images display metal zonation reflecting variation in metal availability during py1 and py2 formation and subsequent dissolution-precipitation processes: (1) the diagenetic py1 core is more enriched in Mo relative to py2, with lesser Co, Ni, and W and minor to traces of Sb, Pb, Ag, Bi and Au; (2) the py1’, incorporated in py2 (i.e., at interface of py2 domains), shows enrichment of Co, Ni, Pb, Ag, Bi and weak Sb; (3) the py2 is composed of two distinctive domains, as confirmed by EBSD imaging, with each domain either enriched in W or Tl compared to the other, but the cores of both are enriched in Co and Ni. The domains are notably depleted in Bi, Au, Mo and Cu; and finally (4) Mo, Au, Sb and minor Cu appear to be enriched on the margin of py2.

Large et al. (2009) studied four sediment-hosted gold deposits (i.e., Sukhoi Log, Bendigo, Spanish Mountain, North Carlin Trend) and proposed chemical criteria to distinguish pyrites of early diagenetic versus metamorphic/hydrothermal orogenic and Carlin type settings (Fig. 4.9). These defined fields are integrated with the dataset herein using individual time-slices of the laser traverse data used to construct the pyrite trace element maps presented above. The fields defined in the Ag versus Ni plot are used therefore to define the nature of the pyrites analyzed and thus establish the origin of the contained metals during pyrite growth. In doing so this provides a means to also assess the type of gold event(s).

Distribution of individual time-slices of data in selected binary plots (Fig. 4.10) suggests the presence of two distinct pyrite types, these being early diagenetic and late metamorphic/hydrothermal, which is consistent with the petrographic observations (Fig. 4.8). Furthermore, by examining the element specific distribution in the context of pyrite types it is possible to relate the element enrichment/depletion in each of these pyrite types to a process. Thus, by integrating the element maps with the binary plots, it appears that py1 and py1' correspond chemically to early diagenetic pyrite, which thus suggests that the associated element enrichments in Co, Ni, Pb, Ag, Bi, Mo, W and Sb are also of the same origin. These elements were remobilized during the conversion of py1 to py2 via dissolution-precipitation processes that resulted in formation of the metamorphic/hydrothermal orogenic-type py2. The binary plots in Figure 4.10 clearly highlight these elemental enrichments and in the case of Bi and Sb allow a clear subdivision of the data into two distinct groups designated by A and B (Fig. 4.10D, J), which can then be used to define other associations. Thus for gold, which overgrows py2 and occurs in py1 (Fig. 4.8I), it appears to have been introduced by late metamorphic/hydrothermal processes based on the distribution of data in Figure 4.10A and is seen to be associated with As, Se, Te, Bi, Sb (group B, Fig. 4.10D, J), Mo and low-Ag. The following points are also noted: (1) Au does not appear to have originated from the early diagenetic py1 (-py1'); and (2) the locally high content of Au in py1 (Fig. 4.8) may be attributed to late precipitation processes in porous py1 (-py1'). Moreover, considering the distribution of selected elements throughout the early diagenetic pyrite (Co, Pb, Ni, W, Mo) and the similar behavior of As-Se-Te to Au (Figs. 4.8, 4.10), only one gold event is suggested in this sample based a compilation of the data in Figure 4.10L, a composite elemental plot.

A pyrrhotite grain was also analyzed from sample AMB-126231 using the traverse mode.

The results show relatively flat chemical patterns (i.e., chemically uniform) with low metal contents, except for Ni, across the analyzed grain (Fig. 4.11). Regarding the Au content, the values are mainly below the detection limit, except for one spot around $t \approx 16$ s where Au = 2.4 ppm. However, no specific elemental association is noted for this Au peak suggesting an erratic distribution and thus it is not possible to relate it to a specific gold event.

A second sample (AMB-126231; Gourcerol et al., 2015a) was also selected for elemental mapping to further characterize the nature of py2 that occurred as disseminations along a chert band in silicate-facies BIF (Fig. 4.12). In this sample, an aggregate of three subhedral to euhedral py2 grains (confirmed by EBSD imaging) showed distinct metal enrichment: (1) two of the grains display Ni-As-Se enrichment in their cores, hence during the growth of the core zones, which are surrounded by distinctive Co (As) -rich and Ni-Se -rich outer growth zones; (2) one pyrite displays a Co-As(-Se) and Ni-As-Se enrichment during its initial formation with an associated Co-Ni-As-Se core growth zone and distinctive Co-As -rich and Ni-Se -rich outer growth zones (Fig. 4.12). The pyrite grains are overgrown by a later stage of pyrite growth that is enriched in Mo, Sb, Te, Bi and Ag (Fig. 4.12). Despite values close to detection limit, the elemental maps suggest the presence of gold mineralization as inclusions (Fig. 4.12L).

Using selected Ag versus Ni plots (Fig. 4.13), as in the previous mapped grains, the elemental distributions show similar trends as for sample AMB-126223 despite the notable absence of an early diagenetic pyrite (i.e., py1). This latter feature may suggest therefore an orogenic metamorphic/hydrothermal affinity for the pyrites (i.e., py2) formed from dissolution/precipitation processes of an earlier diagenetic pyrite not preserved in the sample. Moreover, the distribution of trace elements in the grains (Fig. 4.13) indicates variable element associations: (1) Co, As and variable Se reflect the initial formation of the core zones that were

seen in the pyrite maps (Fig. 4.12); (2) Mo, Sb, Te, Bi, Pb and variable Se reflect the late-stage overgrowth on the py2 aggregate; and (3) minor inclusions of U randomly distributed through the host pyrites. Gold distribution reflects two distinct trace element associations: (1) Co, As, Se, a weak Bi, Pb and Te, along with low Ag contents, which was not clearly seen in Figure 4.12 due to the low Au content; and (2) Ag, As, Sb, Te, Se, Bi and Pb, which may reflect inclusions in py2 based on the maps (cf. white arrows on Fig. 4.12). Considering the plot of Mo-Sb-Te-Bi-Pb versus Co-As (Fig. 4.13K), which correlates with, respectively, the metal-rich rim and core of pyrites, two distinct elemental gold associations are clearly seen, which confirms the presence of two distinct gold events in this sample.

Finally, sample AMB-126228 from the Central BIF was selected based on the presence of py3 grains occurring along a chert band in the oxide-facies BIF. This euhedral py3, seen disseminated in a chert band, shows enrichment in Co, Ni, Pb and Bi (Fig. 4.14). In terms of the elemental distribution and associations using the Ag versus Ni plots, the data suggest the pyrite has chemical affinities with metamorphic/hydrothermal orogenic-type pyrite and is largely metal-poor (e.g., Au = <0.3 ppm). Furthermore, relative to py1 and py2 the sample is metal depleted despite the presence locally of galena inclusions as suggested by punctually high Pb values (Fig. 4.15C). In contrast to py2 from samples AMB-126223 and AMB-126231, py3 does not appear to have been formed from dissolution-precipitation of earlier diagenetic pyrite, as suggested by the data in Figure 4.15. Thus the results for these samples in context of the other data suggest two distinct metamorphic/hydrothermal events were responsible for the formation of sulfides (Figs. 4.10, 4.13 and 4.15).

4.5.1.2 Implications for gold mineralization

Based on integration of petrographic observations with elemental mapping and element associations, it has been shown that pyrite rather than metamorphic pyrrhotite is associated with gold mineralization in selected samples from the Meadowbank deposit as previously suggested by Janvier et al. (2015). Two distinct gold events are demonstrated in this study: (1) the first event is represented by gold inclusions in py2 along with a Ag-Pb-Se-Bi-Te-As-Sb element association, previously recognized by Janvier et al. (2015) as a pre-D2 event (i.e., prior to 1.85 Ga; Fig. 4.16); and (2) a second, newly recognized gold event represented in this study by late-stage growth of pyrite around aggregates of py2; this pyrite has a Se-Bi-Te-As-Sb elemental association (Figs. 4.10, 4.16). It is also noted that the second gold event occurs locally associated with sulfide-rich replacement of pre-existing magnetite bands by late-stage metamorphic pyrrhotite. Furthermore, the gold does not appear to originate from early diagenetic, framboidal pyrite located in the BIFs. Also, py2 seems to form from dissolution/precipitation of framboidal pyrite (py1) due to an increase in the through put of a metamorphic/hydrothermal fluid, which was likely gold-bearing.

4.5.2 The Meliadine gold district

In order to evaluate gold distribution in various sulfide phases and its relationship with other elements in the mineralized Pump and F-Zone BIFs and to identify gold event(s) within the Meliadine gold district, LA-ICP-MS traverse analyses were done on well characterized grains of arsenopyrite and pyrrhotite. Traverses were done because the sulfide grains are characterized by having sieve-textured features associated with various inclusions and fractures. The results of this study are also compared to results of LA-ICP-MS sulfide mapping done on arsenopyrite

grains by Carpenter (2004) and Lawley et al. (2015c).

4.5.2.1 LA-ICP-MS trace element chemistry

Euhedral arsenopyrite grains from the Pump and F-Zone deposits (e.g., Gourcerol et al., 2015c) located along the regional Pyke Fault in the Meliadine gold district were used for LA-ICP-MS analysis. These samples (i.e., MEL-004 and MEL-018) are cut by several late-stage micro-fractures and, given their possible significance, are shown on both the petrographic images of the analyzed grains and their trace element profiles as dashed black lines (Figs. 4.17, 4.18, 4.19). These fractures show significant enrichment in a variety of metals, such as Zn, Ag, Bi, Pb, Ni, Co, Te, Se, Sb and Mo, and are chemically associated with gold mineralization. Furthermore, the data suggests two distinct fracture sets based on element association: (1) a fracture set associated with Ag, Bi, Pb enrichments combined with variable Ni, Zn, Co, Sb and Mo observed in both deposits; and (2) a fracture set associated with enrichment in Se and Te with variable Ni and Zn. Significant depletion in Bi, Pb and Co was also observed, but only in arsenopyrite from the Pump deposit. Moreover, element profiles show that where the arsenopyrite cores are devoid of fractures and inclusions; they are depleted in Ni, Te, Se, Sb and Mo and the other base metals relative to the fractured and sieve-textured arsenopyrite. This observation suggests that metals have been introduced by later fluids that migrated along the fractures whereas zone refining type processes may be responsible for metal depletion.

Examining the gold contents of the traverses, it appears that the arsenopyrite core shows a weak, uniform concentration signifying that invisible gold is present in these arsenopyrite grains. Moreover, the two fracture sets display enrichment in gold content relative to the core of the grain either as invisible gold (Figs. 4.17, 4.18, 4.19; Au >30 ppm) or as visible gold (Fig. 4.19;

Au = 38-156 ppm) suggesting either two distinct gold events: (1) one associated with precipitation of arsenopyrite grains; and (2) a second associated with base metal-rich fractures or remobilization of gold from the core of arsenopyrite grains into fractures by later stage metal-rich fluids. It is noted that Sb and Mo show relatively similar patterns despite variable content, which locally appear to be antithetic to gold mineralization (Figs. 4.17, 4.18; illustrated by black arrows). Additionally, a traverse analysis on a fracture site filled by late-stage pyrrhotite and locally chalcopyrite was performed (Fig. 4.20) and demonstrates that gold and base metals, such as Bi, Pb, Co, Te and Sb, are higher in the bounding arsenopyrite grain rather than in pyrrhotite inclusion. However, for all the elemental profiles, except for Ni, there are diffusion-like shapes, which suggest there has been removal of elements along the fluid flow path, which is best seen for the bottom of the plots for Co and Sb and perhaps Au. Thus, the fluid was undersaturated in these elements and able to remove them, which resulted in the gradients observed.

As done above, the nature of the gold event can be examined using the individual time-slices of data from the three line traverses (Figs. 4.17, 4.18, 4.19). Considering that the Ni-Te-Se-Sb-Mo element association represents the arsenopyrite core, whereas Pb-Bi-Zn represents the late fracture event, it appears that only one event has introduced gold into the system, suggesting that material filling late fractures represents remobilization of gold from the arsenopyrite lattice and precipitation of invisible to visible gold into late fractures (Fig. 4.21A) as the gold content increases with Pb+Bi+Zn content.

Based on element profiles (Figs. 4.17, 4.18, 4.19) and selected diagrams (Fig. 4.21B, C), it appears that fracture sets show multiple element associations and these fracture sets also show variable gold content: (1) enrichment of Te-Se along fractures associated with invisible gold in the Pump deposit sample (Fig. 4.17); (2) enrichment of Co along with Pb-Bi-Zn-Ag in fractures

associated with invisible gold (Fig. 4.21B); (3) the association of Pb-Bi-Zn-Ag with invisible gold (Fig. 4.21B, C); and (4) Pb-Bi-Zn-Ag associated with visible gold (Fig. 4.21B, C). These observations of elemental associations suggest a model for gold that involved a prolonged deformational and hydrothermal history with mobilization of earlier deposited gold, as proposed by Lawley et al. (2015c).

Lastly, the results of elemental LA-ICP-MS mapping by Lawley et al (2015) on late-stage overgrowths of arsenopyrite devoid of inclusions and fractures showed this phase tends to be enriched in a Te-Co-Ni assemblage and depleted in Au-Se-Sb. Although not clearly observed in our element profiles, this statement is observable considering the compilation dataset (Fig. 4.21D).

4.5.2.2 Implications for gold mineralization

The results of LA-ICP-MS elemental mapping of arsenopyrite by Carpenter (2004) and Lawley et al. (2015c) suggested that gold mineralization was introduced during the growth of coarse-grained arsenopyrite and was subsequently remobilized during deformation/metamorphism (Wagner et al., 2007) and pressure-solution processes accompanying the Trans-Hudson Orogeny (i.e., 1.86-1.85 Ga). These latter events resulted in the concentration of gold in later stage recrystallized arsenopyrite and in fracture-fills. These conclusions are compatible with the results presented here based from which it was possible to distinguish multiple mineralizing events, one contemporaneous with the sulfide event and another related to fluid, which infiltrated the arsenopyrite along multiple fracture sets. Our data indicate that an elemental association of As-Ag-Bi-Pb-Se-Te with Au characterizes the mineralized BIF. Furthermore, there is a significant Bi-Mo-Te association, perhaps due to micro-inclusions of

tellurides, that relates to gold mineralization (Fig. 4.21E, F) and which may reflect the late gold event.

4.5.3 The Musselwhite deposit

Several authors have reported that gold in the Musselwhite deposit is associated with the pyrrhotite grains that appear to replace pre-existing Fe-rich material and/or form in coarse-grained, fractured almandine garnet porphyroblasts (e.g., Biczok et al., 2012; Oswald et al., 2015). In order to evaluate this proposal, traverses were performed on several pyrrhotite grains to determine its trace element chemistry. The data were also used to compare to the enrichment of other elements in the silicate BIFs. Additionally, several py1 (referring to fine-grained, annealed grains disseminated as inclusions in metamorphic pyrrhotite) were analyzed using spot mode and one grain of py2 was analyzed via a traverse. The combination of these results is used to identify and chemically characterize the gold event(s) within the Musselwhite deposit.

4.5.3.1 LA-ICP-MS trace element chemistry

Euhedral to subhedral pyrrhotite grains either disseminated in chert bands or as fracture-filling in euhedral garnets (Figs. 4.22, 4.23) display fairly similar features and gold element associations. In general, the core of pyrrhotite shows low base- and precious-metal contents that have been modified either by late fractures, illustrated by dashed black lines on element profiles, and/or local inclusions. Based on petrographic and geochemical studies, it appears that only one set of fractures observed in pyrrhotite grains contains significant base-metal enrichment that includes Zn, Pb, Bi, As, variable Cu, Te, Sb and Ag, along with Au. Local inclusions are also recorded based on selected profiles of trace element concentration (Figs. 4.22, 4.23) that illustrate local enrichment of Cu, Zn, Se, Ag and variable Te and As along with Au. In both

cases, the Au enrichment occurs mainly as micro-grains too small to be observed optically or with the SEM. Considering the Cu-Ag-Te-Se element association within the Au-rich pyrrhotite inclusions and Pb-Bi within late Au-rich fractures, a compilation of individual time-slices of data from ten line traverses on pyrrhotite grains was done and these data suggests there was only a single Au event (Fig. 4.24). Gold may be hosted in the pyrrhotite lattice to be later exsolved and remobilized into late fractures by later stage base-metal - rich fluids (i.e., Pb, Bi; Fig. 4.24) as observed in the Meliadine gold district (Fig. 4.21A).

Traverses and spot analyses done on pyrite samples (i.e., py1 and py2) also detected significant contents of Au (i.e., b.d.l. to 11000 ppm) in py2, which illustrates a later stage sulfide event given that the pyrite locally overprints pyrrhotite (Fig. 4.7D). Typically, the euhedral to subhedral py2 has a core relatively enriched in base metals, such as Zn, Ni, Sc, Sb, Se, Te (Figs. 4.25, 4.26, 4.27), which is cut by several micro-fractures that are also enriched in base- and precious metals such as Zn, Pb, Bi, Te, Se, Ag and Au with variable Sb. The latter data indicates a single set of fractures (Fig. 4.25) but that it shows a significant gold-rich inclusion along with Ag, Te and variable Cu, Zn, Bi, Pb enrichments. A compilation of time-slices datasets from py2 suggest the presence of Ag- rich tellurides closely associated with the fracture set, as illustrated by a Zn-Pb-Bi element association (Fig., 4.26A, B) and Ag-Au- rich tellurides occurring mainly as inclusions in py2 (Fig. 4.26A, B, C) along with the highest Au and Ag concentrations (Fig. 4.26C, D).

Geochemically, py2 differs from the barren py1, which is characterized by annealed grains disseminated in pyrrhotite grains (Fig. 4.27) in addition to variable pyrites from the Meadowbank deposit (cf. Sec. 4.1.1). Selected criteria from the Large et al. (2009) data set cannot be applied to this py2 due to its high Ni and Ag contents (Fig. 4.27A) whereas the few

spot analysis data for py1 suggests a metamorphic/hydrothermal orogenic-type chemical affinity (Fig. 4.27B). Comparison of py1 and py2 data with two distinct pyrites from the Sukhoi Log deposit (Fig. 4.28; Large et al., 2007) show that py1 displays a pattern similar to pyrites formed from metamorphic/hydrothermal conversion of early diagenetic pyrite from sedimentary rocks within the Sukhoi Log deposit (data in Fig. 4.9) whereas py2 from the Musselwhite deposit shows a pattern similar to gold-telluride pyrite from bedding-parallel quartz veinlets from the Sukhoi Log deposit, which were generated by an externally derived fluid. These distinct geochemical relationships suggest therefore that py1 and py2 from the Musselwhite deposit may have formed from different fluids. Moreover, py1 may represent a proxy for metamorphic pyrrhotite as their relationship (py1 versus pyrrhotite) suggests an increase of metamorphic conditions leading to annealing and recrystallization of py1 and crystallization of pyrrhotite confirming that pyrrhotite may be formed from a metamorphic/hydrothermal orogenic-type fluid.

4.5.3.2 Implications for gold mineralization

The LA-ICP-MS trace element chemistry and petrography indicate that the metamorphic pyrrhotite is associated with gold mineralization along with a Cu-Ag-Te-Se-(As) element association reported by Oswald et al. (2015). Gold in this mineralizing event was later remobilized by subsequent fluids having a Pb, Bi signature into a fracture network representing a second gold event. In addition, a probable third gold mineralizing event is reported for the first time at this locality associated with late pyrite (i.e., py2) with an Ag-Te element association, as illustrated by an Au-Ag- rich telluride mineralization. This latter event differs from the gold-bearing pyrrhotite event, thereby suggesting three different mineralizing fluids. It is noted also that py1 is probably formed from metamorphic/hydrothermal orogenic fluids whereas py2 reflects a distinct fluid, which may represent either a metamorphic or magmatic component, as

documented by the isotopic analyses (i.e., $\delta^{15}\text{N}$, $\delta^{18}\text{O}$) of Isaac (2008), which suggest that S-type granite dykes located 1 kilometers west of the deposit may represent a potential fluid source.

4.6 Discussion

In this study, three Canadian Algoma-type BIF-hosted gold deposits (i.e., Meadowbank, and Meliadine districts from the Churchill Province, Musselwhite area from the Superior Province) were selected for detailed *in-situ* LA ICP-MS elemental mapping and point analysis of sulfide phases in order to assess potential sources for mineralizing fluids, assess elemental associations, determine the relative timing of metal and sulfide enrichment event(s), and to evaluate the gold enrichment processes.

The complexity in element associations documented here for nominally similar BIF hosted Au deposits is a function of several aspects: (1) element coupling and decoupling; (2) elemental paragenesis; and (3) the nature of reactivation or overprinting events in orogenic deposits (Kontak, 2015). The variable complexity of mineral geochemistry in hydrothermal ore systems is consistent with longevity of the mineralizing systems (Kontak, 2015). Further, as is considered below, the stratigraphic associations at the level of the greenstone belts where mineralization occurs and the gold source are additional parameters that affect the chemical signal of the sulfides.

4.6.1 LA-ICP-MS method: implications for identifying gold events and their chemical signature

The element distribution maps as well as the traverse and spot analyses reported herein were determined by LA-ICP-MS on carefully selected, sulfide phases such as pyrite, arsenopyrite and

pyrrhotite characterized petrographically and by SEM. This method can provide meaningful quantitative distributions of major, minor and trace elements as maps or profiles in addition to concentrations by resolving the data as time domain slices. Importantly, this latter process then permits evaluating the data in terms of multi-element chemical associations.

The major advantage of LA-ICP-MS maps and time-resolved traverses over various forms of bulk analysis is the ability to recognize precisely any element associations as well as their spatial distribution in the sulfide lattice (e.g., fracture networks, inclusions) as the laser beam scans across each sulfide sample, thus minimizing the averaging effect of more conventional bulk solution-based ICP-MS analyses (e.g., Janvier et al., 2015; Oswald et al. 2015).

Furthermore, this study shows that quantitative traverses, when combined with careful petrographic observations, may provide observations similar to element distribution maps but in a shorter timeframe (e.g., elemental mapping of arsenopyrite grains in Lawley et al. (2015c) versus line traverses of arsenopyrite grains herein) and also for less cost (Note: also not discussed here, one of the limiting factors of LA ICP-MS mapping is the cost, which is time and lab dependent). Furthermore, the compilation of time-slice datasets from LA-ICP-MS analysis provide a means to assess both the number of gold events and the elemental signature of each, which has not been so easily available before, but with this method can be more routine.

However, a limitation at present has to do with the size of the laser beam, which perhaps cannot analyze very small sulfide grains and during rastering and traversing will average data over small (relative to the beam diameter) inclusions and fractures.

4.6.2 Comparison of elemental association and implications for source reservoirs of gold mineralizing events

At the Meadowbank deposit, analysis of sulfides indicates two distinct gold events, as represented by micro-inclusions and invisible gold within the overgrowth rim domain, both associated with the same pyrite generation (i.e., py2). This pyrite is considered to originate via a dissolution/precipitation process (e.g., Putnis, 2002; Putnis et al., 2007; Putnis and Putnis, 2010), which affected the early diagenetic framboidal pyrite (i.e., py1). The fluids, which mediated formation of the pyrite (py2), are considered to be of metamorphic/hydrothermal origin and generated by orogenic processes, hence similar to the origin of pyrites observed in the Sukhoi Log, Bendigo and Spanish Mountain sediment-hosted gold deposits (Large et al., 2007, 2009, 2011). Analysis of the cores of these metamorphic pyrites from the latter localities showed they are enriched in a variety of elements including Mo, Pb, Ni, Co, W.

Although the gold-bearing pyrite (py2) appears from petrographic observations to form after early diagenetic pyrite, Au, as well as Se, Te, As and some part of the Ag, Sb budget, appears to represent an external metamorphic/hydrothermal fluid, which precipitated coevally with/or during the late-stage growth of py2 as part of the sulfidization (i.e., replacement) of pre-existing stratabound magnetite bands.

In the Meliadine gold district, one gold event along with later remobilization is recorded for arsenopyrite grains in the F-Zone and Pump deposits. The first gold mineralizing event is associated with an As-Ag-Se-Te element association as invisible grains in hydrothermal arsenopyrite grains. Late remobilization is illustrated by precipitation of gold into fracture networks or crosscutting veins either as native or invisible gold (Wagner et al., 2007) by base

metal-rich metamorphic fluids (e.g., Pb-, Bi-, Se- and Te- rich fluids).

The Musselwhite deposit also displays three distinct gold events, which are associated with either metamorphic pyrrhotite or late pyrite grains. The first gold event shows a Cu-Ag-Se-Te (As) element association and, based on the data herein, may indicate this mineralization occurs as invisible gold within the pyrrhotite lattice. In contrast, the second event as evidenced by the presence of base metal-enrichment on fracture networks in pyrrhotite grains, presumably reflects a late, metal-rich metamorphic fluid (i.e. Cu-, Zn-, Bi- and Pb- rich fluid), which appears to have remobilized and concentrated gold in fracture sets. Finally, a third gold event, hosted in a late generation of pyrite, exhibits an Ag-Te element association and differs from the first event by its distinct gold source, which may be metamorphic/magmatic rather than metamorphic/hydrothermal orogenic (Isaac, 2008).

These three BIF-hosted gold deposits, located in different geological provinces, exhibit similarities regarding the inferred source and relative timing of gold events based on the element associations (i.e., Au-As-Se-Te-Ag), textural and chemical evidence documented for late remobilization into fracture networks by base metal-rich metamorphic fluids (mainly Pb-Bi-rich) as observed in pyrite, pyrrhotite and arsenopyrite grains. The gold event associated with this element association appears to have been introduced by an external fluid as seen in pyrite at the Meadowbank deposit and in hydrothermal arsenopyrite in the Meliadine gold district or metamorphic pyrrhotite lattice in the Musselwhite deposit. This geochemical similarity among different deposits confirms the epigenetic origin of gold and suggests a common source from which these elements were leached and subsequently channeled along structural conduits (e.g., faults, shear zones) into Algoma-type BIF host rocks, at higher crustal levels. These BIF

horizons represent, in the context of the ore deposit setting, potential sinks as the iron content of these rocks acts as a favorable chemical trap through its highly reactive capacity with the reducing, sulfidic gold-bearing fluid which led to gold precipitation, as discussed by many (e.g., Poulsen et al., 2000; Dubé et Gosselin, 2007; Phillips and Powell, 2010). This process is analogous to that which would occur in other rock types, for example where a similar fluid would interact with carbon-bearing rocks (e.g., graphitic mudstone, black shale) and thereby reducing the gold-complex and precipitating gold within quartz-carbonate veining systems (Phillips and Powell, 2010).

Regarding each constituent of the element association related to gold mineralization, Pitcairn et al. (2006) pointed out that Au, Ag, As, and Se are found in significantly lower concentrations in rocks of higher metamorphic rank compared to their unmetamorphosed protoliths. This observation has been interpreted to suggest the source rock for these elements may initially be unaffected or only weakly affected by a given metamorphic event before the liberation of these elements followed by a significant metamorphic event and transporation by a fluid phase. This process represents a devolatilization model in which the elements of interest may be removed from source rock at the greenschist-amphibolite transition during prograde metamorphism (e.g., Pitcairn et al., 2006; Phillips and Powell, 2010) and carried by a low-salinity, H₂O-CO₂-H₂S rich fluid (Phillips and Powell, 2010). In this study, the metamorphic/hydrothermal orogenic processes appear to have driven fluids leading to the concentration of precious metals and associated elements into the BIF as illustrated by Figures 4.10, 4.13 and 4.27.

This study does not, however, advocate for extraction of Au and other metals from gold-rich diagenetic pyrite hosted within carbonaceous black shale successions, as has been argued for several sediment-hosted orogenic gold deposit settings by Large et al. (2007, 2009, 2011). The

reason for this conclusion relates to the results presented above whereby elemental mapping of framboidal pyrite in the Central BIF from the Meadowbank deposit indicates a lack of significant Au content. In addition, we note that there is also a lack of any gold association with a specific suite of elements (e.g., Co, Ni, Pb, Zn, W, Mo) that are highly concentrated in the diagenetic pyrite (Figs. 4.8, 4.10). Furthermore, a similar argument is made based on data for the Meliadine gold district and Musselwhite deposit.

Finally, the second gold event reported herein for the Musselwhite deposit does not share either geochemical or mineralogical similarities with the other deposits studied in that this gold event is characterized by an Au-Ag- telluride association. As explained previously, this later event may reflect the ingress of a new external Au-Ag-Te rich fluid suggesting a different fluid source than the first event and a different gold enrichment process. The latter is based on the observation that the gold-bearing pyrite does not show an element association typical of a metamorphic/hydrothermal process, as suggested for the Meadowbank deposit and the first gold event in the Musselwhite deposit. This second mineralization event appears, however, to represent a minor part of the Musselwhite deposit relative to first gold event.

4.6.3 Influence of the stratigraphy

Although the three deposits show similarities regarding potential fluid sources and timing of the main gold event, significant differences do exist however as to which sulfides are auriferous: pyrite in Meadowbank, arsenopyrite in Meliadine and pyrrhotite in Musselwhite. This difference in terms of a repository for gold may be influenced by the stratigraphy with which gold-bearing fluids reacted. For instance, formation of arsenopyrite requires As (e.g., Kretschmar and Scott, 1976), which, for the case of sediment-hosted gold deposits, is commonly sourced from

sedimentary wallrocks (e.g., Kontak and Smith, 1993; Bierlein and Crowe, 2000; Thomas et al., 2011). The fact that there is higher proportion of metasedimentary rock in the Meliadine gold district compared to the Meadowbank and Musselwhite deposits is consistent with this interpretation. Furthermore, the influence of stratigraphy is also illustrated by the elemental budgets in sulfides. For instance, pyrrhotite associated with gold mineralization at the Musselwhite deposit, is enriched in Ni, Co, Pd relative to pyrrhotite from the Meliadine gold district, which suggests the mineralizing fluids at the former deposit equilibrated to some extent with an ultramafic-mafic component in the stratigraphy, which is not prominent in the Meliadine gold district. Again, the geology of the settings is consistent with this interpretation.

However, the influence of the stratigraphy on the mineralizing fluid emphasises an important problem regarding preservation of gold tenor during exchange with the wallrock, which may modify fluid pH as well as other parameters encouraging destabilization of the gold complex in the fluid. Of particular relevance in this regard is the suggestion by Phillips and Powell (2010) that a mineralized fluid with some internal buffering, as provided for example by the presence of CO₂ in the mineralizing fluids, would allow interaction with stratigraphy without destabilization of the gold complex.

4.6.4 Influence of late deformation and metamorphism on gold mineralization

The influence of post-ore formation processes such as deformation and metamorphism is an important issue in gold deposits in the context of whether new gold is being introduced or pre-existing gold is being remobilized internally. At two of the deposits studied, there is evidence for later stage events, which partially remobilize gold from earlier sulfide lattice (i.e., arsenopyrite and pyrrhotite) due to introduction of base metal-bearing fluids along fracture networks. This

process results in concentrating gold either as visible native gold or an invisible component within sulfide grains.

Such remobilization and upgrading of gold is not a well-known phenomenon and has previously been studied in several deposit types, including VHMS (e.g., Wagner et al., 2007), sediment-hosted gold (e.g., Large et al., 2007, 2009), and orogenic gold (Tomkins et al., 2004). In these latter studies, these authors refer to a closed-system metamorphic event with gold internally redistributed. In contrast, for the Meliadine and Musselwhite deposits, the element associations of the metal-bearing fluids carrying Pb-Bi-Zn and Pb-Bi-Cu-Zn, respectively, suggest the influence of a similar stratigraphy in the fluid chemistry. Contrary to element associations with Au, such as Ag and As, the base metals do not exhibit variations related to metamorphic grade (Pitcairn et al., 2006) and may therefore represent weak sub-greenschist to amphibolite facies conditions. Furthermore, as pointed out by Lawley et al. (2015), remobilization of gold within a greenstone belt or within a deposit is an event of lesser magnitude relative to the original mineralizing event, thus the original nature of the primary event is retained.

4.6.5 Source of Au

There are many possible source reservoirs for gold in orogenic deposits and constraining their origins is challenging due to the equivocal nature of the fluid chemistry (e.g., isotopes, mass balances, fluid inclusions), as discussed extensively (McCuaig and Kerrich, 1994, 1998; Ridley and Diamond, 2000; Groves et al., 2003; Goldfarb et al., 2005; Pitcairn et al., 2006; Goldfarb and Groves, 2015). Included among the many models suggested are the older granite-greenstone terranes (Frimmel and Hennigh, 2015), clastic sediments in Phanerozoic belts (Pitcairn et al.,

2006), sulfides (e.g., diagenetic) in black shales (Large et al., 2007; Thomas et al., 2011), VHMS-style sulfide precipitates in volcanic-related hydrothermal systems (Moss et al., 2001) or the subcontinental lithosphere (Bierlein et al., 2006) and the mantle (Yue and He, 2008). In the previous sections we have eliminated the possible role of arsenian pyrite hosted in clastic sediments and pyritic black shales associated with the studied BIF-hosted deposits, which may have contributed Au (cf. Sec. 2). However, several lines of evidence pointing to a mantle source for the gold are possible. Several authors proposed that mantle-derived material such as hydrated and carbonated mafic to ultramafic melts (e.g., Groves et al., 1987; Phillips and Powell, 2010) may contribute to precious metal enrichment and in several studies based on Re-Os sulfide geochronology there seems to be some support (e.g., the Witwatersrand, Homestake deposits; Frimmel et al., 2014; Caddey et al., 1991; Morelli et al., 2010). Of particular relevance here is the case for the Homestake gold deposit, as it is hosted by Algoma-type BIF and shows a similar gold-trace element association, this being Au-Ag-As-Te-Se (Caddey et al., 1991; Morelli et al., 2010). Morelli et al. (2010) suggested that gold introduction is coincident with exhumation of crustal blocks. Thus, although not conclusive, there is a consistent element association with another BIF-hosted gold system which is at least suggestive that a common source may be represented for in the two settings.

Therefore, a possible scenario is that the mantle supplied a component of heat to the deep crust to form mafic melts from which gold was extracted by metamorphism/hydrothermal processes. Within the Abitibi greenstone belt, there is a clear spatial association between extensional structures bounding successor basins and earlier Au-rich VMS deposits (Gibson pers. Comm. 2015) and it must be recalled that, whereas the proximal heat source for VMS systems is subvolcanic intrusive granitoids (e.g., Franklin et al., 2005), there is a very clear mantle

component seen in recent studies (Chen et al., 2015). Finally, the Au content of mantle sulfides is an adequate source for gold in mantle-derived systems (Yue and He, 2008).

4.7 Conclusions

In this study of three Canadian Algoma-type BIF-hosted gold we have integrated the results of quantitative element distribution maps and traverse and spot analyses produced by LA-ICP-MS with detailed petrography of the same samples. The data provide the basis for the evaluation of gold distribution patterns in various sulfide phases (i.e., pyrite, pyrrhotite and arsenopyrite) present and determination of element associations and therefore the ability to assess the source and timing of gold event(s). The common gold mineralizing event for these deposits, which are epigenetic and associated with intense sulfide-replacement of stratabound, Fe-rich mineralogy typical of BIF, is characterized by an Au-As-Se-Te-Ag element association in addition to a later stage remobilization along fracture networks by a base metal-bearing metamorphic fluid (mainly a Pb-Bi bearing fluid). The results of this study suggest that gold events in these deposits are related to metamorphic/hydrothermal orogenic processes driven by devolatilization of an unmetamorphosed source rock leading to the generation of gold-bearing fluids which were structurally focused into oxide- and silicate-facies BIF. This latter rock type represents a sink for the gold-bearing fluid as its iron content acts as a favorable reactant for the sulfidic fluid transporting the gold which leads to destabilization of gold in solution assuming transport as a bisulfide complex. This study has also highlights the possible influence of the host stratigraphy which may act to stabilize the dominant sulfide in the system (e.g., arsenopyrite versus pyrite). Furthermore, subsequent deformation and metamorphic events may have acted to remobilize earlier gold which provides a means to upgrade gold tenor, as evidenced by the occurrence of gold along late fracture networks associated with Pb-Bi enrichment.

4.8 Acknowledgments

The authors gratefully acknowledge the staff of Agnico Eagle Mines Ltd. and Goldcorp Ltd. and more particularly the Meadowbank, Meliadine and Musselwhite regional exploration crews. The study is supported by both TGI-4 funding from Natural Resources Canada and funding through a Natural Sciences and Engineering Research Council Collaborative Research and Development agreement with participation by Agnico Eagle Mines Ltd and Goldcorp.

4.9 Figure captions

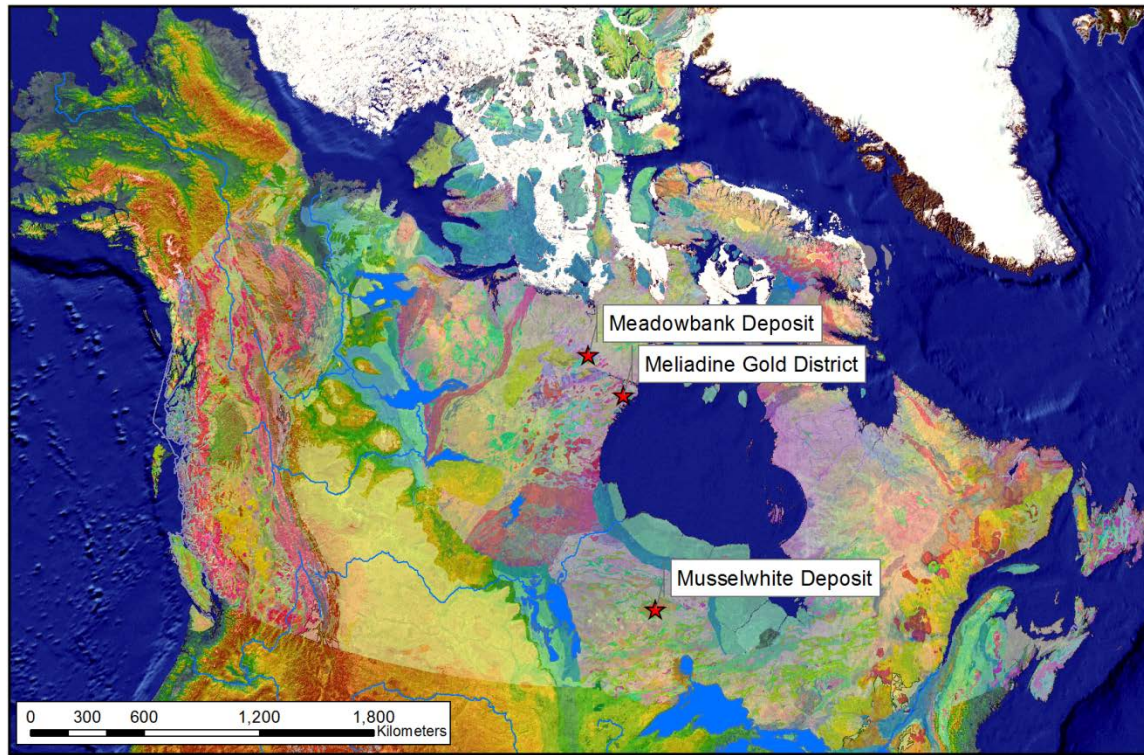


Figure 4.1: Localization of the three deposits investigated in this study. The Meadowbank deposit and the Meliadine gold district are within the Churchill Province, west of the Hudson Bay whereas, the Musselwhite deposit is located within the Superior Province, south of the Hudson Bay (after Wheeler et al., 1996).

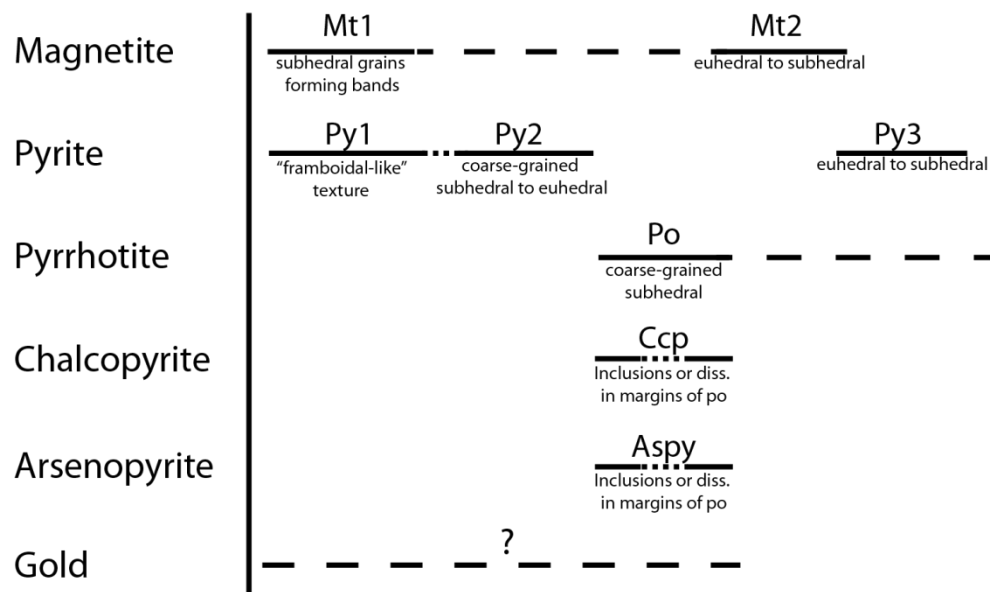


Figure 4.2: .Paragenetic chart for sulfides minerals and magnetite from BIFs in the Meadowbank deposit.

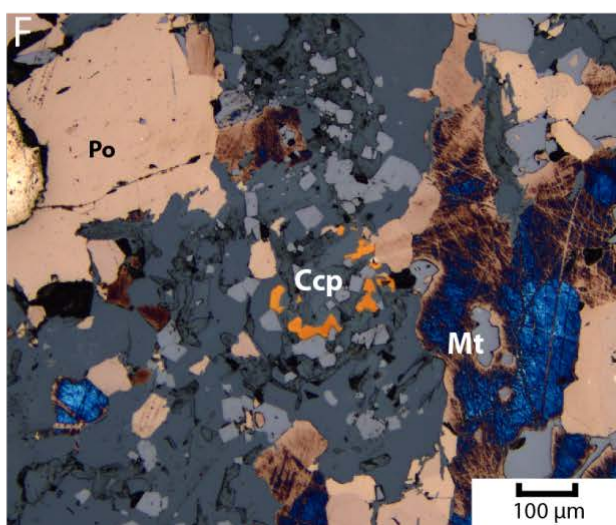
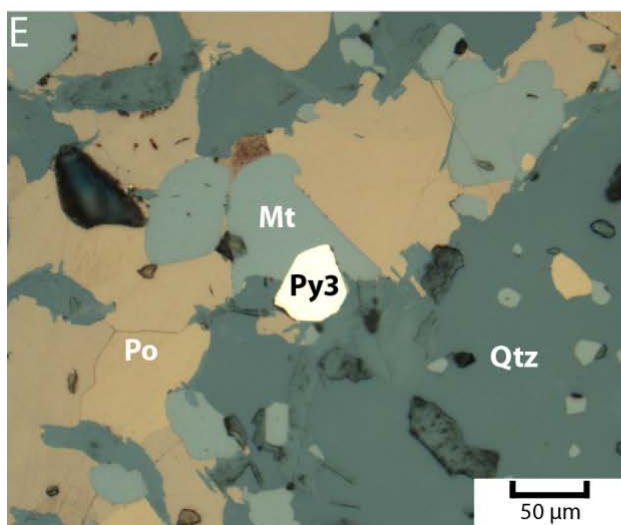
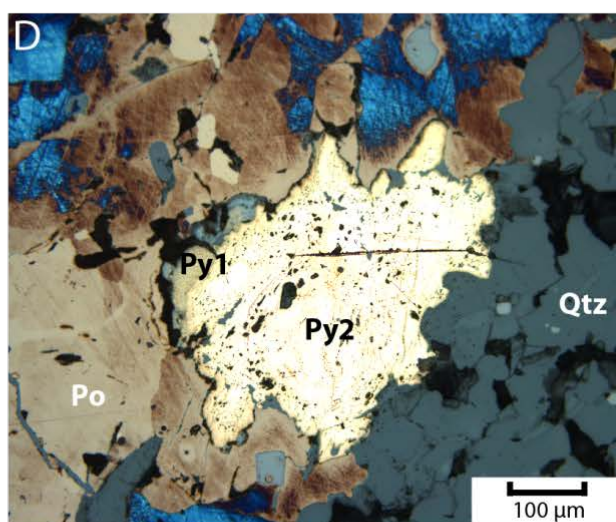
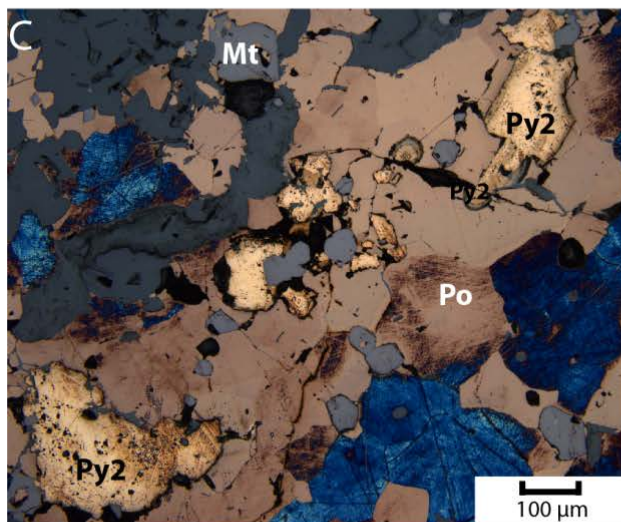
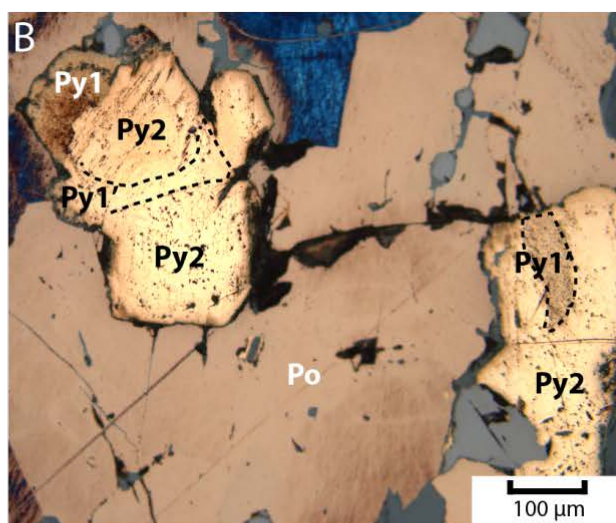
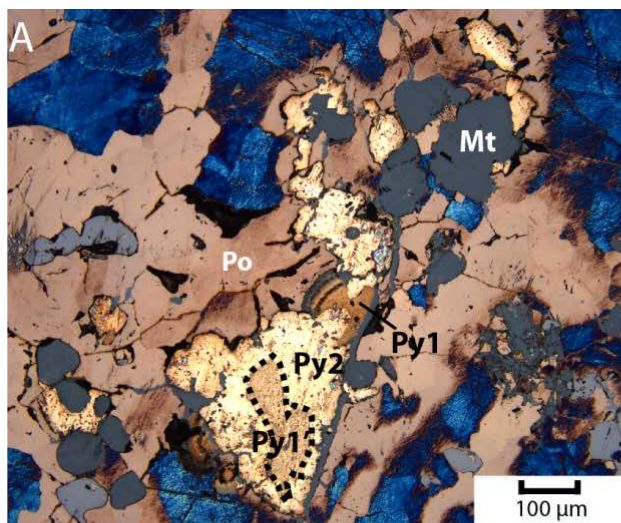


Figure 4.3: Reflected light photomicrographs of sulfide minerals from the Meadowbank deposit.

A to D) Aggregates of fine-grained, sooty pyrite 1 and coarse-grained, sieve-textured pyrite 2 hosted in metamorphic pyrrhotite and overprinted by later stage magnetite. Pyrite 2 may rarely show some internal zonation suggesting pyrite 1' inclusions. E) Euhedral to subhedral grains of pyrite 3 overprinting magnetite and metamorphic pyrrhotite. F) Fine-grained, anhedral to subhedral chalcopyrite at the margin of metamorphic pyrrhotite. Abbreviations: Ccp = chalcopyrite, Mt = magnetite, Po = pyrrhotite, Py = pyrite, Qtz = quartz.

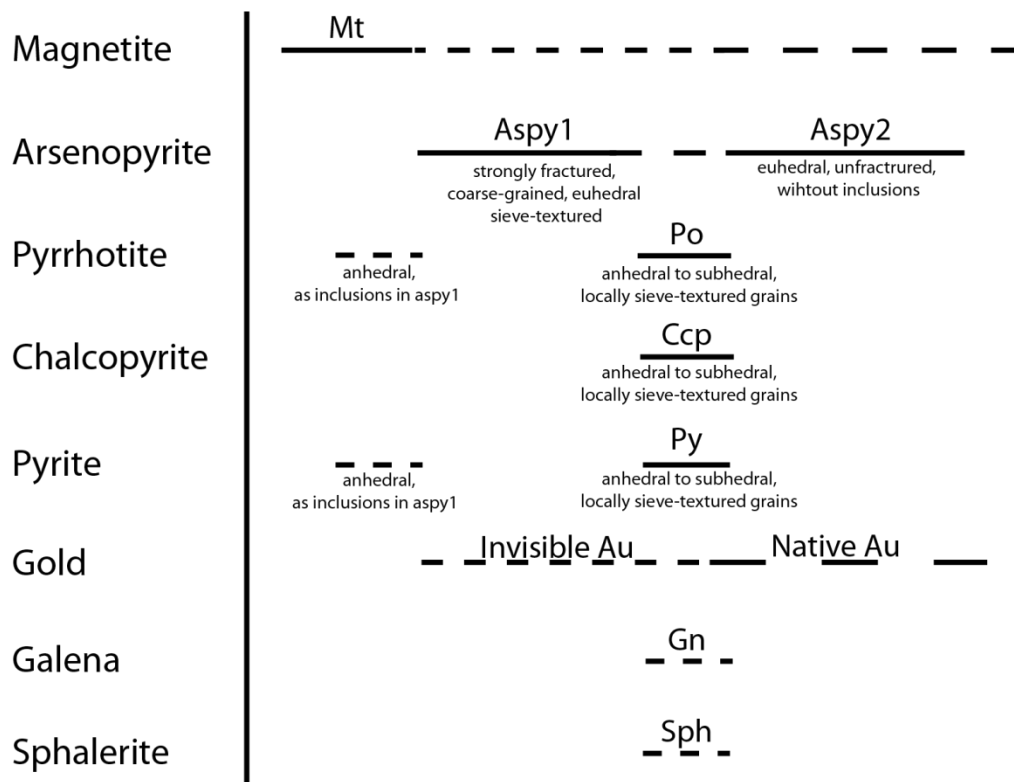


Figure 4.4: Paragenetic chart for sulfides minerals and magnetite from BIFs in the Meliadine gold district.

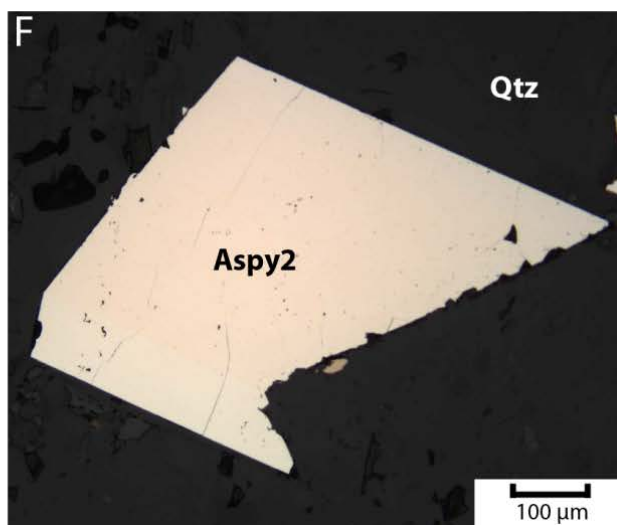
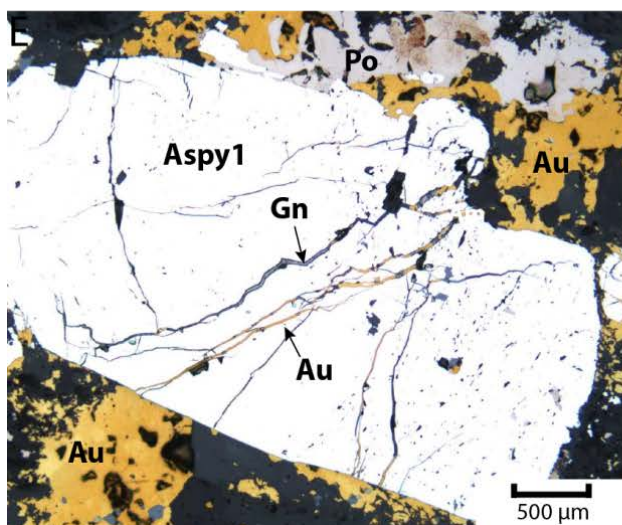
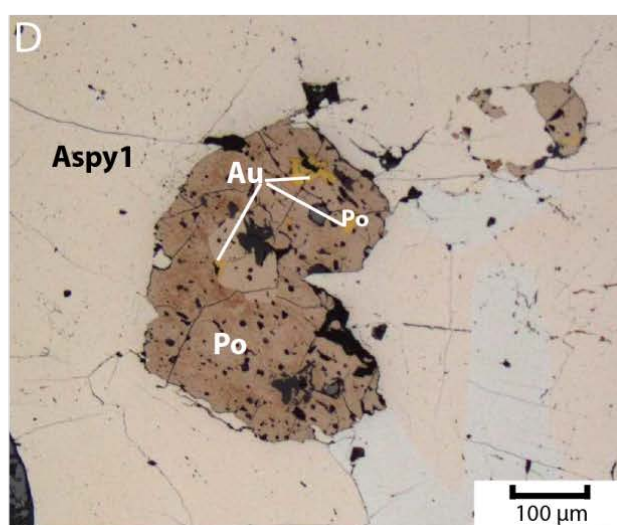
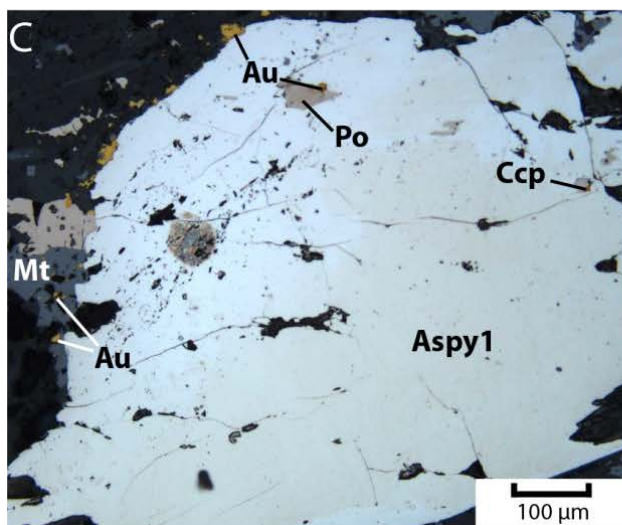
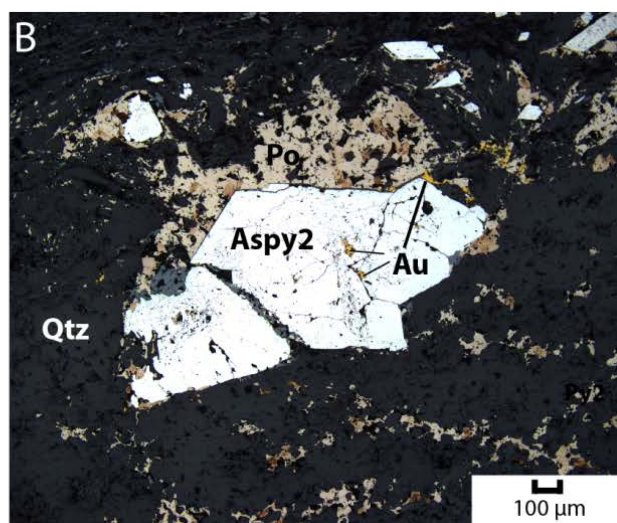
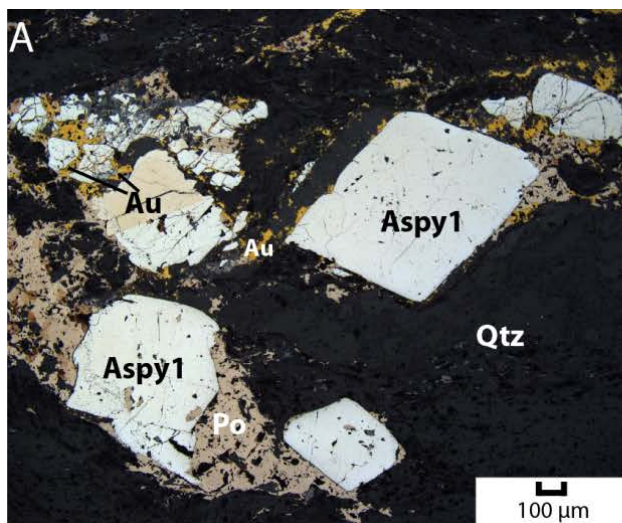


Figure 4.5: Reflected light photomicrographs of sulfide minerals from the Meliadine gold district. A to E) Strongly fractured, coarse-grained, euhedral, sieve-textured arsenopyrite crystals showing anhedral to subhedral grains and aggregates of pyrrhotite, chalcopyrite and galena along late fractures and/or as inclusions with gold. F) Unfractured, inclusion-free, fined-grained euhedral arsenopyrite 2 that occurs along a foliation in a quartz matrix. Abbreviations: Am = amphiboles, Aspy = arsenopyrite, Au = gold, Ccp = chalcopyrite, Gn = galena, Mt = magnetite, Po = pyrrhotite, Py = pyrite, Qtz = quartz.

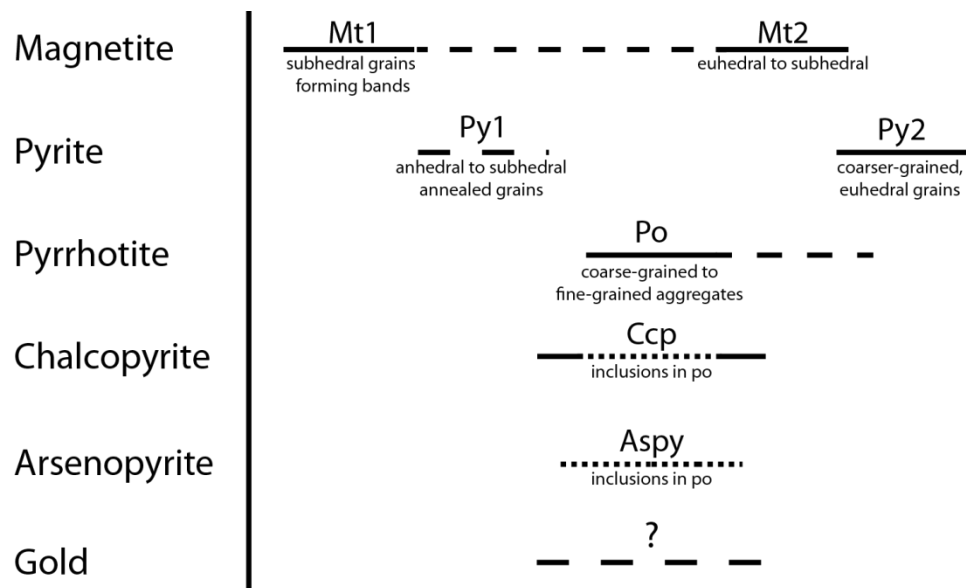


Figure 4.6: Paragenetic chart for sulfides minerals and magnetite from BIFs in the Musselwhite deposit.

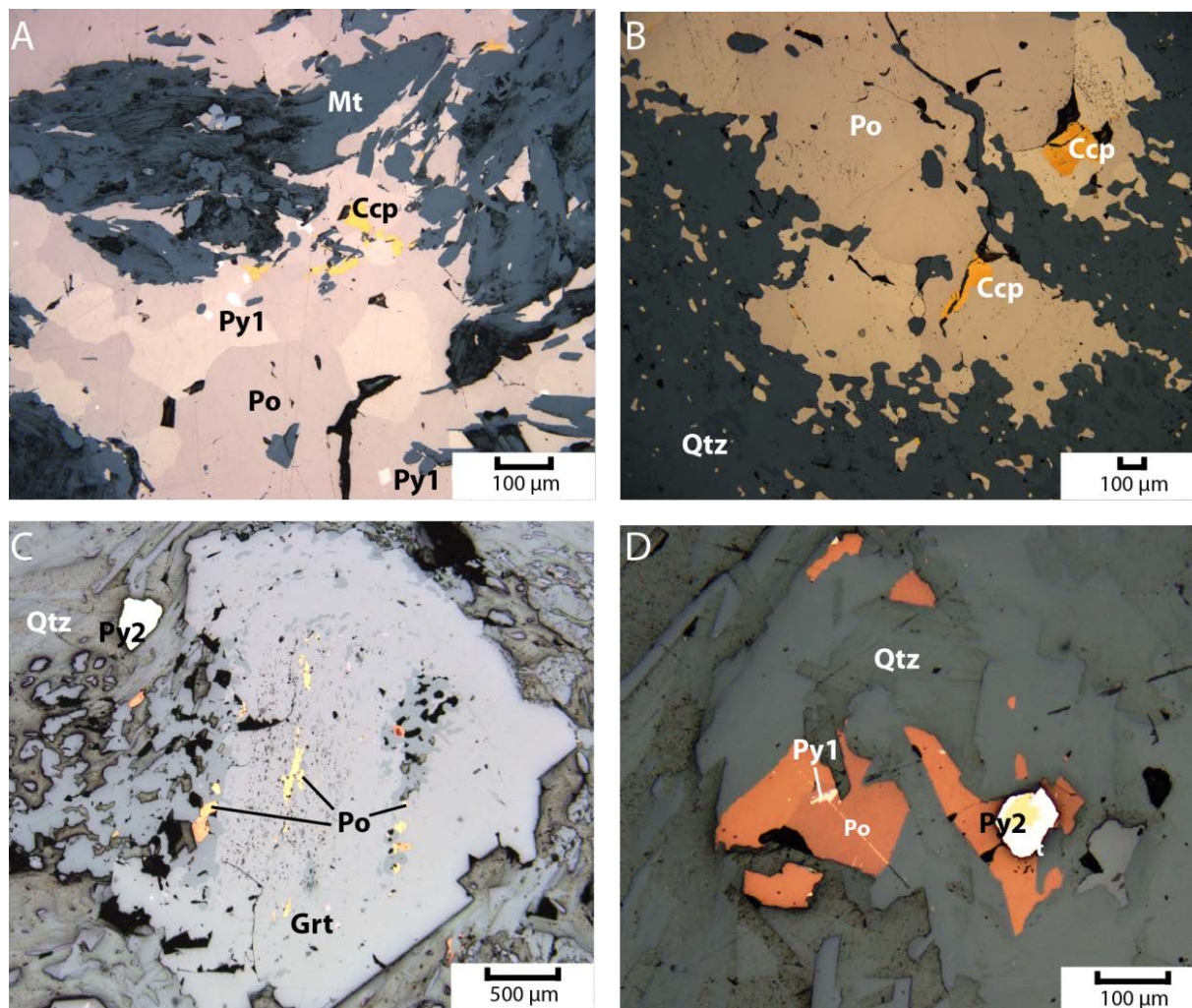


Figure 4.7: Reflected light photomicrographs of sulfide minerals from the Musselwhite deposit.

A, B) Anhedral to subhedral, annealed grains of pyrite and anhedral to subhedral chalcopyrite grains as inclusions and/or along late fractures in metamorphic pyrrhotite. C) Anhedral pyrrhotite inclusions along fractures in porphyroblasts of coarse-grained, almandine garnet along with euhedral to subhedral pyrite as dissemination in quartz matrix. D) Subhedral grains of metamorphic pyrrhotite with minor inclusions of pyrite 1, overprinted by late subhedral, coarse-grained grains of pyrite showing possible pyrrhotite inclusions. Abbreviations: Ccp = chalcopyrite, Grt = garnet, Mt = magnetite, Po = pyrrhotite, Py = pyrite, Qtz = quartz.

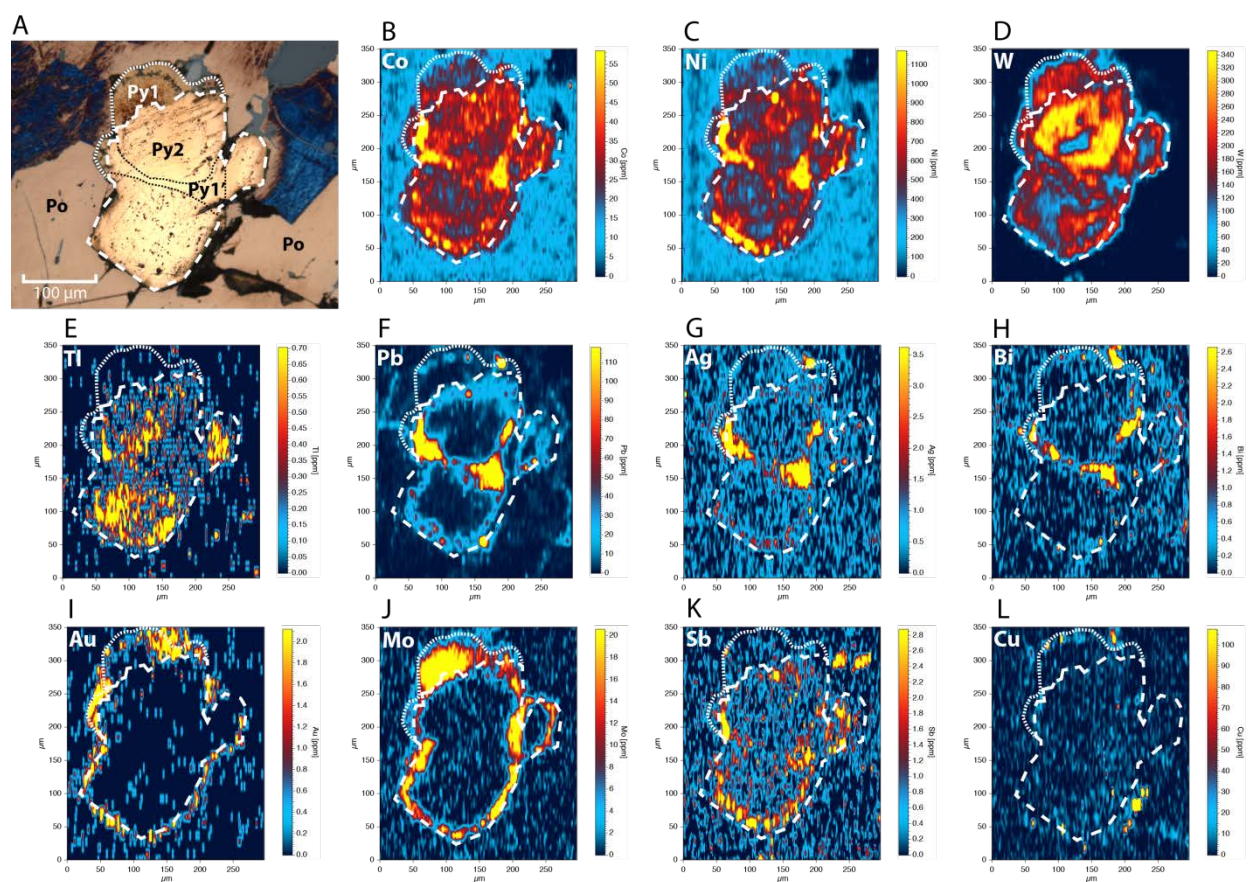


Figure 4.8: LA ICP-MS maps showing the distribution of selected trace elements in pyrites from sample AMB-126223 (Meadowbank deposit). A) Reflected light photomicrograph of the mapped pyrite crystals (i.e., py1, py1' and py2) that occur in a matrix of metamorphic pyrrhotite. B to L) Element maps plotted as concentrations scaled between the data median \pm 3 standard deviations. This plotting was used to maximize the contrast for the majority of data while maintaining a linear scale and, therefore, the maximum concentrations of the scale are not the true maximums present in the sample. The maps illustrate elemental enrichment of Co, Ni, W and Mo with locally minor amounts of Sb, Pb, Ag, Bi and Au in pyrite 1, whereas pyrite 2 has an elemental association of W, Tl, Co and Ni, and finally Mo, Au, Sb and minor Cu appear to envelope pyrite 2. Abbreviations: Po = pyrrhotite; Py = pyrite. Note that white dashed lines on element maps illustrated distribution of py1, py1' and py2.

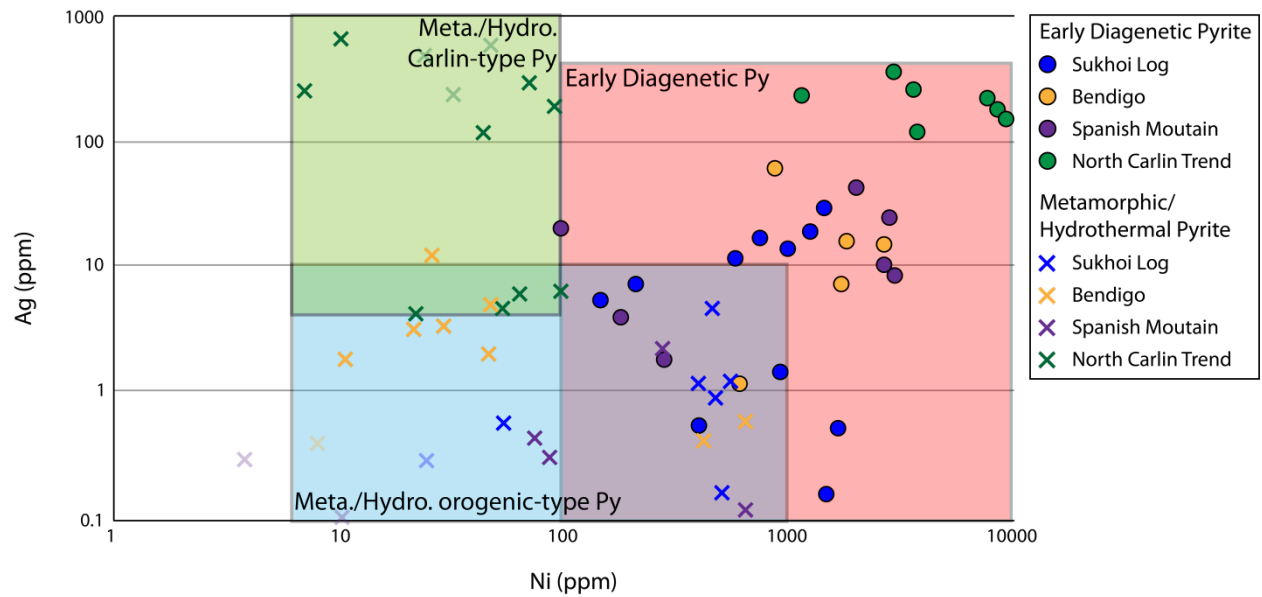


Figure 4.9: Binary plot of Ag versus Ni (ppm) for selected pyrites from four different sediment-hosted gold deposits (i.e., the Sukhoi Log, Bendigo, Spanish Mountain and North Carlin Trend; data from Large et al., 2007). The distribution of these trace elements within these pyrites allows their distinction among early diagenetic (red field), metamorphic/hydrothermal orogenic (blue field) and Carlin-type (green field) deposit settings. Abbreviations: Py = pyrite.

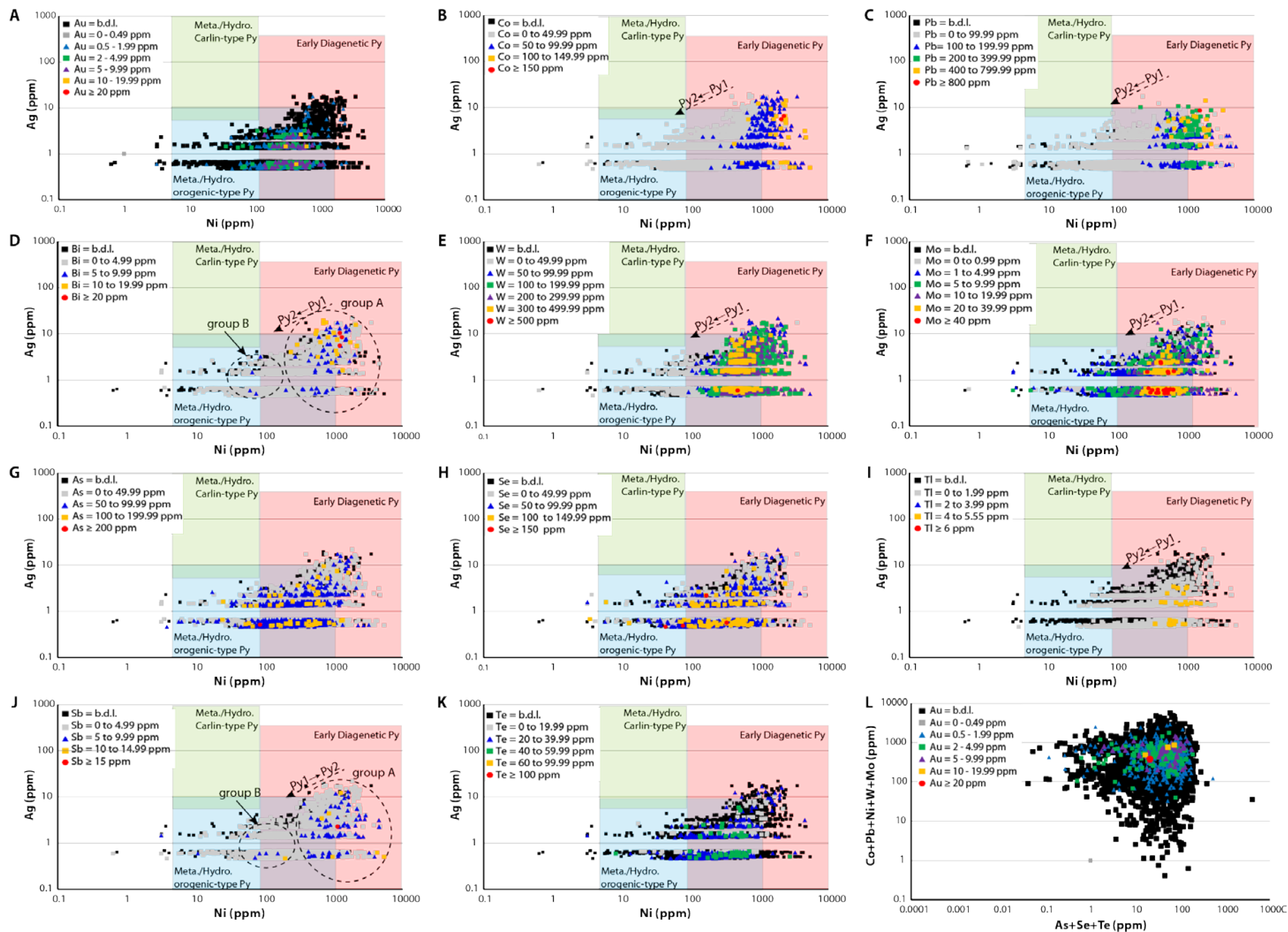


Figure 4.10: Selected binary element plots (in ppm) illustrating the distribution of trace elements amongst variable pyrite events for sample AMB-126223 from the Meadowbank deposit. A to K) Binary element plots of Ag versus Ni grouped by selected trace elements, which show the distribution in the pyrite fields defined by Large et al. (2009). The red field corresponds to early diagenetic pyrite, the blue field corresponds to metamorphic/hydrothermal orogenic-type pyrite and the green field corresponds to metamorphic/hydrothermal Carlin-type pyrite (see Fig. 9 for further explanation). L) Plot of $\Sigma(\text{Co}+\text{Pb}+\text{Ni}+\text{W}+\text{Mo})$ versus $\Sigma(\text{As}+\text{Se}+\text{Te})$ grouped by Au content, which shows that one gold event is associated with high As+Se+Te contents. Note that the detection limit for Ag is at about 0.4 ppm. Groups A and B refer to remobilization of element during the conversion of py1 to py2 via dissolution-precipitation processes which resulted in formation of the metamorphic/hydrothermal orogenic-type py2. Abbreviation: Py = pyrite.

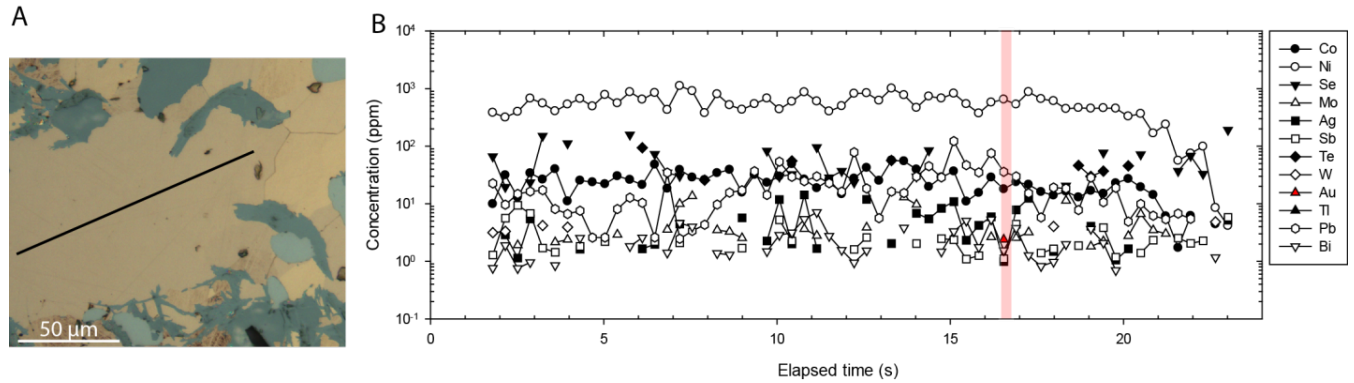


Figure 4.11: Summary of results for a LA ICP-MS traverse of a metamorphic pyrrhotite grain for sample AMB 126231 from the Meadowbank deposit. A) Reflected light photomicrograph of the pyrrhotite grain analysed with the black line showing the LA ICP-MS traverse. B) Concentration profiles (in ppm; note log scale) versus time (in seconds) for selected trace elements along the analysed traverse. It is noted that the only one spot at $t = 16\text{s}$ shows gold mineralization, as indicated by the red field.

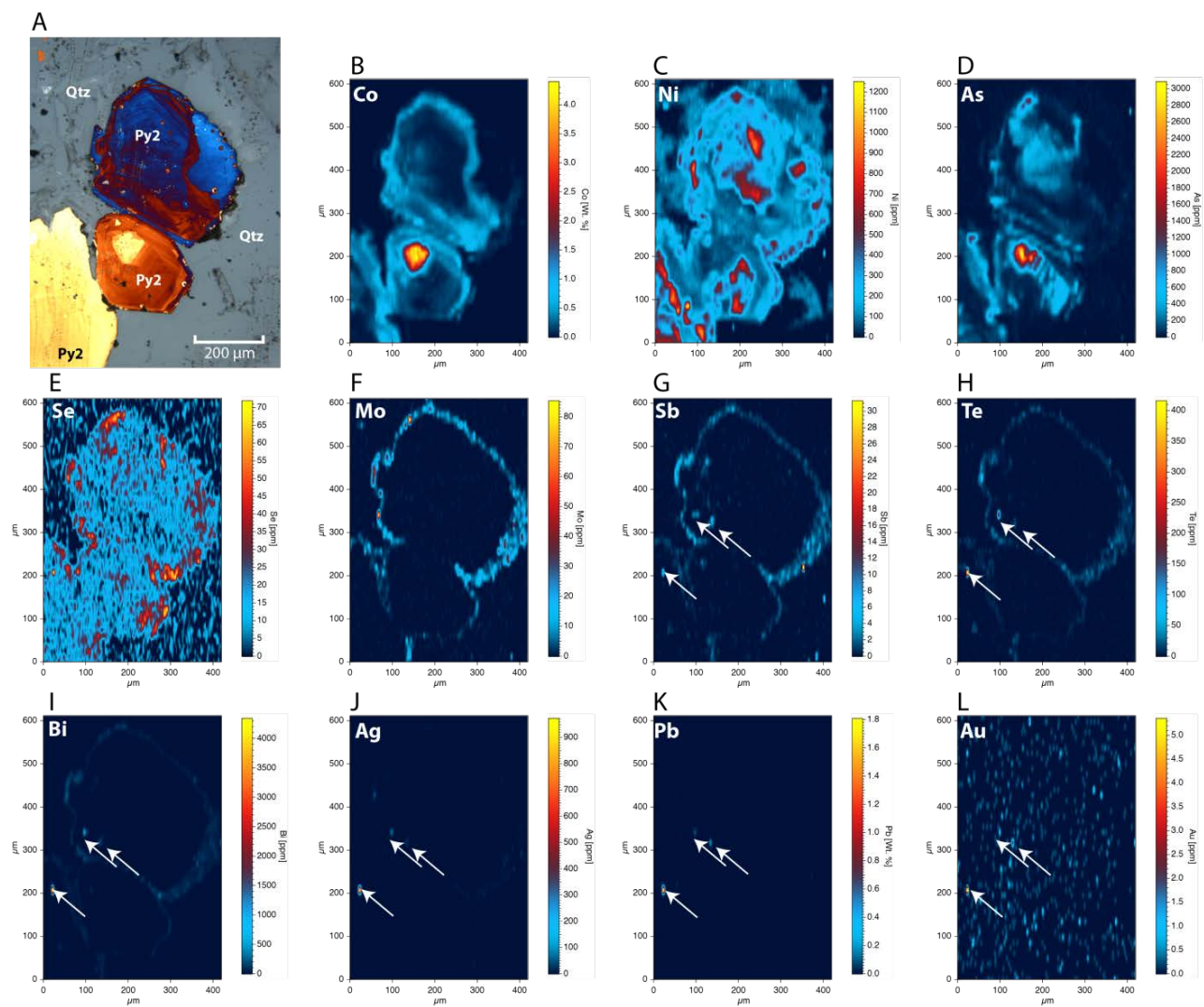


Figure 4.12: LA ICP-MS maps showing the distribution of selected trace elements in pyrites from sample AMB-126231 (Meadowbank deposit). A) Reflected light photomicrograph of mapped pyrite crystals (i.e., py2) disseminated in chert bands. B to L) Element maps plotted as concentrations scaled between the data median \pm 3 standard deviations. This plotting was used to maximize the contrast for the majority of data while maintaining a linear scale and, therefore, the maximum concentrations of the scale are not the true maximums present in the sample. The maps illustrate variable elemental enrichments of Co, Ni, As, Se in core of pyrite 2 and enrichments of Mo, Sb, Te, Bi and Ag enveloping the pyrite 2. Note that white arrows may represent possible inclusions. Abbreviation: Py = pyrite, Qtz = quartz.

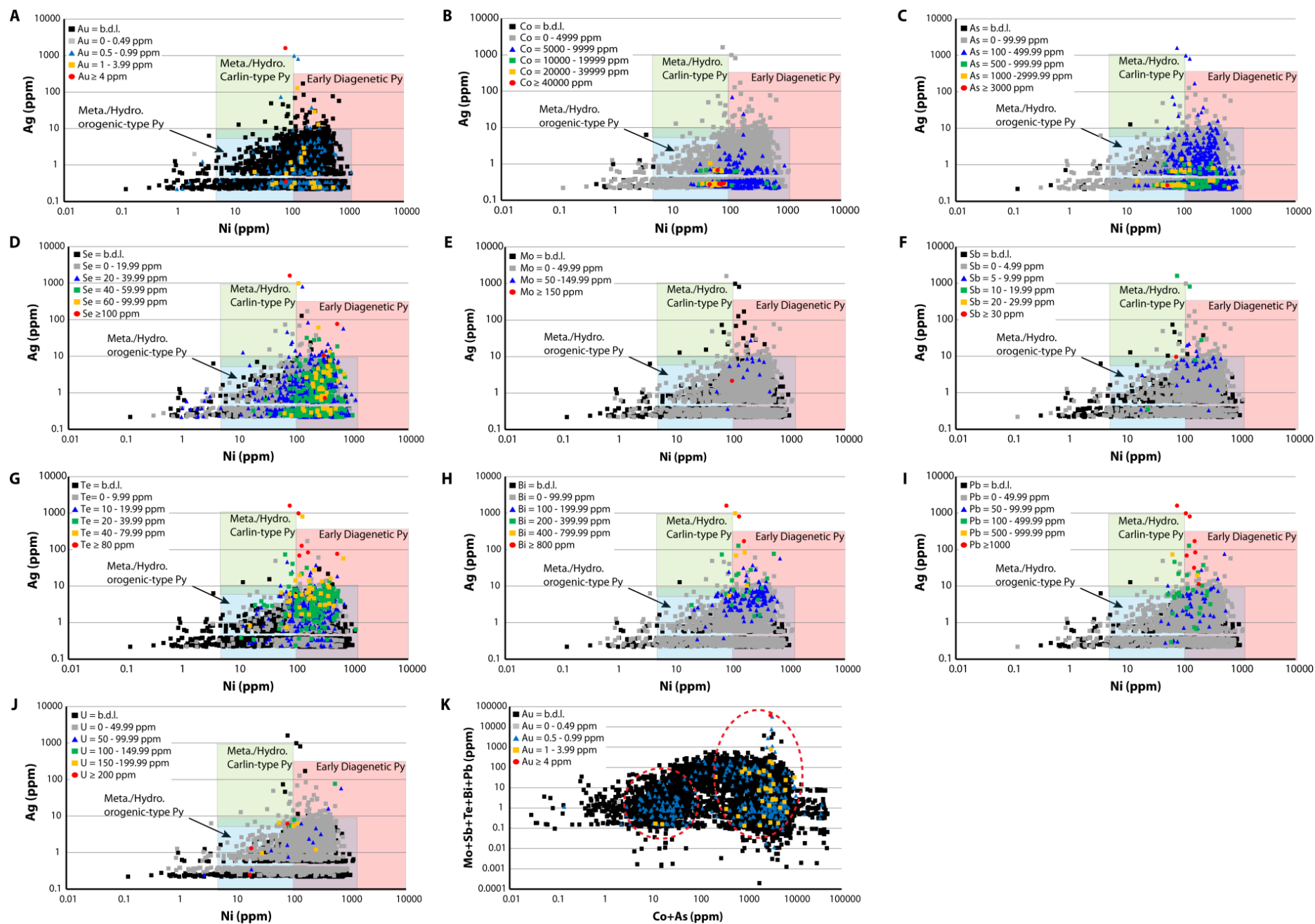


Figure 4.13: Selected element binary plots (in ppm) illustrating the distribution of trace elements amongst variable pyrite events for sample AMB-126231 from the Meadowbank deposit. A to J) Binary element plots of Ag versus Ni grouped by selected trace elements, which show distribution in the pyrite fields defined by Large et al. (2009). The red field corresponds to early diagenetic pyrite, the blue field corresponds to metamorphic/hydrothermal orogenic-type pyrite and the green field corresponds to metamorphic/hydrothermal Carlin-type pyrite (see Fig. 9 for further explanation). K) Plot of $\Sigma(\text{Mo}+\text{Sb}+\text{Te}+\text{Bi}+\text{Pb})$ versus $\Sigma(\text{Co}+\text{As})$ grouped by Au content, which show that two distinct gold events, which are defined by distinct elemental associations, are represented with variable Co+As contents. Note that the detection limit for Ag is at about 0.4 ppm. Abbreviation: Py = pyrite.

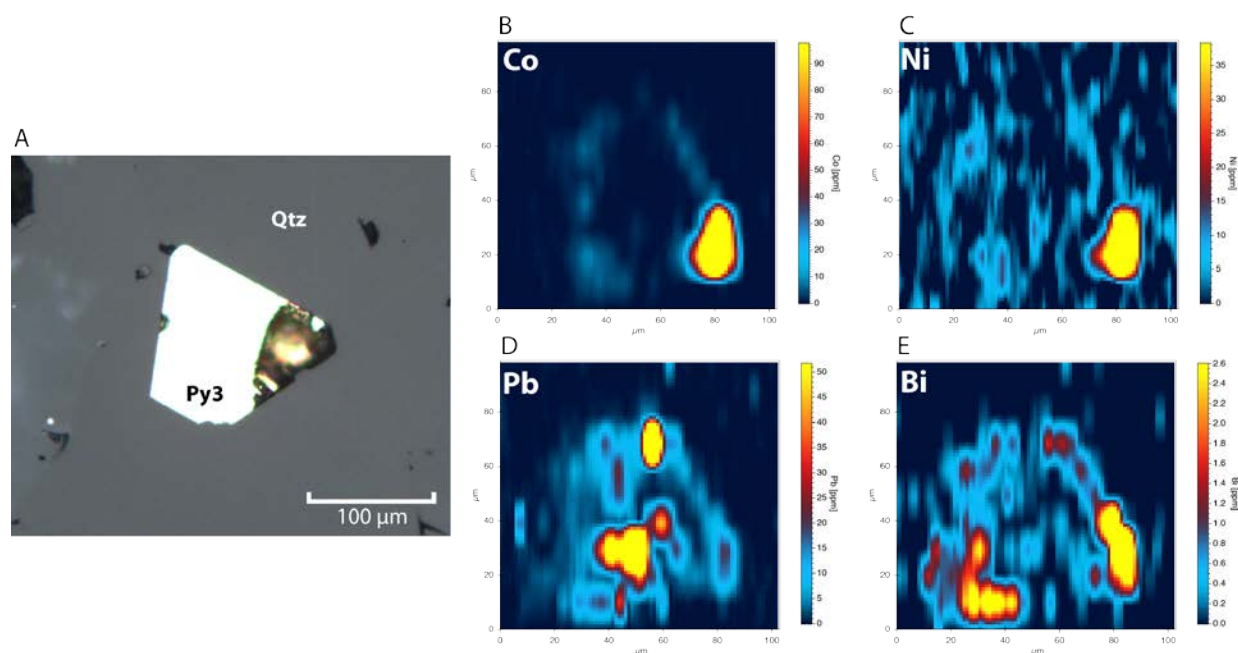


Figure 4.14: LA ICP-MS maps showing the distribution of selected trace elements in pyrite from sample AMB-126228 (Meadowbank deposit). A) Reflected light photomicrograph of the mapped pyrite crystal (i.e., py3) that occurs in a chert band. B to E) Element maps plotted as concentrations scaled between the data median \pm 3 standard deviations. This plotted was used to maximize concentrations for the majority of the data while maintaining a linear scale and, therefore, the maximum concentrations of the scale are not the true maximums present in the sample. The maps illustrate the variable elemental enrichments of Co, Ni, Pb and Bi in the core of pyrite 3. Abbreviation: Py = pyrite, Qtz = quartz.

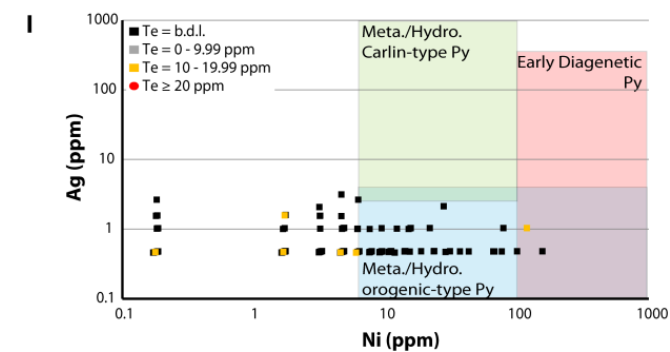
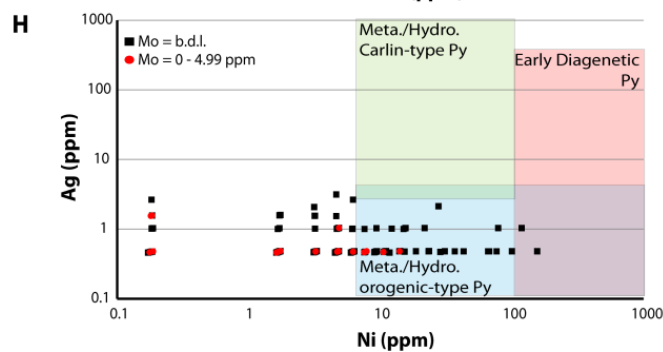
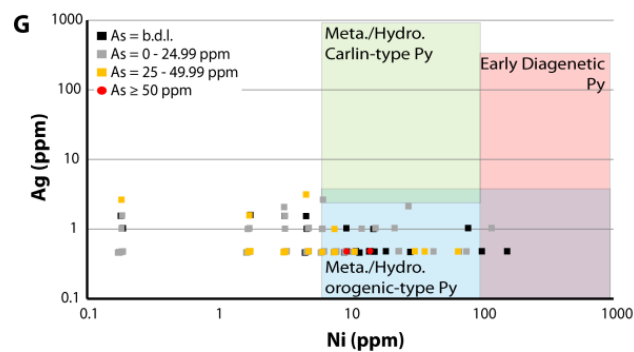
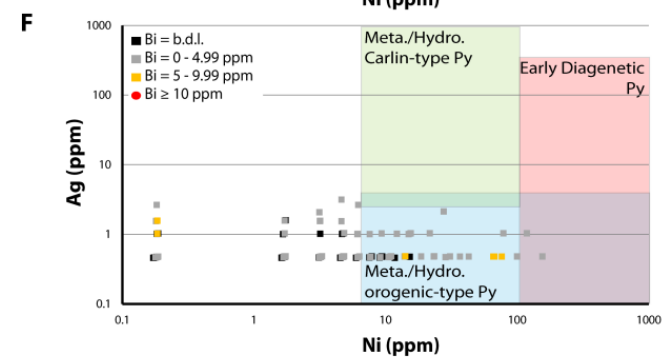
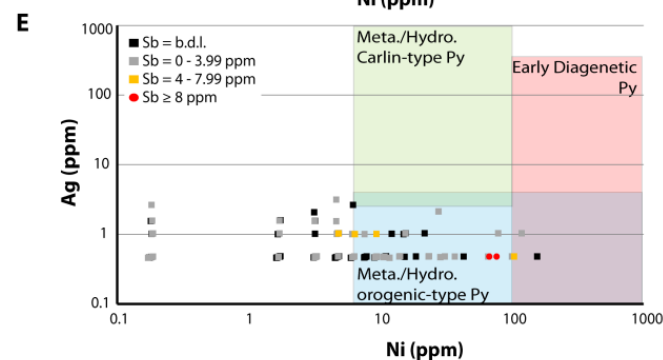
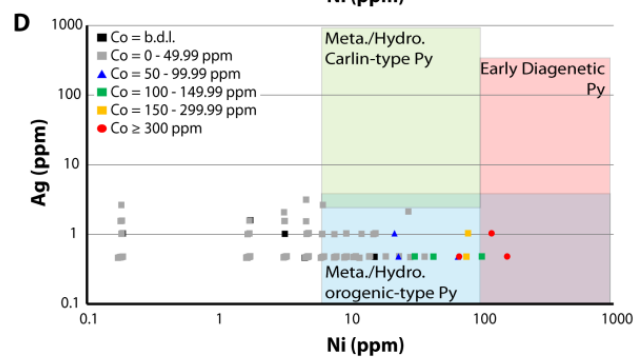
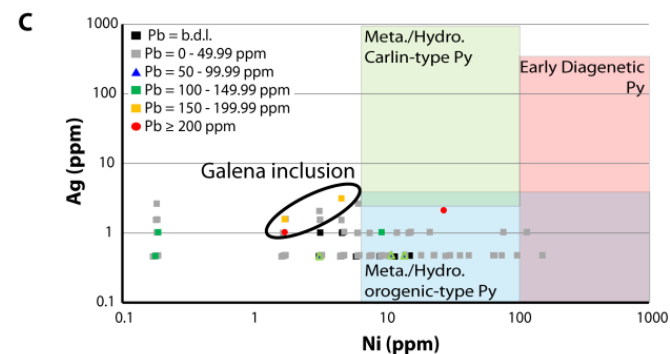
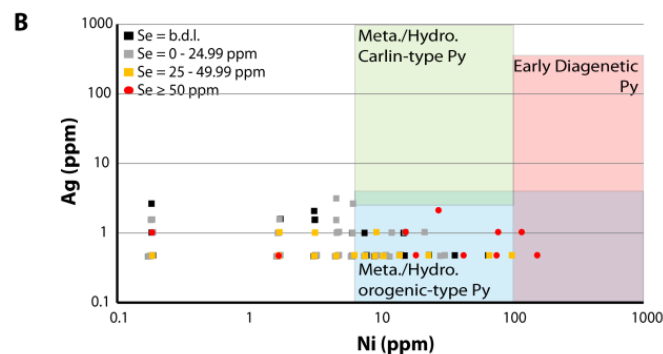
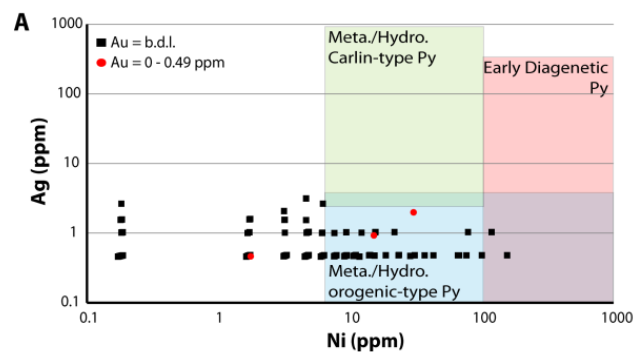


Figure 4.15: Selected binary element plots (in ppm) illustrating the distribution of trace elements amongst variable pyrite events for sample AMB-126228 from the Meadowbank deposit. A to I)

Binary element plots of Ag versus Ni grouped by selected trace elements, which show the distribution in the pyrite fields defined by Large et al. (2009). The red field corresponds to early diagenetic pyrite, the blue field corresponds to metamorphic/hydrothermal orogenic-type pyrite and the green field corresponds to metamorphic/hydrothermal Carlin-type pyrite (see Fig. 9 for further explanation). Note that the detection limit for Ag is at about 0.4 ppm. Abbreviation: Py = pyrite.

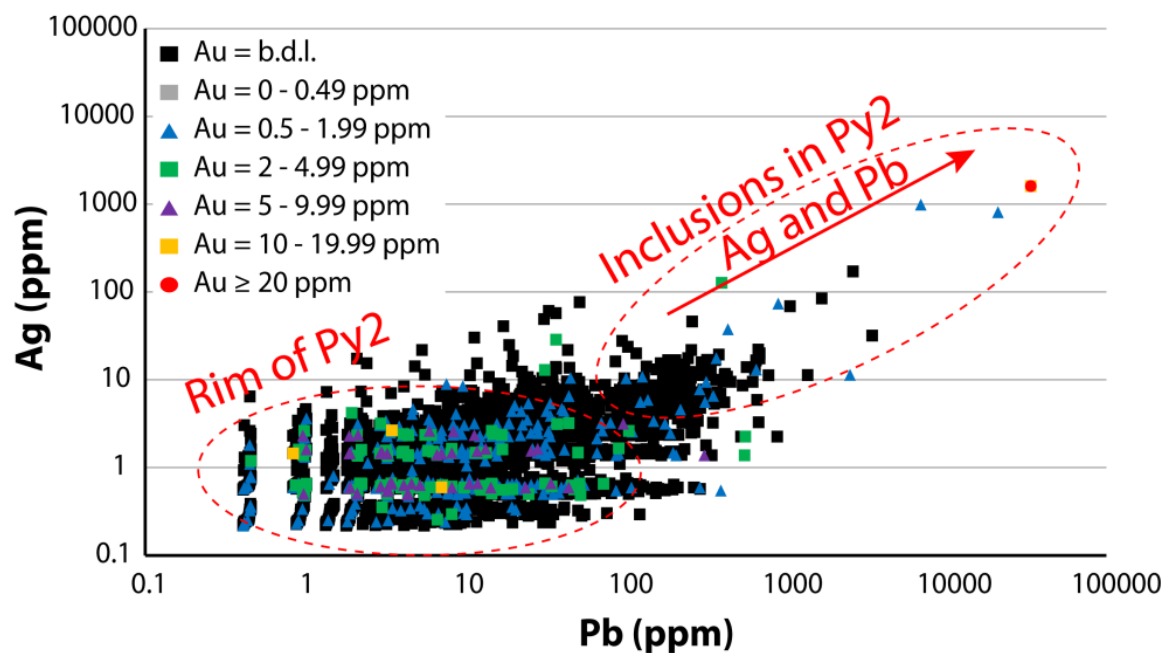


Figure 4.16: Binary element plot (in ppm) of Ag versus Pb using a compilation of individual time-slices of data from the pyrite trace element maps of samples AMB-126223 and AMB-126231 from the Meadowbank deposit. This diagram illustrates the presence of two gold events in the pyrite grains, one indicated by inclusions in pyrite 2 that are associated with high Ag and Pb contents, and a second indicated by the metal-rich rim of pyrite 2 that is associated with weak Ag and variable Pb contents. Abbreviations: Py = pyrite.

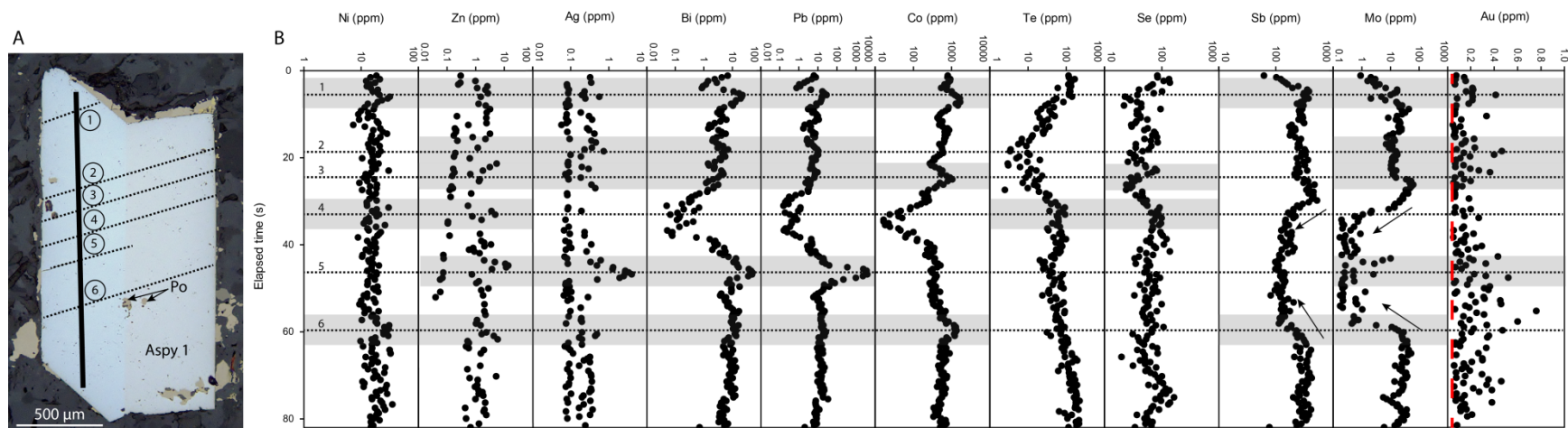


Figure 4.17: LA ICP-MS trace element profiles for a traverse done on an arsenopyrite grain in sample MEL-004 from the Meliadine gold deposit. A) Reflected light photomicrograph of the analyzed arsenopyrite grain. The black solid line represents the traverse whereas the dashed black lines, numbered from 1 to 6, represent micro-fractures. B) Selected trace element profiles (concentrations in ppm) for the traverse shown in A). Note the following features highlighted in the figures: 1) the dashed black lines refer to the micro-fractures observed in the previous image; 2) the grey fields highlight areas of significant elemental enrichments; 3) the black arrows (for Sb and Mo profiles) indicate significant depletions relative to the rest of the grain and correspond to Au enrichment; and 4) the red dashed line in the Au profile refers to the higher detection limit of the time-slice dataset (as each data has their own detection limit). It is noted that all element concentrations except Au, are on a logarithmic scale. Abbreviations: Aspy = arsenopyrite; Po = pyrrhotite.

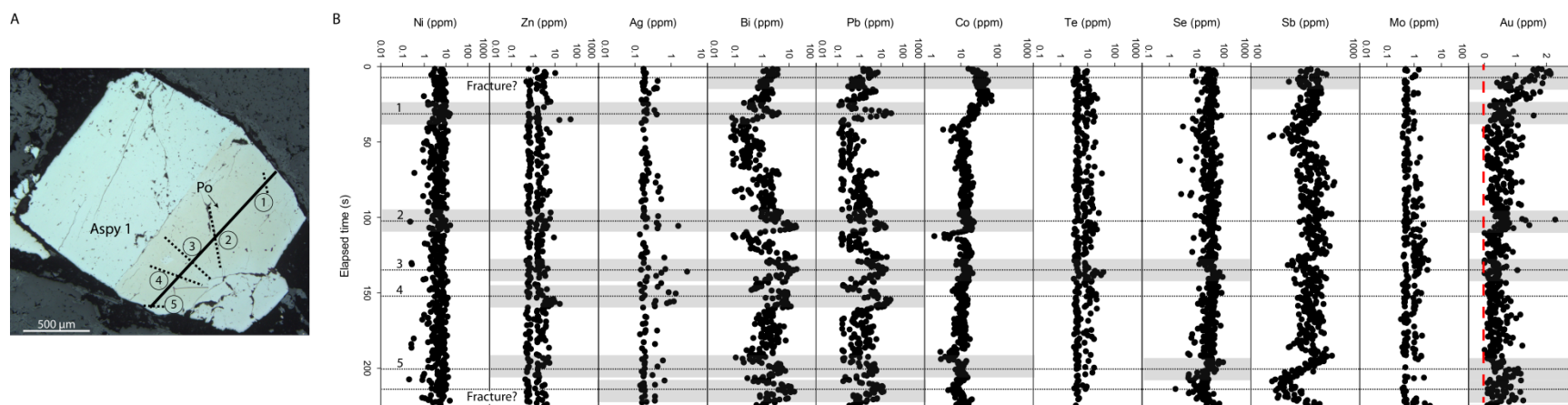


Figure 4.18: LA ICP-MS trace element profiles for a traverse done on an arsenopyrite grain in sample MEL-018 from the Meliadine gold deposit. A) Reflected light photomicrograph of the analyzed arsenopyrite grain. The black solid line represents the traverse, whereas the dashed black lines, numbered from 1 to 5, represent micro-fractures. B) Selected trace element profiles (concentrations in ppm) for the traverse shown in A). Note the following features highlighted in the figures: 1) the dashed black lines refer to the micro-fractures observed in the previous image or suggested by analyses; 2) the grey fields highlight areas of significant elemental enrichments; and 3) the red dashed line in the Au profile refers to the higher detection limit of the time-slice dataset (as each data has their own detection limit). It is noted that all element concentrations except Au, are on a logarithmic scale. Abbreviations: Aspy = arsenopyrite; Po = pyrrhotite.

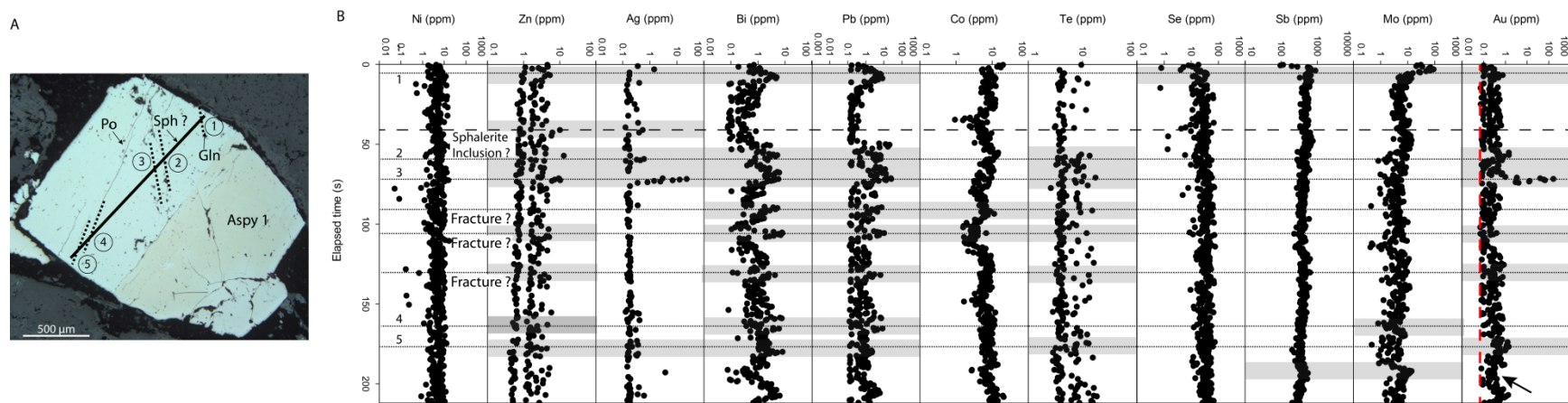


Figure 4.19: LA ICP-MS trace element profiles for a second traverse done on an arsenopyrite grain in sample MEL-018 from the Meliadine gold deposit. A) Reflected light photomicrograph of analyzed arsenopyrite grain. The black solid line represents the traverse whereas the dashed black lines, numbered from 1 to 5, represent micro-fractures. B) Selected trace element profiles (concentrations in ppm) for the traverse shown in A). Note the following features highlighted in the figures: 1) the closely spaced dashed black lines refer to micro-fractures observed in the previous image, or suggested by analyses, the more spaced dashed black line refers to possible sphalerite inclusion; 2) the grey fields highlight areas of reflect significant elemental enrichments; and 3) the red dashed line in the Au profile refers to the higher detection limit of the time-slice dataset (as each data has their own detection limit). It is noted that all element concentrations except Au, are on a logarithmic scale. Abbreviations: Aspy = arsenopyrite; Gln = galena, Po = pyrrhotite, Sph = sphalerite.

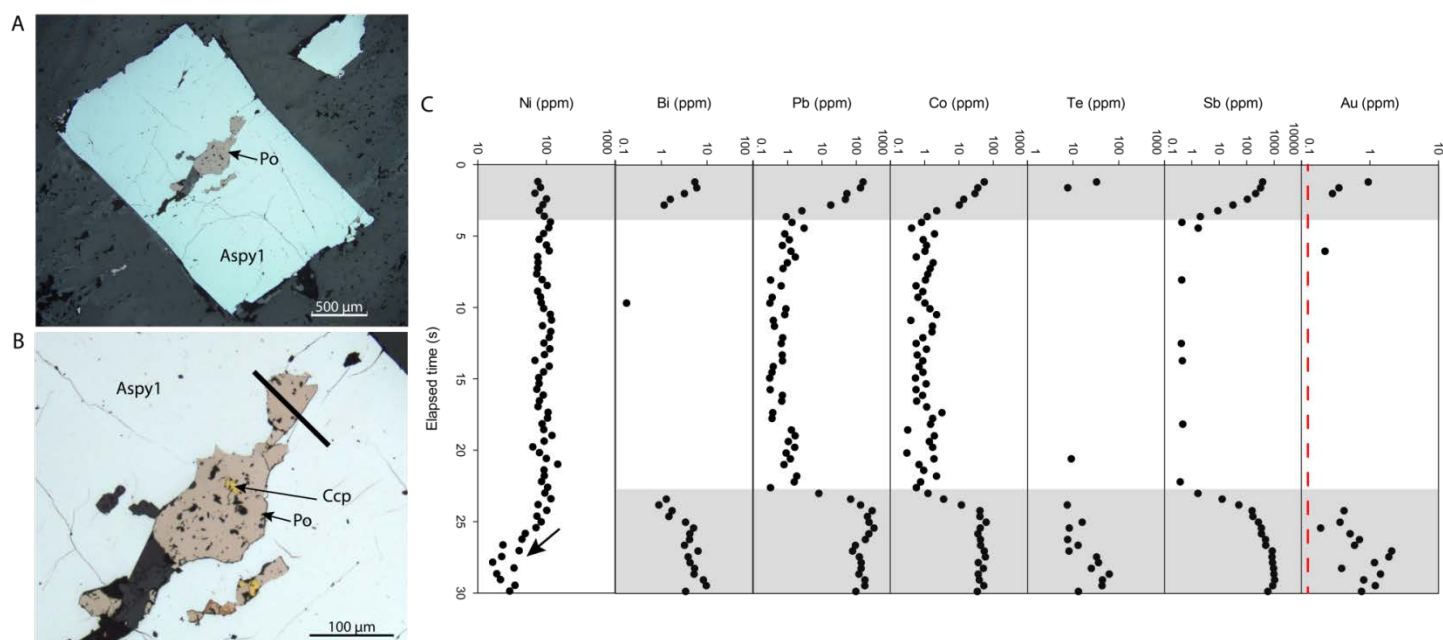


Figure 4.20: LA ICP-MS trace element profiles for a traverse done on an arsenopyrite grain in sample MEL-018 from the Meliadine gold deposit. A) Reflected light photomicrograph of the analyzed arsenopyrite grain with its inclusions of pyrrhotite and chalcopyrite. B) A close up of the previous image showing the location of the laser ablation traverse across arsenopyrite and pyrrhotite, as represented by the solid black line. C) Selected trace element profiles (concentrations in ppm) for the traverse shown in B). Note the following features highlighted in the figures: 1) the grey fields highlight areas of significant elemental enrichments; and 2) the red dashed line in the Au profile refers to the higher detection limit of the time-slice dataset (as each data has their own detection limit). Note that all element concentrations are on a logarithmic scale (as each data has their own detection limit). Abbreviations: Aspy = arsenopyrite; Ccp = chalcopyrite; Po = pyrrhotite.

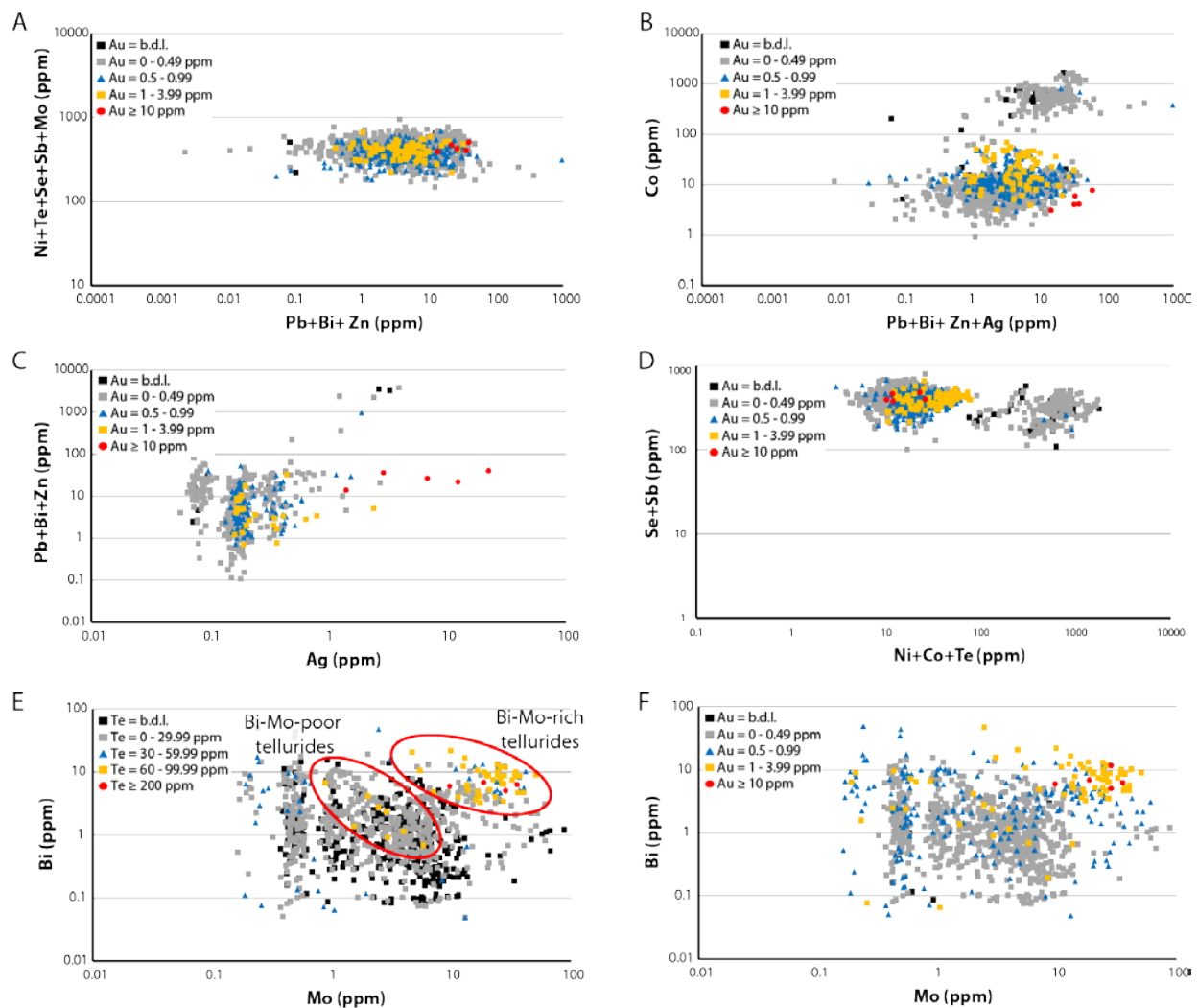


Figure 4.21: Selected binary plots (in ppm) illustrating distribution of Au and Te content in various element associations from the compilation of traverses analyses done on arsenopyrite grains from the Meliadine gold deposit. A) Binary plot of Ni+Te+Se+Sb+Mo versus Pb+Bi+Zn grouped by Au content. B) Binary plot of Co versus Pb+Bi+Zn+Ag, which reflects the presence of Co-rich and Co-poor areas in the arsenopyrite. Note that the areas enriched in Au occur in areas depleted in Co and near fractures. C) Binary plot of Pb+Bi+Zn versus Ag, which reflects two distinct domains based on Au content. D) Binary plot of Se+Sb versus Ni+Co+Te, which shows two domains based on the Au content with the late overgrowth enriched in Ni-Co-Te being relatively depleted in Au. E) Binary plot of Bi versus Mo grouped by Te content. The data reflect the formation of Bi-Mo rich tellurides. F) Binary plot of Bi versus Mo grouped by Au content. Note that the data show a similar trend as seen in the previous image suggesting Au is closely associated with Bi-Mo tellurides.

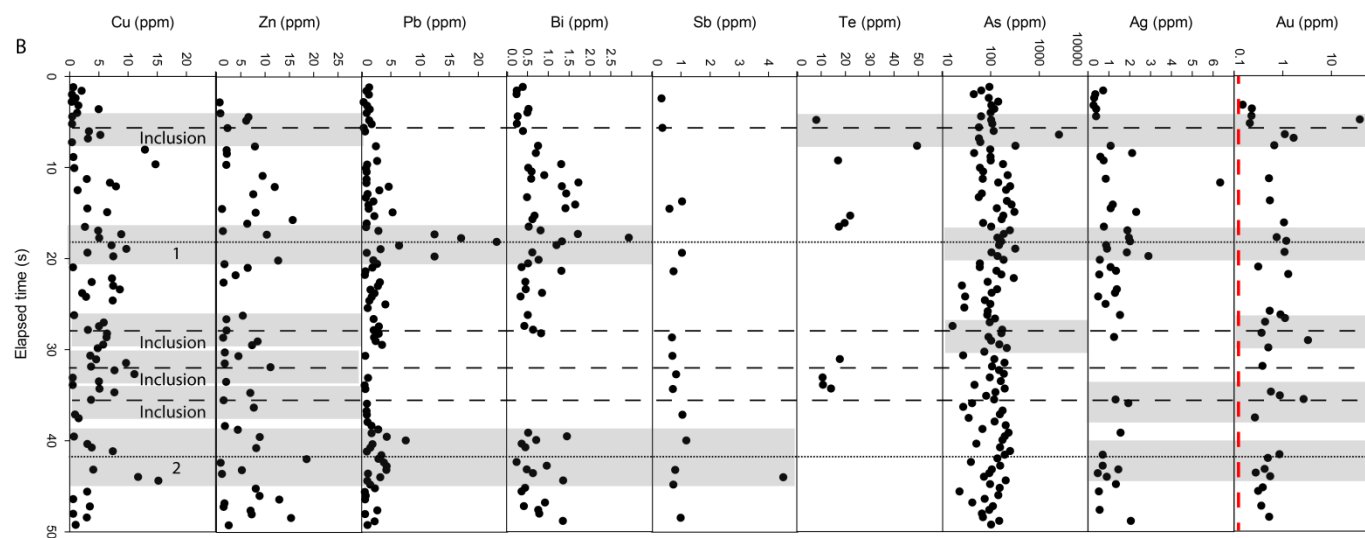
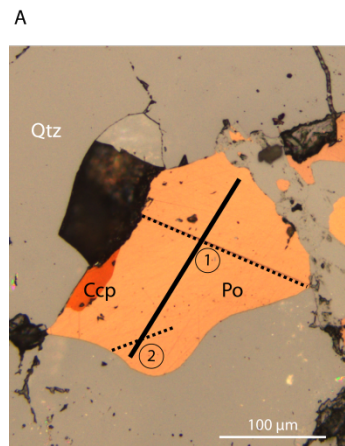


Figure 4.22: LA ICP-MS trace element profiles for a traverse done on a pyrrhotite grain in sample E599654 from the Musselwhite deposit. A) Reflected light photomicrograph of the analyzed pyrrhotite along with local chalcopyrite inclusion. The black solid line represents the traverse whereas the dashed black lines, numbered from 1 to 2, represent micro-fractures. B) Selected trace element profiles (concentrations in ppm) for the traverse shown in A). Note the following features highlighted in the figures: 1) the closely spaced dashed black lines refer to micro-fractures observed in the previous image, the more spaced dashed black lines refer to possible inclusions; 2) the grey fields highlight areas of significant elemental enrichments; and 3) the red dashed line in Au profile refers to the higher detection limit of time-slice dataset (as each data has his own detection limit). It is noted that As and Au concentrations are on a logarithmic scale. Abbreviations: Ccp = chalcopyrite; Po = pyrrhotite; Qtz = quartz.

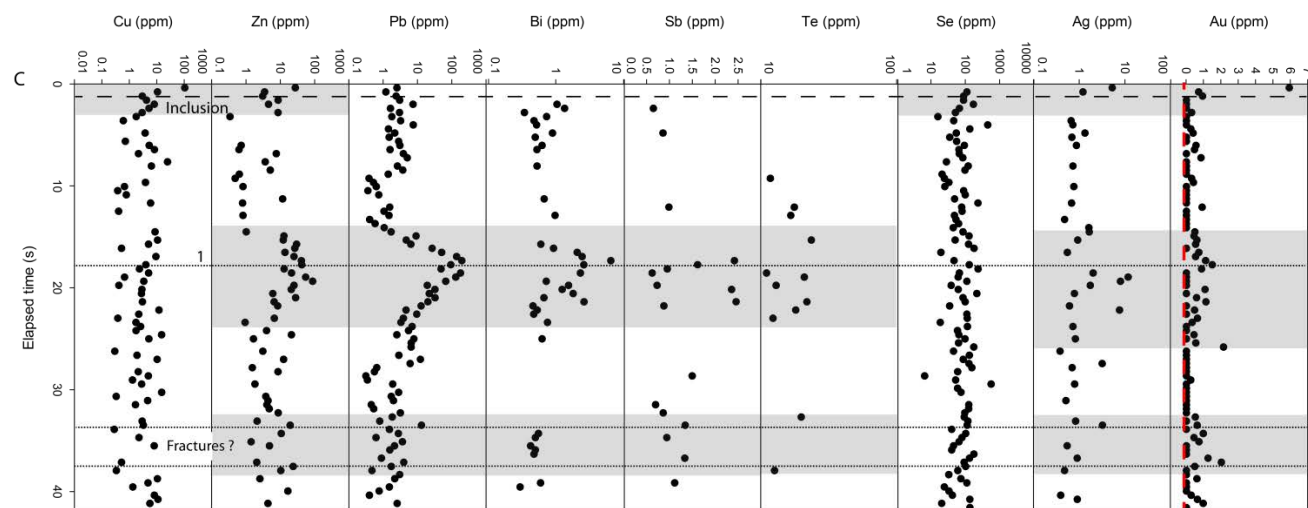
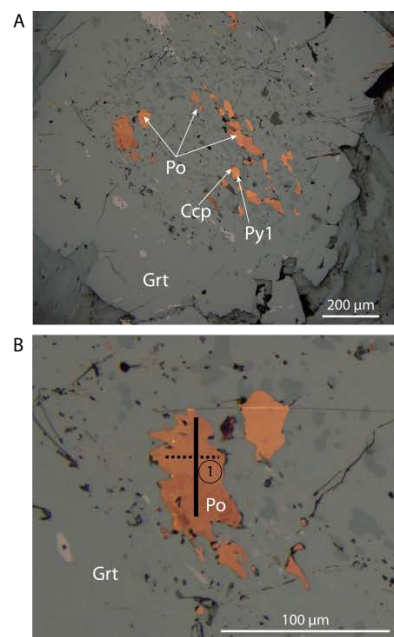


Figure 4.23: LA ICP-MS trace element profiles for a traverse done on a pyrrhotite grain in sample E599658 from the Musselwhite deposit. A) Reflected light photomicrograph of pyrrhotite, pyrite and chalcopyrite inclusions along fractures in garnet grain disseminated in chert. B) A close up of the fracture filled of pyrrhotite in garnet grain. The black solid line represents the traverse whereas the dashed black line referring to 1 represents micro-fracture. C) Selected trace element profiles (concentrations in ppm) for the traverse shown in B). Note the following features highlighted in the figures: 1) the closely spaced dashed black lines refer to micro-fractures observed in the previous image or suggested by analyses, the more spaced dashed black line refers to a possible inclusion; 2) the grey fields highlight areas of significant elemental enrichments; and 3) the red dashed line in the Au profile refers to the higher detection limit of the time-slice dataset (as each data has his own detection limit). It is noted that all element concentrations except Sb and Au, are on a logarithmic scale. Abbreviations: Ccp = chalcopyrite; Grt = garnet; Py = pyrite; Po = pyrrhotite.

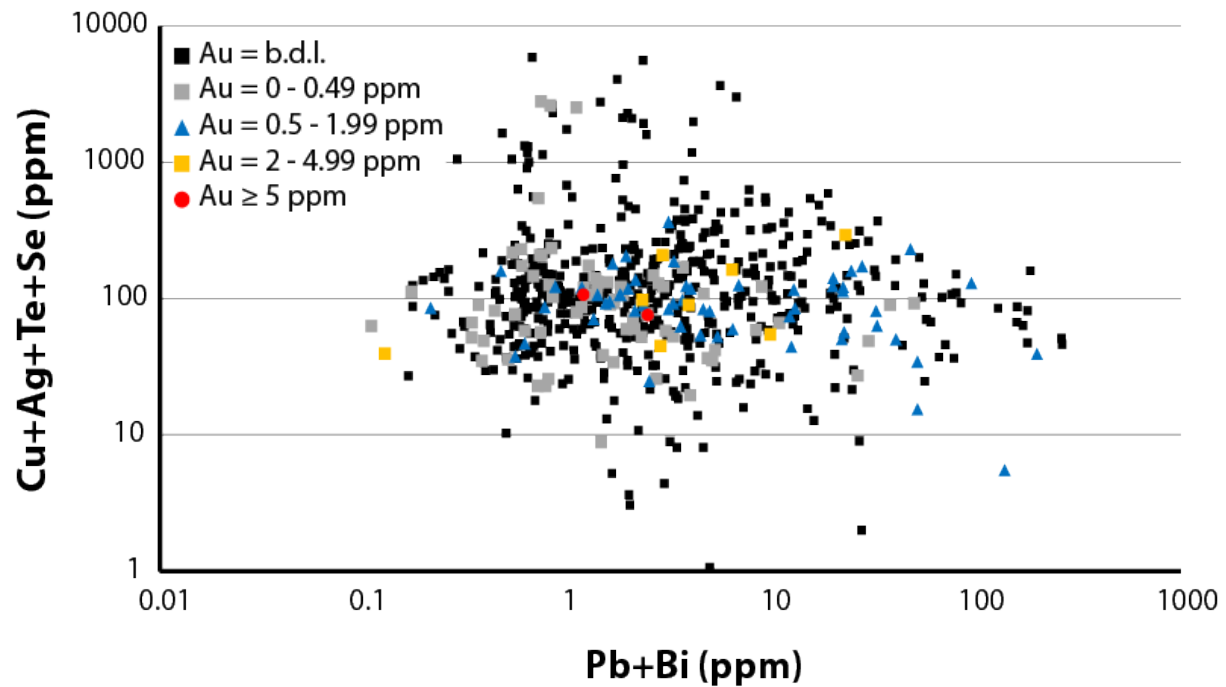


Figure 4.24: Binary plot (in ppm) of Cu+Ag+Te+Se, representing Au element association in the pyrrhotite core, versus Pb+Bi, which represents Au element association in the pyrrhotite fractures, using a compilation of individual time-slices of data from the pyrrhotite trace element traverse of samples E599651, E599654, E599658 and E599666 from the Musselwhite deposit (Gourcerol et al., 2015b). These data suggest that there is only one Au event.

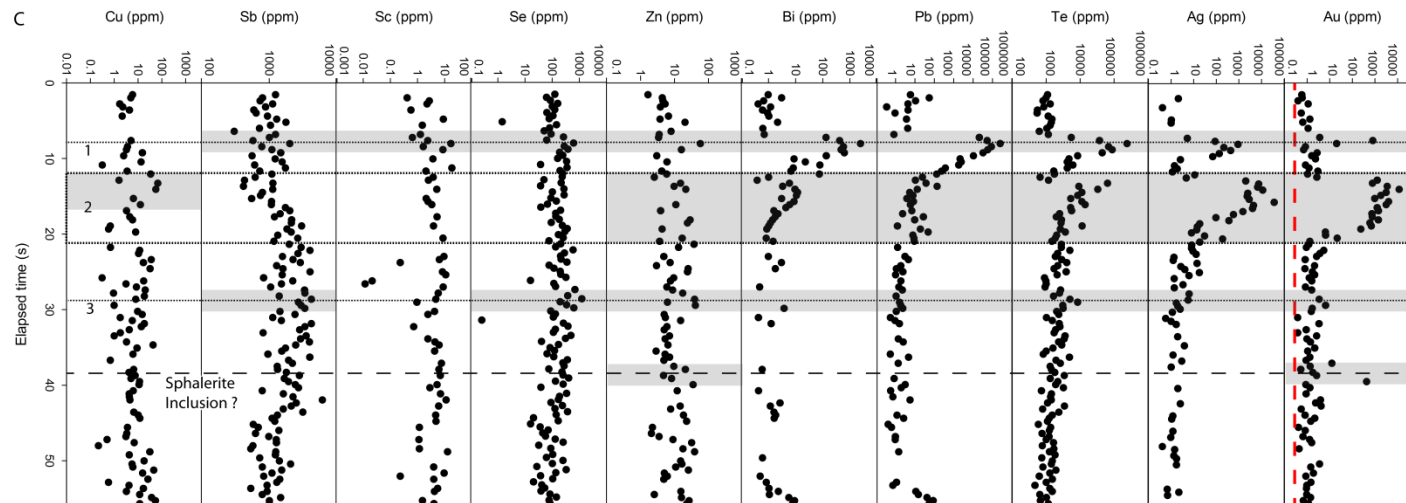
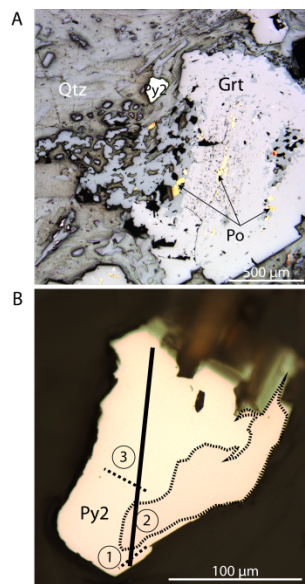


Figure 4.25: LA ICP-MS trace element profiles for a traverse done on a pyrite grain in sample E599658 from the Musselwhite deposit. A) Reflected light photomicrograph of pyrrhotite, pyrite and chalcopyrite inclusions along fractures in garnet grain disseminated in chert. B) A close up of the fracture filled of pyrrhotite in garnet grain. The black solid line represents the traverse whereas the dashed black lines, numbered from 1 to 3, represent micro-fractures in the pyrite. C) Selected trace element profiles (concentrations in ppm) for the traverse shown in B). Note the following features highlighted in the figures: 1) the closely spaced dashed black lines refer to micro-fractures observed in the previous image, the more spaced dashed black line refers to possible sphalerite inclusion; 2) the grey fields highlight areas of significant elemental enrichment; and 3) the red dashed line in the Au profile refers to the higher detection limit of the time-slice dataset (as each data has his own detection limit). It is noted that all element concentrations are on a logarithmic scale. Abbreviations: Grt = garnet; Py = pyrite; Po = pyrrhotite; Qtz = quartz.

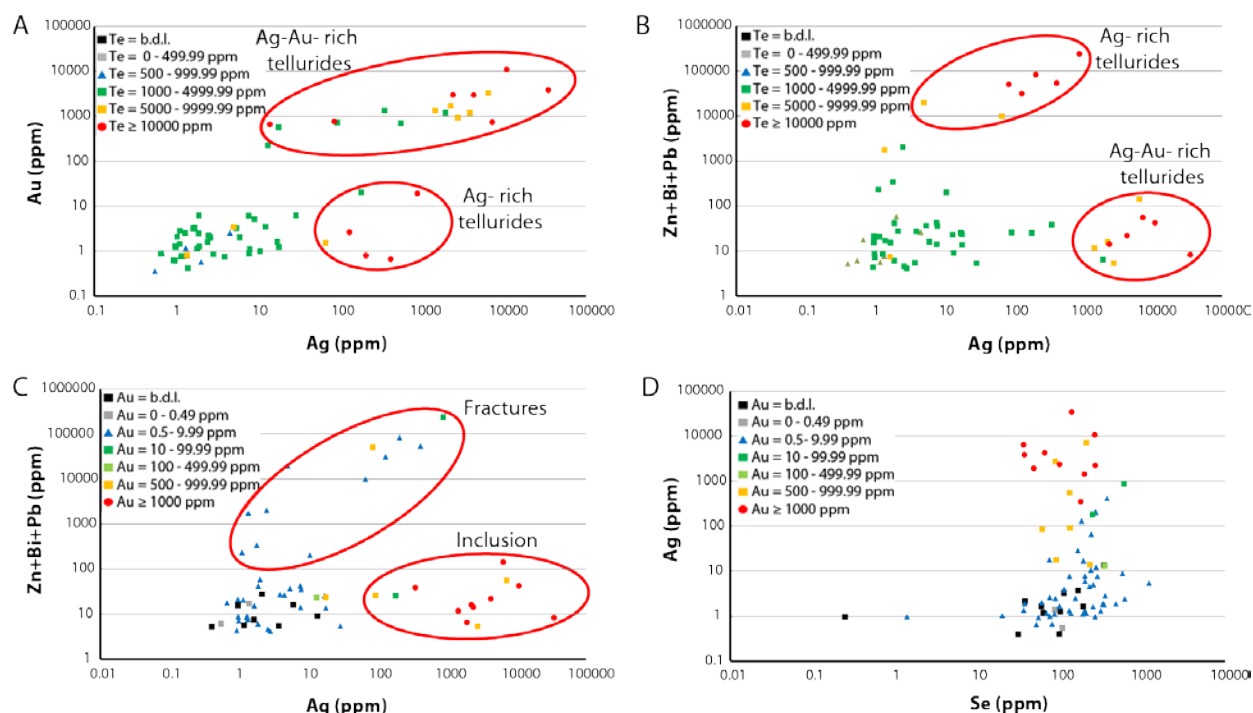


Figure 4.26: Selected binary plots (in ppm) showing the distribution of Au and Te for pyrite data for sample E599658 from the Musselwhite deposit. Note that the data are also grouped by colour according to their Au and Te contents. A) Binary plot for Au versus Ag with Te content color coded, which shows the presence of Ag-Au- and Ag- rich tellurides. B) Binary plot of Zn+Bi+Pb versus Ag with Te color coded which shows Ag-rich and Ag-Au- rich tellurides. C) Binary plot of Zn+Bi+Pb versus Ag with Au colored coded which shows that Au is associated either in fractures or disseminated in pyrite but that the highest Au contents are associated with inclusions. D) Binary plot of Ag versus Se with Au color coded which shows a close relationship between Au and Ag content.

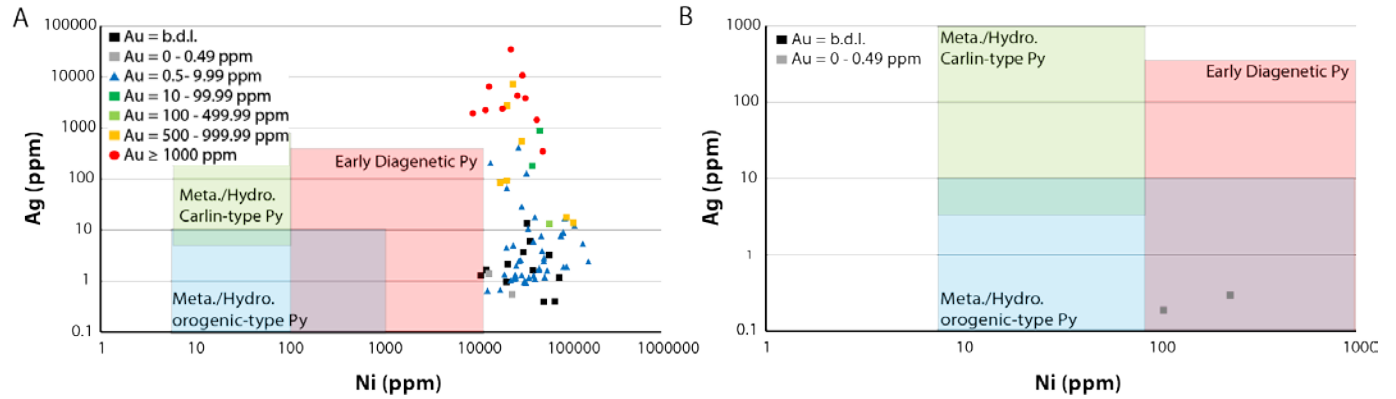


Figure 4.27: Binary element plots (in ppm) of Ag versus Ni for py1 and py2 from the Musselwhite deposit along with the fields for different pyrites, as defined by Large et al. (2009). Note that the data are also grouped by colour according to their Au contents. A) Distribution of data for py2 analyzed by traverse mode from samples E599658 (Fig. 21). Note that the detection limit for the Ag was 0.4 ppm. B) Distribution of data for py1 spot analyses for sample E599656.

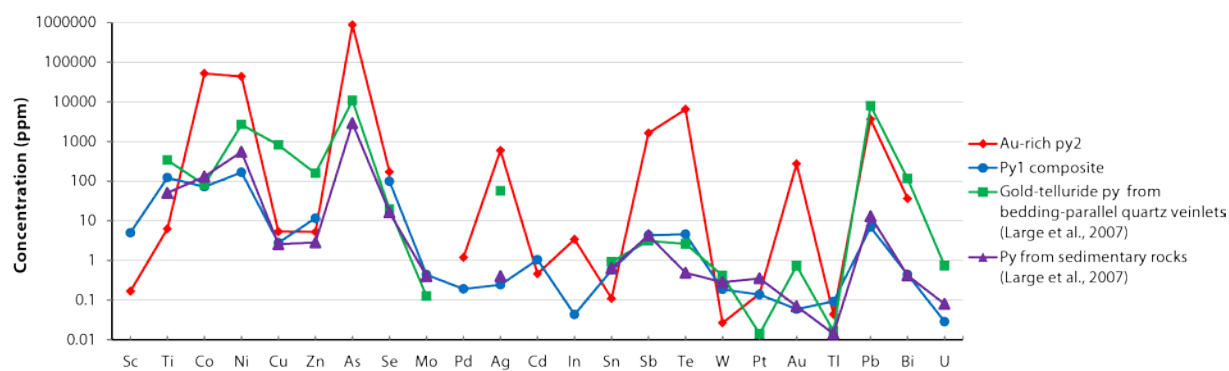


Figure 4.28: Abundance of selected major and trace elements for py1 and py2 from the Musselwhite deposit shown in blue and red lines, respectively. These data are compared to gold-telluride pyrite from bedding-parallel quartz veinlets and pyrite from sedimentary rocks, in green and purple lines, respectively. The latter data are from Large et al. (2007), as indicated in the legend.

4.10 References

- Armitage, A.E., James, R.S., and Goff, S.P., 1996, Gold mineralization in Archean banded iron formation, Third Portage Lake area, Northwest Territories, Canada: *Exploration and Mining Geology*, v. 5, no. 1, p. 1-15.
- Aspler, L.B., and Chiarenzelli, J.R. 1996a, Stratigraphy, sedimentology and physical volcanology of the Henik Group, central Ennadai-Rankin greenstone belt, Northwest Territories, Canada: Late Archean paleogeography of the Hearne Province and tectonic implications: *Precambrian Research*, v. 77, p. 59-89.
- Bestmann, M., and Prior, D.J., 2003, Intragranular dynamic recrystallization in naturally deformed calcite marble: diffusion accommodated grain boundary sliding as a result of subgrain rotation recrystallization: *Journal of Structural Geology*, v. 25, p. 1597-1613.
- Biczok, J., Hollings, P., Klipfel, P., Heaman, L., Maas, R., Hamilton, M., Kamo, S., and Friedman, R., 2012, Geochronology of the North Caribou greenstone belt, Superior Province Canada: Implications for tectonic history and gold mineralization at the Musselwhite mine: *Precambrian Research*, v. 192-195, p. 209-230.
- Bierlein, F.P., Grovs, D.I., Goldfarb, R.J., and Dubé, B., 2006, Lithospheric controls on the formation of provinces hosting giant orogenic gold deposits: *Miner Deposita*, v. 40, p.874-886.
- Bierlein, F.P., and Crowe, D.E., 2000, Phanerozoic orogenic lode gold deposits: Review in *Economic Geology*, v. 13, chapter, 3, p. 103-139.

- Breaks, F.W., Osmani, I.A., and DeKemp, E.A., 2001, Geology of the North Caribou Lake area, northwestern Ontario: Ontario Geological Survey, Open File Report 6023, 80 p.
- Bull, S.W., and Large, R.R., 2015, Setting the stage for the genesis of the giant Bendigo ore system; In: Ore Deposits in an Evolving Earth (Eds.) Jenkin, G.R.T., Lusty, P.A. J., McDonald, I., Smith, M.P., Boyce, A.J. and Wilkinson, J.J.: Geological Society, London, Special Publications, v. 393, p. 1-31.
- Caddey, S.W., Bachman, R.L., Campbell, T.J., Reid, R.R., and Otto, R.P., 1991, The Homestake gold mine, an Early Proterozoic iron-formation-hosted gold deposit, Lawrence County, South Dakota: United States Geological Survey, Bulletin 1857-J, 67 p.
- Carpenter, R.L., 2004, Relative and absolute timing of supracrustal deposition, tectonothermal activity and gold mineralization, West Meliadine region, Rankin Inlet greenstone belt, Nunavut, Canada: PhD. Thesis, Faculty of Graduate Studies, University of Western Ontario, 362 p.
- Carpenter, R.L., Duke, N.A., Sandeman, H.A., and Stern, R., 2005, Relative and absolute timing of gold mineralization along the Meliadine Trend, Nunavut, Canada; evidence for Paleoproterozoic gold hosted in an Archean greenstone belt: Economic Geology and the Bulletin of the Society of Economic Geologists, v. 100, p. 567-576.
- Chen, M., Campbell, I. H., Xue, Y., Tian, W., Ireland, T. R., Holden, P., Cas, R. A. F., Hayman, P. C., and Das, R., 2015, Multiple sulfur isotope analyses support a magmatic model for the volcanogenic massive sulfide deposits of the Teutonic Bore volcanic Complex, Yilgarn Craton, Western Australia: Economic Geology, v. 110, no. 6, p. 1411-1423.

- Cook, N.J., Ciobanu, C.L., Meria, D., Silcock, D., and Wade, B., 2013, Arsenopyrite-Pyrite Association in an Orogenic Gold Ore: Tracing Mineralization History from Textures and Trace Elements: *Economic Geology*, v. 108, p. 1273-1283.
- Davis, W.J., Ryan, J.J., Sandeman, H.A., and Tella, S., 2008, A Paleoproterozoic detrital zircon age for a key conglomeratic horizon within the Rankin Inlet area, Kivalliq region, Nunavut: implications for Archean and Proterozoic evolution of the area: In *Current research 2008-8*, Geological Survey of Canada, 10 p.
- Dubé, B., Mercier-Langevin, P., Castonguay, S., McNicoll, V.J., Bleeker, W., Lawley, C.J.M., De Souza, S., Jackson, S.E., Dupuis, C., Gao, J.-F., Bécu, V., Pilote, P., Goutier, J., Beakhouse, G.P., Yergeau, D., Oswald, W., Janvier, V., Fontaine, A., Pelletier, M., Beauchamp, A.-M., Katz, L.R., Kontak, D.J., Tóth, Z., Lafrance, B., Gourcerol, B., Thurston, P.C., Creaser, R.A., Enkin, R.J., El Goumi, N., Grunsky, E.C., Schneider, D.A., Kelly, C.J., and Lauzière, K., 2015, Precambrian lode gold deposits - a summary of TGI-4 contributions to the understanding of lode gold deposits, with an emphasis on implications for exploration: In: *Targeted Geoscience Initiative 4: Contributions to the Understanding of Precambrian Lode Gold Deposits and Implications for Exploration*, (Eds.) B. Dubé and P. Mercier-Langevin; Geological Survey of Canada, Open File 7852, p. 1-24.
- Dubé, B., Mercier-Langevin, P., Kjarsgaard, I., Hannington, M., Becu, V., Cote, J., Moorhead, J., Legault, M., and Bedard, N., 2014, The Bousquet 2-Dumagami world-class Archean Au-rich volcanogenic massive sulfide deposit, Abitibi, Quebec; metamorphosed submarine advanced argillic alteration footprint and genesis; *Economic Geology and the Bulletin of the Society of Economic Geologists*, v. 109, no. 1, p. 121-166.

- Dubé, B., and Gosselin, P., 2007, Greenstone-hosted quart-carbonate vein deposits: Geological Association of Canada, Mineral Deposits Division, Special Publication 5, p. 49–73.
- Folk, R.L., 2005, Nannobacteria and the formation of framboidal pyrite: Textural evidence: *Journal of Earth System Science*, v. 114, p. 369-374.
- Franklin, J. M., Gibson, H. L., Jonasson, I. R., and Galley, A. G., 2005, Volcanogenic Massive sulfide Deposits: *Economic Geology 100th Anniversary Volume*, v. 100, p. 523-560.
- Frimmel, H. E., and Hennigh, Q., 2015, First whiffs of atmospheric oxygen triggered onset of crustal gold cycle: *Mineralium Deposita*, v. 50, no. 1, p. 5-23.
- Frimmel, H.E., 2014, A giant Mesoarchean crustal gold-enrichment episode: possible causes and consequences for exploration: *Society of Economic Geology, Special publication* v. 18, p. 209-234.
- Frei, R., Dahl, P.S., Duke, E.F., Hansen, T.R., Frandsson, M.M., and Jensen, L.A., 2008, Trace element and isotopic characterization of Neoarchean and Paleoproterozoic iron formations in the Black Hills (South Dakota USA): assessment of chemical change during 2.9-1.9 Ga deposition bracketing the 2.4-2.2 Ga first rise of atmospheric oxygen: *Precambrian Geology*, v. 162, p. 441-474.
- Fripp, R.E.P., 1976, Stratabound gold deposits in Archean banded iron formation, Rhodesia: *Economic Geology*, v. 71, p. 58-75.
- Gao, J.-F., Jackson, S.E., Dubé, B., Kontak, D.J., and De Souza, S., 2015, Genesis of the Canadian Malartic, Côté Gold, and Musselwhite gold deposits: Insights from LA-ICP-MS

- element mapping of pyrite; In: Targeted Geoscience Initiative 4: Contributions to the understanding of Precambrian Lode Gold Deposits and Implications for Exploration, (ed.) B. Dubé and P. Mercier-Langevin; Geological Survey of Canada, Open File 7852, p. 157-175.
- Goldfarb, R.J., and Groves, D.I., 2015, Orogenic gold: common or evolving fluid and metal sources through time: *Lithos*, v. 233, p. 2-26.
- Goldfarb, R.J., Baker, T., Dubé, B., Groves, D.I., Hart, C.J.R., and Gosselin, P., 2005, Distribution, character and genesis of gold deposits in metamorphic terranes. In: *Economic Geology 100th Anniversary Volume*, J.W. Hedenquist, J.F.H. Thompson, R.J. Goldfarb, and J.P. Richards (eds.), p. 407-450. Goldfarb, R.J., Groves, D.I. and Gardoll, S. 2001, Orogenic gold and geologic time: A global synthesis: *Ore Geology Reviews*, v. 18, p. 1–75.
- Gourcerol, B., Thurston, P.C., Kontak, D.J., and Côté-Mantha, O., 2015a, Interpretations and implications of preliminary LA ICP-MS analysis of chert for the origin of geochemical signatures in banded iron formations (BIFs) from the Meadowbank gold deposit, Western Churchill Province, Nunavut: *Chemical Geology*, v. 410, p. 89-107.
- Gourcerol, B., Thurston, P.C., Kontak, D.J., Côté-Mantha, O., and Biczok, J. 2015b, The geochemistry of chert from the Banded Iron Formation-type Musselwhite and Meadowbank gold deposits: Distinguishing primary and mineralization-related signatures of chert: Geological Survey of Canada, Current Research 2015-1, 24 p.
- Gourcerol, B., Thurston, P.C., Kontak, D.J., Côté-Mantha, O., and Biczok, J., 2015c, Depositional setting of Algoma-type banded iron formation from the Meadowbank, Meliadine, and Musselwhite gold deposits; In: Targeted Geoscience Initiative 4:

Contributions to the Understanding of Precambrian Lode Gold Deposits and Implications for Exploration, (Eds.) B. Dubé and P. Mercier-Langevin: Geological Survey of Canada, Open File 7852, p. 55-68.

Groves, D.I., Goldfarb, R.J., Robert, F., and Hart, C.J.R., 2003, Gold deposits in metamorphic belts: Overview of current understanding, outstanding problems, future research and exploration significance: *Economic Geology*, v. 100, p. 203-224.

Groves, D.I., Phillips, G.N., Ho, S.E., Houston, S.M., and Standing C.A., 1987, Craton-scale distribution of Archean greenstone gold deposits; predictive capacity of the metamorphic model: *Economic Geology*, v. 82, p. 2045-2058.

Hall, R.S., and Rigg, D.M., 1986, Geology of the West Anticline Zone, Musselwhite Prospect, Opapimiskan Lake, Ontario, Canada; In: Macdonald, A.J. (Ed.), *Gold '86; an international symposium on the geology of gold deposits; proceedings volume: GOLD '86*, Toronto, ON, Canada, p. 124-136.

Hollings, P., and Kerrich, R., 1999, Trace element systematics of ultramafic and mafic volcanic rocks from the 3 Ga North Caribou greenstone belt, northwestern Superior Province: *Precambrian Research*, v. 93, p. 257-279.

Howell, D., Griffin, W.L., Pearson, N.J., Powell, W., Wieland, P., and O'Reilly, S.Y., 2013, Trace element partitioning in mixed-habit diamonds: *Chemical Geology*, v. 355, p. 134-143.

Hrabi, R.B., Barclay, W.A., Fleming, D., and Alexander, R.B., 2003, Structural evolution of the Woodburn Lake group in the area of the Meadowbank gold deposit, Nunavut; In *Current Research 2003-C27*: Geological Survey of Canada, 10 p.

- Isaac, C., 2008, Stable isotope (N, O, H) geochemistry, petrology and compositions of biotite of the Musselwhite Mine, Ontario: implications for mineralization: Unpublished Master's Thesis, Lakehead University, 104 p.
- Janvier, V., Castonguay, S., Mercier-Langevin, P., Dubé, B., McNicoll, V., Pehrsson, S., Malo, M., De Chavigny, B., and Côté-Mantha, O., 2015a, Preliminary results of geology of the Portage deposit, Meadowbank gold mine, Churchill Province, Nunavut, Canada: Geological Survey of Canada, Current Research 2015-2, 18 p. doi:10.4095/295532.
- Kelly, C.J., and Schneider, D.A., 2015, Insights into the timing of mineralization and metamorphism in the North Caribou Greenstone Belt, Western Superior Province; In: Targeted Geoscience Initiative 4: Contributions to the Understanding of Precambrian Lode Gold Deposits and Implications for Exploration, (Eds.) B. Dubé and P. Mercier-Langevin: Geological Survey of Canada, Open File 7852, p. 245-253.
- Kerswill, J.A., 1993, Models for iron-formation-hosted gold deposits; In: Mineral Deposit Modelling, (Eds.) R.V. Kirkham, W.D. Sinclair, R.I. Thorpe, and J.M. Duke: Geological Survey of Canada, Special Paper 40, p. 171-199.
- Kerswill, J. A., 1996, Iron-formation hosted stratabound gold; In: Geology of Canadian Mineral Deposit Types, (Eds.) O. R. Eckstrand, W. D. Sinclair, & R. I. Thorpe, p. 367-382.
- Kontak, D.J., 2015, Applications and implications of trace element chemistry and elemental mapping of ore minerals to hydrothermal ore deposit discrimination and genetic models: Geological Association of Canada-Mineralogical Association of Canada Joint Annual Meeting, May 3-7, Montreal, Quebec, Program with abstracts, v. 38, p 293.

- Kontak, D.J., and Smith, P.K., 1993, A metaturbidite-hosted lode gold deposit: the Beaver Dam deposit Nova Scotia I. vein paragenesis and mineral chemistry: *Canadian Mineralogist*, v. 31, p. 471-522.
- Large, R.R., Halpin, J.A., Danyushevsky, L.V., Maslennikov, V.V., Bull, S.W., Long, J.A., Gregory, D.D., Lounejeva, E., Lyons, T.W., Sack, P.J., McGoldrock, P.J., and Calver, C.R., 2014, Trace element content of sedimentary pyrite as a new proxy for deep-time ocean-atmosphere evolution: *Earth and Planetary Science Letters*, v. 389, p. 209-220.
- Large, R.R., Bull, S.W., and Maslennikov, V.V., 2011, A Carbonaceous Sedimentary Source-Rock Model for Carlin- Type and Orogenic Gold Deposits: *Economic Geology*, v. 106, p. 331-358.
- Large, R.R., Danyushevsky, L., Hollit, C., Maslennikov, V., Meffre, S., Gilbert, S., Bull, S., Scott, R., Emsbo, P., Thomas, H., Singh, B., and Foster, J., 2009, Gold and Trace Element Zonation in Pyrite Using a Laser Imaging Technique: Implications for the Timing of Gold in Orogenic and Carlin-Style Sediment-Hosted Deposits: *Economic Geology*, v. 104, p. 635-668.
- Large, R.R., Maslennikov, V.V., Robert, F., Danyushevsky, L.V., and Chang, Z., 2007, Multistage sedimentary and metamorphic origin of pyrite and gold in the Giant Sukhoi Log Deposit, Lena Gold Province, Russia: *Economic Geology*, v. 102, p. 1233-1267.
- Lawley, C.J.M., Dubé, B., Mercier-Langevin, P., Kjarsgaard, B., Knight R., and Vaillancourt, D., 2015a, Defining and mapping hydrothermal footprints at the BIF-hosted Meliadine gold district, Nunavut, Canada: *Journal of Geochemical Exploration*, v.155, p. 33-55.

- Lawley, C.J.M., Dubé, B., Mercier-Langevin, P., McNicoll, V.J., Creaser, R.A., Pehrsson, S.J., Castonguay, S., Blais, J.-C., Simard, M., Davis, W.J., and Jackson, S.E., 2015b, Setting, age, and hydrothermal footprint of the emerging Meliadine gold district, Nunavut; In: Targeted Geoscience Initiative 4: Contributions to the Understanding of Precambrian Lode Gold Deposits and Implications for Exploration, (Eds.) B. Dubé and P. Mercier-Langevin: Geological Survey of Canada, Open File 7852, p. 99-111.
- Lawley, C.J.M., Creaser, R.A., Jackson, S., Yang, Z., Davis, B., Pehrsson, S., Dubé, B., Mercier-Langevin, P., and Vaillancourt, D., 2015c, Unravelling the Western Churchill Province paleoproterozoic gold metallotect: constraints from Re-Os arsenopyrite and U-Pb xenotime geochronology and LA-ICP-MS arsenopyrite trace element chemistry at the BIF-hosted Meliadine Gold District, Nunavut, Canada: *Economic Geology*, v. 110, p. 1425-1454.
- Lhotka, P.G., and Nesbitt, B.E., 1989, Geology of unmineralized and gold-bearing iron formation, Contwoyto Lake Point Lake region, Northwest Territories, Canada: *Canadian Journal of Earth Sciences*, v. 26, p.46-64.
- Longerich, H. P., Jackson, S. E., and Günther, D., 1996, Inter-laboratory note. Laser ablation inductively coupled plasma mass spectrometric transient signal data acquisition and analyte concentration calculation: *Journal of Analytical Atomic Spectrometry*, v. 11, p. 899-904.
- McCuaig, T.C., and Kerrich, R., 1998, P-T-t deformation-fluid characteristics of lode gold deposits: Evidence from alteration systematics: *Ore Geology Reviews*, v. 12, n. 6, p. 381-453.
- McCuaig, T.C., and Kerrich, R., 1994, HFSE/REE fractionations in high-MgO magmas as

indicators of mantle source characteristics and melting depths: Program with Abstracts- Geological Association of Canada; Mineralogical Association of Canada: Joint Annual Meeting, v. 19, p. 73.

McNicoll, V., Dubé, B., Biczok, J., Castonguay, S., Oswald, W., Mercier-Langevin, P., Skulski, T., and Malo, M., 2013, The Musselwhite gold deposit, North Caribou greenstone belt, Ontario: new high-precision U-Pb ages and their impact on the geological and structural setting of the deposit: Abstract, Geol. Assoc. of Canada annual meeting, Winnipeg.

Moran, P., 2008, Lithogeochemistry of the sedimentary stratigraphy and metasomatic alteration in the Musselwhite gold deposit. North Caribou Lake metavolcanic-metasedimentary belt, Superior Province, Canada: implications for deposition and mineralization: Unpublished Master's Thesis, Lakehead University, 351 p.

Morelli, R.M., Bell, C.C., Creaser, R.A., and Simonetti, A., 2010, Constraints on the genesis of gold mineralization at the Homestake gold deposit, Black Hills, South Dakota from rhenium-osmium sulfide geochronology: *Miner Deposita*, v. 45, p. 461-480.

Moss, R., Scott, S. D., and Binns, R. A., 2001, Gold content of eastern Manus Basin volcanic rocks; implications for enrichment in associated hydrothermal precipitates: *Economic Geology and the Bulletin of the Society of Economic Geologists*, v. 96, no. 1, p. 91-107.

Müller, W., Shelley, M., Miller, P., and Broude, S., 2009, Initial performance metrics of a new custom-designed ArF excimer LA-ICPMS system coupled to a two-volume laser-ablation cell: *Journal of Analytical Atomic Spectrometry*, v. 24, p. 209-214.

Oswald, W., Castonguay, S., Dubé, B., McNicoll, V.J., Biczok, J., Malo, M., and Mercier-

- Langevin, P., 2015, Geological setting of the world-class Musselwhite gold Mine, Superior Province, northwestern Ontario, and implications for exploration, In: Targeted Geoscience Initiative 4: Contributions to the Understanding of Precambrian Lode Gold Deposits and Implications for Exploration, (Eds.) B. Dubé and P. Mercier-Langevin: Geological Survey of Canada, Open File 7852, p. 69-84.
- Otto, A., 2002, Ore forming processes in the BIF-hosted gold deposit Musselwhite Mine, Ontario, Canada: Unpublished Master's Thesis, Freiberg Institute of Mining and Technology, 86 p.
- Paton, C., Hellstrom, J., Paul, B., Woodhead, J., and Hergt, J., 2011, Iolite: Freeware for the visualisation and processing of mass spectrometric data: Journal of Analytical Atomic spectrometry, v. 26, p. 2508-2518.
- Pehrsson, S.J., Wilkinson, L., and Zaleski, E., 2004, Geology of the Meadowbank gold deposit area, Nunavut: Geological Survey of Canada, Open File 4269, scale 1:20 000.
- Pehrsson, S.J., Berman, R.G., and Davis, W.J., 2013, Paleoproterozoic orogenesis during Nuna aggregation: a case study of reworking of the Rae craton, Woodburn Lake, Nunavut: Precambrian Research, v. 232, p. 167-188.
- Phillips, G.N., and Powell, R., 2010, Formation of gold deposits: a metamorphic devolatilization model: Journal of metamorphic geology, v. 28, p. 689-718.
- Phillips, G.N., Groves, D.N., and Martyn, J.E., 1984, An epigenetic origin for Archean banded iron formation-hosted gold deposits: Economic Geology, v. 79, p. 162-171.

- Pitcairn I.K., Teagle, D.A.H, Craw, D., Olivo, G.R., Kerrich, R., and Brewer, T.S., 2006, Sources of metals and fluids in orogenic gold deposits: Insights from the Otago and Alpine schists, New Zealand: *Economic Geology*, v. 101, p. 1525-1546.
- Poulsen K.H., Robert, F., and Dubé, B., 2000, Geological classification of Canadian gold deposits: Geological Survey of Canada, Bulletin 540, 106 p.
- Prior, D.J., Wheeler, J., Peruzzo, L., Spiess, R., and Storey, C., 2002, Some garnet micro structures: an illustration of the potential of orientation maps and misorientation analysis in microstructural studies: *Journal of Structural Geology*, v. 24, p. 999-1011.
- Putnis, A., and Putnis, C.V, 2010, The mechanism of re-equilibration of solids in the presence of a fluid phase; *Journal of Solid State Chemistry*, v. 180, p. 1783-1786.
- Putnis, C.V., Geisler, T. Schmid-Beurmann, P., Stephan, T., and Giampaolo, C., 2007, An experimental study of the replacement of leucite by analcime; *American Mineralogist*, v. 92, p. 19-26.
- Putnis, A.2002, Mineral replacement reactions: from macroscopic observations to microscopic mechanisms; *Mineralogical Magazine*, v. 66, p. 689-708.
- Ridley, J.R., and Diamond, L.W., 2000, Fluid chemistry of orogenic lobe gold deposits and implications for genetic models: *Reviews in Economic Geology*, v. 13, P. 141-162.
- Rittner, M., and Müller, W., 2012, 2D mapping of LA-ICPMS trace element distributions using R: *Computers & Geosciences*, v. 42, p. 152-161.
- Schieber, J., 2002, Sedimentary pyrite: A window into the microbial past: *Geology*, v. 30, p.

531-534.

Scholz, F., and Neumann, T., 2007, Trace element diagenesis in pyrite-rich sediments of the Achterwasser lagoon, SW Baltic Sea: *Marine Chemistry*, v. 107, p. 516-532.

Sherlock, R.L., Pehrsson, M.S., Logan, A.V., Hrabi, R.B., and Davis, W.J. 2004, Geological Setting of the Meadowbank Gold Deposits, Woodburn Lake Group, Nunavut: *Exploration and Mining Geology*, v. 13, no. 1-4, p. 67-107.

Sherlock, R.L., Alexander, R.B., March, R., and Barclay, W.A., 2001a, Geologic setting of the Meadowbank iron formation-hosted gold deposits; In *Current Research 2001-C11*: Geological Survey of Canada, 23 p.

Sherlock, R.L., Alexander, R.B., March, R., and Barclay, W.A., 2001b, Geologic setting of the Meadowbank iron formation-hosted gold deposits: Geological Survey of Canada, Open File 3149, scale 1:10 000.

Steadman, J.A., Large, R.R., Davidson, G.J., Bull, S.W., Thompson, J., Ireland, T. R., and Holden P., 2014, Paragenesis and composition of ore minerals in the Randalls BIF-hosted gold deposits, Yilgarn Craton, Western Australia: Implications for the timing of deposit formation and constraints on gold sources: *Precambrian Research*, v. 243, p. 110-132.

Sylvester P.C., Cabri L.J., Turbett M.N., McMahon G., Laflamme J.G.H., and Peregoedova A., 2005, Synthesis and evaluation of a fused pyrrhotite standard reference material for platinum-group element and gold analyses by laser ablation-ICPMS: Geological Survey of Finland, Espoo, Finland, 16-20, 10th International Platinum Symposium; Platinum-group elements; from genesis to beneficiation and environmental impact; extended abstracts.

- Tella, S., Paul, D., Berman, R.G., Davis, W.J., Peterson, T.D., Pehrsson, S.J., and Kerswill, J.A., 2007, Bedrock geology compilation and regional synthesis of parts of Hearne and Rae domains, western Churchill Province, Nunavut-Manitoba: Geological Survey of Canada, Open File 5441, scale 1:550 000 (3 sheets and a CD-ROM).
- Thomas, H.V., Large, R.R., Bull, S.W., Maslennikov, V., Berry, R.F., Fraser, R., Froud, S., and Moye, R., 2011, Pyrite and pyrrhotite textures and composition in sediments, laminated quartz veins and reefs at Bendigo gold mine, Australia: Insights for ore genesis; *Economic Geology*, v. 106, p. 1-31.
- Thurston, P., Ayer, J., Goutier, J., and Hamilton, M. A., 2008, Depositional Gaps in Abitibi Greenstone Belt Stratigraphy: a key to exploration for syngenetic mineralization: *Economic Geology*, v. 103, p. 1097-1134.
- Tomkins, A.G., 2010, Windows of metamorphic sulfur liberation in the crust: implication for gold deposit genesis: *Geochimica et Cosmochimica Acta*, v. 74, p. 3246-3259.
- Tomkins, A.G., Pattison, D.R.M., and Zaleski, E., 2004, The Hemlo gold deposit, Ontario; an example of melting and mobilization of a precious metal-sulfosalt assemblage during amphibolite facies metamorphism and deformation: *Economic Geology*, v. 99, p. 1063-1084.
- Wagner, T., Klemm, R., Wenzel, T., and Mattson B., 2007, Gold upgrading in metamorphosed massive sulfide ore deposits: direct evidence from laser-ablation-inductively coupled plasma-mass spectrometry analysis of invisible gold: *Geology*, v. 35, n. 9, p. 775-778.
- Wheeler, J.O., Hoffman, P.F., Card, K.D., Davidson, A., Sanford, B.V., Okulitch, A.V., and

Roest, W.R., 1996, Geological map of Canada: Geological survey of Canada, Map 1806A, CD-ROM.

Wohlgemuth-Ueberwasser, C.C., and Jochum, K.P., 2015, Capability of fs-LA-ICP-MS for sulfide analysis in comparison to ns-LA-ICP-MS: Reduction of laser induced matrix effects?: *Journal of Analytical Atomic spectrometry*; DOI: 10.1039/c5ja00251f.

Woodhead, J., Hellstrom, J., Hergt, J., Greig, A., and Maas, R., 2007, Isotopic and elemental imaging of geological materials by laser ablation Inductively Coupled Plasma mass spectrometry: *Journal of Geostandards and Geoanalytical Research*, v. 31, p. 331-343.

Wright, G.M., 1967, Geology of the southeastern barren grounds, Parts of the Districts of Mackenzie and Keewatin: Geological Survey of Canada, Memoire 350, 91 p.

Yue, K., and He, Y., 2008, Gold contents of both mantle-derived xenoliths and sulfides in them from eastern China: *Science in China Series D; Earth Sciences*, v. 51, no. 4, p. 499-508.

Chapter 5: Conclusions

The study of the Algoma-type BIFs represents two distinct challenges: firstly, their characterization provides an important contribution to extending our understanding of the geochemical evolution of early Earth through the Archean to the early Proterozoic, and secondly, as many of them host world-class gold deposits (e.g., the Homestake, Lupin, Musselwhite deposits; Frei et al., 2009; Biczok et al., 2012.), understanding their chemistry potentially contributes to identification of new deposits. In this thesis project, four different Algoma-type BIF-hosted gold deposits from Canada (i.e., the ~4 Moz Au Meadowbank deposit; the ≥ 2.8 Moz Au Meliadine district; the ~6 Moz Au Musselwhite deposit; and the ~4 Moz Au Beardmore-Geraldton district) were selected for study in order to : (1) define the depositional setting of the BIFs using REE+Y systematics of chert as proxy for their primary signature; (2) assess gold enrichment processes through examining the textures and trace element zoning of variable sulfides (i.e., pyrite, arsenopyrite and pyrrhotite); and (3) establish whether there is a particular geochemical type of Algoma-type BIF associated with gold mineralization.

The initial approach illustrated in Chapter 2 and 3, was to analyze barren versus mineralized chert samples from the four Algoma-type BIFs by LA-ICP-MS method in order to define the depositional setting of the BIFs regarding their primary signature using REE+Y systematics. The study recognized a similar signature for the four different Algoma-type BIFs showing: (1) interaction of seawater with Fe-oxyhydroxides, as suggested by their heavy REE enrichment coupled with La and Y enrichments; (2) contributions from high-temperature ($>250^{\circ}\text{C}$) hydrothermal fluids, as suggested by positive Eu excursions; and (3) detrital contamination, suggested by relatively consistent REE concentrations and a chondritic Y/Ho ratio (i.e., $\text{Y}/\text{Ho} \approx 27$). Moreover, based on an *in-situ* SIMS oxygen isotopic study, the influence of seawater

reacting with cherts during the diagenesis was documented. These chemical indicators help to define the geodynamic setting for the BIFs (i.e., restricted basin versus open seawater) but also to better understand Archean processes (e.g., diagenesis). However, it appears from the results of this study that the primary signature of the chert does not record a chemical signature that may be used as a vector for potential gold mineralization, as barren and mineralized chert samples show similar primary signatures that suggest therefore an epigenetic gold mineralizing model for these deposits rather than an initial syngenetic gold enrichment event, which has long been suggested and debated.

Several questions emerged from the findings in this thesis, among them is whether gold in the BIF-hosted gold deposits originates from the same source rock (e.g., black shale; Large et al., 2007, 2009) and therefore might the gold represent a similar process of enrichment in this deposit type (e.g., Steadman et al., 2014; Gao et al., 2015). Based on quantitative element distribution maps of sulfide phases combined with line traverses and spot analyses on similar sulfides (i.e., pyrite, pyrrhotite, arsenopyrite) using LA-ICP-MS, the main gold event in the Meadowbank, Meliadine and Musselwhite gold deposits has been shown to be characterized by an Au-As-Se-Te-Ag trace metal association in chapter 4. This event is associated with intense stratabound sulfide-replacement of Fe-rich material with a later remobilization into fracture networks by late stage, base metal-rich metamorphic fluids (Pb-Bi-rich). The epigenetic origin of the gold mineralization is confirmed and the origin of the fluids is attributed to metamorphic/hydrothermal orogenic processes that were driven by devolatilization of weakly to unmetamorphosed source rocks of similar character in all the deposit sites studied. Generation of gold-bearing fluid along with the specific element suite was channelled via major crustal faults and/or shear zones within low tensile strength rocks reacting with stratigraphic units. Due to its

high iron content, Algoma-type BIF acts as a favorable chemical trap with a high efficiency for reducing gold-rich fluid due to sulfidation reactions in the pre-existing oxide, silicate and/or carbonate facies of the BIF to generate iron-bearing sulfides (e.g., pyrite, pyrrhotite and arsenopyrite). Therefore, it appears that precipitation of gold in Algoma-type BIF represents a confluence of favorable conditions (e.g., structural, lithogeochemical, fluid conditions, stratigraphic units, etc.) rather than a specific geochemical type of Algoma-type BIF associated with gold.

5.1 Unreturned question and suggestion for future work

Several questions have been raised from this thesis project, such as detrital contamination in BIF as well as the potential source of gold within Algoma-type BIF. Within chapter 2 and 3, some elements were used as proxies to identify apatite, zircon or various shale contaminations. However, elements such as Al, P and Ga were not included in the analyses, which may represent an oversight from us; therefore, we recommend including them in future work. As shown in chapter 4, it appears that gold originates from a broadly analogous source in all the studied areas which is consistent with the overall model of Large et al. (2007, 2009, 2011), which argues for a gold-rich diagenetic pyrite hosted within carbonaceous black shale successions. However, early framboidal pyrite from the Meadowbank deposit does not show a significant Au content, which would have been consistent with this hypothesis, nor is there a correlation of Au with a specific suite of elements (e.g., Co, Ni, Pb, Zn, W, Mo), which are highly concentrated in diagenetic pyrites. Moreover, this specific suite of elements is not related to gold in the Meliadine gold district or in the Musselwhite deposit (e.g., Gao et al., 2015) which suggests, therefore, another source for gold which has not been identified in this study. Proximity of this potential gold source may represent a vectoring tool in combination with structural study for mineralized

Algoma-type BIFs.

5.2 References

- Biczok, J., Hollings, P., Klipfel, P., Heaman, L., Maas, R., Hamilton, M., Kamo, S. and Friedman, R., 2012. Geochronology of the North Caribou greenstone belt, Superior Province Canada: Implications for tectonic history and gold mineralization at the Musselwhite mine; *Precambrian Research*, v. 192-195, p. 209-230.
- Frei, R., Dahl, P.S., Duke, E.F., Hansen, T.R., Frandsson, M.M. and Jensen, L.A., 2008. Trace element and isotopic characterization of Neoarchean and Paleoproterozoic iron formations in the Black Hills (South Dakota USA): assessment of chemical change during 2.9-1.9 Ga deposition bracketing the 2.4-2.2 Ga first rise of atmospheric oxygen; *Precambrian Geology*, v. 162, p. 441-474.
- Gao, J.-F., Jackson, S.E., Dubé, B., Kontak, D.J. and De Souza, S., 2015. Genesis of the Canadian Malartic, Côté Gold, and Musselwhite gold deposits: Insights from LA-ICP-MS element mapping of pyrite; *In: Targeted Geoscience Initiative 4: Contributions to the understanding of Precambrian Lode Gold Deposits and Implications for Exploration*, (ed.) B. Dubé and P. Mercier-Langevin; Geological Survey of Canada, Open File 7852, p. 157-175.
- Large, R.R., Bull, S.W. and Maslennikov, V.V., 2011. A Carbonaceous Sedimentary Source-Rock Model for Carlin- Type and Orogenic Gold Deposits; *Economic Geology*, v. 106, p. 331-358.
- Large, R.R., Danyushevsky, L., Hollit, C., Maslennikov, V., Meffre, S., Gilbert, S., Bull, S., Scott, R., Emsbo, P., Thomas, H., Singh, B. and Foster, J., 2009. Gold and Trace Element Zonation in Pyrite Using a Laser Imaging Technique: Implications for the Timing of Gold in Orogenic and Carlin-Style Sediment-Hosted Deposits; *Economic Geology*, v. 104, p. 635-

668.

Large, R.R., Maslennikov, V.V., Robert, F., Danyushevsky, L.V. and Chang, Z., 2007.

Multistage sedimentary and metamorphic origin of pyrite and gold in the Giant Sukhoi Log Deposit, Lena Gold Province, Russia; *Economic Geology*, v. 102, p. 1233-1267.

Steadman, J.A., Large, R.R., Davidson, G.J., Bull, S.W., Thompson, J., Ireland, T. R. and

Holden P., 2014. Paragenesis and composition of ore minerals in the Randalls BIF-hosted gold deposits, Yilgarn Craton, Western Australia: Implications for the timing of deposit formation and constraints on gold sources; *Precambrian Research*, v. 243, p. 110-132.

Appendix A: The geochemistry of chert from the Banded Iron Formation-type Musselwhite and Meadowbank gold deposits: Distinguishing primary and mineralization-related signatures of chert

A.1 Abstract

Algoma-type banded iron formations (BIFs) are generally Archean chemical sedimentary rocks comprised of alternating layers of iron-rich minerals and chert of that are stratigraphically associated with submarine volcanic rocks and localized within greenstone belts. Although much research has been done on Algoma-type BIFs, their depositional and overall geologic settings are contentious due to overprinting effects of post depositional deformation and metamorphism and the absence of modern analogues for comparative studies.

Geochemical study of the gold-hosting Algoma-type BIFs at the Musselwhite and Meadowbank deposits provide comparable information on the depositional context for these Algoma-type BIFs. Geochemical tools, such as rare-earth elements REE+Y systematics, indicate that chert bands in Algoma-type BIF record contributions from: (1) seawater, characterized by enrichment in HREE relative to LREE, positive La, Gd and Y anomalies; (2) hydrothermal fluids, characterized by a positive Eu anomaly and a flat pattern; and (3) hydrogeneous contamination. A detailed study of each of the aforementioned deposits was undertaken to evaluate the origin of the chert in these BIF settings. A hydrothermal overprint on BIFs from the Musselwhite deposit is evidenced by negative Ce anomalies that may be due to late hydrothermal fluid circulation in the chert bands replacing the initial seawater component. This hydrothermal alteration phase may be associated with the gold mineralization.

A.2 Résumé

Les formations de fer rubanées (FFR) de type Algoma sont généralement des roches sédimentaires Archéenne constituées d'alternance de minéraux riche en fer et de chert qui sont stratigraphiquement associés à des roches volcaniques de type sous-marines et localisées dans des ceintures de roches vertes. Bien que beaucoup de recherches ont été effectuées sur ces formations de fer, leurs paramètres de déposition et caractéristiques géologiques sont controversés en raison de la surimpression des différentes épisodes de déformations et métamorphiques mais également l'absence d'analogue moderne pour des études comparatives.

L'étude géochimique des FFR de type Algoma dans les zones de Musselwhite et Meadowbank fournit des informations comparables sur le contexte de déposition pour les FFR de type Algoma. Les outils géochimiques, tels que des éléments de terres rares REE+Y, indiquent que les bandes de chert dans les FFR de type Algoma enregistre la ou les contributions de : (1) l'eau de mer, caractérisée par un enrichissement en terres rares lourdes par rapport à terres rares légères, des anomalies positives en La, Gd et Y ; (2) des fluides hydrothermaux, caractérisés par une anomalie positive en Eu et un spectre plat ; et (3) d'une contamination crustale. Une étude détaillée de chacun de ces dépôts précités a été entreprise pour évaluer l'origine du chert dans ces FFR. Une surimpression hydrothermale pour certain FFR localisés dans les zones de Musselwhite est démontrée par des anomalies négatives en Ce qui pourraient être associées à la circulation en fluides hydrothermaux tardifs dans les bandes de chert remplaçant la composante initiale de l'eau de mer. Cette altération hydrothermale pourrait être associée à la minéralisation aurifère.

A.3 Introduction

Algoma-type BIFs are thinly bedded chemical sedimentary rocks comprising alternating layers of iron-rich minerals and chert (James, 1954), stratigraphically associated with submarine, volcanic rocks in Eoarchean to Paleoproterozoic greenstone belts (Goodwin, 1973; Bekker et al., 2010). Studies of gold deposits associated with Algoma-type BIF in Archean cratons have shown that gold is associated with localized sulfide-facies zones within regionally extensive oxide-facies units (e.g., Kaapvaal, Zimbabwe, Superior, Slave and Churchill; Phillips et al., 1984; Bleeker, 2006; Biczok et al., 2012). The depositional and geologic settings of these deposits are contentious due to post depositional overprinting and the absence of modern analogues. The iron-bearing minerals in iron formations precipitated from basin waters and hydrothermal vents; they include siderite or/and iron oxy-hydroxides diagenetically transformed to hematite, magnetite, iron silicates and sulfides. The origin of chert is controversial, but the consensus is that it, like the iron-bearing minerals, originated as a seawater precipitate (Bolhar et al., 2005; Thurston et al., 2011) or as a hydrothermal precipitate (Allwood et al., 2010; Thurston et al., 2011) or by replacement (Hanor and Duchac, 1990). Because of the possibility of alteration during diagenesis, we examine the geochemistry of chert beds in that they more likely preserve their original chemistry.

In regard to BIF-hosted gold deposits, do the gold mineralizing fluids prefer one geochemical type of iron formation versus another? Lode-gold and BIF-hosted gold deposits are widely conceded to be epigenetic (Goldfarb et al., 2001, 2005), thus, at a regional scale the geochemical signature of the chert component of BIFs may provide a vector towards zones with an enhanced potential to host gold mineralization. Consequently, a study of the geochemical characteristics of Algoma-type BIF, both barren and those associated with gold mineralization,

may address important issues regarding these deposits by: (1) providing insights on which type of iron formation makes a better host for gold mineralization by identifying and using the pre-mineralized chemical signal; (2) allowing a better understanding of the mineralizing processes; (3) providing a geochemical footprint of the mineralized system; and (4) collectively providing a vectoring tool from least or unaltered to altered-mineralized zones.

This article presents the results of *in-situ* laser ablation inductively coupled mass spectrometric (LA ICP-MS) analysis of chert from BIF-hosted lode-gold deposits in the Superior and Churchill cratons, namely: (1) the Musselwhite deposit (11.23 Mt proven/probable grading 6.34 g/t gold in 2011), in the North Caribou greenstone belt of the Superior Province (Biczok et al., 2012), and (2) the Meadowbank deposit (24.5 Mt proven/probable ore reserve @ 2.8 g/t in 2011), located in the Woodburn Lake Group of the Rae Domain (Churchill Province).

A.4 Geological Setting

A.4.1 The Superior Province

The Archean Superior Province consists of east-west trending continental fragments interspersed with linear meta-sedimentary basins (Percival, 2007). The 2.9-3 Ga North Caribou Superterrane (NCS) was divided into multiple domains and terranes (Thurston et al., 1991). The NCS comprises granitoid basement (Thurston et al., 1991; Percival, 2007) and overlying volcanic belts (e.g., North Caribou greenstone belt), all cratonised at ca.2.87 Ga (Stott et al., 1989).

The North Caribou greenstone belt lies at the northern boundary of the North Caribou Terrane (Biczok et al., 2012). This greenstone belt comprises a core of metasedimentary rocks

flanked by metavolcanic units; all subdivided into eight supracrustal assemblages (Fig. A.1; Breaks et al., 2001). Recent geochronological work (Biczok et al., 2012; McNicoll et al., 2013) dated the units of the greenstone belt between 2980 and 2856 Ma. These results also indicate that the Opapimiskan Lake package in the vicinity of the Musselwhite mine is overturned (McNicoll et al., 2013) and likely thrust over the younger metasediments. Further complicating the picture is the recent discovery of volcanic units immediately south of the mine dated at ~2863 Ma and 2734 Ma (V. McNicoll, pers. comm.). Similar BIFs are found in at least three of the volcanic units of very different ages and it is hoped that this study will help distinguish these various BIFs. The belt is bounded by metamorphosed felsic plutonic rocks, in particular the ~2.87 Ga North Caribou Lake batholith and the Schade Lake gneissic complex (ca. 2856-2857 Ma (DeKemp, 1987; Biczok et al., 2012)).

A.4.1.1 The Musselwhite deposit

Located in the North Caribou greenstone belt (Fig. A.1), the Musselwhite mine is a giant deposit with past production and current reserves and resources totaling 5.41 million ounces (Biczok et al., 2012). The lithostratigraphy is dominated by BIFs and mafic to ultramafic metavolcanic rocks of the 2973<2967 Ma Opapimiskan-Markop metavolcanic assemblage (OMU) plus tholeiitic basalts and minor felsic volcanics of the 2980-2982 Ma South Rim Metavolcanic assemblage (SRV) (Biczok et al., 2012; McNicoll et al., 2013). Recent geochronology and field mapping indicate that the mine stratigraphy is overturned. The deposit itself is composed of multiple ore-bodies within two main iron formations within the Opapimiskan Lake metavolcanic assemblage.

The Opapimiskan-Markop metavolcanic assemblage is composed, from the structural base

to the top, of the “Lower Basalt” unit, the Southern Iron Formation, “Basement Basalt” unit and the Northern Iron Formation. The South Rim metavolcanic assemblage is composed, from base to top, of metamorphosed mafic volcanoclastic and flow units named the Bvol unit, and by dacitic to rhyolitic rocks named the Avol unit (Otto, 2002; Moran, 2008; Biczok et al., 2012).

The North Iron Formation, the main host to mineralization, is subdivided, from the structural base to top, into: pyrrhotite-rich mudstone (4H), chert-grunerite (4A), chert-magnetite (4B), clastic-chert-magnetite (“clastic”4B), garnet-grunerite-chert (4EA), garnetiferous amphibolite (4E) and garnet-biotite schist (4F) (Otto, 2002; Moran, 2008; Biczok et al., 2012). The main mineralized horizons are the 4EA and 4B. The Southern Iron Formation consists of two sub-parallel BIF horizons generally not mineralized (Biczok et al., 2012).

The Basement Basalt unit lying between the Northern and Southern Iron Formations is a thick sequence of massive- and pillowed tholeiitic basalt (Moran, 2008). The “Lower Basalt” unit is the structural footwall (Otto, 2002) and is composed of basalt and ultramafic rocks but includes extensive andesite (Hollings and Kerrich, 1999). The presence of pillow structures suggests a submarine environment (Otto, 2002; Moran, 2008).

A.4.1.1.1 Deformation

Three deformation events were recognized in the North Caribou greenstone belt (Hall and Rigg, 1986; Breaks et al., 2001). The first deformation (D1) is seen in tight F1 folds up to several metres long with a well-developed S1 fabric in schistose ultramafic units, and the property-scale repetition of units (Oswald et al., 2014). The second deformation (D2) is the most important structural fabric, which produced a moderate to strong, subvertical north-trending S2 foliation axial-planar to mesoscopic F2 folds (Breaks et al., 2001). The third deformation (D3) is

relatively weak and is recognized by a crenulation cleavage overprinting D2 in grunerite-rich BIF.

A.4.1.1.2 Metamorphism

Regional metamorphism of the North Caribou greenstone belt varies from lower greenschist to low-mid amphibolite facies (Breaks et al., 2001). The Musselwhite area is affected by two events, one middle amphibolite prograde ($>600^{\circ}\text{C}$) and the other a chlorite retrograde (210° to 250°C ; Otto, 2002; Isaac, 2008).

A.4.1.1.3 Mineralization

Mineralization consists of epigenetic gold associated with high-strain zones mainly along the steep limbs of the folded iron formation (Biczok et al., 2012). Gold mineralization developed under amphibolite conditions (i.e., 540° to 600°C ; Otto, 2002).

The most important host of gold mineralization in the Musselwhite mine is the silicate-facies iron formation (4EA) composed mainly of grunerite-garnet interlayered with chert. Garnets in barren 4EA are anhedral to subhedral, medium-grained, and contain numerous inclusions of grunerite, and other silicates. The continuation of strain after the formation of brittle hydrothermal garnets within the relatively more ductile grunerite matrix led to the development of extensive fractures in the garnets, as well as pressure shadows, into which pyrrhotite and gold are deposited (Biczok et al., 2012; Kolb, 2010). Retrograde phases such as chlorite are developed locally (Otto, 2002). The 4B unit consists of finely laminated layers of quartz, magnetite with minor grunerite. The typical, “pure” 4B is relatively unaltered adjacent to any mineralized zone compared to the 4EA. Mineralized 4B is cut by quartz +/- pyrrhotite veins and may develop grunerite replacement of the quartz-magnetite layers. The “clastic” variety of 4B contains diffuse

layers of very fine-grained chert, magnetite, amphiboles +/- garnets. In the vicinity of the high-strain zones on the limbs of the F2 folds, these silicate layers are prone to replacement by hydrothermal biotite, garnet +/- green amphiboles (Otto, 2002).

A.4.2 The Churchill Province

The Archean Churchill Province has been subdivided into the Hearne and Rae domains, (Fig. 2.1; Hoffman 1989). The Rae Domain consists of the ca. 2.7 Ga Woodburn Lake Group (Ashton, 1985; Roddick et al., 1992; Aspler and Chiarenzelli, 1996a) and the ca. 2.9 Ga Prince Albert Group (Schau, 1982; Aspler and Chiarenzelli, 1996a) which includes granitoids and mafic-ultramafic volcanic rocks, iron formation, shallow-water quartz arenite and minor felsic volcanic rocks (Miller and Tella, 1995). Aspler and Chiarenzelli (1996a) proposed the quartzites and komatiites of the Rae Domain were deposited during extension of “Nunavutia” a basement block (Pehrsson et al., 2013) that was later overlain by volcanic rocks of a back-arc sequence or an arc-trench system.

The Hearne Domain is a granite-greenstone terrane composed of multi-cyclic, mafic- to felsic volcanic rocks intercalated with immature sandstones, pelites, and iron formation with rare quartz arenites and spinifex-textured ultramafic rocks (Miller and Tella, 1995; Aspler and Chiarenzelli, 1996a).

A.4.2.1 The Meadowbank deposit

The Meadowbank deposit in the Rae Domain is contained within the Woodburn Lake Group (ca. 2.71 Ga) consisting of tholeiitic and komatiitic metavolcanic rocks with minor calc-alkaline felsic tuffs and flows with intercalated iron formation and clastic metasedimentary rocks (Armitage et al., 1996; Pehrsson et al., 2004; Sherlock et al., 2001a, b, 2004; Hrabi et al., 2003).

All of these units are intruded by mafic and felsic plutonic rocks.

The Meadowbank area (Fig. 2.2) contains two main gold deposits: the Meadowbank mine and the Vault deposit. The Meadowbank mine is mainly hosted within strongly altered and deformed, sulfide-bearing portions of the Central BIF (Sherlock et al., 2001a; Hrabí et al., 2003; Sherlock et al., 2004), whereas the Vault deposit is hosted by sericite-chlorite-pyrite and carbonate-altered intermediate- to felsic volcanic rocks (Hrabí et al., 2003; Sherlock et al., 2004).

Numerous units of Algoma-type BIF, 0.2 to 10 m thick, have been identified. These BIFs include the Far West IF, West IF, Central BIF, East BIF, and Grizzly IF, all generally interlayered with the volcanic rocks and locally with a quartzite unit (Fig. 2.2; Gourcerol et al., 2013; Sherlock et al., 2001a, b; 2004). These BIF are described more in detail in Gourcerol et al., 2013.

A.4.2.1.1 Deformation

The structural setting of the Meadowbank area is complex, consisting of six regional-scale ductile deformation events spanning the Neoarchean to Paleoproterozoic (e.g., Henderson et al., 1991; Ashton, 1985; Pehrsson et al., 2013). The D1 and D2 events had a significant effect on the geometry of the mineralized bodies in the Third Portage area (Ashton, 1985; Sherlock et al., 2004; Janvier et al., 2013). Some relict bedding (S0) is preserved in the quartz arenite and in the iron formation (Armitage et al., 1996). D2 represents the main structural event in the Meadowbank area (Janvier et al., 2013).

A.4.2.1.2 Metamorphism

Three distinct regional metamorphic events are recognized in the Meadowbank area. The

M1 is greenschist grade event dated at <2.60 Ga- >1.8-1.9 Ga. The M2 varies across the property from a mid-greenschist to amphibolite grade illustrated. This event is dated coeval with D2. The M3 shows a mid-upper greenschist to amphibolite grade, characterized by a new generation of biotite, garnet, cummingtonite and actinolite and is dated post mineralization (ca. 1.8 Ga).

A.4.2.1.3 Mineralization

Five principal mineralized zones are defined (Armitage et al., 1996; Davis and Zaleski, 1998; Pehrsson et al., 2000; Sherlock et al., 2001a, b; Pehrsson et al., 2004; Hrabi et al., 2003) and these are: Vault, North Portage, Third Portage, Bay Zone and Goose Island (Fig. 2.2).

The orebodies of the Meadowbank Mine in the Central BIF consist of several sub-parallel bands of auriferous iron formation. Sherlock et al. (2001a, b) suggested that the orebodies are mostly developed at the contact between an ultramafic body and the volcano-sedimentary package. According to Armitage et al., (1996) and Sherlock et al., (2001a, b), epigenetic gold mineralization is closely associated with D1-D2 deformation and originated from the circulation of fluids enriched in Mg, K, Ca, S, As, Cu and Au (Janvier et al., 2013).

A.5 Analytical methods and data treatment

Twenty-three samples of iron formation from drill core and outcrop were collected from the Musselwhite deposit (i.e., chert-magnetite (4B), garnet-grunerite-(chert) (4EA), garnetiferous amphibolite (4E) and garnet-biotite schist (4F)), and thirty-nine from the Meadowbank deposit (i.e., the Far West, West IF, Central BIF, East BIF and Grizzly). These samples were selected for petrographic study with an emphasis on the chert or chert-carbonate phases. An effort was made to avoid BIF with chert bands <0.05 centimeters thick since analysis of such thin bands presents

challenges. In addition, chert bands were analyzed in preference to Fe-rich bands to minimize the effects of any diagenetic alteration. Polished thin sections from these samples were examined in detail, using both transmitted and reflected light microscopy followed by SEM-EDS imaging and analysis.

Trace-elements and REE chemistry was obtained on 100 μm thick polished sections following petrographic study. Based on the latter observations, areas for analysis were selected to minimize the presence of phases other than silica replacing chert, alteration, and mineral inclusions. Analyses were made using a Resonetics Resolution M-50 laser ablation instrument coupled to a Thermo X-Series II quadrupole ICP-MS at the Geochemical Fingerprinting Laboratory of Laurentian University, in Sudbury, Ontario, using the protocol of Kamber and Webb (2007). Line traverses were made on the pre-selected areas using 140 and 190 μm beam diameters with a repetition rate of 10 Hz and an energy density of 7 J/cm². The elemental concentrations reported herein represent, therefore, the integrated signal over the length of the traverse. The element list used for each analysis included the 14 REEs in addition to Li, Be, Si, Sc, Ti, V, Cr, Mn, Fe, Co, Ni, Cu, Zn, Ga, As, Rb, Sr, Zr, Nb, Mo, Ag, Cd, In, Sn, Sb, Cs, Ba, Hf, Ta, W, Tl, Pb, Th and U. Silica was used as the internal standard and the NIST 612 glass standard was analyzed at the beginning and at the end of each line traverse. The final concentrations were determined by integration of the signals over the selected length of the traverse.

Only data from samples where all the REE were above the detection limit are discussed below. In addition, the Queensland (MUQ) shale standard was used for normalizing the REE+Y values. This shale standard is commonly used for normalization of Archean BIF data due to its dominantly mafic volcanic provenance that is similar to the expected average terrigenous input

into the ocean from weathering of upper continental crust (e.g., Bolhar et al., 2005; Thurston et al., 2011). Furthermore, where discussed below, La, Ce, Eu, Gd anomalies are calculated following the procedure of Lawrence and Kamber (2006) and Pr using the procedure of Bau and Dulsli (1996):

$$(La/La)^*_{MUQ} = La/(Pr_{MUQ} * (Pr_{MUQ}/Nd_{MUQ})^2) \quad (1)$$

$$(Ce/Ce)^*_{MUQ} = Ce/(Pr_{MUQ} * (Pr_{MUQ}/Nd_{MUQ})) \quad (2)$$

$$(Pr/Pr)^*_{MUQ} = Pr/(0.5Ce_{MUQ} + 0.5Nd_{MUQ}) \quad (3)$$

$$(Eu/Eu)^*_{MUQ} = Eu/(Sm_{MUQ}^2 * Tb_{MUQ})^{1/3} \quad (4)$$

$$(Gd/Gd)^*_{MUQ} = Gd/(Tb_{MUQ}^2 * Sm_{MUQ})^{1/3} \quad (5)$$

$$(Lu/Lu)^*_{MUQ} = Lu/(Yb_{MUQ} * (Yb_{MUQ}/Tm_{MUQ})) \quad (6)$$

A.6 Review of REE+Y systematics in BIF

The abundance of REE+Y in chert is controlled by three possible processes: (1) precipitation from open marine seawater (e.g., Bau and Dulsli, 1996); (2) precipitation from hydrothermal (i.e., vent sourced) fluids (e.g., Allwood et al., 2010; Danielson et al., 1992); and (3) replacement (e.g., Hanor and Duchac, 1990). All of these processes can be influenced by terrigenous input (Alexander et al., 2008) and oceanographic processes, such as phosphate precipitation. It is customary to normalize samples using a shale standard to minimize the influence of terrigenous input. Yttrium is a rare-earth element with a valence of 3⁺, though not a lanthanide, thus it is inserted into the conventional rare-earth diagram between Dy and Ho based on its geochemical behavior. Given the large beam size used for the analysis, if other phases were present, they

would affect the REE+Y pattern and values for elements such as Ga (i.e., clay mineral contamination), Zr (felsic ash contamination), and Th/U (phosphate contamination). In a modern setting, the shale normalized REE+Y pattern for material precipitated from seawater shows:

- a. Depletion in light rare-earth elements (LREE) relative to heavy rare-earth elements (HREE);
- b. A strongly super-chondritic Y/Ho ratio (i.e., >27), which produces a positive Y anomaly that is often between 40-90;
- c. A slightly positive La anomaly (La/La^* between 1.15 and 1.3);
- d. A positive Gd anomaly (Gd/Gd^* between 1.3 and 1.5);
- e. A well-developed negative Ce anomaly resulting from the oxidation of Ce^{+3} to Ce^{+4} in the water column;
- f. A minor positive Lu anomaly where analysis of Lu at an appropriate level is available.

Due to the anoxic character of Archean seawater, the shale-normalized REE+Y patterns for Archean seawater is very similar to modern seawater except that Ce shows a negative anomaly (Planavsky et al., 2010).

Based on the above criteria, samples with an Archean seawater pattern should be characterized by the following in shale-normalized REE+Y plots:

- a. Depletion in LREE relative to middle (M) and HREE;
- b. A strongly super-chondritic Y/Ho ratio between 50 and 65;

- c. Positive La and Gd anomalies (0.3 to 0.5 and 0.15 to 0.3, respectively);
- d. Variable, but well-developed positive Eu anomalies (Kamber et al., 2004);

Positive La, Y and Gd anomalies indicate precipitation from seawater under anoxic conditions (absence of a negative Ce anomaly) with the presence of a positive Eu anomaly indicating the influence of high temperature (>250°C) hydrothermal fluids (Kamber et al., 2004; Bau and Dulski, 1996).

Hydrothermal precipitates are characterized by the lack of LREE depletion, absence of both La and Gd anomalies, and the presence of a variably developed Eu anomaly. Crustal contamination may include mineral phases, such as phosphates, clays, and/or resistant minerals (e.g., zircon, xenotime, etc.), all of which induce cause a range of effects upon the REE+Y patterns depending on their modal abundances.

A.7 Results

A.7.1 Musselwhite

Samples from the chert-magnetite (4B), garnet-grunerite-(chert) (4EA), garnetiferous amphibolite (4E) and garnet-biotite schist (4F) were normalized to MUQ (Tables 3.4, 3.5 and A.1, and Figs. A.2A, A.3A, A.4A, A.5A).

REE+Y normalized data for the 4B, 4EA and 4E samples show, with some minor exceptions, relatively uniform patterns. The data include a moderate enrichment in the HREEs relative to both the LREE and the MREE and La, Gd and Eu positive anomalies (Tables 3.4, 3.5 and A.1; Figs. A.2A, A.3A, A.4A, A.5A). The garnet-biotite schist (4F) facies samples illustrate, however, a different pattern signature and very slightly positive to no Eu anomaly (Fig. A.5A).

Due to the low concentrations of the REE+Y, the Y/Ho ratios of samples are weakly positive (i.e., chondritic values) and are carefully used in this study.

The chert-magnetite (4B) facies (Fig. A.2) shows moderate enrichment in the HREE relative to both the MREE and the LREE ($\text{Nd/Yb}_{\text{MUQ}} = 0.04\text{-}0.67$), positive La, Gd and Eu anomalies ($\text{La/La}^*_{\text{MUQ}} = 1.5\text{-}2.6$, $\text{Gd/Gd}^*_{\text{MUQ}} = 0.9\text{-}1.2$ and $\text{Eu/Eu}^*_{\text{MUQ}} = 1.7\text{-}3.5$; Table 3.4). Samples E599668 and E599655 (Fig. A.2A) show, however, stronger enrichment in the MREE relative to LREE ($\text{Pr/Sm}_{\text{MUQ}} = 0.12\text{-}0.36$ (Fig. A.2A) relative to the majority of samples. The chert-magnetite facies illustrates, therefore, both a seawater and hydrothermal component. To understand the difference in the ΣREE of the patterns, $\text{Pr/Sm}_{\text{MUQ}}$ ratios and the Sr, Mn and Ga contents are plotted in Figures A.2B, C, and D. The elevated Sr and Mn values (Fig. A.2C and B, respectively) suggest samples E599668 and E599655 may be influenced by a source having enrichment in Mn and also to some extent Sr (i.e., proxy of calcium). Observations made with the SEM-EDS confirmed the presence of iron-amphiboles (grunerite-cummingtonite), but also the occurrence of calcium-rich amphiboles (actinolite) and iron-carbonate around the line traverse and overprinting the chert that could explain the higher concentrations of both Mn and Sr in these samples.

The data for the garnet-grunerite-(chert) (4EA) (Fig. A.3) indicate the samples can be subdivided into two distinct groups:

- (a) Samples E599660, E599662, E599663, E599665 and E599666 show enrichment in the HREE relative to both the MREE and the LREE ($\text{Nd/Yb}_{\text{MUQ}} = 0.15\text{-}0.46$), and negative La, Gd and strong positive Eu anomalies ($\text{La/La}^*_{\text{MUQ}} = 0.02\text{-}0.51$, $\text{Gd/Gd}^*_{\text{MUQ}} = 0.3\text{-}0.8$, and $\text{Eu/Eu}^*_{\text{MUQ}} = 2.1\text{-}3.48$; Table 3.5).

(b) Samples E599654, E599659 and E599667 show variable enrichment in the HREE relative to both the MREE and the LREE ($\text{Nd/Yb}_{\text{MUQ}} = 0.6\text{-}2.97$), and positive La, Gd and Eu anomalies ($\text{La/La}^*_{\text{MUQ}} = 1.5\text{-}3.02$, $\text{Gd/Gd}^*_{\text{MUQ}} = 0.94\text{-}1.2$, and $\text{Eu/Eu}^*_{\text{MUQ}} = 2.3\text{-}3.9$; Table 3.5).

The first group reflects a strong hydrothermal component without the presence of seawater input and the second group reflects a hydrothermal and seawater combination for the formation of chert. Based on $\text{Pr/Sm}_{\text{MUQ}}$ ratios and the Mn, Ga and Sr content, these data suggest sample E599667 may be influenced by a source enriched in Mn, Sr and Ca (Fig. A.3). Enrichment of these elements could be explained by the presence of iron-rich (i.e., grunerite-cummingtonite) and aluminium- and calcium-rich (actinolite) (due to high correlation between the two elements) amphiboles occurring as inclusions in the chert and around the line traverse as was also suggested for the chert-magnetite facies.

The garnetiferous amphibolite (4E) facies (Fig. A.4) shows enrichment in the HREE relative to both the MREE and the LREE ($\text{Nd/Yb}_{\text{MUQ}} = 0.16\text{-}0.71$), and variably developed positive La, Gd and Eu anomalies ($\text{La/La}^*_{\text{MUQ}} = 0.71\text{-}1.6$, $\text{Gd/Gd}^*_{\text{MUQ}} = 0.92\text{-}1.05$ and $\text{Eu/Eu}^*_{\text{MUQ}} = 2.42\text{-}2.59$; Table 3.4). For this facies, both a seawater and hydrothermal contribution are suggested from the data. Based on the $\text{Pr/Sm}_{\text{MUQ}}$ ratios and Sr and Ga contents, a correlation is observed between Sr and Ga contents for sample E5996551 which suggests the sample may be influenced by a Sr-, Ga- rich source (i.e., proxies of Ca and Al; Fig. A.4B, C). This source could be explained by presence of aluminium- and calcium-rich (actinolite) amphiboles in the chert around the line traverse which would also explain the difference in ΣREE contents for the samples. However, the low concentration of Ga and particularly Sr in the other samples could be due to analytical error. Therefore this discrimination has to be used carefully.

Finally, the garnet-biotite schist (4F) facies (Fig. A.5) shows variable enrichment in the MREE relative to both the HREE and LREE ($\text{Pr}/\text{Sm}_{\text{MUQ}} = 0.18\text{-}0.8$) and only moderate positive Eu anomalies ($\text{Eu}/\text{Eu}^*_{\text{MUQ}} = 1.08\text{-}1.94$; Table A.1). This unit is distinguished from the other units by its REE+Y signature and, furthermore, is similar to the argillite studied by Thurston et al (2011) which illustrated only weak hydrothermal influence. Based on $\text{Pr}/\text{Sm}_{\text{MUQ}}$ ratios and the Sr and Ga contents (Fig. A.5B, C), sample E599657 could be affected by the presence of garnet which would explain the Ga/Sr ratios. The other samples show a strong correlation among Sr, Ga and Ta content relative to $\text{Pr}/\text{Sm}_{\text{MUQ}}$ ratios (Fig. A.5B, C, D), which could be explained by the presence of plagioclase and biotite (e.g., Moran, 2008).

To define the environment of precipitation for the garnet-grunerite-(chert) (4EA) and the garnet-biotite schist (4F) facies which only show the hydrothermal influence, the Th/U ratio is used. This ratio in epiclastic sedimentary rocks does not vary much and falls close to the Th/U ratio of average upper continental crust (i.e., 3.9; Bau and Alexander, 2009). Therefore, in river water draining continental areas the ratio will be close to 3.9 (or within a 15% error margin); whereas in seawater it will be closer to 1 if it is considered that the Archean seawater is anoxic (Fig. A.6A). However, for the Musselwhite samples, all the data plot far from the field for river water, hence it is suggested that the initial seawater signature expected in all the BIFs was completely overprinted/or replaced due to the influence of a hydrothermal fluid either during or post diagenesis in these samples.

All of the BIF facies in the Musselwhite area show a variable seawater component and positive Eu anomalies (Figs. A.2A, A.3A, A.4A, A.5A) which suggest that these samples have been influenced by both seawater and hydrothermal fluids. In order to evaluate the contribution of end-member seawater and hydrothermal fluids, a conservative mixing calculation was done

(Fig. A.7A) which indicates that a high-T hydrothermal fluid contribution of less than 20% is needed to produce the observed Eu/Sm ratios (Fig. A.7A).

A.7.2 Meadowbank

The data set from the Meadowbank area was reported and discussed by Gourcerol et al. (2013). The Far West, West IF, Central BIF, East BIF and Grizzly were analyzed and normalized to MUQ (Fig. 2.7) and with some minor exceptions; seawater and hydrothermal inputs were observed in each deposit. The West BIF and East IF showed a detrital component, as indicated by relatively flat REE patterns, particularly for the LREE. Using a conservative mixing calculation, an estimate of the detrital input is calculated for each sample using MUQ as a shale reference.

For the West IF, sample AMB-128328 was used as an initial composition lacking any hydrogeneous input which was then mixed incrementally with detritus. The detrital input has the effect of producing flatter REE patterns commencing with 0.1% contaminant (Fig. A.8A). The contamination is very efficient at modifying the primary REE pattern and, therefore, can account for most of the patterns observed for samples from this area. The mixing calculations suggest that the majority of samples were affected by less than 5% shale contamination (Fig. A.8B).

For the East BIF, sample AMB-126246 is used as the initial composition to assess contamination. In this case, contamination with shale does not appear to account for the REE patterns as well as observed for the West IF (Fig. A.8C) as only four samples (i.e., AMB-126245, AMB-126247, AMB-126248 and AMB-126250) are located on/or close to the mixing trend (Fig. A.8D). Thus it appears that samples from the West IF have been more affected than the East BIF by shale contamination, as constrained by the composition used for the mixing

calculations.

For the samples of Meadowbank deposit area, the Th/U versus $(\text{Ce}/\text{Ce}^*)_{\text{MUQ}}$ diagram is used to further test the importance of seawater (Fig. A.6B). The data confirm the dominance of seawater, as suggested previously using the positive La, Gd, Y anomalies and enrichment in HREE relative to MREE and LREE. The samples from the West BIF show a larger dispersion relative to the other Meadowbank data and, even more so to that observed for the Musselwhite samples. This dispersion of data may be produced by the more extensive shale contamination postulated for the Meadowbank BIF. This is supported by the conservative mixing calculations shown in Figure A.7B which indicate that a high-T hydrothermal fluid contribution of higher than 20% is adequate to explain the Eu/Sm ratios

A.8 Summary and Discussion

The trace-element signatures for chert in Algoma-type BIFs from these gold deposit settings have been determined in order to: (1) constrain the origin of the BIF units, (2) assess the effect of superimposed hydrothermal processes possibly related to gold mineralization on the cherts; and (3) assess the consequent implications for BIF-hosted gold deposits in general. This report represents the second part of this study (Gourcerol et al., 2013). Importantly, in this phase of the study we validated the application of using LA ICP-MS analysis in traverse mode on carefully selected chert bands within BIFs with the appropriate analytical protocols to provide quantitatively meaningful data. It was also shown that these data, when plotted in $\text{MUQ}_{\text{shale}}$ -normalized patterns, provided internally consistent patterns that reflect the nature and origin of the fluids from which the chert precipitated. The consistency of the patterns noted in this study indicates that potentially primary chemical signatures have been retained within the selected

chert samples despite the fact that several post-formation deformation and metamorphic events, in some cases to amphibolite facies, have affected the rocks.

A.8.1 Implications for the depositional processes of BIFs

Although Musselwhite and Meadowbank differ in their petrographic features, style of gold mineralization and geologic tectonic setting, the chert samples show similar geochemistry and depositional setting:

- (1) A seawater component is recognized in most of the BIFs, as reflected by enrichment in the HREE relative to LREE and MREE, and positive La, Gd, Y anomalies. In some BIFs (e.g., 4EA, 4F), the combination of the Th/U ratios and Eu/Eu* values suggest that a hydrothermal component overprinted or replaced the seawater component either during or after diagenesis and thus likely during mineralizing processes.
- (2) A hydrothermal contribution is recognized in all the BIFs as reflected in positive Eu anomalies. This hydrothermal component is estimated at 0.1 to 30%, using the trace element chemistry of black smoker fluids as an end member, thus confirming that BIFs formed in areas where black smoker systems formed part of the geological setting.
- (3) A detrital contribution is observable in all the BIFs either as a trace contaminant or observable volcanic detritus, depending on the proportion of detritus involved. The shale contamination appears, however, to be more significant in the data for samples from the West IF and East BIF.

The results of this study indicate that Algoma-type BIFs were formed in a marine setting close to discharge zones for hydrothermal fluids (here, black smoker type fluids).

A.8.2 Implications for the gold mineralization

A significant outcome of this phase of the study is the recognition of a possible chemical overprinting by hydrothermal fluids on the cherts bands close to gold mineralized zones, as recorded by the modification of the original seawater-type REE+Y patterns. At the Musselwhite deposit, this possible overprint is illustrated by the 4EA and 4F units. Although unit 4F is largely an argillite and is not strictly considered as a BIF (i.e., as chemical sedimentary rocks composed of iron rich mineral interlayered with chert bands but more as an IF (22.7% Fe₂O₃, n = 70), it still is inferred to show the influence of an overprinting hydrothermal fluid. Unit 4EA, a BIF, shows strong Eu anomalies that coincide with negative Ce anomalies ($((\text{Ce}/\text{Ce}^*)_{\text{MUQ}} = 0.04\text{-}1.59$, average = 0.66, standard deviation at 1.13), which should be close to 1 in Archean seawater (i.e., anoxic conditions). This unit also represents the more mineralized BIF facies in the Musselwhite area.

A.9 Acknowledgements

The authors gratefully acknowledge the staff of Agnico Eagle Mines Ltd. and Goldcorp Ltd. and more particularly the Meadowbank and Musselwhite regional exploration crews. The authors also thank Dr. Sally Pehrsson, Dr. Olivier Côté-Mantha, and John Biczok for discussions regarding the regional geological setting of the study areas. Finally, we sincerely acknowledge the contribution of Dr. Benoit Dubé of the Geological Survey of Canada for initiating the TGI-4 Lode-Gold Project and for his input and continued support. The study is supported by both TGI-4 funding from Natural Resources Canada and funding through a Natural Sciences and Engineering Research Council Collaborative Research and Development agreement with participation by Agnico Eagle Mines Ltd and Goldcorp.

A.10 Figures and Captions

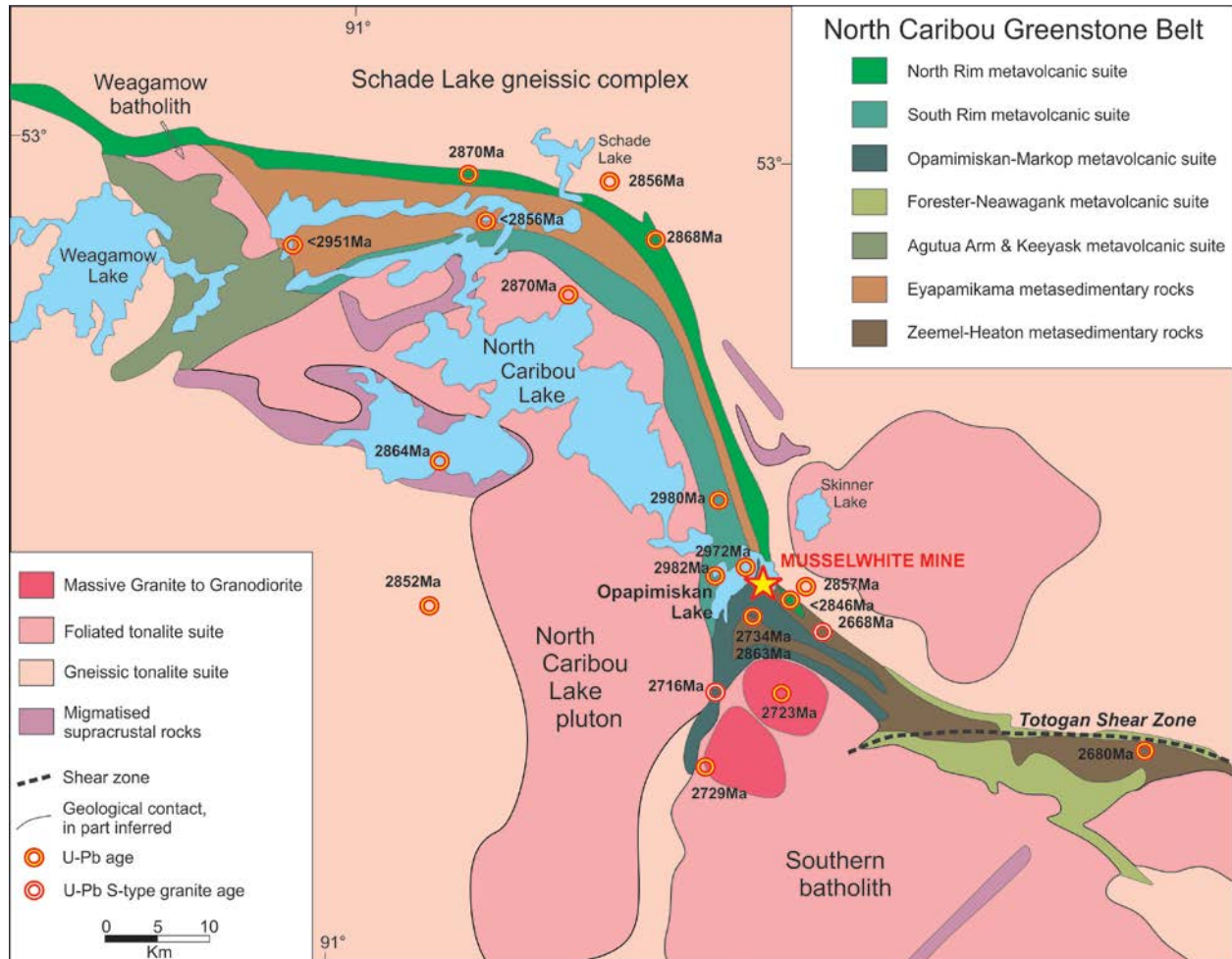


Figure A.1: Geological map of the Musselwhite area (Biczok et al., 2012).

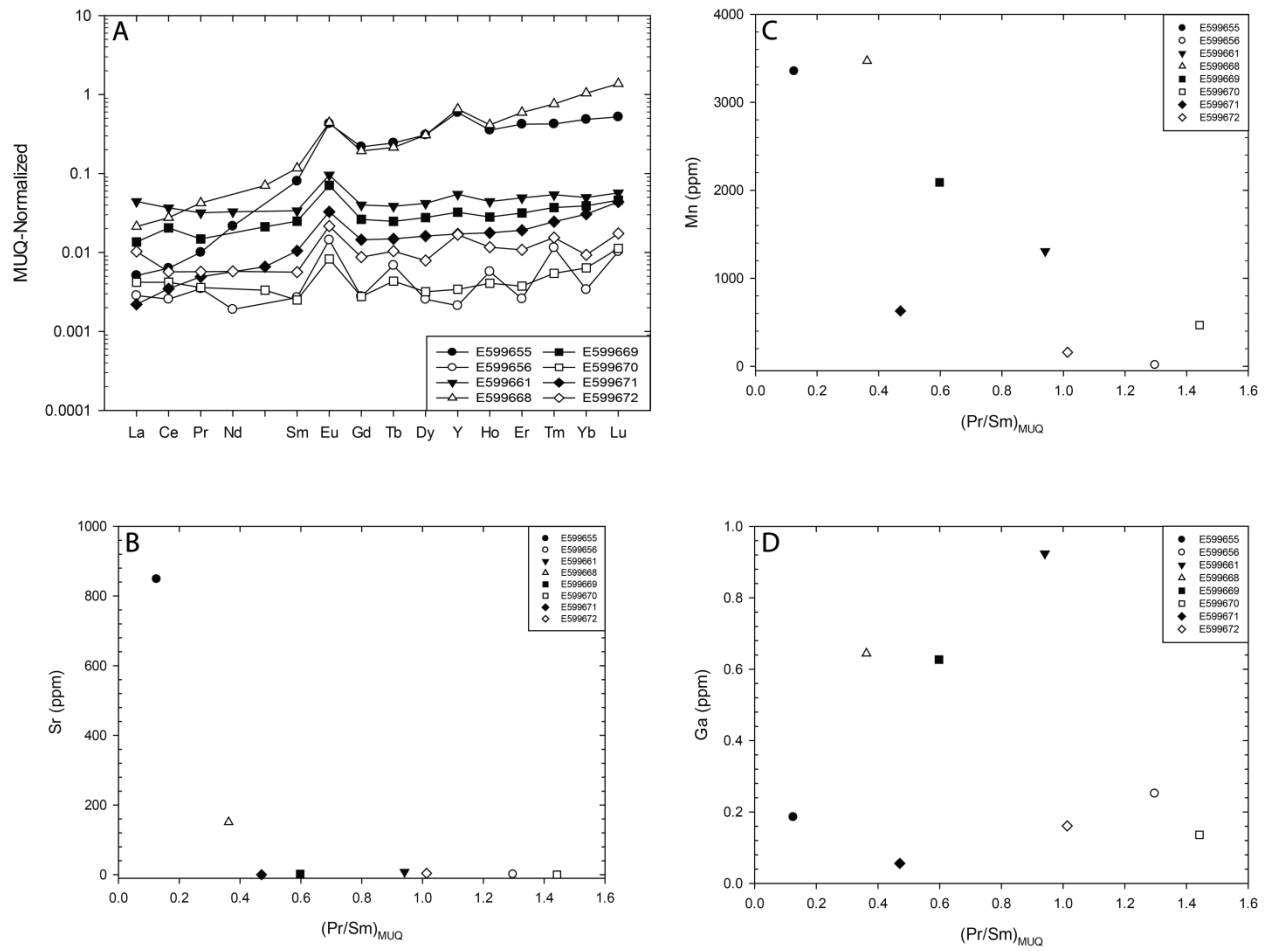


Figure A.2: Plots of geochemical data for chert samples from the 4B unit at Musselwhite: A) Shale (MUQ) -normalized REE patterns reflecting the influence of ambient seawater and hydrothermal fluids; B) plot of Sr vs. $(Pr/Sm)_{MUQ}$; C) plot of Mn vs. $(Pr/Sm)_{MUQ}$; D) plot of Ga vs. $(Pr/Sm)_{MUQ}$.

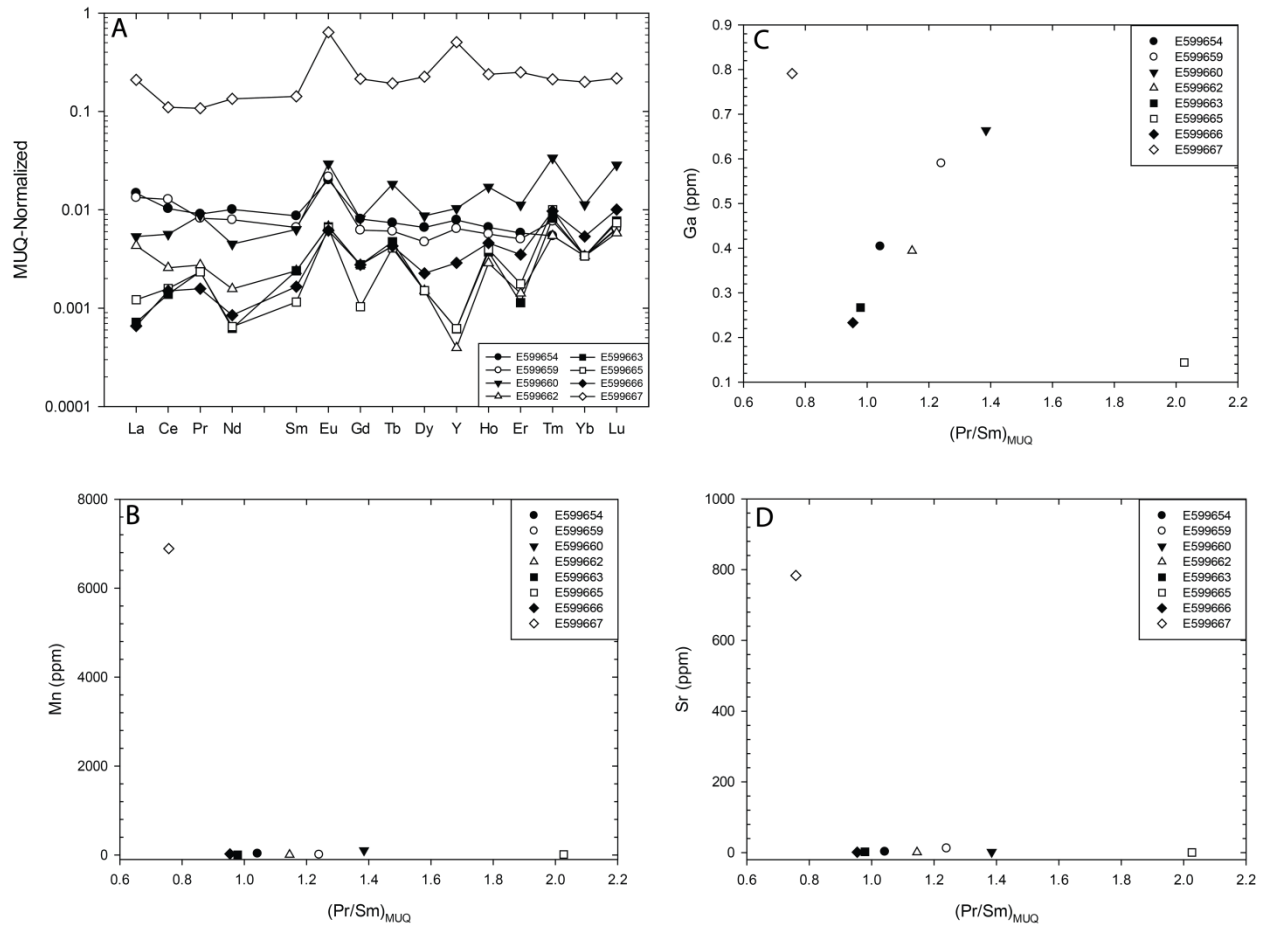


Figure A.3: Geochemical data for chert samples from the 4EA unit at Musselwhite: A) Shale (MUQ) -normalized REE patterns reflecting the influence of ambient seawater and hydrothermal fluids; B) Mn vs. $(Pr/Sm)_{MUQ}$; C) Ga vs. $(Pr/Sm)_{MUQ}$; D) Sr vs. $(Pr/Sm)_{MUQ}$.

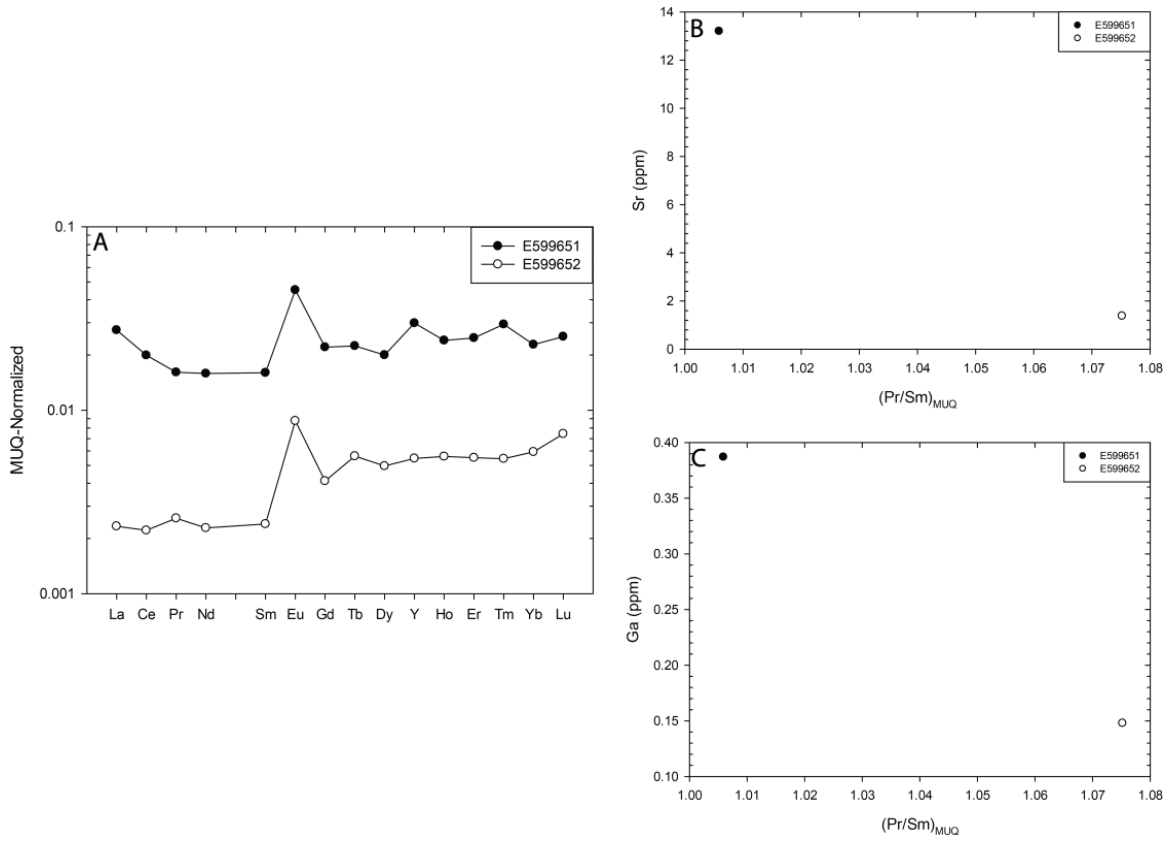


Figure A.4: Geochemical data for chert samples from the 4E unit at Musselwhite: A) Shale (MUQ) -normalized REE patterns reflecting the influence of ambient seawater and hydrothermal fluids; B) Sr vs. $(Pr/Sm)_{MUQ}$; C) Ga vs. $(Pr/Sm)_{MUQ}$.

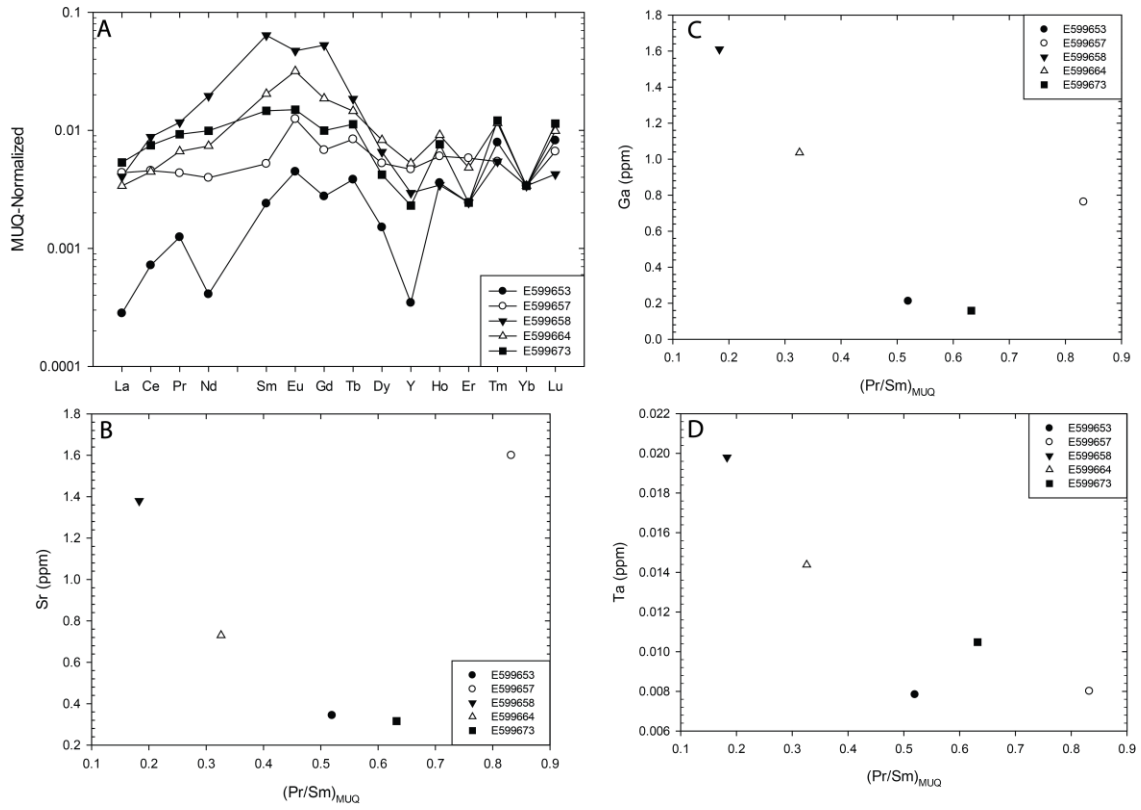


Figure A.5: Geochemical data for chert samples from the 4F unit at Musselwhite: A) Shale (MUQ) -normalized REE patterns reflecting the influence of ambient seawater and hydrothermal fluids; B) Sr vs. Pr/Sm_{MUQ} ; C) Ga vs. Pr/Sm_{MUQ} ; D) Ta vs. Pr/Sm_{MUQ} .

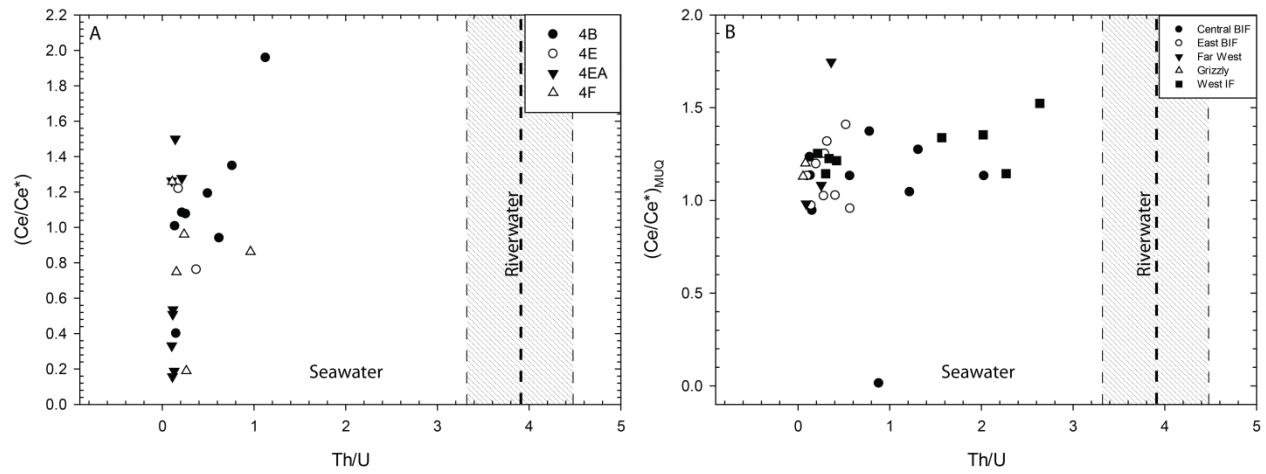


Figure A.6: Plot of Th/U versus $(Ce/Ce^*)_{MUQ}$ for samples from Musselwhite (A), and Meadowbank (B) deposits compared to the fields for river water and seawater based on the continental crust Th/U value of 3.9. A margin of errors of 15% is applied here (after Bau and Alexander, 2009).

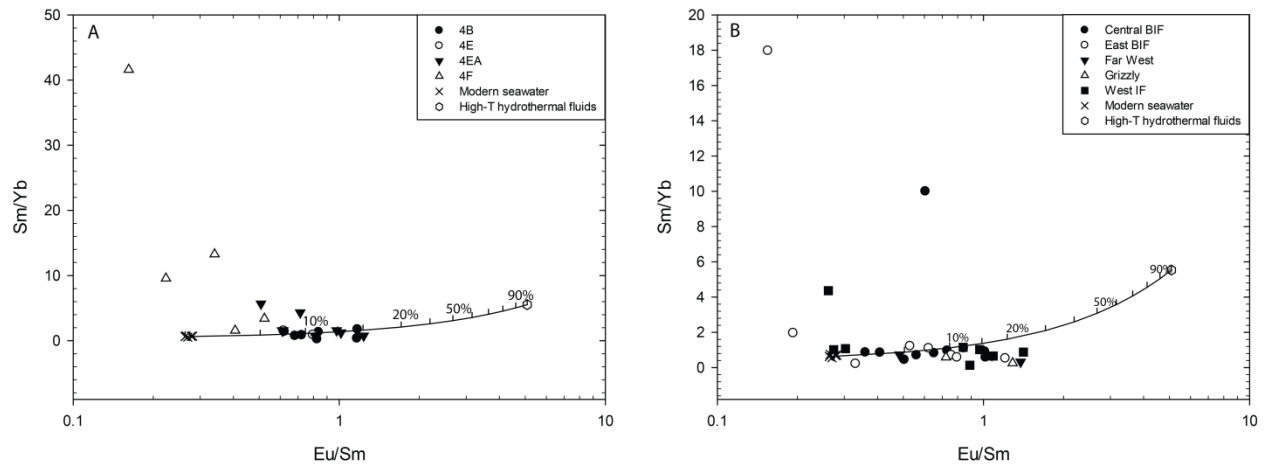


Figure A.7: A plot of elemental ratio data (Eu/Sm and Sm/Yb) for samples from Musselwhite (A), and Meadowbank (B) deposits which is used to assess potential contamination of samples with a high-T hydrothermal fluid, as illustrated with the two-component conservative mixing lines. The data for the black smoker fluid is from Bau and Dulski (1999) and data for seawater is from Alibo and Nozaki (1999).

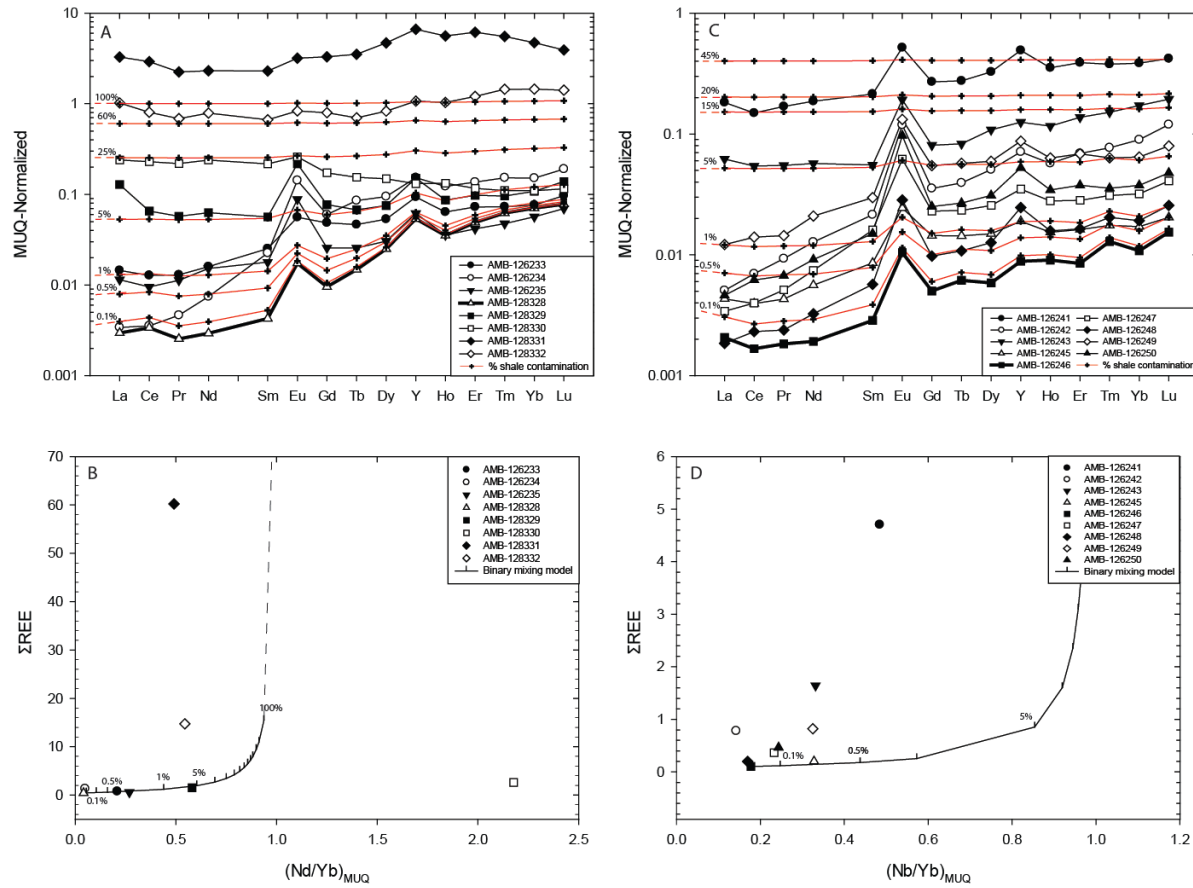


Figure A.8: Influence of variable detrital contamination on chert samples. Geochemical data for chert samples from the West BIF (A) and the East BIF (C) at the Meadowbank deposit compared to variable amounts of shale contamination (red lines) using sample AMB-128328 as the initial sample without any contamination. A plot of $(\text{Nd/Yb})_{\text{MUQ}}$ versus ΣREE content (ppm) of samples from the West BIF (B) and the East BIF (D) in the Meadowbank area. Except for three of the 8 samples, all are close to or on the mixing line and suggest up to 5% shale contamination.

A.11 Table and captions

Table A.1: Abundances of elements and REE+Y for samples from the 4F facies in the Musselwhite area

Samples	E599653	E599657	E599658	E599664	E599673
Si (ppm)	437300	418000	423500	450200	367100
Li (ppm)	7.400	4.290	3.390	1.189	0.193
Be (ppm)	0.061	0.061	0.061	0.061	0.061
Sc (ppm)	4.348	3.499	3.542	3.251	3.134
Ti (ppm)	5.710	43.000	185.000	15.200	5.660
V (ppm)	0.325	5.530	11.300	2.770	0.990
Cr (ppm)	4.590	2.770	6.200	2.840	4.050
Mn (ppm)	3.640	59.600	7.400	30.500	11.000
Fe (ppm)	326	1840	3030	1020	700
Co (ppm)	1.620	1.630	4.300	1.730	1.100
Ni (ppm)	43.300	13.700	46.000	15.300	9.100
Cu (ppm)	199.000	55.000	82.000	45.800	21.600
Zn (ppm)	318.000	125.000	59.000	83.800	64.000
Ga (ppm)	0.212	0.763	1.610	1.036	0.159
As (ppm)	2.860	1.205	1.190	1.740	11.000
Rb (ppm)	0.118	3.140	8.100	1.410	0.109
Sr (ppm)	0.344	1.600	1.380	0.730	0.316
Y (ppm)	0.011	0.154	0.097	0.173	0.076
Zr (ppm)	0.570	0.164	0.156	0.142	0.383
Nb (ppm)	0.035	0.084	0.275	0.114	0.046
Mo (ppm)	1.170	0.210	0.330	3.900	0.235
Ag (ppm)	0.359	0.182	1.000	0.187	0.182
Cd (ppm)	2.740	0.993	0.900	1.333	1.321
In (ppm)	0.206	0.084	0.063	0.162	0.130
Sn (ppm)	0.494	0.665	0.990	0.422	0.246
Sb (ppm)	0.941	0.775	0.880	1.260	0.451
Cs (ppm)	0.030	0.118	0.234	0.144	0.073
Ba (ppm)	0.279	2.160	13.600	2.030	0.278
La (ppm)	0.011	0.163	0.151	0.126	0.199
Ce (ppm)	0.058	0.368	0.710	0.360	0.603
Pr (ppm)	0.012	0.041	0.111	0.063	0.088
Nd (ppm)	0.015	0.144	0.710	0.268	0.360
Sm (ppm)	0.018	0.038	0.470	0.150	0.108
Eu (ppm)	0.007	0.020	0.076	0.051	0.024
Gd (ppm)	0.018	0.045	0.350	0.124	0.066
Tb (ppm)	0.004	0.009	0.019	0.015	0.012
Dy (ppm)	0.009	0.032	0.040	0.050	0.026
Ho (ppm)	0.004	0.008	0.004	0.011	0.010
Er (ppm)	0.008	0.020	0.008	0.017	0.008
Tm (ppm)	0.004	0.003	0.003	0.006	0.006
Yb (ppm)	0.011	0.011	0.011	0.011	0.011
Lu (ppm)	0.004	0.003	0.002	0.005	0.006
Hf (ppm)	0.011	0.008	0.008	0.008	0.008
Ta (ppm)	0.008	0.008	0.020	0.014	0.011
W (ppm)	0.540	0.300	0.470	0.374	0.160
Au (ppm)	0.195	0.035	2.700	0.034	0.030
Tl (ppm)	0.335	0.105	0.104	0.135	0.129
Pb (ppm)	10.740	5.720	14.300	6.810	2.850
Th (ppm)	0.007	0.006	0.007	0.014	0.082
U (ppm)	0.025	0.024	0.065	0.093	0.085
Y/Ho	2.545	20.424	22.558	15.175	7.983
Eu/Eu*	1.503	1.942	1.084	1.672	1.068
La/La*	0.024	0.842	0.970	0.631	0.659
Y/Y*	0.115	0.790	1.002	0.753	0.459
Ce/Ce*	0.062	0.878	2.105	0.832	0.922
Gd/Gd*	0.796	0.904	1.818	1.097	0.775
Pr/Sm	0.667	1.073	0.236	0.420	0.815
Nd/Yb	1.310	12.743	62.832	23.717	31.858

A.12 References

- Alexander, B.W., Bau, M., Andersson, P. and Dulski, P. 2008. Continentally-derived solutes in shallow Archean sea water; rare earth element and Nd isotope evidence in iron formation from the 2.9 Ga Pongola Supergroup, South Africa; *Geochimica et Cosmochimica Acta* 72, p. 378-394.
- Alibo D. S. and Nozaki Y. 1999. Rare earth elements in seawater: particle association, shale-normalization, and Ce oxidation; *Geochimica et Cosmochimica Acta* 63, 363-372.
- Allwood, A.C., Kamber, B.S., Walter, M.R., Burch, I.W. and Kanik, I. 2010. Trace element record depositional history of an Early Archean stromatolitic carbonate platform; *Chemical Geology*, v. 270, p. 148-163.
- Armitage, A.E., James, R.S. and Goff, S.P. 1996. Gold mineralization in Archean banded iron formation, Third Portage Lake area, Northwest Territories, Canada; *Exploration and Mining Geology*, v. 5, no. 1, p. 1-15.
- Ashton, K.E. 1985. Archean orthoquartzites from the Churchill Structural Province near Baker Lake, N.W.T.; *Geological Association of Canada, Mineralogical Association of Canada, Program with Abstracts*, v. 10, p. A2.
- Aspler, L.B. and Chiarenzelli, J.R. 1996a. Stratigraphy, sedimentology and physical volcanology of the Henik Group, central Ennadai-Rankin greenstone belt, Northwest Territories, Canada: Late Archean paleogeography of the Hearne Province and tectonic implications; *Precambrian Research*, v. 77, p. 59-89.

Agnico Eagle Mine Ltd., 2012. Meadowbank project exploration compilation and best targets in the mine area. Prepared by Côté-Mantha, O., scale 1:20 000.

Bau, M. and Dulski, P. 1996. Distribution of Y and rare-earth elements in the Penge and Kuruman Iron Formations, Transvaal Supergroup, South Africa; *Precambrian Research*, v. 79, p. 37-55.

Bau, M. and Alexander, B. W. 2009. Distribution of high field strength elements (Y, Zr, REE, Hf, Ta, Th, U) in adjacent magnetite and chert bands and in reference standards FeR-3 and FeR-4 from the Temagami iron-formation, Canada, and the redox level of the Neoproterozoic ocean; *Precambrian Research*, v. 174, p. 337-346.

Bekker, A., Slack, J.F., Planavsky, N., Krapez, B., Hofmann, A., Konhauser, K.O. and Rouxel, J., 2010. Iron formation: the sedimentary product of a complex interplay among mantle, tectonic, oceanic and biospheric processes; *Economic Geology*, v. 105, p. 467-508.

Biczok, J., Hollings, P., Klipfel, P., Heaman, L., Maas, R., Hamilton, M., Kamo, S. and Friedman, R., 2012. Geochronology of the North Caribou greenstone belt, Superior Province Canada: Implications for tectonic history and gold mineralization at the Musselwhite mine; *Precambrian Research*, v. 192-195, p. 209-230.

Bleeker, W., 2006. The Slave Craton: Geological and Metallogenic Evolution. In Goodfellow, W.D. (Ed.), *Mineral Resources of Canada: A Synthesis of Major Deposit-types, District Metallogeny, the Evolution of Geological Provinces, and Exploration Methods*, Geological Survey of Canada.

Bolhar, R., Van Kranendonk, M.J. and Kamber, B.S. 2005. A trace element study of siderite-

- jasper banded iron formation in the 3.45 Ga Warrawoona Group, Pilbara craton-Formation from hydrothermal fluids and shallow seawater; *Precambrian Research*, v. 137, p. 93-114.
- Breaks, F.W., Osmani, I.A. and DeKemp, E.A., 2001. Geology of the North Caribou Lake area, northwestern Ontario; Ontario Geological Survey, Open File Report 6023, 80 p.
- Castonguay, S., Janvier, V., Mercier-Langevin, P., Dubé, B., McNicoll, V., Malo, M., Pehrsson, S. and Bécu, V., 2012. Recognizing optimum banded-iron formation-hosted gold environments in ancient, deformed and metamorphosed terranes: Preliminary results from the Meadowbank deposit, Nunavut: 40th Annual Yellowknife Geoscience Forum, Yellowknife, NWT, November 15-17.
- Danielson, A., Moeller, P. and Dulski, P. 1992. The europium anomalies in banded iron formations and the thermal history of the oceanic crust; *Chemical Geology*, v. 97, p. 89-100.
- Davis, W.J. and Zaleski, E. 1998. Geochronological investigations of the Woodburn Lake group, Western Churchill province, Northwest Territories: Preliminary results; Radiogenic Age and Isotopic Studies: Report 11; in *Current Research 1998-F*, Geological Survey of Canada Research, p. 89-97.
- Davis, D.W. and Stott, G.M., 2001. Geochronology of several greenstone belts in the Sachigo Subprovince, northwestern Ontario. Ontario Geological Survey, OFR6070.018.
- DeKemp, E.A., 1987. Stratigraphy, provenance, and geochronology of Archean supracrustal rocks of western Eyapamikama Lake area, Northwestern Ontario; Unpublished Master's Thesis, Carleton University, Ottawa, Ontario, 98 p.

- Goodwin, A.M., 1973. Archean iron-formations and tectonic basins of the Canadian Shield; *Economic Geology*, v. 68, p. 915-933.
- Goldfarb, R.J., Baker, T., Dubé, B., Groves, D.I., Hart, C.J.R. and Gosselin, P., 2005. Distribution, character and genesis of gold deposits in metamorphic terranes. In: *Economic Geology 100th Anniversary Volume*, J.W. Hedenquist, J.F.H. Thompson, R.J. Goldfarb, and J.P. Richards (eds.), p. 407-450.
- Goldfarb, R.J., Groves, D.I. and Gardoll, S., 2001. Orogenic gold and geologic time: A global synthesis: *Ore Geology Reviews*, v. 18, p. 1–75.
- Gourcerol, B., Thurston, P.C., Kontak, D.J. and Côté-Mantha, O., 2013. Interpretations and implications of preliminary LA ICP-MS analysis of chert for the origin of geochemical signatures in banded iron formations (BIFs) from the Meadowbank gold deposit, Western Churchill Province, Nunavut. In *Current research 2013-20*, Geological Survey of Canada, 22 p.
- Hall, R.S. and Rigg, D.M., 1986. Geology of the West Anticline Zone, Musselwhite Prospect, Opapimiskan Lake, Ontario, Canada, in: Macdonald, A.J. (Ed.), *Gold '86; an international symposium on the geology of gold deposits; proceedings volume; GOLD '86*, Toronto, ON, Canada, p. 124-136.
- Hanor, J.S. and Duchac, K.C. 1990. Isovolumetric silicification of early Archean komatiites; geochemical mass balances and constraints on origin; *Journal of Geology*, v. 98, p. 863-877.
- Henderson, J.R., Henderson, M.N., Pryer, L.L. and Cresswell, R.G. 1991. Geology of the Whitehills-Tehek area, District of Keewatin: An Archean supracrustal belt with iron-formation hosted gold mineralization in the central Churchill province; In *Current Research*,

- 1991-2001C, Geological Survey of Canada, p. 149-156.
- Hoffman, P.F. 1989. Precambrian geology and tectonic history of North America. In *The Geology of North America-An overview*. Edited by A.W. Bally and A.R. Palmer; Geological Society of America, *The Geology of North America, Part A*, p. 447-512.
- Hollings, P. and Kerrich, R., 1999. Trace element systematics of ultramafic and mafic volcanic rocks from the 3 Ga North Caribou greenstone belt, northwestern Superior Province. *Precambrian Research* 93 (1999), p. 257-279.
- Hrabi, R.B., Barclay, W.A., Fleming, D. and Alexander, R.B., 2003. Structural evolution of the Woodburn Lake group in the area of the Meadowbank gold deposit, Nunavut; in *Current Research 2003-C27*, Geological Survey of Canada, 10 p.
- Isaac, C., 2008. Stable isotope (N, O, H) geochemistry, petrology and compositions of biotite of the Musselwhite Mine, Ontario: implications for mineralization. Unpublished Master's Thesis, Lakehead University, 104 p.
- James, H.L., 1954. Sedimentary facies iron-formation; *Economic Geology*, v. 49, p. 235-293.
- Janvier, V., Castonguay, S., Mercier-Langevin, P., Dubé, B., McNicoll, V., Malo, M., Pehrsson, S. and Bécu, V., 2013. Recognizing optimum banded-iron formation hosted gold environments in ancient, deformed and metamorphosed terranes: Preliminary results from the Meadowbank deposit, Nunavut; Geological Survey of Canada, Open File 7409.
- Kamber, B.S., Bolhar, R. and Webb, G.E., 2004. Geochemistry of late Archean stromatolites from Zimbabwe: evidence for microbial life in restricted epicontinental seas; *Precambrian*

Research, v. 132, p. 379-399.

Kamber, B.S. and Webb, G.E., 2007. Transition metal abundances in microbial carbonate: a pilot study based on in-situ LA-ICP-MS analysis; *Geobiology*, v. 5, p. 375-389.

Kamber, B.S., 2010. Archean mafic-ultramafic volcanic landmasses and their effect on ocean-atmosphere chemistry; *Chemical Geology*, v. 274, p. 19-28.

Kolb, M.J., 2010. A microstructural study of Musselwhite Mine and Hammond Reef shear-zone-hosted gold deposits. Unpublished M.Sc. thesis, Lakehead University, Thunder Bay, Ontario, 197 p.

Lawrence, M. G. and Kamber, B. S., 2006. The behavior of the rare earth elements during estuarine mixing- revisited; *Marine Chemistry*, v. 100, p.147-161.

McNicoll, V., Dubé, B., Biczok, J., Castonguay, S., Oswald, W., Mercier-Langevin, P., Skulski, T. and Malo, M., 2013. The Musselwhite gold deposit, North Caribou greenstone belt, Ontario: new high-precision U-Pb ages and their impact on the geological and structural setting of the deposit. Abstract, Geol Assoc of Canada annual meeting, Winnipeg.

Miller, A.R. and Tella, S. 1995. Stratigraphic settings of semi-conformable alteration in the Spi Lake area, Kaminak greenstone belt, Churchill province, Northwest Territories. In *Current Research 1995-C*, Geological Survey of Canada, p. 175-186.

Moran, P., 2008. Lithogeochemistry of the sedimentary stratigraphy and metasomatic alteration in the Musselwhite gold deposit. North Caribou Lake metavolcanic-metasedimentary belt, Superior Province, Canada: implications for deposition and mineralization; Unpublished

Master's Thesis, Lakehead University, 351 p.

Ontario, 1992. Bedrock geology of Ontario: Ontario Geological Survey, Maps 2541, 2542, 2543, 1:1 000 000.

Oswald, W., Dubé, B., Castonguay, S., McNicoll, V., Biczok, J., Mercier-Langevin, P., Malo, M. and Skulski, T., 2014. New insights on the structural and geological setting of the world-class Musselwhite gold deposit, Superior Province, northwestern Ontario; Geological Survey of Canada, Open File 7633.

Otto, A., 2002. Ore forming processes in the BIF-hosted gold deposit Musselwhite Mine, Ontario, Canada. Unpublished Master's Thesis, Freiberg Institute of Mining and Technology, 86 p.

Percival, J.A., 2007. Geology and metallogeny of the Superior Province, Canada. *In* Goodfellow, W.D., ed., Mineral Deposits of Canada: A Synthesis of Major Deposit-Types, District Metallogeny, the Evolution of Geological Provinces, and Exploration Methods: Geological Association of Canada. Special Publication No. 5. Mineral Deposits Division, p. 903-928.

Pehrsson, S., Wilkinson, L., Zaleski, E., Kerswill, J. and Alexander, R.B., 2000. Structural geometry of the Meadowbank deposit area, Woodburn Lake group—implications for a major gold deposit in the western Churchill province; in Geo-Canada 2000—The Millennium Geoscience Summit CD-ROM, Calgary.

Pehrsson, S.J., Wilkinson, L. and Zaleski, E., 2004. Geology of the Meadowbank gold deposit area, Nunavut; Geological Survey of Canada, Open File 4269, scale 1:20 000.

- Pehrsson, S.J., Berman, R.G. and Davis, W.J., 2013. Paleoproterozoic orogenesis during Nuna aggregation: a case study of reworking of the Rae craton, Woodburn Lake, Nunavut; *Precambrian Research* 232 (2013), p. 167-188.
- Phillips, G.N., Groves, D.I. and Martyn, J.E., 1984. An epigenetic origin for Archean banded iron-formation-hosted gold deposits; *Economic Geology and the Bulletin of the Society of Economic Geologists* 79, p. 162-171.
- Planavsky, N., Bekker, A., Rouxel, O.J., Kamber, B.S., Hofmann, A.W., Knudsen, A. and Lyons, T.W., 2010. Rare Earth Element and yttrium compositions of Archean and Paleoproterozoic Fe formations revisited: New perspectives on the significance and mechanisms of deposition; *Geochimica et Cosmochimica Acta* 74.
- Roddick, J.C., Henderson, J.R. and Chapman, H.J., 1992. U-Pb ages from the Archean Whitehills-Tehek Lakes Supracrustal Belt, Churchill Province, District of Keewatin, Northwest Territories; in *Radiogenic Age and Isotopic Studies: Report 6. Geological Survey of Canada, Paper 1992-2*, p. 31-40.
- Schau, M., 1982. Geology of the Prince Albert Group in parts of Walker Lake and Laughland Lake map areas, District of Keewatin; *Geological Survey of Canada, Bulletin* 337, 62 p.
- Sherlock, R.L., Pehrsson, M.S., Logan, A.V., Hrabí, R.B. and Davis, W.J., 2004. Geological Setting of the Meadowbank Gold Deposits, Woodburn Lake Group, Nunavut; *Exploration and Mining Geology*, v. 13, no. 1-4, p. 67-107.
- Sherlock, R.L., Alexander, R.B., March, R. and Barclay, W.A., 2001a. Geologic setting of the Meadowbank iron formation-hosted gold deposits; in *Current Research 2001-C11*,

Geological Survey of Canada, 23 p.

Sherlock, R.L., Alexander, R.B., March, R. and Barclay, W.A., 2001b. Geologic setting of the Meadowbank iron formation-hosted gold deposits; Geological Survey of Canada, Open File 3149, scale 1:10 000.

Stott, G.M., Corfu, F., Breaks, F.W. and Thurston, P.C., 1989. Multiple orogenesis in northwestern Superior Province: Geological Association of Canada, Abstracts 14, p. A56.

Thurston, P., Osmani, I. and Stone, D., 1991. Northwestern Superior Province: review and terrane analysis. In Thurston, P.C., Williams, H.R., Sutcliffe, R.H., Stott, G.M. (eds.), Geology of Ontario, Special Vol. 4, Part 1. Ontario Geological Survey, p. 80-142.

Thurston, P.C., Kamber, B.S. and Whitehouse, M., 2011. Archean cherts in banded iron formation: Insight into Neoproterozoic ocean chemistry and depositional processes; Precambrian Research, v. 214-215, p. 227-257.

Appendix B: Do magnetite layers in Algoma-type BIF preserve their primary geochemical signature: A case study of samples from three Archean BIF-hosted gold deposits?

B.1 Abstract

The geochemistry of chert layers in Algoma-type banded iron formation (BIF) has been used to constrain the depositional setting of the BIFs, as rare earth element (REE) and yttrium (Y) systematics are a function of their chemical environment of formation. In contrast, the chemistry of the interbedded oxide-rich layers (i.e., magnetite) has not been analyzed for this purpose because of the presumed potential effects related to diagenetic changes during conversion from primary iron-bearing mineralogy to magnetite. Here, we explore the validity of this latter hypothesis by examining the results of LA ICP-MS analysis of iron-oxide layers at three Canadian BIF-hosted gold deposit settings (i.e., Meadowbank, Meliadine, Musselwhite) to assess whether the primary REE+Y systematics of the oxide layers are preserved and, if so, what are the implications. The results indicate that, regardless of their diagenetic, later metamorphic and hydrothermal histories, the chemistry of the iron-oxides retains a primary signal in all cases with the following indicated: (1) interaction of the primary Fe-oxyhydroxide phases with seawater, as reflected by heavy REE enrichment relative to light REE depletion that is coupled with variable La and Y enrichment; and (2) some input of moderate-temperature (>250°C) hydrothermal vent fluids, as suggested by positive Eu anomalies. The chemical data are also used to evaluate currently used classification diagrams for ore deposits based on magnetite chemistry. Our new data indicate that the fields for magnetite geochemistry in BIF are too restricted or lead to misclassification of samples. In the case of the latter, it may be that interaction of fluids with the

immediate substrate influences the chemical signature of samples. Therefore, caution is suggested in using these diagrams where hydrothermal fluids are involved in magnetite formation.

B.2 Introduction

Algoma-type BIFs are thinly bedded, chemical sedimentary rocks comprised of alternating layers of iron-bearing minerals and chert. The iron-bearing minerals are considered to have originally precipitated as iron oxyhydroxides due to mixing of acidic to neutral, iron-rich Archean seawater and alkaline moderate-temperature hydrothermal fluids (Shibuya et al., 2010; Gourcerol et al., 2015b) combined with possible photoautotrophic bacterial activity (i.e., Kappler et al., 2005; Konhauser et al., 2005; Gourcerol et al., 2015b). These primary iron-bearing minerals are transformed during diagenesis and/or by later metamorphic recrystallization to hematite, magnetite, various iron-silicates and carbonates, and pyrite (e.g., Posth et al., 2013). The interbedded chert layers have been shown to reflect a primary geochemical signature that suggests precipitation upon interaction of seawater and moderate-temperature hydrothermal fluids with variable amounts of detrital contamination (e.g., Gourcerol et al., 2015a, b, c). An essential question in this regard, therefore, is whether the iron-bearing minerals, despite having experienced multiple recrystallization events (e.g., Pickard et al., 2003), retain a geochemical signature indicative of their primary environment, this being a combination of marine seawater and hydrothermal vent fluids.

The compositional variability of oxide minerals (e.g., magnetite, hematite), which collectively form in a wide variety of ore forming environments (e.g., hydrothermal vs. magmatic), has been the focus of many studies in recent years, in part due to the advances of

analytical instrumentation such as the laser ablation-inductively coupled plasma-mass spectrometry (LA-ICP-MS) (e.g., Grigsby, 1990; Dare et al., 2012, 2014; Nadoll et al., 2014). Of particular significance is that several studies have demonstrated that the geochemical signature of the oxides, in particular magnetite, can be a genetic indicator of ore deposit environments, in part due to the ability of the analytical method to provide the resolution necessary to distinguish various geochemical types (Dupuis and Beaudoin, 2011; Dare et al., 2014). As a result of these recent advances, it is now possible to distinguish geochemically between hydrothermal and magmatic magnetite. For example, whereas hydrothermal magnetite compositions may vary depending on various factors such as fluid composition, host rock buffering, and re-equilibration processes (Nadoll et al., 2014), they are generally characterized by depletion in Ti and an elevated Ni/Cr ratio compared to their magmatic equivalent and are enriched in elements which do not nominally enter the lattice of magmatic magnetite (e.g., Si and Ca). Magmatic magnetite is enriched in Ti with a lower Ni/Cr ratio (Dare et al., 2014). However, despite geochemical characteristics which have not been well documented, magnetite may also be precipitated by hydrogeneous processes during formation of BIF, as discussed above (e.g., Kappler et al., 2005; Konhauser et al., 2005; Shibuya et al., 2010; Gourcerol et al., 2015b) and may show depletion in compatible elements (Cr, Ni, V, Co, Zn, Ti) which are characteristic of magnetite formed from low temperature environments (Dare et al., 2014).

Only a few studies have explored the REE geochemistry of iron oxides in Algoma-type BIF (e.g., Pecoits et al., 2009; Angerer et al., 2012; Li et al., 2014), but in such cases, analyses of the accompanying chert bands are lacking. These analyses would provide an internal check on geochemical concordance, that is, each providing the same chemical signature of their environment of formation. Thus, the occurrence of geochemical parallelism and hence genetic

processes between the chemistry of magnetite and chert (i.e., LREE depletion relative to HREE, variable positive La/La* and Y/Y* anomalies, positive Eu/Eu* anomalies) has yet to be documented. The purpose of this paper is to present the first such data and validate this hypothesis.

In this contribution, we explore the geochemistry of iron-oxide layers at three Archean BIF-hosted gold deposits located in Canada: the ~4 Moz Au Meadowbank deposit, hosted by the 2.71 Ga Woodburn Lake greenstone belt; the ≥ 2.8 Moz Au Meliadine gold district, hosted by the 2.6 Ga Rankin Inlet greenstone belt; and the ~6 Moz Au Musselwhite deposit, hosted by the 2.9-3 Ga North Caribou greenstone belt. Importantly, in each of these studied areas we have previously characterized the chemistry of the interbedded chert (Fig. B.1; Gourcerol et al., 2015a, b, c). Also relevant is that the BIFs at each of these deposits are either intercalated with mafic to ultramafic volcanic rocks or associated interflow sedimentary rocks, which may represent different potential sources for the iron-rich minerals composing the Fe-oxide layers.

The main objective of this study is, therefore, to assess the potential of using the REE+Y systematics of magnetite bands to identify their primary geochemical signature, as we have done for the associated cherts (Gourcerol et al., 2015b). If this study is successful, it provides the possibility of using the geochemistry of magnetite from magnetite-rich bands to constrain the genesis of BIF units. In addition, we also use these data to assess the validity of the currently defined field for magnetite from BIF settings in chemical classification diagrams using magnetite.

B.3 Geological setting of the selected BIFs

B.3.1 The Meadowbank gold deposit

The Meadowbank deposit which is mined since 2010, contains a total of about 4 Moz of gold including 1.3 Moz produced from 2010 to 2013 (Janvier et al., 2015). Located in the Rae Domain of the Churchill Province, the deposit is hosted by the Woodburn Lake greenstone belt (ca. 2.71 Ga) which consists of tholeiitic and komatiitic metavolcanic rocks with minor calc-alkaline felsic tuffs and flows with intercalated BIF and clastic metasedimentary rocks (Armitage et al., 1996; Sherlock et al., 2001a, b, 2004; Hrabí et al., 2003; Pehrsson et al., 2004). The regional metamorphic grade ranges from middle greenschist to amphibolite facies (Pehrsson et al., 2004) and the sequence was deformed at least by six regional-scale Archean and Paleoproterozoic deformation events (e.g., Pehrsson et al., 2013).

Numerous units of oxide-, silicate- and locally sulfide-facies Algoma-type BIF have been identified which include the West IF, Central BIF and East BIF; all of the BIFs are generally interlayered with the volcanic rocks and locally with a quartzite unit (Gourcerol et al., 2015c; Sherlock et al., 2001a, b, 2004).

B.3.2 The Meliadine gold district

The Meliadine gold district which is one of the Canada's largest BIF-hosted gold districts, contains 2.8 Moz Au in reserves as well as an indicated and inferred resource of 5.8 Moz Au (Lawley et al., 2015). The gold district is hosted by the 2.6 to 2.7 Ga Rankin Inlet greenstone belt (Wright, 1967; Aspler and Chiarenzelli, 1996a) which lies along the boundary between the Central and the North Western Hearne domains of the Churchill Province (Tella et al., 2007;

Davis et al., 2008). The Rankin Inlet greenstone belt consists of poly-deformed massive and pillowed mafic volcanic rocks, felsic pyroclastic rocks and associated interflow sedimentary units, gabbro sills and oxide-facies BIFs; all of these units are intruded by minor granite and undeformed biotite lamprophyre, as well as late gabbro and diabase dykes of Archean and Proterozoic age. These rocks have been metamorphosed from lower greenschist to lower-middle amphibolite facies (Carpenter, 2004; Carpenter, et al., 2005).

B.3.3 The Musselwhite gold deposit

The Musselwhite deposit which has been mined since 1997 contains a total of about 6 Moz of gold including 4 Moz produced and 1.85 Au reserves (Oswald et al., 2015). Located in the North Caribou terrane of the Superior Province, the deposit is hosted by the North Caribou greenstone belt dominated by mafic to ultramafic metavolcanic rocks of the 2973 to <2967 Ma Opapimiskan-Markop metavolcanic assemblage and tholeiitic basalts and minor felsic volcanics of the 2980 to 2982 Ma South Rim metavolcanic assemblage (Biczok et al., 2012; McNicoll et al., 2013). These rocks have been metamorphosed from lower greenschist to lower-mid amphibolite facies (Breaks et al., 2001) and deformed by three deformation events (Hall and Rigg, 1986; Breaks et al., 2001). The Opapimiskan-Markop metavolcanic assemblage consists, from the structural base to the top, of the “Lower Basalt” unit, the Southern Iron Formation, “Basement Basalt” unit and the Northern Iron Formation (e.g., Moran, 2008; Biczok et al., 2012). The nature of the BIFs is described in more detail in Gourcerol et al. (2015a).

B.4 Sample description, analytical methods and data treatment

The samples collected for the study include: (1) seven samples from the Meadowbank deposit (Fig. B.1A, B); (2) eight samples from the Meliadine gold district; and (3) three samples

from the Musselwhite deposit. These samples represent bands of Fe-oxides (Fig. B.2A, B, C, D) that are mainly composed of anhedral and amalgamated (i.e., polycrystalline texture of anhedral and annealed crystals) magnetite with rare cryptocrystalline hematite that is locally overprinted by late euhedral magnetite grains. The iron-rich bands form millimetric- to centimetric-layers that are interbedded with chert layers. The Fe-oxide layers are dominated by magnetite, but they may also contain variable proportions of mineral inclusions such as quartz, hematite, pyrite, pyrrhotite, apatite +/-chlorite and variable silicates (Fig. B.2A, B, C, D). It is also noted that no specific attention was paid to recognition of and deciphering the different events responsible for formation of the Fe-oxide layers, that is, primary versus later recrystallization stages, as only the continuous Fe-oxides layers (i.e., anhedral and amalgamated magnetite phase) were selected for analysis.

Each of the Fe-oxide layers analyzed in this study is located immediately adjacent to the chert layers analyzed in our earlier study (Gourcerol et al., 2015b; Fig. B.1C, D). Polished thin sections (100 μm thick) were examined, using both transmitted and reflected light microscopy, and selected material was studied in more detail using a JEOL JSM-6400 scanning electron microscope coupled to an energy dispersive spectrometer (EDS). Based on previous petrographic work, areas for analysis were selected to minimize the presence of phases other than magnetite, including alteration, and mineral inclusions. Operating conditions were accelerating voltage of 20 keV, 1.005 nA beam current, acquisition count times of 10 seconds, and a working distance of 15 mm. The SEM-EDS was used to select the most suitable magnetite layers having minimal amounts of paragenetically later stage minerals related to metamorphic, hydrothermal or ore-forming processes, such as garnets, variable amphiboles, and sulfides.

Using the same protocol applied to the chert layers analyzed in Gourcerol et al. (2015a, b, c),

the magnetite layers were analyzed by line traverses rather than spots (Fig. B.2E, F) using a Resonetics RESolution M-50 193 nm ArF excimer laser ablation system coupled to a Thermo X Series II quadrupole ICP-MS in a two-volume Laurin Technic sample cell. The instrument operated with a forward power of 1450 W. Gas flows were 800 ml/min for argon, 650 ml/min for He and 6 ml/min for N. Dwell times for elements analysed were 10 ms. These conditions should minimize interferences such as ^{69}Ga with $^{29}\text{Si}^{40}\text{Ar}$. Stage movement speed was 20 $\mu\text{m/s}$. As chert and magnetite layers show very low concentrations of REE, spot analyses may yield data below the detection limit for many elements, therefore, line traverses on polycrystalline aggregates were made using both 140 and 190 μm beam diameters with a repetition rate of 10 Hz and an energy density of 7 J/cm^2 to optimize the time-signal acquisition, representing therefore an average for each element along the analyzed traverse. However, since the line traverse method increases the possibility of detrital contaminants, present as inclusions or minerals disseminated along the traverse line, the Queensland alluvial shale composite (MUQ) was used to normalize the REE+Y values to minimize the influence of any potential terrigenous input whereas trace elements were normalized to bulk continental crust (values from Rudnick and Gao, 2003). The MUQ composition represents a mixed bimodal felsic and mafic volcanic provenance (Kamber et al., 2005), which acts as a proxy for the expected average terrigenous input from a typical bimodal greenstone belt into the Archean ocean (e.g., Bolhar et al., 2005; Thurston et al., 2012).

The final concentrations of elements were determined using off-line calculations following the protocol of Longerich et al. (1996). Data were processed with Iolite (Paton et al., 2011) and the NIST 612 glass standard was used as a primary external reference material (e.g., Nadoll et al., 2014) and iron concentrations were used as an internal standard for calibration of the LA ICP-MS data.

The elemental concentrations reported in this study represent the integrated signal over the length of the traverse. The element list used for each analysis included (^{139}La , ^{140}Ce , ^{141}Pr , ^{146}Nd , ^{147}Sm , ^{153}Eu , ^{157}Gd , ^{159}Tb , ^{163}Dy , ^{165}Ho , ^{166}Er , ^{169}Tm , ^{172}Yb and ^{175}Lu), in addition to ^7Li , ^9Be , ^{29}Si , ^{45}Sc , ^{47}Ti , ^{51}V , ^{52}Cr , ^{55}Mn , ^{56}Fe , ^{59}Co , ^{60}Ni , ^{65}Cu , ^{66}Zn , ^{69}Ga , ^{75}As , ^{85}Rb , ^{88}Sr , ^{89}Y , ^{90}Zr , ^{93}Nb , ^{95}Mo , ^{107}Ag , ^{111}Cd , ^{115}In , ^{118}Sn , ^{121}Sb , ^{133}Cs , ^{137}Ba , ^{178}Hf , ^{181}Ta , ^{182}W , ^{197}Au , ^{205}Tl , ^{208}Pb , ^{232}Th and ^{238}U . In this study, the detection limits achieved were significantly lower than the concentration of REEs in magnetite samples (Tables B.1, B.2, B.3). The La, Ce, Eu and Y anomalies are calculated (Equations (1) to (4)) following the procedure of Lawrence and Kamber (2006):

$$(\text{La/La})^*_{\text{MUQ}} = \text{La}_{\text{MUQ}} / (\text{Pr}_{\text{MUQ}} * (\text{Pr}_{\text{MUQ}}/\text{Nd}_{\text{MUQ}})^2) \quad (1)$$

$$(\text{Ce/Ce})^*_{\text{MUQ}} = \text{Ce}_{\text{MUQ}} / (\text{Pr}_{\text{MUQ}} * (\text{Pr}_{\text{MUQ}}/\text{Nd}_{\text{MUQ}})) \quad (2)$$

$$(\text{Eu/Eu})^*_{\text{MUQ}} = \text{Eu}_{\text{MUQ}} / (\text{Sm}_{\text{MUQ}}^2 * \text{Tb}_{\text{MUQ}})^{1/3} \quad (3)$$

$$(\text{Y/Y})^*_{\text{MUQ}} = \text{Y}_{\text{MUQ}} / (0.5\text{Er}_{\text{MUQ}} * 0.5\text{Ho}_{\text{MUQ}}) \quad (4)$$

The Gd values in Archean iron formation are considered to reflect a combination of a small positive Gd anomaly associated with seawater (Bau and Dulski, 1996) and slightly negative Gd anomaly associated with hydrothermal vent fluid (e.g., Allwood et al., 2010). Thus, as Archean seawater was influenced by hydrothermal vent fluids, the Gd anomalies are variable in magnitude and sign (+ vs. -) suggesting precipitation under influence of seawater and hydrothermal input. We note that the Gd anomalies reported and discussed in previous articles on REE+Y systematics from BIF precipitated in Archean seawater (e.g., Bolhar et al., 2005; Thurston et al., 2012) were small to nonexistent, thus Gd anomalies are not discussed here.

B.5 REE+Y Systematics

Despite some minor exceptions, the REE+Y normalized data presented in the tables (Tables B.1, B.2, B.3) and diagrams (Fig. B.3) show relatively uniform REE+Y patterns for the magnetite layers sampled from the three different gold deposits (i.e., Meadowbank, Meliadine and Musselwhite) and these data are discussed separately below. Comparisons to other studies of magnetite geochemistry are discussed in subsequent sections.

In the Meadowbank area (Fig. B.3A), the magnetite bands show depletion in light REE (LREE) relative to middle and heavy REE (HREE) with $\text{Nd/Yb}_{\text{MUQ}} = 0.1\text{-}0.4$ associated with slight to moderate positive La, Y and Eu anomalies ($\text{La/La}^*_{\text{MUQ}} = 1.4\text{-}2.7$; $\text{Y/Y}^*_{\text{MUQ}} = 1.01\text{-}1.6$; $\text{Eu/Eu}^*_{\text{MUQ}} = 1.7\text{-}3.7$) and super-chondritic Y/Ho values ($\text{Y/Ho} = 30.9\text{-}43.9$). In addition, slight positive Ce anomalies are notable ($\text{Ce/Ce}^*_{\text{MUQ}} = 1.09\text{-}1.38$).

In the Meliadine gold district (Fig. B.3B), most of the magnetite layers also show depletion in the LREE relative to middle and HREE ($\text{Nd/Yb}_{\text{MUQ}} = 0.08\text{-}0.6$) with associated slight to moderate positive La, Y and Eu anomalies ($\text{La/La}^*_{\text{MUQ}} = 0.7\text{-}1.8$; $\text{Y/Y}^*_{\text{MUQ}} = 0.9\text{-}1.3$; $\text{Eu/Eu}^*_{\text{MUQ}} = 0.9\text{-}1.9$) and super-chondritic to chondritic Y/Ho values ($\text{Y/Ho} = 24.7\text{-}34.9$). In detail, samples MEL-032 and MEL-033 yield slightly anomalous HREE-depleted concentrations ($\text{Nd/Yb}_{\text{MUQ}} = 1.4\text{-}1.9$) which are also associated with moderate positive La, Y and Eu anomalies. Minor to moderate positive Ce anomalies are also recognized in these samples ($\text{Ce/Ce}^*_{\text{MUQ}} = 0.9\text{-}1.2$).

In the Musselwhite area (Fig. B.3C), magnetite layers show depletion in LREE relative to middle and HREE ($\text{Nd/Yb}_{\text{MUQ}} = 0.3\text{-}0.5$) with associated slight to moderate positive La, Y and Eu anomalies ($\text{La/La}^*_{\text{MUQ}} = 1.14\text{-}2.45$; $\text{Y/Y}^*_{\text{MUQ}} = 1.2\text{-}1.6$; $\text{Eu/Eu}^*_{\text{MUQ}} = 2.1\text{-}2.8$), super-

chondritic Y/Ho values ($Y/Ho = 35.8-41.3$) and slightly to moderate positive Ce anomalies ($Ce/Ce^*_{MUQ} = 1.1-1.3$).

B.6 Additional major and trace element data

Magnetite layer samples from the three deposits show relatively similar abundances of major and trace elements, as indicated in Figure B.4, which attests to their similar overall geochemistry. As expected, high concentrations of Fe, Ti, V, Cr, Mn, Ni and Zn occur in the magnetite, whereas the relatively high Si concentrations, as noted in the three deposits, are attributed to the presence of quartz and/or other silicate grains present along the line traverses. The moderate concentrations of Ba and Sr detected may reflect presence of feldspar, likely of metamorphic origin.

In previous geochemical studies of magnetite, data have been normalized to bulk continental crust (values from Rudnick and Gao, 2003) in order to emphasize the partitioning behavior of the trace elements between magnetite, the magma, hydrothermal fluid, and co-crystallizing phases (Dare et al., 2014). Therefore, in order to assess and compare the trace element data from this study to that of other magnetite studies, the data for our samples have also been normalized to bulk continental crust in multi-element variation diagrams in which elements are plotted in order of increasing compatibility with respect to magnetite (Dare et al., 2014). Most of the major and trace-elements show consistent patterns (Fig. B.5A, B, C) with concentration less than one times bulk continental crust. In detail, however, the magnetite samples from the Meadowbank, Meliadine and Musselwhite deposits show slight to moderate relative depletions in Ti, Co, V, Ni and Cr compared to magnetite of high-temperature origin (Dare et al., 2014). This latter feature is in general similar to the data for both whole rock (Pecoits et al., 2009; Angerer et al., 2012)

and *in-situ* (Dare et al., 2014; Dupuis et al., 2014; Nadoll et al., 2014) analyses of magnetites from BIFs in the literature (Fig. B.5A, B, C). It must be noted that the composition of iron formations associated with gold mineralization do not differ substantially from non-mineralized iron formations (e.g., Gourcerol et al., 2015c; Thurston et al., 2012). Compared to the relatively high-temperature (i.e., >500°C) hydrothermal magnetite samples from Dare et al. (2014), the magnetites in this study formed in part from lower temperature fluids, including a component of hydrothermal vent fluids (<250°C). Thus, based on the latter, it is not surprising that the BIF magnetites are seen to be notably depleted in these compatible elements (Fig. B.5) which is probably a reflection of their lower solubility in these fluids (e.g., Ray and Webster, 2007; Nadoll et al., 2012, 2014; Dare et al., 2014). Hence, it appears that magnetite from BIF is characterized by lower overall abundances of the compatible trace elements relative to high-temperature hydrothermal magnetite (e.g. Angerer et al., 2012; Nadoll et al., 2014; Dare et al., 2014; Chen et al., 2015). In contrast to these elements, similar or higher normalized values are noted for Pb, Zr, Hf, Mn, Mo, Nb and/or Cu, which might be attributable to the high solubility of Pb and contamination from ubiquitous micro- to nanometer scale inclusions (Duparc, 2014) such as zircon, various sulfide and Nb-bearing oxide grains in magnetite layers.

B.7 Discussion

It is now widely accepted that abundance of REE+Y and the MUQ-normalized patterns of chert bands from Algoma-type BIFs may reflect primary geochemical signatures inherited through precipitation from a mixed reservoir of seawater and moderate-temperature hydrothermal vent fluids with variable amounts of detrital contamination (e.g., Bau and Dulski, 1996; Thurston et al., 2012; Gourcerol et al., 2015a, b, c). Below, we assess the validity of this chemical pattern that is also present in the magnetite layers interbedded with the cherts using the

data from the three Archean Algoma-type BIFs examined in this study. In addition, these data are then used to assess the validity of the currently defined fields for magnetite from BIF in magnetite classification diagrams (e.g., Dupuis and Baudoin, 2011; Dare et al., 2014).

B.7.1 Assessing the primary geochemical signature for magnetite layers

Comparison of the REE+Y distribution patterns of metalliferous sediments (on a carbonate-free basis) composed mainly of poorly crystalline to amorphous Fe-Mn oxyhydroxides and variable amorphous silicate phases from the Pacific (Fig. B.6; Barrett and Jarvis, 1987; Dekov et al., 2010) and the magnetite layers in this study highlights that, other than the differences in the Ce anomalies between modern metalliferous sediments versus Archean BIFs, which is due to oxidation of Ce^{+3} to Ce^{+4} in the oxic water column, the REE+Y distribution patterns of these two sample suites are very similar. In addition, both modern metalliferous sediments and ancient magnetite layers in BIFs show depletion in LREE relative to middle and HREE with associated slight to moderate positive La, Y and Eu anomalies. It is widely accepted that the depletion in LREE relative to HREE with associated variable positive La and Y anomalies represents fractionation of the REE and Y in an ambient seawater column due to the preferential removal of these elements onto Fe-oxyhydroxides, organic matter, and clay particles (e.g., Bau and Dulski, 1996; Thurston et al., 2012; Gourcerol et al., 2015a, b, c). Furthermore, a positive Eu anomaly is a common feature in rocks considered to have precipitated from Archean seawater modified by moderate-temperature (i.e. $>250^{\circ}\text{C}$) hydrothermal or vent sourced fluids (e.g., Bau and Dulski, 1996; Kamber et al., 2004). We note that these aforementioned features are present even though the magnetite layers record some contamination, as indicated by high Si concentrations (Fig. B.4) (due to primary chert and/or detrital quartz or silicates) which have partly diluted the primary geochemical signature. However, as Si concentration is around 10% of Fe concentration,

it is unlikely that the primary signature in oxide layers may be completely dissolved.

We conclude based on the data presented that the analyzed magnetites record a primary geochemical signature that reflects the influence of ambient seawater and a variable input of moderate-temperature ($>250^{\circ}\text{C}$) hydrothermal vent fluids (Figs. B.1, B.2) during Fe-oxyhydroxide deposition despite the overprinting effects of later diagenetic processes and/or later metamorphic and/or hydrothermal events pointed out by petrographic observations (e.g., various magnetite events). Additionally, the chondritic Y/Ho ratios associated with high REE content may be indicative of variable detrital contamination with the positive Ce anomalies observed in most of the samples reflecting precipitation of primary Fe-oxyhydroxide at pH values <5 , as suggested in Gourcerol et al. (2015b). The chondritic Y/Ho ratios would also indicate that the hydrothermal fluids did not contain significant F and Cl which would serve to fractionate Y and Ho (Loges et al., 2013).

Magnetites from all three deposits have similar REE+Y characteristics, which indicate that the gold mineralizing process has not altered the primary geochemistry of the magnetite layers in the iron formations. Given that the REE+Y signatures of the magnetite layers is similar to the REE+Y signatures of the chert bands as well, we can state that the primary geochemical signature of the iron formation as a whole is preserved in spite of subsequent diagenetic and metamorphic/hydrothermal processes based on this study. Establishing any further effects of low temperature diagenesis will require *in-situ* O isotopic research.

B.7.2 Assessing and comparing the primary geochemical signatures between chert and magnetite layers

Based on the above discussion of the magnetite layers and our previous work on the adjacent

chert bands (Gourcerol et al., 2015a, b), a reasonable case is made here that these two data sets record the primary geochemical signal of the ocean water column at the time of their initial formation as Fe- and Si-rich chemical precipitates, respectively. In order to compare and contrast the signals present in these layers, the data are compared in Figure B.7 where a binary mixing line was calculated using seawater and hydrothermal vent fluids as end members. This latter diagram allows us to: (1) explore the relative influence of these end-member components during precipitation of the primary Fe-oxyhydroxide material; and (2) evaluate the variation between chert and magnetite regarding their primary geochemical signatures. The two end-members of this mixing line represented in Figure B.7 are: (1) modern seawater composition from the North Pacific (Alibo and Nozaki, 1999); and (2) an Archean hydrothermally-precipitated chert from the Abitibi greenstone belt (i.e., 06PCT001M; Thurston et al., 2012). The selection of the latter chert sample is explained in detail by Gourcerol et al. (2015b).

Most of the samples in this study fall on the mixing line despite the fact that some of the samples analyzed exhibit high Sm/Yb ratios (Fig. B.7). The Sm/Yb ratio is particularly sensitive to the presence of high-pressure metamorphic phases that may be present in the samples as contaminants, such as amphibole and garnet, which may overprint the primary geochemical signature of the BIFs. It is noticed that the Sm/Yb ratios are, relatively speaking, a bit higher for magnetite samples (Fig. B.7A) than for adjacent chert samples (Fig. B.7B). The variable input of the moderate-temperature hydrothermal vent fluid displayed in Figure B.7A suggests a contribution of less than 10%, which is very similar to the corresponding chert layers which record a hydrothermal fluid contribution of between 0 and 15%, excluding one sample that records 46% (Fig. B.7B). These observations confirm the influence of moderate-temperature hydrothermal fluids during Fe-oxyhydroxide precipitation, but also that magnetite can be used as

well as chert bands to assess the origin of BIFs.

B.7.3 Assessment of discriminant diagrams for magnetite layers

The advent of modern analytical methods, such as LA ICP-MS, has provided a means to assess the use of discriminant diagrams based on chemistry of magnetite to define fields for different ore deposit types due to its occurrence in a wide variety of environments (Dupuis and Beaudoin, 2011). This classification scheme also includes chemical space for samples from BIF, but the defined area is controversial, as magnetite layers from Algoma-type BIF do not correspond to the simple binary magmatic or hydrothermal sources, but rather reflects interaction of hydrothermal vent fluids with seawater (i.e., hydrogeneous origin). According to Nadoll et al. (2014), the composition of magnetite from BIFs is mainly controlled by the chemistry of the ocean water column and its related reservoirs (i.e., seawater versus vent fluid), and/or temperature and fO_2 . In addition, the substrate may also be important in terms of determining some elemental components of the magnetite chemical signature via leaching of the underlying rock by the vent fluids which may be reflected by the relative enrichment in Sc, Mn, Ti, Zn and Cr (Pecoits et al., 2009; Dare et al., 2014). In regards to the relative enrichment in Ti for magnetite samples, this may relate to the influence of higher fluid temperatures (e.g., Thorne et al., 2008; Nadoll et al., 2014).

Using the data from this study, it may be possible to evaluate the proposed classification diagrams with regard to BIFs, as shown with the relevant diagrams in Figure B.8. In the Ti vs. Ni/Cr diagram of Dare et al. (2014), 60% of our samples plot in the magmatic field with the remainder falling in the hydrothermal field (Fig. B.8A). We propose that the distribution of the data in this plot may illustrate a combination of a moderate-temperature hydrothermal influence

(>250°C) and variable leaching of magnetite-bearing mafic/ultramafic rocks by hydrothermal fluids, as most of the samples in this study are located close to the boundary line of the two magmatic and hydrothermal fields. This hypothesis is also supported by the fact that Ni and Cr are decoupled probably due to higher solubility of Ni compared to Cr in hydrothermal fluids (Dare et al., 2014). Moreover, as magnetite layers may reflect the earlier precipitation of Fe-oxyhydroxides, trace elements which show a good to moderate correlation with Fe may reflect water-column geochemistry of the environment in which they were precipitated (either from hydrothermal fluids or weathering of basement or detrital contamination) and in which they were scavenged by adsorption onto Fe-oxyhydroxide surface. However, we conclude that this diagram should be used with caution regarding to provenance or source discrimination for a given magnetite.

As for the Ni/(Cr + Mn) versus Ti + V diagram of Dupuis and Beaudoin (2011), the samples do not plot in the expected BIF field, as defined by several previous studies (e.g. Duparc et al., 2015; Nadoll et al., 2014; Chen et al., 2015; Fig. B.8B), and instead depart markedly in regard to both of the chemical parameters used. These findings are consistent with the more recent studies which also indicate that these classifications scheme are not always reliable in classifying correctly magnetite from low- to moderate-temperature hydrothermal deposits or BIF (Hu et al., 2014; Chen et al., 2015; Zhao and Zhou, 2015) and, therefore, indicates that such plots need to be used with caution with regards to Algoma-type BIF. We suggest an extended BIF field based on our samples illustrating by dashed lines on Fig. B.8.

B.8 Conclusions

This LA ICP-MS study of the trace element chemistry of magnetite from BIF-hosted gold

deposit settings, in particular the REE+Y systematics, suggests that, despite the potential influence of diagenetic processes and/or later stage metamorphism, interaction with hydrothermal fluids and mineralizing events on the original Fe oxide material, the magnetite layers apparently retain their primary geochemical signature (e.g., seawater and moderate-temperature hydrothermal vent fluids). That this latter hypothesis is validated by the fact that the same conclusions were previously determined based on a similar LA ICP-MS trace element study of adjacent chert layers from the same material. Furthermore, these data, in conjunction with appropriate binary mixing diagrams, provide a means to evaluate the proportional contributions of the two end member fluids involved in formation of BIF material, both the chert and magnetite layers. The additional chemical data obtained in this study have been used to examine the current use of discriminant diagrams for distinguishing magmatic versus hydrothermal magnetite and also to which ore deposit type the magnetite chemistry shows the closest affinity. Based on the data for these samples, we would caution using such diagrams for at least BIF samples, although we note that some of the problems encountered may also be relevant to other hydrothermal type settings.

B.9 Acknowledgements

The authors gratefully acknowledge the staff of Agnico Eagle Mines Ltd. and Goldcorp Ltd. and more particularly the Meadowbank, Meliadine and Musselwhite regional exploration crews. The study is supported by both TGI-4 funding from Natural Resources Canada and funding through a Natural Sciences and Engineering Research Council Collaborative Research and Development agreement with participation by Agnico Eagle Mines Ltd and Goldcorp. We thank also Drs. C. J. Duran and L.A. Groat for their constrictive comments that helped to substantially improve the manuscript.

B.10 Figures and captions

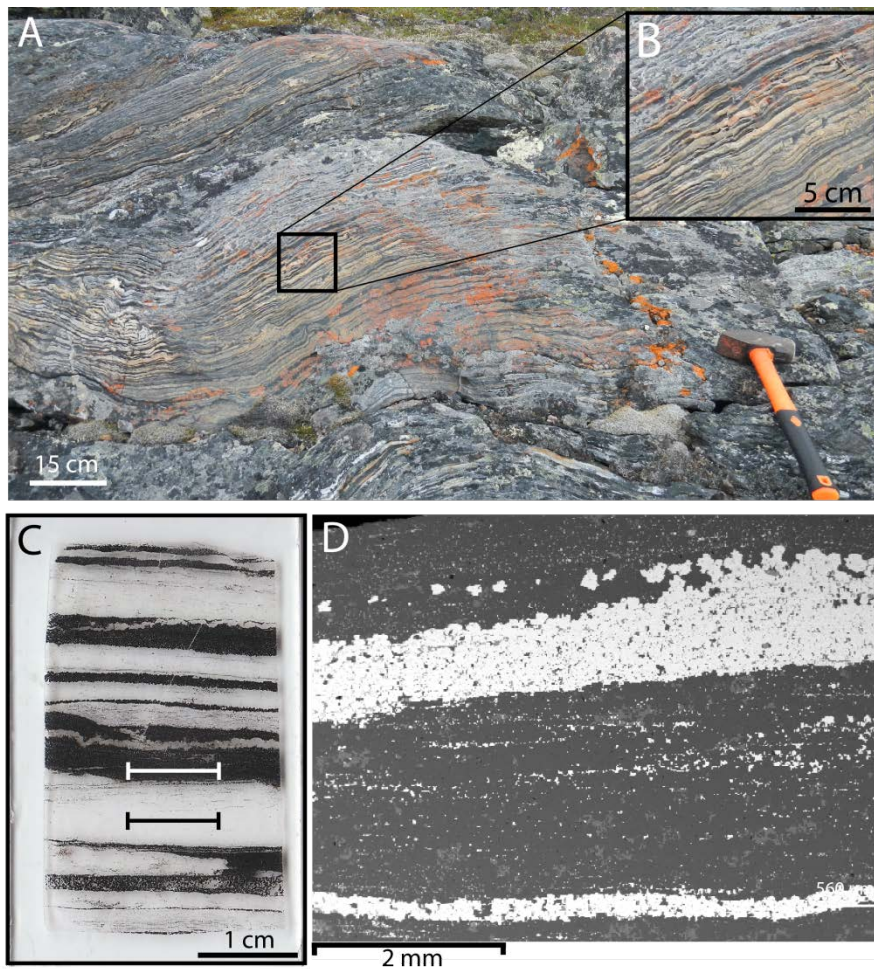


Figure B.1: Photographs at different scales that illustrate the nature of the BIFs in the field, their microscopic features and traces of the laser ablation traverses.

(A) Outcrop photograph of BIF at the Meadowbank gold deposit area showing the characteristic layers of chert and iron-rich layers, in this case

magnetite; (B) Close up of the outcrop showing alternating layers of chert and magnetite; (C) Scanned thin section of BIF from outcrop in image which shows the chert and magnetite layers. The black solid line represents the laser ablation traverse done on the chert as part of our previous LA ICP-MS study (Gourcerol et al., 2015a, b, c) whereas the white solid line represents the line traverse done on the magnetite rich layer in this study; and (D) SEM back-scattered electron image of the BIF layering showing alternating layers of chert and magnetite.

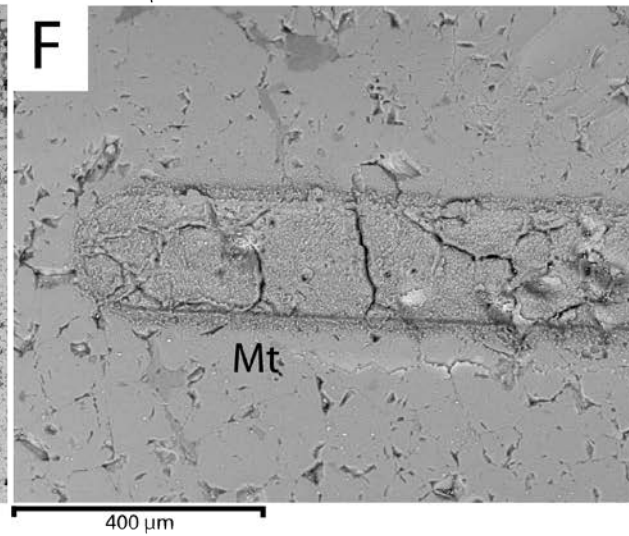
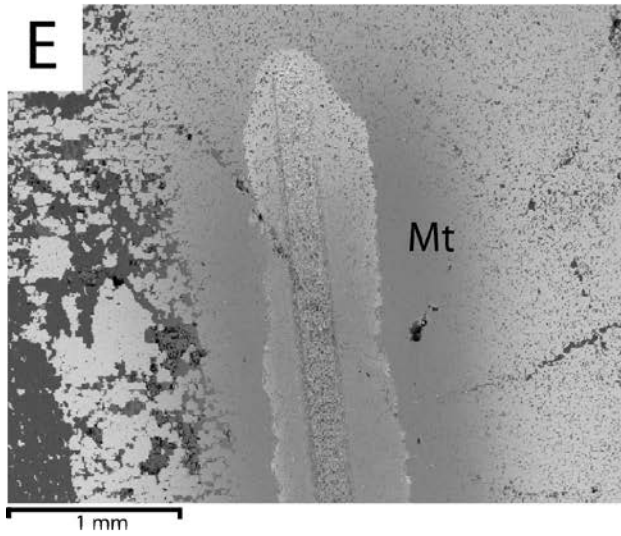
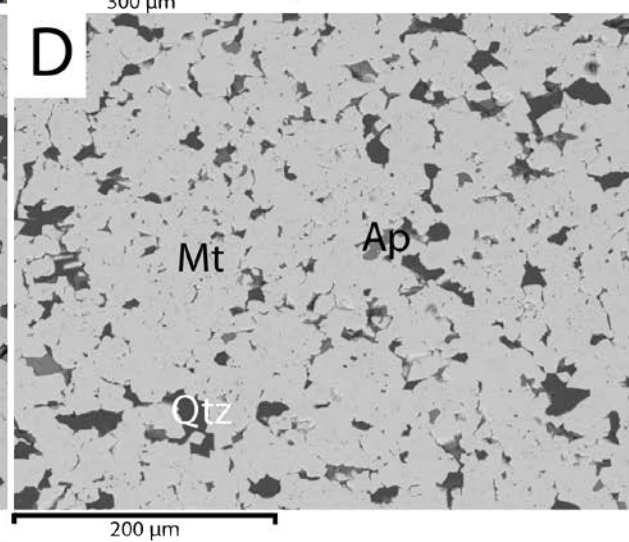
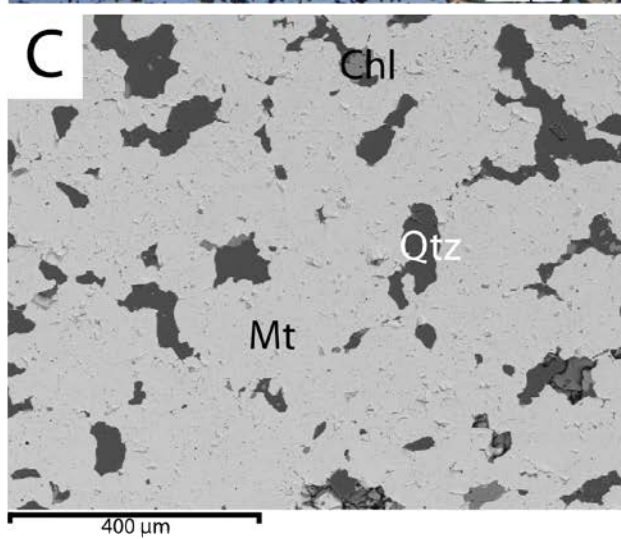
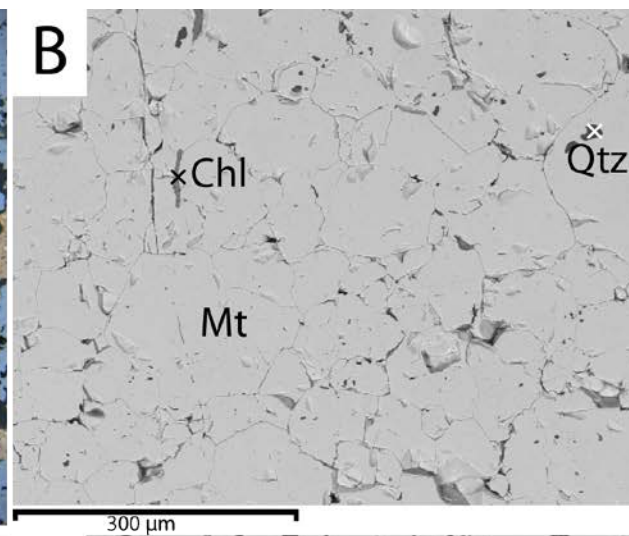
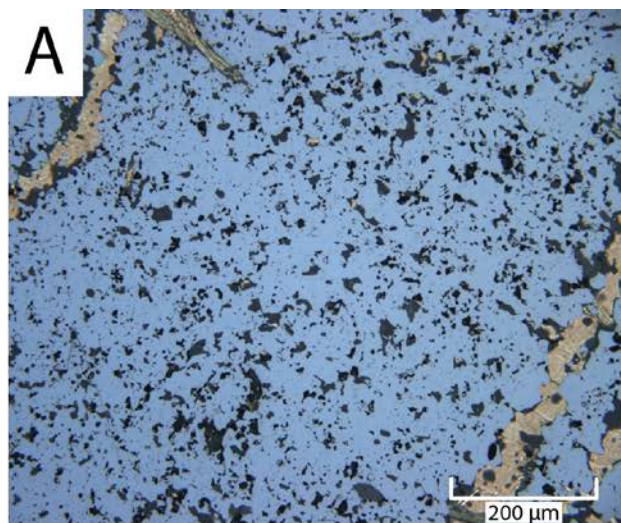


Figure B.2: Images showing typical Fe-oxide layers sampled for this study: (A) Reflected light image of a polished thin section of sample AMB-126225 showing its groundmass which consists of magnetite with minor quartz (yellowish color) and minor recrystallized magnetite +/-hematite (darker grey) inclusions; (B) Back-scattered electron (BSE) image from the SEM of sample MEL-025 which illustrates a magnetite band with inclusions of minor chlorite and quartz; (C) BSE image from the SEM of sample MEL-028 which illustrates magnetite layers associated with minor inclusions of quartz and chlorite; (D) BSE image from the SEM of sample AMB-126242 showing magnetite bands associated with minor inclusions of quartz and apatite; (E) BSE image from the SEM showing the trace of the laser ablation traverse used for LA ICP-MS analysis in thick section of sample AMB-126249; and (F) BSE image from the SEM showing the laser ablation line traverse used for LA ICP-MS analysis in thick section of sample MEL-025. AMB-XXXXXX refers to samples from Meadowbank deposit whereas MEL-XXX refers to Meliadine gold district. Abbreviations are: Ap = Apatite, Chl = Chlorite, Mt = Magnetite, Qtz = Quartz.

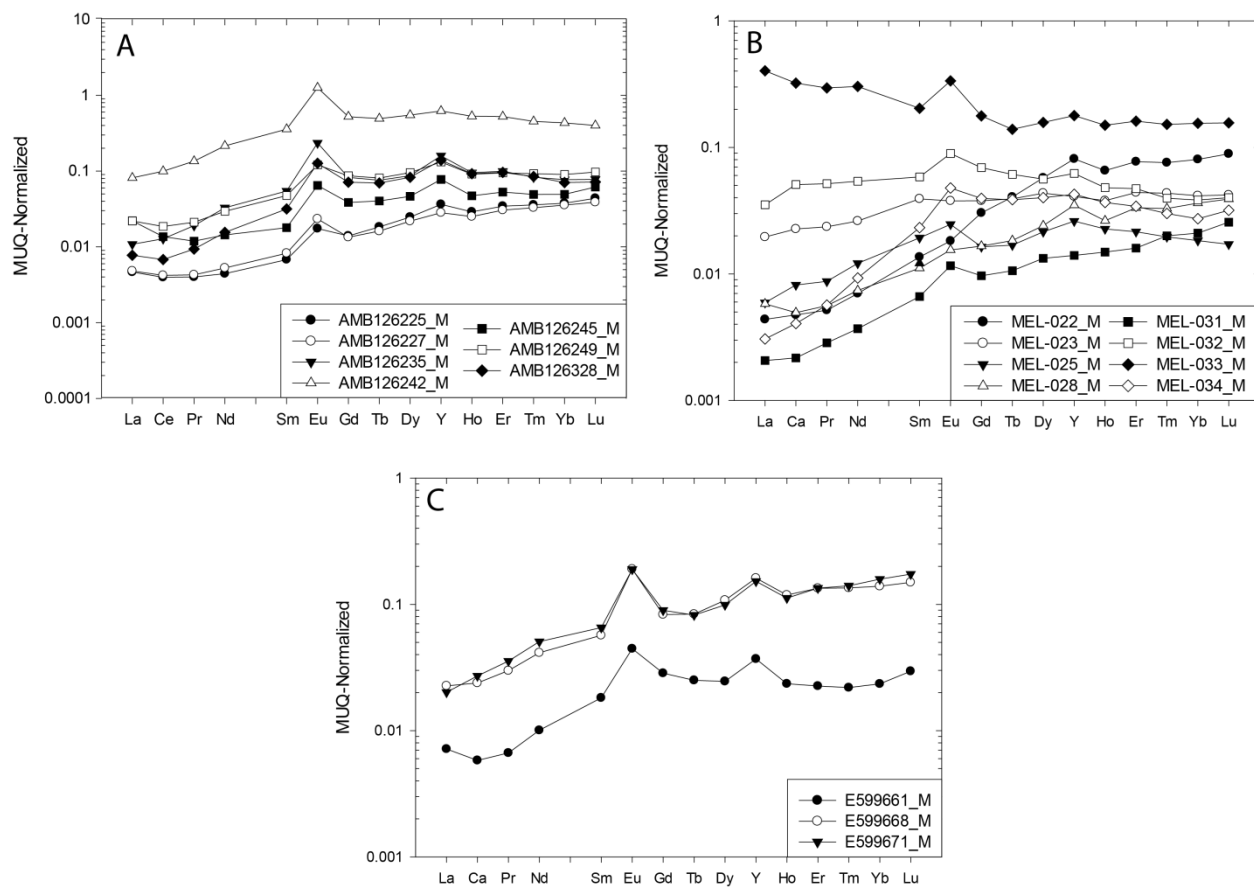


Figure B.3: Shale (MUQ) - normalized REE patterns for magnetite layers sampled from the (A) Meadowbank, (B) Meliadine, and (C) Musselwhite BIF-hosted gold deposits.

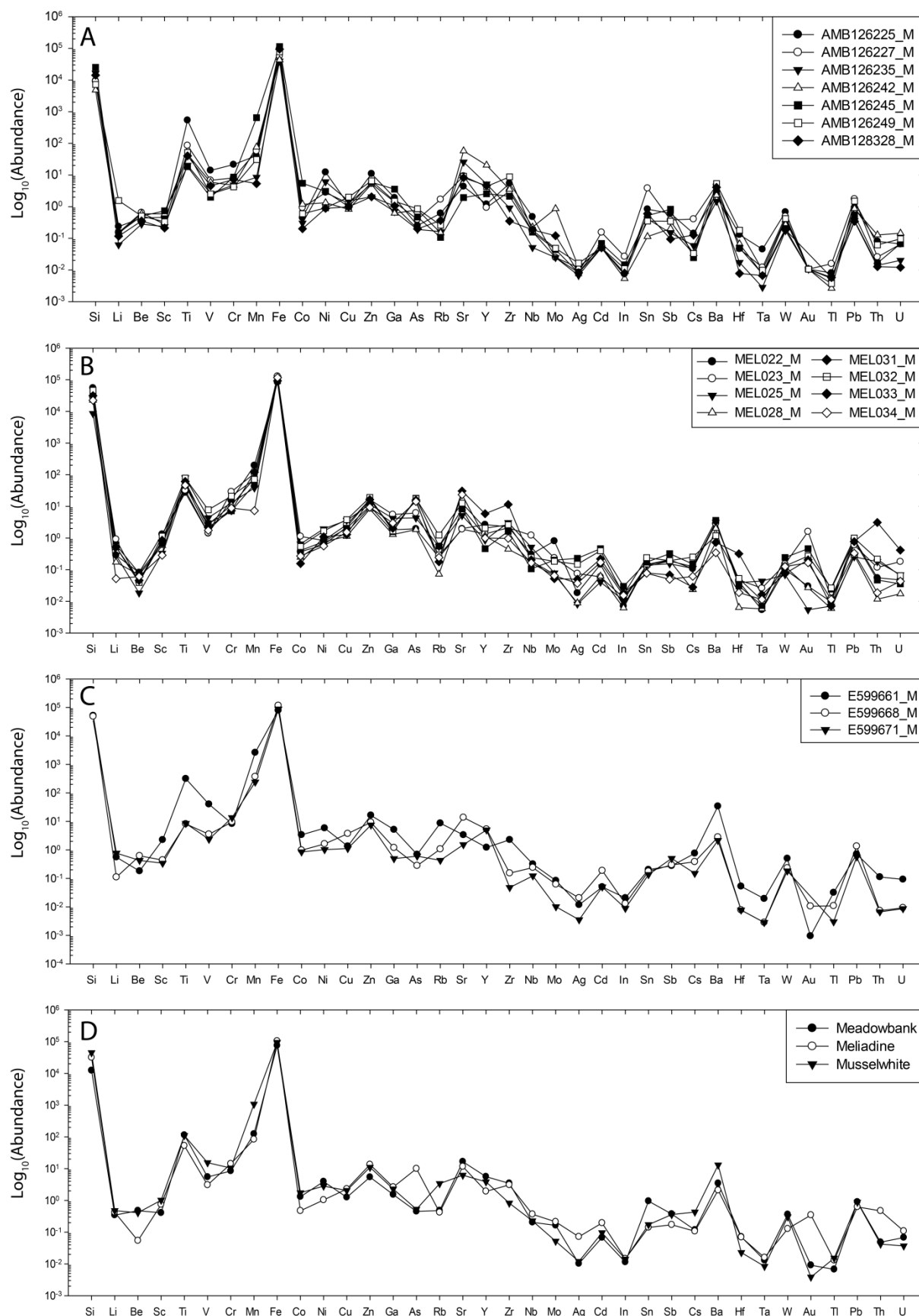


Figure B.4: Spider-type plots summarize the abundances of major and trace-elements for magnetite layers from the Meadowbank (A), Meliadine (B), and Musselwhite (C) BIF-hosted gold deposits and the average of each deposit (D).

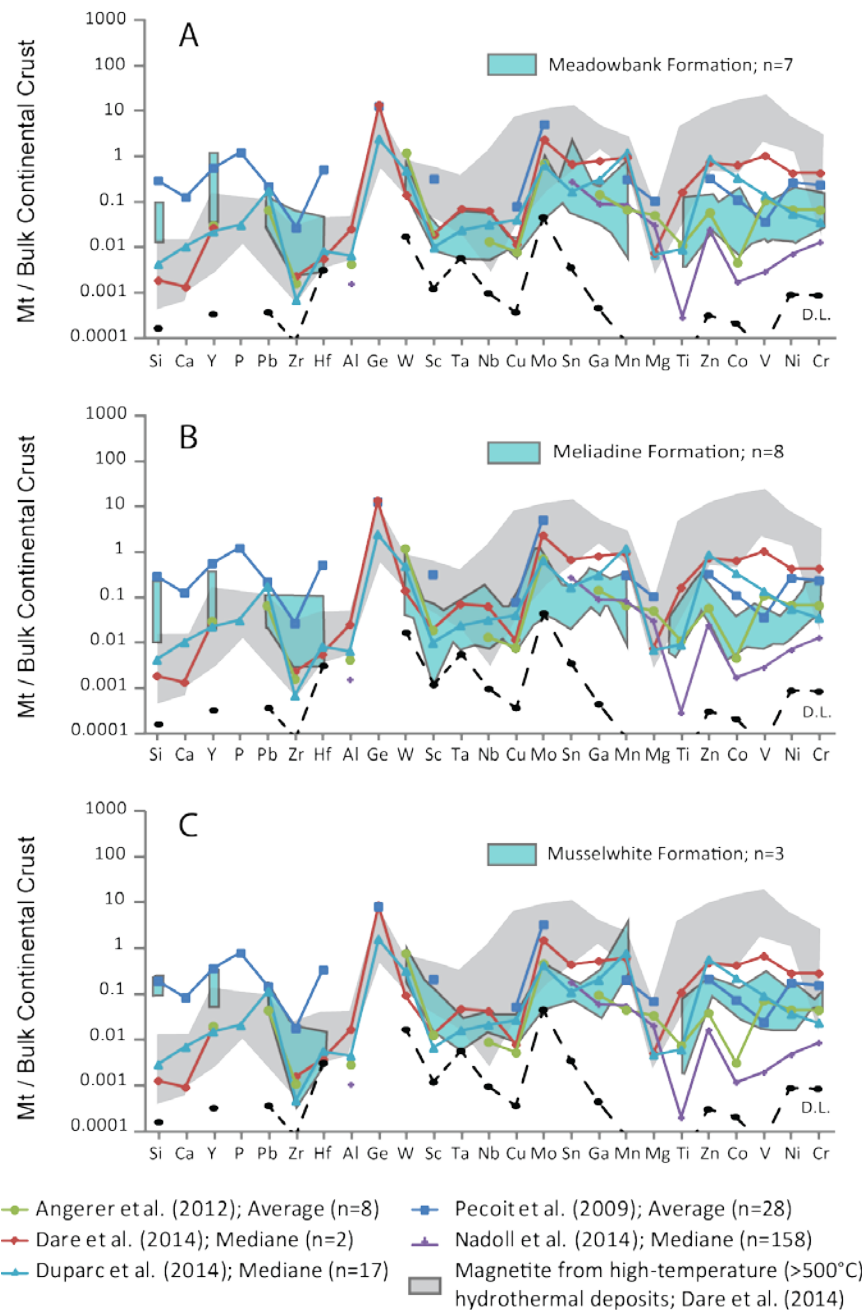


Figure B.5: Multi-element extended spider diagrams (for various analyses of magnetite normalized to bulk continental crust (values from Rudnick and Gao, 2003)). The plots show a comparison of magnetite samples from the (A) Meadowbank, (B) Meliadine, and (C) Musselwhite BIF-hosted gold deposits with data for both whole rock (Pecoits et al., 2009; Angerer et al., 2012) and *in-situ* (Dare et al., 2014; Dupuis et al., 2015; Nadoll et al., 2014)

analyses of magnetites from BIFs in the literature. For comparison, the patterns for samples of low-temperature BIF magnetite in the BIFs of this study (in blue) are seen to contrast with the field (in grey) for high-temperature hydrothermal magnetites (from Dare et al., 2014). The detection limit for the data in this study is illustrated by the dashed black line entitled D.L.

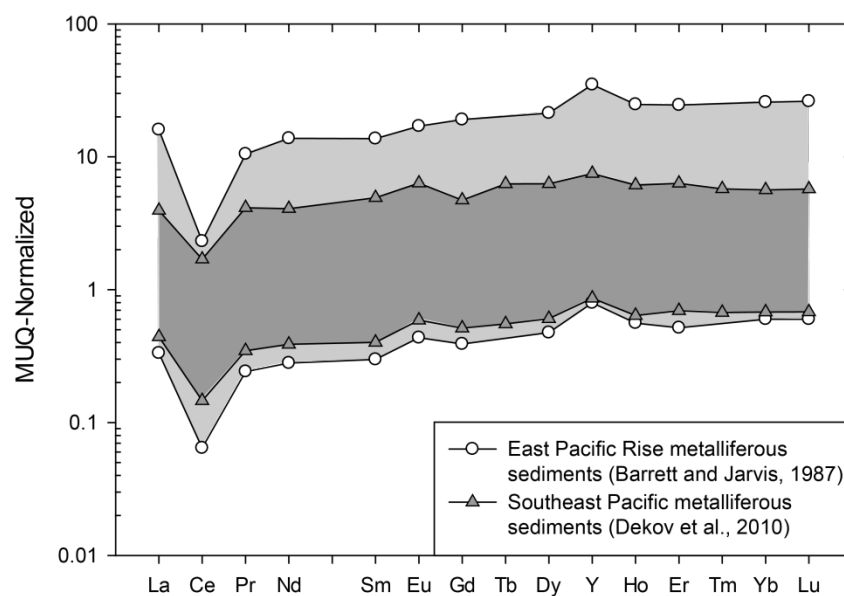


Figure B.6: Shale (MUQ) - normalized REE distribution patterns for metalliferous sediments (on a carbonate-free basis) from the East Pacific Rise (light grey; Barrett and Jarvis, 1987) and from the southeast Pacific (dark grey; Dekov et al., 2010). These metalliferous sediments are composed of poorly crystalline to X-ray amorphous Fe-Mn oxyhydroxides and variable amounts of amorphous silicate phases.

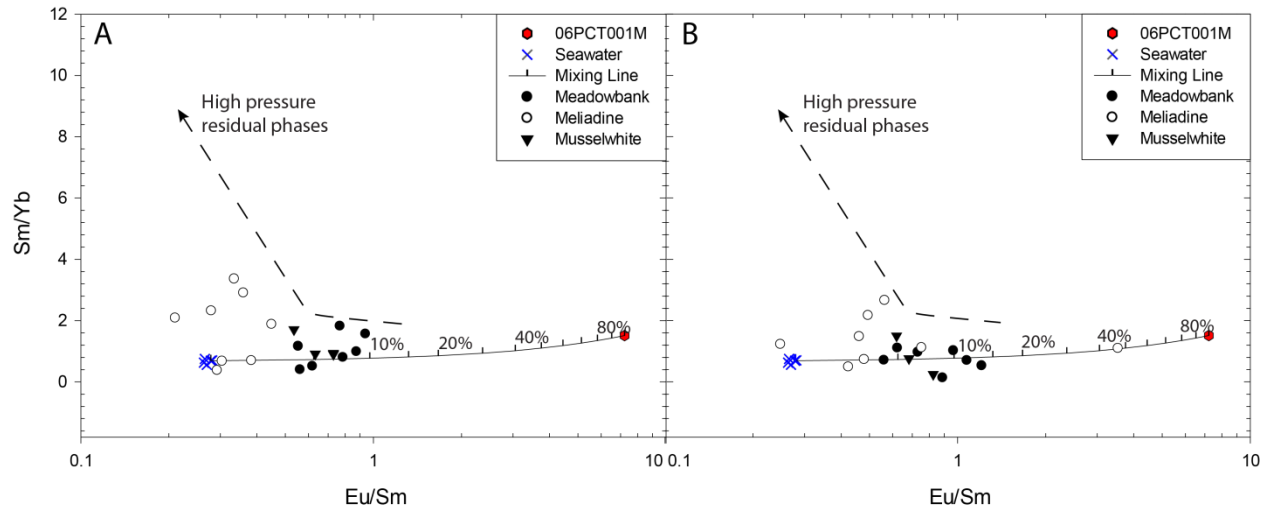


Figure B.7: Binary plots of elemental ratio data (Eu/Sm and Sm/Yb) for magnetite samples and corresponding chert samples respectively (A) and (B), from the Meadowbank, Meliadine and Musselwhite BIF-hosted gold deposits. This type of plot is used to assess the potential influence of high-T hydrothermal fluids on the chemistry of iron oxides versus low-T fluids (i.e., ambient seawater). The data for the high-T hydrothermal fluid, represented by 06PCT001M, is from Thurston et al. (2012) whereas the data for seawater is from Alibo and Nozaki (1999).

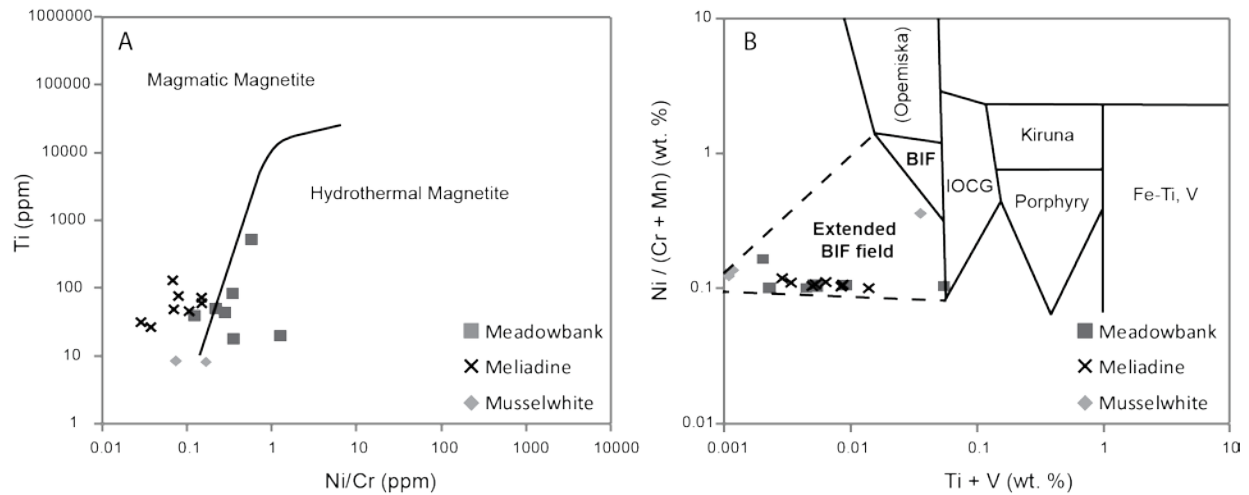


Figure B.8: Genetic classification diagrams for magnetite from a variety of ore deposit settings:

A) The Ti (ppm) versus Ni/Cr ratio (un-normalized) diagram of Dare et al. (2014) that is used to discriminate magnetite from magmatic and hydrothermal settings. It is noted that two samples of the Musselwhite deposit are superimposed to each other explaining why there is only two visible points. B) The $Ni/(Cr + Mn)$ versus $Ti+V$ discriminant diagram of Dupuis and Beaudoin (2011) that is used to discriminate magnetite in a variety of ore deposit types: BIF, Kiruna apatite-magnetite, iron-oxide-copper-gold (IOCG), porphyry Cu, magmatic Fe-Ti-V oxide and Opemiska-type Cu veins. A new extended BIF field associated with dashed black lines is proposed for this diagram according to the studied samples.

B.11 Tables and captions

Table B.1: Abundances of elements and REE+Y for magnetite samples from Meadowbank

Samples	AMB126225_M	AMB126227_M	AMB126235_M	AMB126242_M	AMB126245_M	AMB126249_M	AMB128328_M
Si (ppm)	9450	9120	16400	4800	25200	7220	14230
Li (ppm)	0.235	0.151	< 0.011	0.141	0.149	1.556	0.116
Be (ppm)	0.436	0.649	0.281	0.596	0.504	0.505	0.354
Sc (ppm)	0.461	0.275	0.235	0.591	0.741	0.332	0.212
Ti (ppm)	537.000	85.300	20.280	44.850	18.350	51.500	40.280
V (ppm)	13.970	6.776	2.610	5.893	1.989	2.511	4.534
Cr (ppm)	21.400	8.070	4.850	4.741	8.600	4.193	7.210
Mn (ppm)	41.000	57.200	8.490	76.200	646.000	30.770	5.300
Fe (ppm)	99610	57200	39820	43090	113600	77860	94470
Co (ppm)	0.444	0.924	0.302	1.186	5.470	0.595	0.201
Ni (ppm)	12.290	2.787	6.120	1.331	3.030	0.915	0.884
Cu (ppm)	1.160	1.270	1.520	0.820	1.010	2.000	0.992
Zn (ppm)	11.000	5.300	2.050	5.100	5.890	6.510	2.050
Ga (ppm)	1.906	1.398	0.700	0.622	3.569	1.472	1.054
As (ppm)	0.252	0.394	0.191	0.790	0.472	0.856	0.199
Rb (ppm)	0.617	1.690	0.162	0.149	0.108	0.260	0.367
Sr (ppm)	4.320	9.260	25.600	57.800	1.940	9.080	8.190
Y (ppm)	1.198	0.929	5.230	20.440	2.550	4.340	4.590
Zr (ppm)	5.400	3.090	0.910	3.500	2.130	8.720	0.349
Nb (ppm)	0.476	0.162	0.051	0.224	0.157	0.178	0.185
Mo (ppm)	0.025	0.025	0.025	0.860	0.044	0.049	0.121
Ag (ppm)	0.012	0.008	0.007	0.012	0.008	0.016	0.008
Cd (ppm)	< 0.71	0.154	< 0.71	< 0.71	< 0.71	< 0.71	< 0.71
In (ppm)	0.007	0.027	0.007	0.005	0.015	0.011	0.008
Sn (ppm)	0.830	3.820	0.410	0.113	0.520	0.350	0.601
Sb (ppm)	0.612	0.380	0.147	0.202	0.828	0.346	0.094
Cs (ppm)	0.142	0.404	0.059	0.033	0.024	0.033	0.127
Ba (ppm)	2.563	4.800	1.479	2.299	3.490	5.355	4.094
La (ppm)	0.173	0.179	0.403	3.030	0.821	0.820	0.289
Ce (ppm)	0.320	0.339	1.030	8.030	1.100	1.500	0.550
Pr (ppm)	0.038	0.041	0.181	1.284	0.113	0.201	0.089
Sm (ppm)	0.050	0.061	0.402	2.635	0.132	0.350	0.233
Eu (ppm)	0.028	0.038	0.378	2.028	0.104	0.194	0.204
Gd (ppm)	0.093	0.089	0.549	3.480	0.257	0.576	0.474
Tb (ppm)	0.019	0.017	0.078	0.507	0.042	0.083	0.072
Dy (ppm)	0.151	0.133	0.530	3.340	0.283	0.582	0.505
Ho (ppm)	0.036	0.031	0.119	0.661	0.059	0.114	0.115
Er (ppm)	0.120	0.106	0.346	1.822	0.184	0.329	0.334
Tm (ppm)	0.019	0.017	0.043	0.236	0.026	0.048	0.044
Yb (ppm)	0.126	0.119	0.257	1.446	0.165	0.301	0.236
Lu (ppm)	0.022	0.019	0.039	0.200	0.031	0.049	0.036
Hf (ppm)	0.130	0.046	0.017	0.066	0.049	0.180	< 0.011
Ta (ppm)	0.045	0.012	0.003	0.007	0.008	0.010	0.007
W (ppm)	0.678	0.494	0.176	0.381	0.205	0.420	0.186
Au (ppm)	0.011	0.011	0.011	0.011	0.011	0.011	0.000
Tl (ppm)	0.008	0.016	0.006	0.003	0.005	0.004	0.006
Pb (ppm)	0.927	1.750	0.360	0.865	0.550	1.490	0.343
Th (ppm)	0.081	0.026	0.014	0.128	0.017	0.062	0.013
U (ppm)	0.067	0.065	0.020	0.145	0.068	0.096	0.012
Y/Ho	33.094	29.586	43.950	30.923	43.220	38.171	39.775
La/La* _{MUQ}	1.426	1.700	1.677	1.521	2.691	2.014	2.295
Y/Y* _{MUQ}	1.149	1.014	1.632	1.180	1.548	1.421	1.480
Eu/Eu* _{MUQ}	1.764	2.166	3.752	3.138	2.649	2.064	2.984
Ce/Ce* _{MUQ}	1.097	1.208	1.151	1.170	1.381	1.222	1.213
Eu/Sm	0.562	0.619	0.940	0.770	0.788	0.554	0.876
Sm/Yb	0.398	0.511	1.564	1.822	0.800	1.163	0.987
(Nd/Yb) _{MUQ}	0.118	0.148	0.426	0.497	0.290	0.327	0.220

Table B.2: Abundances of elements and REE+Y for magnetite samples from Meliadine

Samples	MEL022_M	MEL023_M	MEL025_M	MEL028_M	MEL031_M	MEL032_M	MEL033_M	MEL034_M
Si (ppm)	55100	28100	8600	22500	38000	46200	31500	22400
Li (ppm)	0.287	0.914	0.286	0.173	0.611	0.523	0.522	0.052
Be (ppm)	0.081	0.040	< 0.028	0.069	0.078	0.039	0.046	0.061
Sc (ppm)	1.319	0.799	0.330	0.578	0.668	1.140	0.849	0.286
Ti (ppm)	27.190	32.190	79.530	49.690	46.780	78.400	61.200	46.400
V (ppm)	1.404	1.443	4.375	2.710	2.847	7.790	2.156	1.752
Cr (ppm)	16.140	28.900	12.920	10.850	7.260	21.000	7.330	8.860
Mn (ppm)	196	109.3000	38.1000	76.7000	49.4000	71.2000	121	7.3000
Fe (ppm)	83500	128500	112350	110200	93550	97200	92000	117000
Co (ppm)	0.370	1.130	0.650	0.246	0.402	0.539	0.156	0.271
Ni (ppm)	0.607	0.830	1.948	0.760	0.770	1.670	1.096	0.560
Cu (ppm)	2.230	2.640	3.610	1.130	2.020	3.800	1.290	1.530
Zn (ppm)	16.490	16.500	11.510	8.240	10.260	19.100	16.360	9.300
Ga (ppm)	1.825	5.547	4.192	1.291	1.588	1.677	2.021	2.972
As (ppm)	1.970	6.170	4.300	1.840	18.000	17.600	15.800	14.300
Rb (ppm)	0.244	0.283	0.543	0.072	0.560	1.240	0.178	0.243
Sr (ppm)	1.980	1.900	5.170	8.800	8.300	12.600	30.600	23.500
Y (ppm)	2.670	1.348	0.860	1.151	0.461	2.050	5.870	1.000
Zr (ppm)	2.270	2.110	3.080	0.444	1.640	2.610	11.500	0.973
Nb (ppm)	0.306	1.215	0.516	0.187	0.107	0.242	0.205	0.164
Mo (ppm)	0.803	0.236	0.079	0.072	0.200	0.184	0.052	0.065
Ag (ppm)	0.019	0.075	0.008	0.009	0.228	0.148	0.050	0.037
Cd (ppm)	0.146	0.060	0.041	0.063	0.462	0.396	0.219	0.170
In (ppm)	0.007	0.013	0.011	0.006	0.030	0.016	0.018	0.015
Sn (ppm)	0.147	0.126	0.139	0.142	0.173	0.239	0.079	0.077
Sb (ppm)	0.206	0.189	0.153	0.195	0.321	0.193	0.068	0.050
Cs (ppm)	0.107	0.125	0.110	0.023	0.151	0.251	0.028	0.062
Ba (ppm)	2.836	2.880	3.160	2.015	3.610	1.183	0.725	0.341
La (ppm)	0.163	0.730	0.221	0.216	0.077	1.310	15.000	0.080
Ce (ppm)	0.383	1.830	0.660	0.399	0.175	4.100	26.000	0.258
Pr (ppm)	0.049	0.224	0.083	0.053	0.027	0.490	2.800	0.039
Nd (ppm)	0.254	0.950	0.440	0.269	0.134	1.960	11.000	0.231
Sm (ppm)	0.100	0.289	0.142	0.082	0.049	0.430	1.500	0.090
Eu (ppm)	0.029	0.061	0.040	0.025	0.019	0.144	0.540	0.049
Gd (ppm)	0.202	0.252	0.109	0.111	0.064	0.460	1.180	0.152
Tb (ppm)	0.042	0.040	0.017	0.019	0.011	0.063	0.143	0.023
Dy (ppm)	0.350	0.265	0.131	0.147	0.081	0.342	0.960	0.153
Ho (ppm)	0.082	0.047	0.028	0.033	0.019	0.060	0.187	0.032
Er (ppm)	0.268	0.153	0.075	0.116	0.056	0.164	0.561	0.087
Tm (ppm)	0.039	0.023	0.010	0.017	0.010	0.021	0.079	0.011
Yb (ppm)	0.268	0.139	0.061	0.121	0.070	0.128	0.517	0.054
Lu (ppm)	0.044	0.021	0.009	0.020	0.013	0.020	0.078	0.009
Hf (ppm)	0.041	0.048	0.039	< 0.009	0.031	0.053	0.318	0.019
Ta (ppm)	0.005	0.026	0.044	0.006	0.007	0.011	0.016	0.011
W (ppm)	0.102	0.151	0.070	0.128	0.242	0.131	0.075	0.126
Au (ppm)	0.030	1.600	0.005	0.027	0.460	0.270	0.204	0.166
Tl (ppm)	0.010	0.013	0.007	0.006	0.024	0.027	0.007	0.012
Pb (ppm)	0.925	0.599	0.255	0.288	0.834	1.000	0.770	0.331
Th (ppm)	0.055	0.118	0.180	0.012	0.047	0.215	3.100	0.019
U (ppm)	0.048	0.180	0.069	0.017	0.036	0.065	0.414	0.043
Y/Ho	32.561	28.439	30.389	34.985	24.785	34.167	31.390	30.568
La/La ₀ MUQ	1.548	1.021	1.304	1.799	1.210	0.745	1.441	1.449
Y/Y ₀ MUQ	1.137	1.000	1.182	1.173	0.907	1.309	1.147	1.200
Eu/Eu ₀ MUQ	0.895	0.932	1.285	1.128	1.429	1.467	1.840	1.675
Ce/Ce ₀ MUQ	1.241	1.066	1.297	1.162	0.982	1.030	1.122	1.171
Eu/Sm	0.293	0.210	0.280	0.304	0.383	0.335	0.360	0.449
Sm/Yb	0.374	2.087	2.320	0.675	0.696	3.359	2.901	1.879
(Nd/Yb) ₀ MUQ	0.087	0.631	0.661	0.204	0.176	1.408	1.956	0.340

Table B.3: Abundances of elements and REE+Y for magnetite samples from Musselwhite

Samples	E599661_M	E599668_M	E599671_M
Si (ppm)	51670	48700	34000
Li (ppm)	0.553	0.111	0.771
Be (ppm)	0.182	0.620	0.429
Sc (ppm)	2.258	0.440	0.340
Ti (ppm)	315.400	8.190	8.490
V (ppm)	40.290	3.541	2.358
Cr (ppm)	8.290	9.550	13.600
Mn (ppm)	2602	372	240
Fe (ppm)	79000	116700	88200
Co (ppm)	3.377	0.978	0.850
Ni (ppm)	5.830	1.624	1.021
Cu (ppm)	1.350	3.720	1.120
Zn (ppm)	16.440	9.300	7.450
Ga (ppm)	5.170	1.195	0.495
As (ppm)	0.692	0.281	0.605
Rb (ppm)	8.660	1.066	0.430
Sr (ppm)	3.350	13.760	1.530
Y (ppm)	1.217	5.310	5.010
Zr (ppm)	2.270	0.154	0.048
Nb (ppm)	0.318	0.240	0.123
Mo (ppm)	0.084	0.062	0.010
Ag (ppm)	0.012	0.021	0.004
Cd (ppm)	< 0.071	0.187	< 0.071
In (ppm)	0.021	0.013	0.009
Sn (ppm)	0.203	0.177	0.136
Sb (ppm)	0.277	0.298	0.502
Cs (ppm)	0.759	0.382	0.150
Ba (ppm)	34.100	2.811	2.150
La (ppm)	0.267	0.843	0.750
Ce (ppm)	0.469	1.926	2.190
Pr (ppm)	0.063	0.284	0.338
Nd (ppm)	0.366	1.505	1.840
Sm (ppm)	0.134	0.419	0.482
Eu (ppm)	0.072	0.306	0.305
Gd (ppm)	0.190	0.553	0.598
Tb (ppm)	0.026	0.086	0.085
Dy (ppm)	0.150	0.658	0.604
Ho (ppm)	0.029	0.148	0.140
Er (ppm)	0.079	0.467	0.468
Tm (ppm)	0.011	0.070	0.073
Yb (ppm)	0.078	0.465	0.529
Lu (ppm)	0.015	0.075	0.087
Hf (ppm)	0.053	< 0.011	< 0.011
Ta (ppm)	0.019	0.003	0.003
W (ppm)	0.501	0.232	0.182
Au (ppm)	< 0.015	< 0.015	< 0.015
Tl (ppm)	0.032	0.011	0.003
Pb (ppm)	0.708	1.355	0.570
Th (ppm)	0.112	0.007	0.007
U (ppm)	0.092	0.009	0.009
Y/Ho	41.395	35.806	35.786
La/La ₀ MUQ	2.457	1.452	1.146
Y/Y ₀ MUQ	1.604	1.276	1.234
Eu/Eu ₀ MUQ	2.117	2.859	2.615
Ce/Ce ₀ MUQ	1.318	1.105	1.085
Eu/Sm	0.535	0.730	0.633
Sm/Yb	1.709	0.901	0.911
(Nd/Yb) ₀ MUQ	0.429	0.298	0.320

B.12 References

- Alibo D.S. and Nozaki Y., 1999. Rare earth elements in seawater: particle association, shale-normalization, and Ce oxidation: *Geochimica et Cosmochimica Acta*, v. 63, p. 363-372.
- Allwood, A.C., Kamber, B.S., Walter, M.R., Burch, I.W. and Kanik, I., 2010. Trace element record depositional history of an Early Archean stromatolitic carbonate platform; *Chemical Geology*, v. 270, p. 148-163.
- Angerer T., Hagemann S.G. and Danyushevsky L., 2012. Geochemical evolutions of the banded iron formation-hosted high-grade iron ore system in the Koolyanobbing Greenstone Belt, Western Australia; *Economic Geology*, v. 107, p. 599-644.
- Armitage, A.E., James, R.S. and Goff, S.P., 1996. Gold mineralization in Archean banded iron formation, Third Portage Lake area, Northwest Territories, Canada; *Exploration and Mining Geology*, v. 5, no. 1, p. 1-15.
- Aspler, L.B. and Chiarenzelli, J.R. 1996a. Stratigraphy, sedimentology and physical volcanology of the Henik Group, central Ennadai-Rankin greenstone belt, Northwest Territories, Canada: Late Archean paleogeography of the Hearne Province and tectonic implications; *Precambrian Research*, v. 77, p. 59-89.
- Barrett, T.J. and Jarvis, I., 1988. Rare-earth-element geochemistry of metalliferous sediments from DSDP LEG 92: The East Pacific Rise Transect; *Chemical Geology*, v. 67, p. 243-259.
- Bau, M. and Dulski, P., 1996. Distribution of Y and rare-earth elements in the Penge and Kuruman Iron Formations, Transvaal Supergroup, South Africa; *Precambrian Research*, v.

79, p. 37-55.

- Biczok, J., Hollings, P., Klipfel, P., Heaman, L., Maas, R., Hamilton, M., Kamo, S. and Friedman, R., 2012. Geochronology of the North Caribou greenstone belt, Superior Province Canada: Implications for tectonic history and gold mineralization at the Musselwhite mine; *Precambrian Research*, v. 192-195, p. 209-230.
- Bolhar, R., Van Kranendonk, M.J. and Kamber, B.S., 2005. A trace element study of siderite-jasper banded iron formation in the 3.45 Ga Warrawoona Group, Pilbara craton-Formation from hydrothermal fluids and shallow seawater; *Precambrian Research*, v. 137, p. 93-114.
- Breaks, F.W., Osmani, I.A. and DeKemp, E.A., 2001. Geology of the North Caribou Lake area, northwestern Ontario; Ontario Geological Survey, Open File Report 6023, 80 p.
- Carpenter, R.L., 2004. Relative and absolute timing of supracrustal deposition, tectonothermal activity and gold mineralization, West Meliadine region, Rankin Inlet greenstone belt, Nunavut, Canada; PhD. Thesis, Faculty of Graduate Studies, University of Western Ontario, 362 p.
- Carpenter, R.L., Duke, N.A., Sandeman, H.A. and Stern, R., 2005. Relative and absolute timing of gold mineralization along the Meliadine Trend, Nunavut, Canada; evidence for Paleoproterozoic gold hosted in an Archean greenstone belt.; *Economic Geology and the Bulletin of the Society of Economic Geologists*, v. 100, p. 567-576.
- Chen, W.T., Zhou M.-F., Li, X., Gao, J.F. and Hou, K., 2015. In-situ LA-ICP-MS trace elemental analyses of magnetite: Cu-(Au, Fe) deposits in the Khetri copper belt in Rajasthan Province, NW India. *Ore Geology Reviews* 65 (2015) 929-939.

- Dare, S.A.S., Barnes, S.J. and Beaudoin, G., 2012. Variation in trace element content of magnetite crystallized from a fractionating sulfide liquid, Sudbury, Canada: Implications for provenance discrimination; *Geochimica et Cosmochimica Acta*, v. 88, p. 27-50.
- Dare, S.A.S., Beaudoin, G., Méric, J., Boutroy, E. and Potvin-Doucet, C., 2014. Trace elements in magnetite as petrogenetic indicators; *Miner Deposita*, v. 49, Issue 7, p. 785-796.
- Davis, W.J., Ryan, J.J., Sandeman, H.A. and Tella, S., 2008. A Paleoproterozoic detrital zircon age for a key conglomeratic horizon within the Rankin Inlet area, Kivalliq region, Nunavut: implications for Archean and Proterozoic evolution of the area; In *Current research 2008-8*, Geological Survey of Canada, 10 p.
- Dekov, V.M., Cuadros, J., Kamenov, G.D., Weiss, D., Arnold, T., Basak, C. and Rochette, R., 2010. Metalliferous sediments from the H.M.S. Challenger voyage (1872-1876); *Geochimica et Cosmochimica Acta*, v. 74, p. 5019-5038.
- Duparc, Q., 2014. Corrélations de formations sédimentaires du nord-est de la sous-province de La Grande, Québec, Canada; Unpublished Master's Thesis, Université du Québec à Chicoutimi, 243 p.
- Duparc, Q., Dare, S.A.S., Cousineau, P.A. and Goutier, J., 2015. Magnetite chemistry as a provenance indicator in Archean metamorphosed sedimentary rocks; *Journal of Sedimentary Research* (accepted in June).
- Dupuis, C. and Beaudoin, G., 2011. Discriminant diagrams for iron oxide trace element fingerprinting of mineral deposit types; *Miner Deposita*, v. 46, p. 319-335.

- Gourcerol, B., Thurston, P.C., Kontak, D.J., Côté-Mantha, O. and Biczok, J., 2015a. The geochemistry of chert from the Banded Iron Formation-type Musselwhite and Meadowbank gold deposits: Distinguishing primary and mineralization-related signatures of chert; In Current research 2015-1, Geological Survey of Canada, 24 p.
- Gourcerol, B., Thurston, P.C., Kontak, D.J., Côté-Mantha, O. and Biczok, J. 2015b. Depositional Setting of Algoma-type Banded Iron Formation from the Meadowbank, Meliadine and Musselwhite gold deposits; In: Targeted Geoscience Initiative 4: Contributions to the Understanding of Precambrian Lode Gold Deposits and Implications for Exploration, (eds.) B. Dubé and P. Mercier-Langevin; Geological Survey of Canada, Open File 7852, p. 55-68.
- Gourcerol, B., Thurston, P.C., Kontak, D.J. and Côté-Mantha, O., 2015c. Interpretations and implications of preliminary LA ICP-MS analysis of chert for the origin of geochemical signatures in banded iron formations (BIFs) from the Meadowbank gold deposit, Western Churchill Province, Nunavut: Chemical Geology, v. 410, p. 89-107.
- Grigsby, J., 1990. Detrital magnetite as a provenance indicator; Journal of Sedimentary Research, v. 60, p. 940-951.
- Hall, R.S. and Rigg, D.M., 1986. Geology of the West Anticline Zone, Musselwhite Prospect, Opapimiskan Lake, Ontario, Canada, In: Macdonald, A.J. (Ed.), Gold '86; an international symposium on the geology of gold deposits; proceedings volume; GOLD '86, Toronto, ON, Canada, p. 124-136.
- Hrabi, R.B., Barclay, W.A., Fleming, D. and Alexander, R.B., 2003. Structural evolution of the Woodburn Lake group in the area of the Meadowbank gold deposit, Nunavut; In Current

Research 2003-C27, Geological Survey of Canada, 10 p.

Hu, H., Li, J.W., Lentz, D., Ren, Z., Zhao, X.F., Deng, X.D. and Hall, D., 2014. Dissolution-reprecipitation process of magnetite from the Chengchao iron deposit: insights into ore genesis and implication for in-situ chemical analysis of magnetite; *Ore Geology Reviews*, v. 57, p. 393-405.

Janvier, V., Castonguay, S., Mercier-Langevin, P., Dubé, B., McNicoll, V., Pehrsson, S., Malo, M., De Chavigny, B. and Cote-Mantha, O., 2015a. Preliminary results of geology of the Portage deposit, Meadowbank gold mine, Churchill Province, Nunavut, Canada; Geological Survey of Canada, Current Research 2015-2, 18 p. doi:10.4095/295532

Kappler, A., Pasquero, C., Konhauser, K.O. and Newman D.K., 2005. Deposition of banded iron formations by anoxygenic phototrophic Fe(II)-oxidizing bacteria; *Geology*, v. 33, p. 865-868.

Kamber, B.S., Bolhar, R. and Webb, G.E. 2004. Geochemistry of late Archean stromatolites from Zimbabwe: evidence for microbial life in restricted epicontinental seas; *Precambrian Research*, v. 132, p. 379-399.

Kamber, B.S., Greig, A. and Collerson, K.D., 2005. A new estimate for the composition of weathered young upper continental crust from alluvial sediments, Queensland, Australia. *Geochimica et Cosmochimica Acta*, v. 69, p. 1041-1058.

Konhauser, O.K., Newman, D.K. and Kappler, A., 2005. The potential significance of microbial Fe(III) reduction during deposition of Precambrian banded iron formations; *Geobiology*, v. 3, p.167-177.

- Konhauser, O.K., Pecoits, E., Lalonde, S.V., Papineau, D., Nisbet, E.G., Barley, M.E., Arndt, N.T., Zahnle, K. and Kamber, B.S., 2009. Oceanic nickel depletion and a methanogen famine before the Great Oxidation Event; *Nature*, v. 458, p. 750-753.
- Lawley, C.J.M., Dubé, B., Mercier-Langevin, P., Kjarsgaard, B., Knight R. and Vaillancourt, D., 2015a. Defining and mapping hydrothermal footprints at the BIF-hosted Meliadine gold district, Nunavut, Canada; *Journal of Geochemical Exploration*, v.155, p. 33-55.
- Lawrence, M. G. and Kamber, B. S., 2006. The behavior of the rare earth elements during estuarine mixing- revisited; *Marine Chemistry*, v. 100, p.147-161.
- Loges, A., Migdisov, A.A., Wagner, T., Williams-Jones, A.E. and Markl, G., 2013. An experimental study of the aqueous solubility and speciation of Y(III) fluoride at temperatures up to 250°C. *Geochim. Et Cosmochim. Acta* 123: 403-415.
- Li, W., Jin, X., Gao, B., Wang, C. and Zhang, L., 2014. Analysis of ultra-low level rare earth elements in magnetite samples from banded iron formations using HR-ICP-MS after chemical separation; *Analytical Methods*, v. 6, p. 6125-6132.
- McNicoll, V., Dubé, B., Biczok, J., Castonguay, S., Oswald, W., Mercier-Langevin, P., Skulski, T., and Malo, M., 2013. The Musselwhite gold deposit, North Caribou greenstone belt, Ontario: new high-precision U-Pb ages and their impact on the geological and structural setting of the deposit; Abstract, Geol. Assoc. of Canada annual meeting, Winnipeg.
- Moran, P., 2008. Lithogeochemistry of the sedimentary stratigraphy and metasomatic alteration in the Musselwhite gold deposit. North Caribou Lake metavolcanic-metasedimentary belt, Superior Province, Canada: implications for deposition and mineralization; Unpublished

Master's Thesis, Lakehead University, 351 p.

Nadoll, P., Angerer T., Mauk, J.L., French, D. and Walshe, J., 2014. The chemistry of hydrothermal magnetite: A review; *Ore Geology Reviews*, v. 61, p. 1-32.

Nadoll, P., Mauk, J.L., Hayes, T.S., Koenig, A.E. and Box, S.E., 2012. Geochemistry of magnetite from hydrothermal ore deposits and host rocks of the Mesoproterozoic Belt Supergroup, United States; *Economic Geology*, v. 107, p. 1275-1292.

Oswald, W., Castonguay, S., Dubé, B., McNicoll, V.J., Biczok, J., Malo, M. and Mercier-Langevin, P., 2015. Geological setting of the world-class Musselwhite gold Mine, Superior Province, northwestern Ontario, and implications for exploration, In: *Targeted Geoscience Initiative 4: Contributions to the Understanding of Precambrian Lode Gold Deposits and Implications for Exploration*, (ed.) B. Dubé and P. Mercier-Langevin; Geological Survey of Canada, Open File 7852, p. 69-84.

Paton, C., Hellstrom, J., Paul, B., Woodhead, J. and Hergt, J., 2011. Iolite: Freeware for the visualisation and processing of mass spectrometric data; *Journal of Analytical Atomic Spectrometry*, v. 26, p. 2508-2518.

Pecoits, E., Gringas, M.K., Barley, M.E., Kappler, A., Posth, N.R. and Konhauser, K.O., 2009. Petrography and geochemistry of the Dales Gorge banded iron formation: Paragenetic sequence, source and implications for palaeo-ocean chemistry; *Precambrian Research*, v. 172, p. 163-187.

Pehrsson, S.J., Wilkinson, L. and Zaleski, E., 2004. Geology of the Meadowbank gold deposit area, Nunavut; Geological Survey of Canada, Open File 4269, scale 1:20 000.

- Pehrsson, S.J., Berman, R.G. and Davis, W.J., 2013. Paleoproterozoic orogenesis during Nuna aggregation: a case study of reworking of the Rae craton, Woodburn Lake, Nunavut; *Precambrian Research*, v. 232, p. 167-188.
- Pickard, A.L., Barley, M.E. and Krapez, B., 2003. Deep-marine depositional setting of banded iron formation: sedimentological evidence from interbedded clastic sedimentary rocks in the early palaeoproterozoic Dales Gorge member of Western Australia. *Sedimentary Geology* 170, 37-62.
- Posth, N.R., Kohler, I., Swanner, E.D., Schroder, C., Wellmann, E., Binder, B., Konhauser, K.O., Neumann, U., Berthold, C., Nowak, M. and Kappler, A., 2013. Simulating Precambrian banded iron formation diagenesis; *Chemical Geology*, v. 362, p. 66-73.
- Ray, G. and Webster, I., 2007. Geology and chemistry of the low Ti magnetite-bearing Heff Cu-Au skarn and its associated plutonic rocks, Heffley Lake, south-central British Columbia; *Exploration and Mining Geology*, v. 16, p.159-186.
- Rudnick R. L. and Gao S., 2003. Composition of the continental crust; In: *The Crust* (ed. R. L. Rudnick). In *Treatise on Geochemistry*, vol. 3 (eds. H. D. Holland and K. K. Turekian); Elsevier, Oxford, p. 1-64.
- Sherlock, R., Pehrsson, S., Logan, A.V., Hrabi, R.B. and Davis, W.J., 2004. Geologic setting of the Meadowbank gold deposits, Woodburn Lake group, Nunavut; *Exploration Mining Geology*, v. 13 (1-4), p. 67-107.
- Sherlock, R.L., Alexander, R.B., March, R. and Barclay, W.A., 2001a. Geologic setting of the Meadowbank iron formation-hosted gold deposits; In *Current Research 2001-C11*,

Geological Survey of Canada, 23 p.

Sherlock, R.L., Alexander, R.B., March, R. and Barclay, W.A., 2001b. Geologic setting of the Meadowbank iron formation-hosted gold deposits; Geological Survey of Canada, Open File 3149, scale 1:10 000.

Shibuya, T., Komiya, T., Nakamura, K., Takai, K. and Maruyama, S., 2010. Highly alkaline, high-temperature hydrothermal fluids in the early Archean ocean; *Precambrian Research*, v. 182, p.230-238.

Tella, S., Paul, D., Berman, R.G., Davis, W.J., Peterson, T.D., Pehrsson, S.J. and Kerswill, J.A., 2007. Bedrock geology compilation and regional synthesis of parts of Hearne and Rae domains, western Churchill Province, Nunavut-Manitoba; Geological Survey of Canada, Open File 5441, scale 1:550 000 (3 sheets and a CD-ROM).

Thorne, W.S., Hagemann, S.G., Webb, A. and Clout, J., 2008. Banded iron formation-related iron ore deposits of the Hamersley Province, Western Australia; In: Hagemann, S.G., Rosière, .A., Gutzmer, J., Beukes, N.J. (Eds.), *Banded Iron Formation-related High-Grade Iron Ore*, p. 197-222.

Thurston, P.C., Kamber, B.S. and Whitehouse, M., 2012. Archean cherts in banded iron formation: Insight into Neoproterozoic ocean chemistry and depositional processes; *Precambrian Research*, v. 214-215, p. 227-257.

Wright, G.M., 1967. Geology of the southeastern barren grounds, Parts of the Districts of Mackenzie and Keewatin. Geological Survey of Canada, Memoire 350.91 p.

Zhao, W.W. and Zhou, M.F., 2015. In-situ LA-ICP-MS trace elemental analyses of magnetite: the Mesozoic Tengtie skarn Fe deposit in the Nanling Range, South China; *Ore Geology Reviews*, v. 65, p. 872-883.

Appendix C: Chemical concordance of iron oxide and chert layers in Archean Algoma-type BIF: implications for Earth ocean chemistry

C.1 Abstract

The geochemistry of chert layers, in particular their rare earth element (REE) and Y systematics, from Algoma-type banded iron formation (BIF) are used to constrain their chemical environment of deposition, which is critical for evaluating the geochemical evolution of the Archean to early Proterozoic Earth. Shale-normalized REE+Y patterns for Archean hydrogenous cherts in BIF are characterized by light REE depletion (LREE) and positive La, Y anomalies, whereas their hydrothermal equivalents show positive Eu anomalies, lesser La and Y anomalies and are not depleted in LREE. In order to assess the potential influence of post-depositional processes on such primary geochemical signatures, we present for the first time data complementary chert and magnetite layers in BIF which provide a test of chemical concordance. The data indicate that, regardless of their post-depositional histories, both the chert and iron-rich layers retain identical primary geochemical signals and reflect a dominant input of seawater with a lesser contribution from high-temperature ($>250^{\circ}\text{C}$) hydrothermal vent fluids. Furthermore, a complementary study of $\delta^{18}\text{O}$ values of selected chert determined *in-situ* using secondary ion mass spectrometry (SIMS) indicates $\delta^{18}\text{O}$ values of +6.6 to +19.1‰ (n = 70), which contrast with expected $\delta^{18}\text{O}$ values of +27‰ for Archean chert. Modelling of these $\delta^{18}\text{O}$ data suggests that the primary $\delta^{18}\text{O}$ signal of original amorphous silica was altered via dissolution-precipitation processes during diagenesis due to interaction with heated ($>100^{\circ}\text{C}$) fluids having $\delta^{18}\text{O}_{\text{H}_2\text{O}} = 0$ to +5‰, hence modified seawater. Thus, this integrated trace element and isotopic study indicates that, whereas exchange of oxygen occurred in the chert during diagenesis, the primary REE and

trace element signatures of interlayered silica- and iron-rich domains were not significantly modified.

C.2 Introduction

Algoma-type BIF are chemical sedimentary rocks characterized by alternating layers of chert and iron-rich minerals (James, 1954) that are generally interstratified with bimodal volcanic rocks and/or sedimentary sequences in multiply deformed and metamorphosed Archean greenstone belts. These Fe-rich sequences have long been appreciated as an important contributor to furthering our understanding of the geochemical evolution of the Earth, in particular its atmosphere and hydrosphere (e.g., Huston and Logan, 2004; Holland, 2005; Van den Boorn et al., 2010; Bekker et al., 2010). Thus, it is paramount that the geochemical origin and integrity of BIF be fully documented, which we explore herein.

Based on the abundance of REE+Y, it is now largely accepted that carefully selected chert layers from BIF may reflect primary geochemical signatures that suggest precipitation from interaction of seawater and high-temperature hydrothermal fluids (>250°C) with variable amounts of detrital contamination (e.g., Bolhar et al., 2005; Thurston et al., 2012; Gourcerol et al., 2015a, b). In contrast, the interbedded iron-rich layers, which were transformed from primary iron-bearing minerals, such as siderite and/or iron (Fe) oxyhydroxides, to hematite, magnetite, various iron-silicates and carbonates, and pyrite, may show a resetting of their trace element geochemistry (e.g., Pickard et al., 2003) due to diagenesis and/or by later metamorphic recrystallization (e.g., Posth et al., 2013). Although previous studies have independently explored both the geochemistry of chert and iron-oxide layers from BIF (e.g., Angerer et al., 2012; Thurston et al., 2012; Li et al., 2014) and the isotopic (^{18}O) signals of chert (e.g., Marin et

al., 2010), there has not been a fully integrated study at a single BIF locality which compares the chemical signal of both the silica- and iron-rich domains to test for chemical concordance with complementary $\delta^{18}\text{O}$ data on the chert to assess any post-depositional chemical modification. Consequently, in order to explore the influence of post-depositional processes on the primary geochemical signal of the original opaline material and iron-oxide layers, samples of such material from several BIF horizons within the Meliadine gold district (Churchill Province, Canada) have been analyzed using *in-situ* laser ablation (LA) inductively coupled mass spectrometry (ICP-MS) for trace elements and secondary ion mass spectrometry (SIMS) for oxygen isotopes. These independent data sets are used for the first time on the same BIF samples to evaluate: (1) the genesis of the cherts and magnetite using REE+Y systematics; (2) whether diagenetic changes affected the primary chemical signals of these phases; and (3) the diagenetic history of the chert bands using $\delta^{18}\text{O}$ as a proxy for post-depositional exchange.

C.3 Materials and methods

Twenty four samples of BIF from drill core and outcrops from the Meliadine gold district were selected from earlier work (Gourcerol et al. 2015a, b; Fig. C.1). Trace-element and REE concentrations were obtained on 100 μm thick polished sections using a Resonetics RESolution M-50 laser ablation instrument coupled to a Thermo X Series II quadrupole ICP-MS at the Geochemical Fingerprinting Laboratory of Laurentian University (Sudbury, Canada). Representing a mixed bimodal felsic and mafic volcanic provenance, the Queensland alluvial shale composite (MUQ) was used to normalize the REE+Y values to minimize the influence of potential terrigenous input (Kamber et al., 2005). *In-situ* $\delta^{18}\text{O}$ measurements were made on polished thin sections by secondary ion mass spectrometry (SIMS) using a Cameca 7f ion microprobe at the University of Manitoba (Canada). The oxygen isotope data reported here are

from a subset of a more extensive study of these samples (i.e., MEL-008C, MEL-016C and MEL-033C). The data are reported in the conventional form as per mil (‰) deviations from the Vienna Standard Mean Ocean Water (V-SMOW). Details of the operating conditions for the various analytical techniques are explained in Gourcerol et al. (2015a).

C.4 Results

C.4.1 REE+Y systematics

All of the chert samples in this study (Fig. C.2A), except for two (MEL-007C and MEL-008C), show relatively uniform normalized patterns characterized by LREE depletion relative to middle and HREE ($\text{Nd/Yb}_{\text{MUQ}} = 0.06\text{-}0.86$) that are associated with slight to moderate positive La, Y and Eu anomalies ($\text{La/La}^*_{\text{MUQ}} = 0.7\text{-}2.0$; $\text{Y/Y}^*_{\text{MUQ}} = 0.8\text{-}1.2$; $\text{Eu/Eu}^*_{\text{MUQ}} = 1.0\text{-}7.4$) and chondritic to super-chondritic Y/Ho values ($\text{Y/Ho} = 19.7\text{-}36.46$). In contrast, the chert in samples MEL-007C and MEL-008C are characterized by LREE-depleted patterns ($\text{Nd/Yb}_{\text{MUQ}} = 0.06\text{-}0.18$), chondritic to sub-chondritic Y/Ho values ($\text{Y/Ho} = 17.7\text{-}24.7$), negative La, Y anomalies ($\text{La/La}^*_{\text{MUQ}} = 0.08\text{-}0.22$, $\text{Y/Y}^*_{\text{MUQ}} = 0.68\text{-}0.90$) and positive Eu anomalies ($\text{Eu/Eu}^*_{\text{MUQ}} = 2.17\text{-}2.70$).

Most of the magnetite layers show depletion in the LREE relative to middle and HREE ($\text{Nd/Yb}_{\text{MUQ}} = 0.08\text{-}0.6$) in the normalized plots with associated slight to moderate positive La, Y and Eu anomalies ($\text{La/La}^*_{\text{MUQ}} = 0.7\text{-}1.8$; $\text{Y/Y}^*_{\text{MUQ}} = 0.9\text{-}1.3$; $\text{Eu/Eu}^*_{\text{MUQ}} = 0.89\text{-}3.0$) and super-chondritic to chondritic Y/Ho values ($\text{Y/Ho} = 24.7\text{-}34.9$) (Fig. C.2B). In detail, the magnetite layers in samples MEL-029 and MEL-032 yield slightly anomalous HREE-depleted concentrations ($\text{Nd/Yb}_{\text{MUQ}} = 1.40\text{-}1.42$) which are also characterized with moderate positive La, Y and Eu anomalies.

C.4.2 Oxygen isotopes

The $\delta^{18}\text{O}$ values for chert sample MEL-008 show a range from +6.6 to +19.1‰ with a mean of +14.1‰ (n = 10), whereas in chert sample MEL-016 values range from +7.0 to +17.3‰ (mean of +12.2‰; n = 10), and for chert sample MEL-033, values range from +11.0 to +16.3‰ (mean of +14‰; n = 10). Of particular significance in this study are those analyses that depart from values close to +27‰, which is the $\delta^{18}\text{O}$ value of precursor amorphous silica predicted by Marin et al. (2010) for Archean chert. Instead, the data reported here are significantly lower by about +20 to +8‰ (Fig. C.3).

C.5 Discussion

C.5.1 REE+Y systematics

Most of the chert and magnetite samples in this study show similar shale-normalized patterns despite the fact that both of these domains represent the diagenetic transformation of different precursor materials (i.e., opaline silica and Fe oxyhydroxides, respectively). In both cases these patterns are characterized by: (1) HREE enrichment coupled with La and Y enrichments which strongly suggest interaction of seawater with Fe-oxyhydroxides (e.g., Bolhar et al., 2005; Thurston et al., 2012); (2) positive Eu anomalies which suggest the influence of high-temperature (>250°C) hydrothermal fluids (e.g., Allwood et al., 2010; Thurston et al., 2012); and (3) relatively consistent REE concentrations and chondritic Y/Ho values (i.e., Y/Ho \approx 27) which are indicative of a minor amount of detrital contamination (e.g., Bau and Dostal, 1994; Gourcerol et al., 2015a). In contrast, analyses on MEL-007C and MEL-008C samples are characterized by sub-chondritic Y/Ho ratios associated with negative La and Y anomalies which suggest coeval precipitation of Fe-oxyhydroxides in a restricted basin involving no REE+Y

recharge from the open ocean to re-equilibrate the REE+Y budget (e.g., Masuda et al., 1987; Bau, 1999). Thus, the dataset indicate that both of silica- and Fe-rich layers record the same signature of the chemical environment from which their precursor material precipitated. We refer here to the similar chemical behavior of the coexisting domains as chemical concordance which is important in that it provides evidence for the robustness of these materials which retain their primary chemical signatures despite post-depositional transformation. This conclusion therefore validates our earlier work (Gourcerol et al., 2015a) and that of others which uses such information to make inferences about the chemistry of the hydrosphere from which such materials precipitated. Moreover, this study demonstrates that beyond the capacity of *in-situ* LA-ICP-MS analyses to extract the primary signature information from chert bands in Archean Algoma-type BIFs, this method gives relatively important information on the Archean seawater geochemistry (e.g., open seawater vs. restricted basin environments).

C.6 Oxygen isotopes

The *in-situ* SIMS $\delta^{18}\text{O}$ data for the analyzed chert material reported here deviate markedly from the inferred primary $\delta^{18}\text{O}$ values of +27‰ that characterize Archean chert, the stable diagenetic product formed after primary amorphous opaline material (Marin et al., 2010). That the $\delta^{18}\text{O}$ data reported here are so much lower than the inferred starting material implies that there must have been considerable exchange of the original opaline material, or its subsequent replacive phase chert, with a fluid at high temperature. That modification of chert can occur has been noted in previous studies (e.g., Knauth and Lowe, 2003), due to interaction with high temperature (i.e., >200°C) hydrothermal fluids. What is explored here is the nature and origin of the fluid which interacted with the chert or its precursor and the thermal conditions under which this exchange occurred.

As the fractionation of oxygen isotopes is temperature-sensitive, modelling of the replacement of primary amorphous silica (i.e., $\delta^{18}\text{O} = +27\text{‰}$; Marin et al., 2010) with four different reacting fluids (i.e., $\delta^{18}\text{O}_{\text{H}_2\text{O}} = 0, +5, +10$ and $+15\text{‰}$) at variable temperature (30° to 300°C) was done (Fig. C.4) to evaluate which conditions were most likely to produce chert with the observed $\delta^{18}\text{O}$ values of $+6.6$ to $+19.1\text{‰}$. This modelling was done in the context of fluid:rock reactions using the equation of Taylor (1978) and we assume that the process by which the exchange proceeded was via dissolution-precipitation (e.g., Putnis, 2002; Putnis et al., 2007; Putnis and Putnis, 2010) which here involved transformation of the original opaline material to chert, as has been discussed in detail by Martin et al. (2010). As shown in Figure C.4, the fluid most likely fluid to have exchanged with the original opaline material during conversion to chert had $\delta^{18}\text{O}_{\text{H}_2\text{O}}$ values between 0 and $+5\text{‰}$ with the reaction permissible up to temperatures of 250°C ; the water:rock ratios implied by the model are considered to be reasonable. Furthermore, the modelling also shows that fluids with $\delta^{18}\text{O}$ values of $+10$ to $+15\text{‰}$, typical of metamorphic fluids (Sheppard, 1986), cannot account entirely for the observed range of $\delta^{18}\text{O}$ values of the chert, although it is noted that a fluid with $\delta^{18}\text{O}$ of $+10\text{‰}$ can accommodate some of the more enriched values (i.e., $+17$ to $+20\text{‰}$) if reaction occurred at 250° to 300°C . Thus, based on the model calculations, the most likely scenario to account for the observed $\delta^{18}\text{O}$ values of the chert involves transformation of the original amorphous opaline material in the presence of seawater during diagenesis. As this reaction progressed, it involved water which became hotter and modified, that is enriched in ^{18}O due to fluid:rock interaction, which would have been facilitated by increasing temperature.

C.6.1 Comparison and implications of the $\delta^{18}\text{O}$ and trace element data for chert

This study has demonstrated that the primary chemical signature of silica- and iron-rich layers in Archean BIF can survive post-depositional processes such as burial and metamorphism. The conclusion is verified by the observed chemical concordance of the REE+Y, as seen in shale-normalized plots (Fig. C.2) for these coexisting phases in this and other studies (Gourcerol et al., 2015a). In contrast to the latter and as noted by previous workers (e.g., Knauth and Lowe, 2003), the $\delta^{18}\text{O}$ signature of the siliceous material in some cases does not survive. This apparent difference between the trace element (e.g., REE+Y) and $\delta^{18}\text{O}$ signatures is considered to merely reflect the relative abundances of these respective elements in the starting material versus the reacting fluid. Thus, whereas oxygen makes up nearly 90% of the reacting fluid by weight, the trace elements of interest are $<10^{-5}$ chondritic values in this fluid (i.e., ocean water data from Alibo and Nozaki, 1999) versus $>10^{-2}$ chondritic values in the chert. Thus, during the coupled process of dissolution-precipitation and conversion of opaline material to chert, the low levels the REEs+Y in the reacting fluid were insufficient to modify the primary signal of the silica material. This observation and conclusion is similar to that observed in many alteration studies (e.g., Mercier-Langevin et al., 2014; Dostal et al., 2015) where the normalized chemical profiles of immobile elements (e.g., REEs, Ti, Nb, Zr) are retained despite there being a large amount of exchange of oxygen, as demonstrated by the change in $\delta^{18}\text{O}$ values for fresh versus altered whole rock material samples. In addition, the lack of change in the Si isotopic composition in some cherts despite changes in their $\delta^{18}\text{O}$ signature was similarly attributed to the low content of Si in the altering fluids by Marion-Carbonne et al. (2014) in their study of a variety of Precambrian cherts.

C.7 Conclusions

This integrated study of the trace element (REE+Y) and oxygen isotopic signature of interbedded chert and magnetite layers for a singular BIF has been used to assess the influence of post-depositional exchange of these materials, for both silica- and iron-rich layers, with fluids of diagenetic, metamorphic or hydrothermal (i.e., mineralizing type) origin. In the case of the trace element data, it has been shown that the primary REE+Y signals of these layers are preserved, as demonstrated through their chemical concordance. Thus, the chemistry of these contrasting chemical domains (i.e., chert and iron-rich) can be used with confidence to characterize the fluid reservoir(s) from which they originated, in this case the hydrosphere of the early Earth. In contrast, the $\delta^{18}\text{O}$ values of chert layers depart distinctly from their inferred primary values and record exchange with post-depositional fluids as a result of dissolution-precipitation reactions during burial of the material. In this case we suggest that the $\delta^{18}\text{O}$ data reflect exchange of the original amorphous opaline material with seawater during burial with a fluid that was progressively heated and enriched in ^{18}O due to fluid:rock interaction. Lastly, that the trace element chemistry and ^{18}O data should convey different conclusions is a function of both the water:rock ratio and the fact that the reacting fluid was dominated by oxygen versus its very low levels (i.e., $<10^{-5}$ chondrite) of the relevant trace elements (REE+Y).

C.8 Acknowledgments

The authors gratefully acknowledge the assistance of staff of the staff of Agnico Eagle Mines Ltd. and Goldcorp Ltd. who provided access to property for sampling. The LA-ICP-MS analyses were done in the Geochemical Fingerprinting Laboratory at Laurentian University with the capable assistance of Dr. J. Petrus and the oxygen isotope analyses were performed in the

SIMS laboratory at the University of Manitoba (Winnipeg) with the capable assistance of Mr. R. Sharp.

C.9 Figures and captions

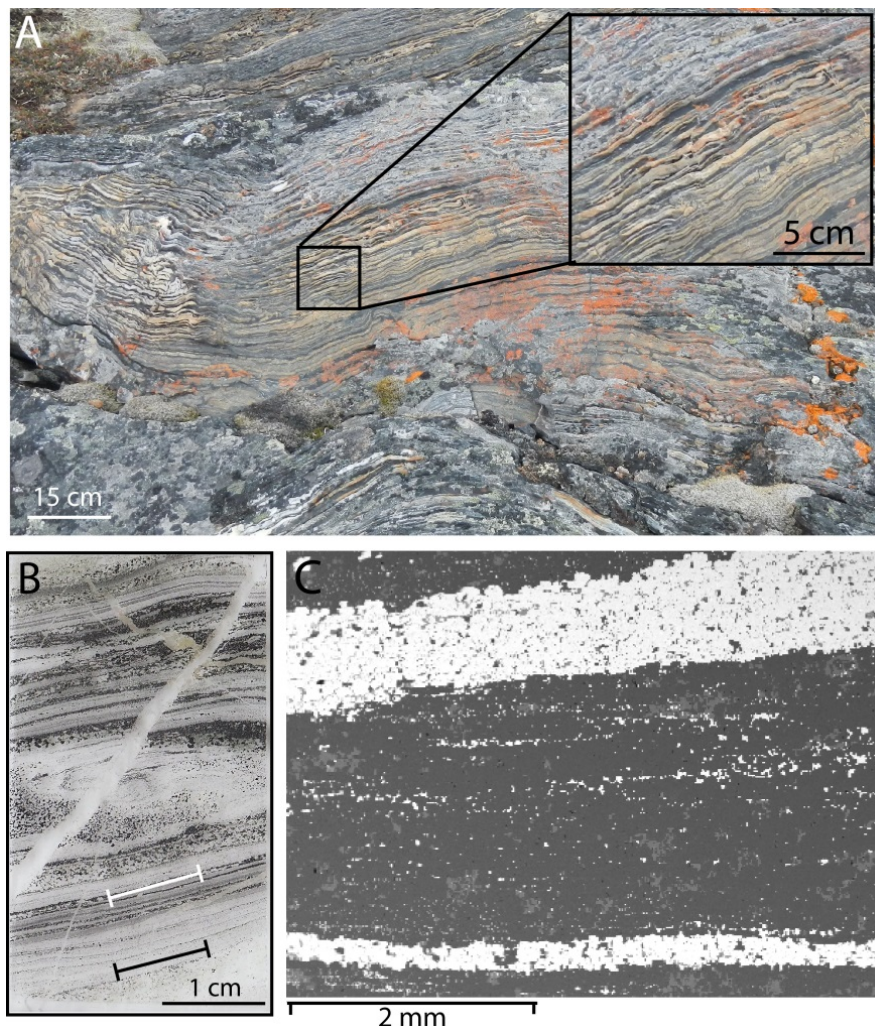


Figure C.1: Photographs taken at different scales that illustrate the nature of the layered chert and magnetite material in the BIFs from the Meliadine area that were used in this study: (A) Outcrop photo showing the well layered nature of the BIF that characterizes material from this locality. Note the alternating layers of chert and magnetite that

can be seen in the enlarged part of the outcrop shown as the inset image; (B) Image of the polished thin section of the BIF from the outcrop in previous image which shows the alternating chert and magnetite layers. The black solid line represents the laser ablation traverse done on the chert layer as part of our previous LA-ICP-MS study (Gourcerol et al., 2015a, b), whereas the white solid line represents the line traverse of the magnetite layer done in this study; and (C) A SEM back-scattered electron image (SEM-BSE) of the BIF showing alternating layers of chert (dark) and magnetite (bright).

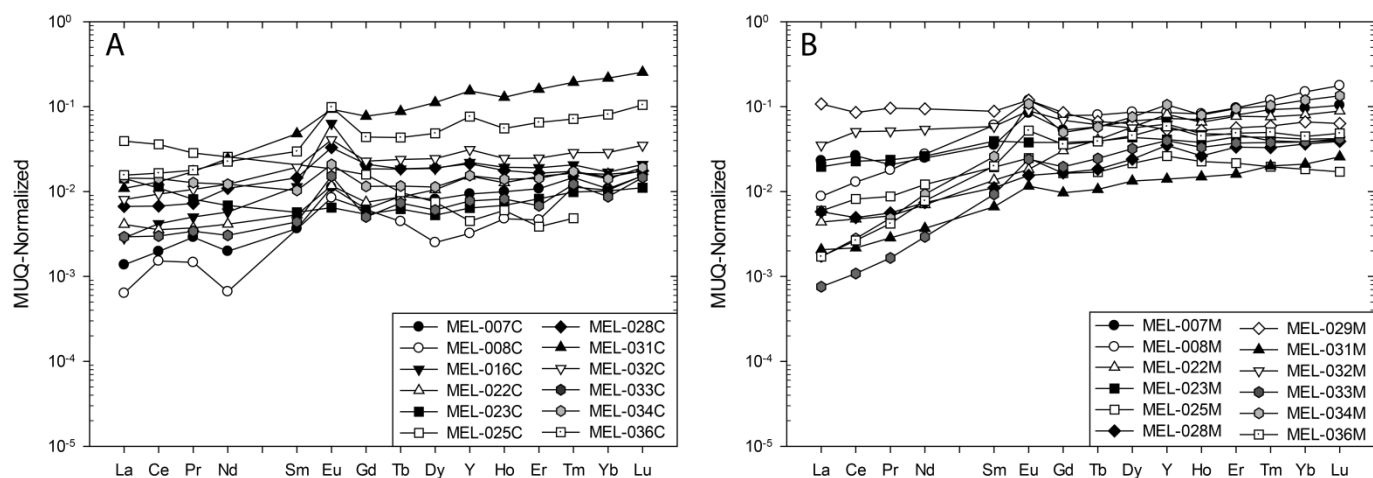


Figure C.2: Shale (MUQ) - normalized rare earth element (REE) patterns for (A) chert layers and (B) magnetite layers from BIF material from Meliadine. Note how both the REE concentrations and the normalized profiles for these different materials are similar.

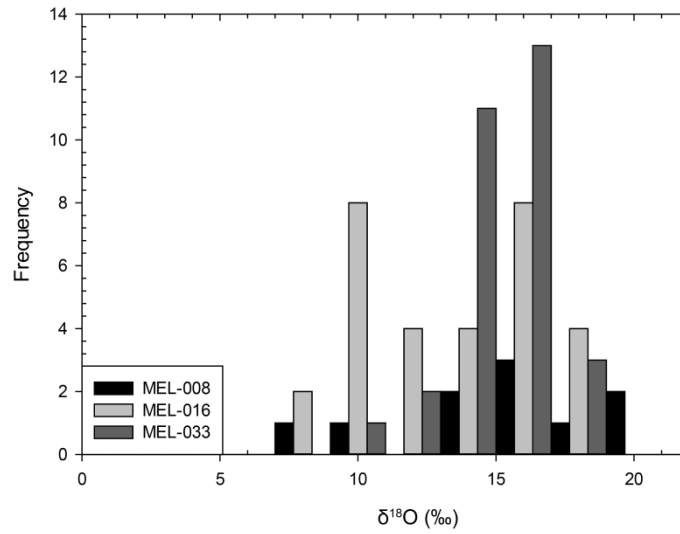


Figure C.3: A histogram plot summarizing the $\delta^{18}\text{O}$ values for three chert samples from Meliadine: MEL-008 (black), MEL-016 (light grey) and MEL-033 (dark grey). Note the large spread of the data and departure from the +27 ‰ value which is the value of precursor amorphous silica in Archean BIF settings (Marin et al., 2010).

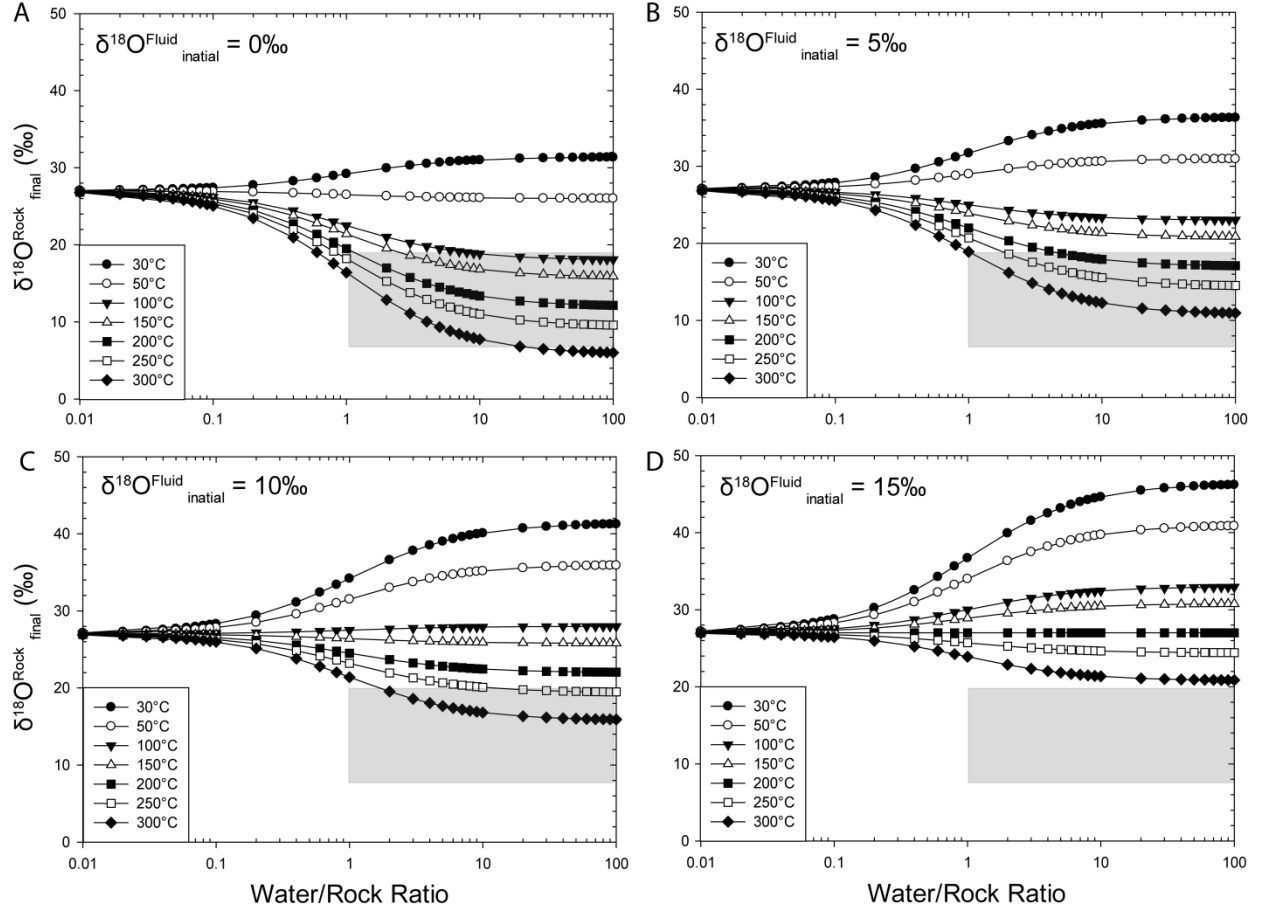


Figure C.4: Diagram summarizing the variation of calculated values of $\delta^{18}\text{O}_{\text{chert}}$, using the equations of Taylor (1978) and variety of appropriate silica- H_2O ^{18}O fractionation factors (Kawabe, 1978; Matsuhisa et al., 1979; Kita et al., 1985), as a function of temperature (30° to 300°C) and water/rock ratios for four reacting fluids having $\delta^{18}\text{O}_{\text{H}_2\text{O}} = 0, +5, +10$ and $+15\text{‰}$ (respectively A, B, C, and D). The shaded area represents the range of $\delta^{18}\text{O}$ values (i.e., $+6.6$ to $+19.1\text{‰}$) obtained for chert from the Meliadine gold district (see Fig. C.3). Note that the value of the initial $\delta^{18}\text{O}_{\text{chert}}$ was assumed to be $+27\text{‰}$, which is the value of precursor amorphous silica in Archean BIF settings (Marin et al., 2010).

C.10 References

- Allwood, A.C., Kamber, B.S., Walter, M.R., Burch, I.W. and Kanik, I., 2010. Trace element record depositional history of an Early Archean stromatolitic carbonate platform; *Chemical Geology*, v. 270, p. 148-163.
- Angerer T., Hagemann S.G., and Danyushevsky L., 2012. Geochemical evolutions of the banded iron formation-hosted high-grade iron ore system in the Koolyanobbing Greenstone Belt, Western Australia; *Economic Geology*, v. 107, p. 599-644.
- Bau, M., 1999. Scavenging of dissolved yttrium and rare-earths by precipitating iron oxyhydroxide: Experimental evidence for Ce oxidation, Y-Ho fractionation, and lanthanide tetrad effect; *Geochimica et Cosmochimica Acta*, v. 63, no. 1, p.67-77.
- Bau, M. and Dulski, P., 1994. Evolution of the yttrium-holmium systematics of seater through time; *Mineralogical Magazine - Goldschmidt Conference Abstracts*, v. 58A, p. 61-62.
- Bolhar, R., Van Kranendonk, M.J. and Kamber, B.S., 2005. A trace element study of siderite-jasper banded iron formation in the 3.45 Ga Warrawoona Group, Pilbara craton-Formation from hydrothermal fluids and shallow seawater; *Precambrian Research*, v. 137, p. 93-114.
- Dostal, J., Kontak, D.J., Gerel, O., Shellnut, G. and Fayek, M., 2015. Origin of Cretaceous ongonites (topaz-bearing albite-rich micro-leucogranites) from Ongon Khairkhan, Central Mongolia; *Lithos*, v. 236-237, p. 173-189.
- Gourcerol, B., Thurston, P.C., Kontak, D.J. and Côté-Mantha, O., 2015a. Interpretations and implications of preliminary LA ICP-MS analysis of chert for the origin of geochemical

signatures in banded iron formations (BIFs) from the Meadowbank gold deposit, Western Churchill Province, Nunavut; *Chemical Geology*, v. 410, p. 89-107.

Gourcerol, B., Thurston, P.C., Kontak, D.J., Côté-Mantha, O. and Biczok, J., 2015b.

Depositional Setting of Algoma-type Banded Iron Formation from the Meadowbank, Meliadine and Musselwhite gold deposits; In: Targeted Geoscience Initiative 4: Contributions to the Understanding of Precambrian Lode Gold Deposits and Implications for Exploration, (eds.) B. Dubé and P. Mercier-Langevin; Geological Survey of Canada, Open File 7852, p. 55-68.

Holland, H.D., 2005. Sedimentary mineral deposits and the evolution of Earth's near-surface environments; *Economic Geology*, v. 100, p. 1489–1509.

Huston, D.L. and Logan, G.A., 2004. Barite, BIFs and bugs: Evidence for the evolution of the Earth's early hydrosphere; *Earth and Planetary Science Letters*, v. 220, p. 41–55.

James, H.L., 1954. Sedimentary facies iron-formation; *Economic Geology*, v. 49, p. 235-293.

Kawabe, I., 1978. Calculation of oxygen isotope fractionation in quartz-water system with special reference to the low temperature fractionation. *Geochimica et Cosmochimica Acta*, v.42, p. 613-621.

Kita, I., Taguchi, S. and Matsubaya, O., 1985. Oxygen isotope fractionation between amorphous silica and water at 34-93°C. *Nature*, v. 314, p. 83-84.

Knauth, L.P. and Lowe, D.R., 2003. High Archean climatic temperature inferred from oxygen isotope geochemistry of chert in the 3.5 Ga Swaziland Supergroup; *Geological Society of*

- America Bulletin, v. 115, p. 566-580.
- Li, W., Jin, X., Gao, B., Wang, C. and Zhang, L., 2014. Analysis of ultra-low level rare earth elements in magnetite samples from banded iron formations using HR-ICP-MS after chemical separation; *Analytical Methods*, v. 6, p. 6125-6132.
- Matsuhisa, Y., Goldsmith, J.R. and Clayton, R.N., 1979. Oxygen isotopic fractionation in the system quartz-albite-anorthite-water. *Geochimica et Cosmochimica Acta*, v. 43, p. 1131-1140.
- Mercier-Langevin, P., Lafrance, B., Becu, V., Dubé, B., Kjarsgaard, I. and Guha, J., 2014. The Lemoine auriferous volcanogenic massive sulfide deposit, Chibougamau Camp, Abitibi Greenstone Belt, Quebec, Canada: Geology and genesis; *Economic Geology*, v. 109, p. 231-269.
- Marin, J., Chaussidon, M. and Robert, F., 2010. Microscale oxygen isotope variations in 1.9 Ga Gunflint cherts: assessments of diagenesis effects and implications for oceanic paleo-temperature reconstructions; *Geochimica et Cosmochimica Acta*, v. 74, p. 116-130.
- Marin-Carbonne, J., Robert, F. and Chaussidon, M., 2014. The silicon and oxygen isotope compositions of Precambrian cherts: A record of oceanic paleo-temperatures? *Precambrian Research*, v. 247, p. 223-234.
- Masuda, A., Kawakami, O., Dohmoto, Y. and Takenaka, T., 1987. Lanthanide tetrad effects in nature: two mutually opposite types, W and M; *Geochemical Journal*, v. 21, p. 119-124.
- Pickard, A.L., Barley, M.E. and Krapez, B., 2003. Deep-marine depositional setting of banded

iron formation: sedimentological evidence from interbedded clastic sedimentary rocks in the early palaeoproterozoic Dales Gorge member of Western Australia. *Sedimentary Geology* 170, 37-62.

Posth, N.R., Kohler, I., Swanner, E.D., Schroder, C., Wellmann, E., Binder, B., Konhauser, K.O., Neumann, U., Berthold, C., Nowak, M. and Kappler, A., 2013. Simulating Precambrian banded iron formation diagenesis; *Chemical Geology*, v. 362, p. 66-73.

Putnis, A. 2002. Mineral replacement reactions: from macroscopic observations to microscopic mechanisms; *Mineralogical Magazine*, v. 66, p. 689-708.

Putnis, A. and Putnis, C.V, 2010. The mechanism of re-equilibration of solids in the presence of a fluid phase; *Journal of Solid State Chemistry*, v. 180, p. 1783-1786.

Putnis, C.V., Geisler, T. Schmid-Beurmann, P., Stephan, T. and Giampaolo, C., 2007. An experimental study of the replacement of leucite by analcime; *American Mineralogist*, v. 92, p. 19-26.

Sheppard, S.M.F., 1986. Characterization and isotopic variations in natural waters. In: *Stable isotopes in high temperature geological processes*, Valley, J.W., Taylor, H.P.Jr. and O'Neil, J.R. (eds.); *Reviews in Mineralogy*, v. 16, p. 165-184.

Taylor, H.P., 1978. Oxygen and hydrogen isotope studies of plutonic granitic rocks; *Earth Planetary Science Letter*, v. 38, p. 177-210.

Thurston, P.C., Kamber, B.S. and Whitehouse, M., 2012. Archean cherts in banded iron formation: Insight into Neoarchean ocean chemistry and depositional processes;

Precambrian Research, v. 214-215, p. 227-257.

Van den Boorn, S.H.J.M., Van Bergen, M.J., Vroon, P.Z., de Vries, S.T. and Nijman, W., 2010.

Silicon isotope and trace element constraints on the origin of 3.5 Ga cherts: implications for early Archaean marine environments; *Geochemica et Cosmochimica Acta*, v. 74, p. 1077-1103.

Van Kranendonk, M. J., 2006. Volcanic degassing, hydrothermal circulation and the flourishing of early life on Earth: A review of the evidence from c. 3490-3240 Ma rocks of the Pilbara Supergroup, Pilbara Craton, Western Australia; *Earth-Science Reviews*, v. 74, p. 197-240.

Westall, F., Campbell, K.A., Bréhéret, J.G., Foucher, F., Gautret, P., Hubert, A., Sorieul, S., Grassineau, N. and Guido, D.M., 2015. Archean (3.33 Ga) microbe-sediment systems were diverse and flourished in a hydrothermal context; *Geology*, v. 43, p. 615-618.